DTU Library

Application of Phasor Measurements for Online Monitoring and Adaptive Control of Electromechanical Oscillations

Haugdal, Hallvar

Link back to DTU Orbit

Application of Phasor Measurements for Online Monitoring and Adaptive Control of Electromechanical Oscillations

Hallvar Haugdal
January 2022

NTNU

DTU

Preface

This thesis is submitted in partial fulfillment of the requirements for acquiring a joint PhD Degree at the Norwegian University of Science and Technology (NTNU) and the Technical University of Denmark (DTU).

The PhD project was funded by NTNU, and the research was carried out at the Department of Electric Power Engineering at NTNU and at the Department of Electrical Engineering at DTU in the period between 1 January 2018 and 14 January 2022.

Acknowledgements

First, I would like to express my gratitude to my team of supervisors. At NTNU, Kjetil Uhlen was my supervisor. First of all, thanks for encouraging me to apply for this position. Before starting on the PhD I had a position as a scientific assistant at NTNU, and was enjoying my time studying electromagnetic fields inside electric machines. Although I had limited experience with power system dynamics and stability at the time, I'm very happy that I applied for the position. Kjetil provided me with lots of useful insights along the way, and pointed me in the right direction many times.

At DTU, Hjörtur Jóhannsson and Arne Hejde Nielsen were my supervisors. As Arne retired, Jacob Østergaard took his place for the last semester. Thanks for all the good advice, and for welcoming me to DTU for my external stay, making this a memorable experience. I was introduced to Hjörtur's (among others') work on real-time applications for monitoring and control of power systems, which inspired me a lot. Also, I enjoyed the Friday bar tradition at DTU, which was a nice, informal setting to hang out with PhDs, professors, and others at the department.

Furthermore, I'd like to thank all my friends and colleagues. In particular, Daniel Müller at DTU for the nice collaboration, for welcoming me at DTU during my external stay and for the help with finalizing the thesis; Daniel Baltensperger at NTNU, for all the interesting discussions and coffee breaks; Robert Nilssen, who got me my first position at NTNU after my studies; Frank Mauseth, for all the entertaining coffee breaks; Trond Leiv Toftevaag, who has shared his passion for both electric machines and music; and the Power Challengers, the football team at the department, for all the exhausting but fun football practices and matches.

Finally, a very special thanks to my parents, for encouraging me to study engineering; to Line and Solveig, for the love and support at home; and Hedvig (the cat), for the good company in the home office during the lockdown.

Summary

Transmission system operators around the globe are facing challenges related to ensuring the secure and resilient operation of the future power system. These challenges are in large part caused by trends associated with climate change: Fossil fuel power plants are being decommissioned and replaced by renewable energy sources, and both the demand for electricity and imports/exports of electric energy between countries are increasing, which causes faster fluctuations and higher variability in the power flows in the system. This makes it more difficult to design and tune control systems responsible for stabilizing the system.

In parallel to this development, heavy investments are being made in measurement and communication infrastructure targeting monitoring, control, and protection of the power system, and the number of controllable devices, in the form of Converter-Interfaced Generation, Flexible AC Transmission System devices and HVDC links, is increasing. In this thesis, we investigate how the increasing availability of real-time measurements and potential control actuators can be used for the purpose of stabilizing the system.

Specifically, periodic small signal rotor angle stability is targeted. If the system is not stable in this sense, standing or growing rotor angle oscillations might appear spontaneously, often referred to as electromechanical oscillations due to the interaction between electrical and mechanical elements. The typical problem related to this instability in today's power systems is oscillations between weakly connected areas of generation with high power transfers between them, referred to as inter-area oscillations, typically occurring within a frequency range of 0.1 to 0.8 Hz. The system is particularly vulnerable to this instability when it is in an unusual or unscheduled state of operation.

The most important research contributions presented in this thesis target two equally crucial sides of the stability problem: *Measuring/monitoring* oscillations and *damping control* for mitigating oscillations.

The first contribution is a monitoring method based on statistical learning methods, which provides information about the frequency and observability of oscillatory modes by analyzing phasor measurements. The method is targeted toward online operation, aiming to continuously provide operators with situational awareness in the form of information about the oscillatory modes in the system.

Three contributions targeting damping control of oscillations are presented, which represent enhancements of a specific, well known type of oscillation damping controller known as the Phasor Power Oscillation Damper in the literature. Two of the contributions are investigations into how more knowledge about the system (among others, the information provided by the monitoring method) and higher availability of measurements can be exploited for damping control purposes. Another contribution concerns developing this type of controller into a self-tuning, adaptive controller, capable of following changing operating conditions. Simulation results indicate that enhanced performance can be achieved by taking more information into account, and that the adaptive variant of the controller outperforms a comparable variant in the literature under the tested conditions.

Finally, a simulation tool was developed throughout the work with the thesis, which is the last contribution. The aim of the tool is to provide an open and transparent platform for prototyping monitoring, control, and protection applications of the future power system, and was developed specifically for testing the presented control methods.

With these contributions, it is the aim of this thesis to provide operators with methods and tools to gain increased situational awareness and new options for remedial action for handling instabilities, with the ultimate goal of facilitating stable, secure, and resilient operation of the future power system.

Contents

Abbreviations

AVR	Automatic Voltage Regulator
CIG	Converter-Interfaced Generation
CIM	Control-Input Model
CPC	Complex Principal Component
CPCA	Complex Principal Component Analysis
DAE	Differential Algebraic Equations
DBSCAN	Density-Based Spatial Clustering of Applications with Noise
EMD	Empirical Mode Decomposition
FACTS	Flexible AC Transmission Systems
HVDC	High Voltage Direct Current
LPF	Low-Pass Filter
MMAE	Multiple Model Adaptive Estimation
ODE	Ordinary Differential Equations
OPTICS	Ordering Points To Identify the Clustering Structure
P-POD	Phasor POD
P-POD-0	Conventional Phasor POD
P-POD-CIM	Phasor POD with Control-Input Model
PCA	Principal Component Analysis
PDC	Phasor Data Concentrator
PI	Proportional Integral
PMU	Phasor Measurement Unit
POD	Power Oscillation Damper
PSS	Power System Stabilizer
RLS	Recursive Least Squares
SVC	Static Var Compensator
TCR	Thyristor Controlled Reactor
TCSC	Thyristor Controlled Series Capacitor
WAMPAC	Wide Area Monitoring, Protection, and Control

Chapter 1

Introduction

Ensuring stable and secure operation of the power system is an increasingly complex challenge that system operators will face in the coming years and decades. Global trends associated with climate change are affecting the development of power systems to a great extent, and will continue to do so in the future. Through the Paris Agreement [1], most nations have agreed to reduce their climate gas emissions. New pledges were made in the Glasgow Climate Pact [2], and the ambitions are expected to increase in the future. This causes an increased interest in renewable energy sources, an increasing electricity demand, increasing exchange of energy between countries, and decommissioning of fossil fuel power plants [3–5]. These trends affect power systems around the globe in many ways, but in general, it must be expected that in most systems, ensuring safe and resilient operation will become more challenging in the future.

Renewable energy sources like wind and solar power are variable, weather dependent sources whose production can only be controlled to a limited extent compared to, for instance, hydro power with reservoirs. Furthermore, this type of generation is often interfaced to the grid through power electronics converters, whose behavior is substantially different from synchronous generation. This introduces new stability concerns [6].

Due to the increasingly volatile generation mix, the flow of electric power through the transmission system will fluctuate more rapidly and unpredictably. Traditionally, the typical direction of the power flow was from large power plants toward consumption centers. In the near future, the range of typical power flows in the system will be much wider; for instance, systems might have to be able to operate with a high share of renewable production during windy and sunny weather, while during

low renewable production, the system demand might have to be covered by imports. Thus, in many transmission systems, there will be a larger variety of operating conditions that must be taken into account when designing and tuning control systems responsible for stabilizing the system. On the one hand, designing control systems that are effective under all the expected operating conditions is a challenge in itself. On the other hand, an increasingly complex system with higher variability must also be expected to end up in an alert or unscheduled state more often, where stability problems are more likely to occur. Further, climate change is already causing an increased frequency of extreme weather events, which further aggravates the situation.

On the demand side, an increasing share of the energy consumption is shifting toward electricity. Within transportation, fossil fuel-driven cars, buses, ferries, and soon airplanes, are gradually being phased out and replaced by electric alternatives. The increasing demand requires building new transmission lines to avoid overloading, and incentivizes maximizing the transfer capacity by operating the system closer to the stability limits. To ensure the stability of the system, it is of crucial importance that the operators have methods for monitoring emerging instabilities, and methods for remedial action in case instabilities occur.

During recent decades, there has been an extensive development of measurement and communication infrastructure targeted toward monitoring, control, and protection of power systems. Phasor Measurement Units (PMUs) are being installed in the power grid in most countries, and in many grids we are approaching a deployment level where the system dynamics can be monitored accurately in real-time. The number of controllable units is also increasing. Converter-Interfaced Generation (CIG) or loads and Flexible AC Transmission System (FACTS) devices can be used for ancillary services like voltage support or power oscillation damping [7]. This leaves the transmission system operators (TSOs) with an increasing amount of measurement data that must be digested into useful information, and an increasing number of potential actuators through which remedial action can be applied. On a high level, the problem that is addressed in this thesis can be stated as the following research question:

> How can we make use of the increasing availability of real-time measurements and potential actuators to ensure the stability and resilience of the future power system?

In this thesis, the specific stability problem of *periodic small signal rotor angle stability* is addressed, discussed in further detail in Section 1.1.1. If the system is not sufficiently stable in this sense, then the response fol-

lowing a disturbance or event might be dominated by sustained or growing low frequency oscillations. The characteristics of these oscillations are determined by the interaction of mechanical dynamics of rotating parts in synchronous machines, and electric dynamics of the transmission network, windings in synchronous machines, loads, etc., and are therefore often referred to as *electromechanical oscillations*. The term *power oscillations* is also often used, since these oscillations are highly observable in active power measurements. Throughout this thesis, these terms are used interchangeably.

Electromechanical oscillations, usually appearing in the frequency range 0.1 to 2.0 Hz [8], were mitigated from the mid 1960s onwards [9] by deployment of Power System Stabilizers (PSS) on all major generating plants. However, this instability was far from eliminated, illustrated by events like the 10 August 1996 blackout in the US [10], discussed in closer detail in Section 1.1.2. In this case, and in many other cases of severe electromechanical oscillations, the system was in a stressed condition, e.g., high load in combination with loss of lines or outage of important equipment.

The above outlined aspects motivating the work in this thesis can be summarized in the following four key points:

- The design and tuning of stabilizing control systems will become more difficult as a wider range of operating points must be accommodated.

- Due to a more complex system with faster and larger fluctuations, and due to more extreme weather, the system must be expected to end up in unscheduled operating points more often, which were not taken into account when designing and tuning the stabilizing control systems.

- There is an increasing amount of real-time measurement data that can be used for monitoring and for stabilizing control.

- There is an increasing availability of actuators in the form of FACTS, HVDC links, and CIG, through which stabilizing control actions can be applied.

Motivated by these points, the objective is to develop methods that make use of the increasing availability of measurements and actuators, specifically: Methods for monitoring electromechanical oscillations, providing useful information and situational awareness, and control methods for mitigating unstable electromechanical oscillations.

In the following, relevant background on electromechanical oscillations is presented, before the contributions, the publications, and the outline of the thesis are given.

1.1 Background

Three topics are elaborated on in this section: Definition and classification of power system stability; previous events with unstable electromechanical oscillations; and finally, PMU-based Wide Area Monitoring, Protection, and Control.

1.1.1 Power System Stability Classification

The power system stability definition proposed by the IEEE/CIGRE Joint Task Force on Stability Terms and Definitions [11] in 2004 is as follows:

> Power system stability is the ability of an electric power system, for a given initial operating condition, to regain a state of operating equilibrium after being subjected to a physical disturbance, with most system variables bounded so that practically the entire system remains intact.

Three subcategories of power system stability were proposed in [11]: Rotor Angle Stability, which refers to the ability of the synchronous machines in the system to remain in synchronism following a disturbance; and Frequency Stability and Voltage Stability, which refer to the ability of the system to maintain a steady frequency and voltage following a disturbance, respectively. In recent years, the penetration of Converter-Interfaced Generation has increased steadily, and to account for this, two additional subcategories were proposed recently in [12]: Resonance Stability and Converter-driven Stability. The resulting classification tree is shown in Fig. 1.1

Rotor Angle Stability can be further classified into Small-Disturbance Angle Stability or Transient Stability. Periodic/Oscillatory Rotor Angle Stability is one special case of Small-Disturbance Angle Stability, and refers to the situation where the system responds to a disturbance with pronounced electromechanical oscillations. These oscillations are commonly classified as either local oscillations or inter-area oscillations. Local oscillations involve a single generator oscillating against the rest of the system, or generators within a local area oscillating against each other. Inter-area oscillations involve areas of generation interconnected by long inter-ties oscillating against each other. Local oscillations are
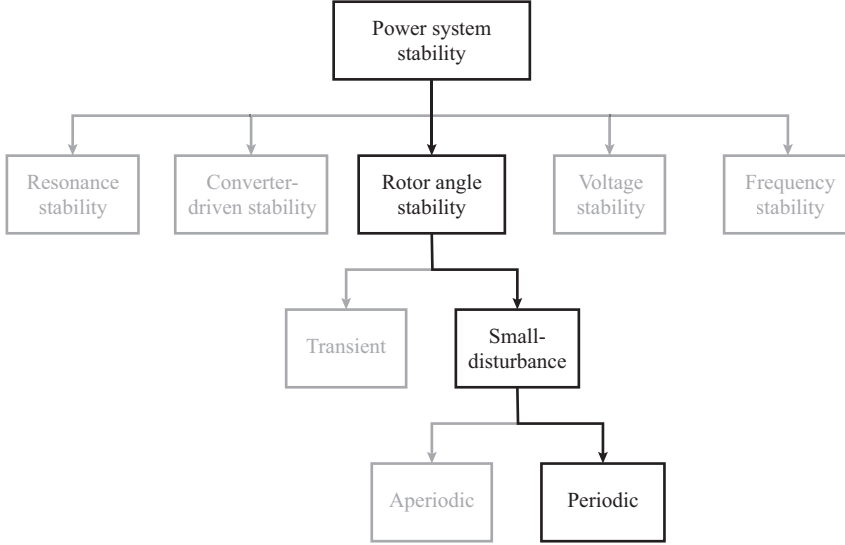
Figure 1.1: The subcategories of power system stability proposed in [12] , where Periodic Small-Disturbance Rotor Angle Stability is emphasized.

typically in the frequency range $0.7 - 2\,\mathrm{Hz}$, while inter-area oscillations have a lower frequency, typically in the range $0.1 - 0.8\,\mathrm{Hz}$ [8].

Electromechanical oscillations are an inherent characteristic of the synchronous machine-dominated power system. One or more dominant inter-area modes (i.e., modes with low damping) are most often visible to some extent during normal operation, and can not be eliminated completely. However, oscillations might become problematic if the damping is very low, and are certainly problematic if the damping approaches zero or becomes negative. In this case, the system operators are forced to take remedial action to avoid further deterioration of the situation. In practice, inter-area oscillations are typically the most troublesome category in modern power systems, as illustrated by the events described in the succeeding section.

1.1.2 Previous Events

Numerous incidents due to insufficient periodic rotor angle stability are described in the literature, e.g., in [13]. One of the most frequently referenced events is the failure that occurred in the Western Systems Coordinating Council (WSCC) system on 10 August 1996 [10]. Prior to the blackout, the system experienced high loading on multiple lines. Ad-

ditionally, two lines were disconnected, and a transformer was out due
to maintenance. During these operating conditions, an important line
was tripped due to sagging close to a tree. The power transfer shifted
to other lines, which were overloaded and tripped. Following sequential
tripping of 13 generating units at a power plant, the system ended up
in an unstable operating point with sustained oscillations with a fre-
quency of about 0.2 Hz. Interestingly, as described in [10], a simulation
model based on dynamic data assembled from individual utilities pre-
dicted that the unstable operating point was stable. This illustrates the
difficulty in establishing sufficiently accurate dynamic system models,
despite availability of the required dynamic data.

In 2011, two oscillatory events were recorded in the Continental Eu-
rope (CE) power system [14], on February 19 and 24, respectively. The
two events were highly similar. No direct cause was identified; however,
the oscillations started around the turn of the hour. This could indi-
cate that the planned changes in generation around Europe resulted in
an unstable operating condition. It is also noted in [14] that the load-
ing of the system was low, and that "the dispersed generation (such as
wind and PV) don't influence negatively but subtract 'stabilized inertia'
from classical groups equipped with PSS." Italy experienced the highest
amplitude of the 0.25 Hz oscillations, oscillating in opposite phase to,
among others, Denmark. This led to reinforcement of the PSS controls
in Italy in the aftermath of the events.

In 2016, an unexpected tripping of a line in France caused 0.15 Hz
oscillations where the Iberian Peninsula oscillated against the central
part of the Continental European system, and in phase (approximately)
with Turkey [15]. After three minutes, the oscillations were successfully
damped by reducing the exchange between Spain and France. In [15], it
is concluded that "The event demonstrates that coincidence and combi-
nation of different factors can influence the system stability", and that
"The event has confirmed the need for improving our knowledge of the
oscillatory properties of the CE system."

In 2017, 0.3 Hz oscillations were experienced in the Continental Eu-
ropean system [16], where plants in Southern Italy oscillated in phase
with Southern France and Switzerland, among others, and in opposite
phase to Germany, Denmark, and France. Very low consumption, high
imports in the southern part of the system, and unusual power flow due
to unavailability of generators have been identified as potential causes
leading to the event. It is concluded that "...additional innovative damp-
ing countermeasures and devices must be developed and introduced into
the grid in order to minimize serious consequences of inter-area oscilla-
tions."

The above events demonstrate that large power systems are still vulnerable to unstable low frequency oscillations, in particular during unusual operating conditions or following unexpected disturbances. There is also reason to believe that events like these will become more frequent in the future, in particular due to larger and faster fluctuations in operating conditions and increasing frequency of extreme weather events. This motivates the research work in this thesis on development of online methods for monitoring oscillations and control methods for mitigating oscillations.

1.1.3 Wide Area Monitoring, Protection, and Control

Severe blackouts, like the mentioned 1996-blackout in the US [10], boosted the development and deployment of the Phasor Measurement Unit (PMU) technology. Some of the first important research work on developing PMUs is given in [17] and [18]; eventually, this technology has reached the power grid in most countries around the globe.

A PMU measures voltage and/or current at a strategic location in the power system, extracts the amplitude and phase angle from the waveform in the measured signal, and transmits the result to a Phasor Data Concentrator (PDC) at a rate commonly around 10-50 Hz (or 60 Hz, depending on the system frequency). PMUs deployed over wide areas are synchronized using GPS signals, so that angle differences can be reliably compared. The PDC receives PMU data from multiple locations, and either stores the data or transmits it further to a higher level PDC, or to applications for Wide Area Monitoring, Protection, and Control (WAMPAC).

The reporting rate of PMUs is sufficiently high that detailed information about the state of the system can be extracted, given that sufficiently many units are deployed. Stored PMU data can be applied for offline analysis of disturbances or events, and tuning and validation of dynamic power system models [19]. Online monitoring applications continuously analyze the stream of PMU data from the PDC. Applications targeting, e.g., voltage stability [20], aperiodic rotor angle stability [21], or periodic rotor angle stability [22] provide operators with useful insights on emerging instabilities, critical areas or elements, stability margins and more. Typical applications of PMU data for real-time control or protection include power flow control, emergency control against voltage or frequency instability, or power oscillation damping control [19].

1.2 Contributions and Publications

Seeking to contribute to the outlined areas of research, five contributions are presented in this thesis. The contributions are published/submitted for publication in six papers, which are listed after the contributions.

Contribution I: This contribution, published in Papers I & II, represents an online method for estimating mode frequency and observability mode shapes from PMU measurements, which is based on techniques from the statistical learning domain. Mode shapes, as discussed in closer detail in Section 2.3, give information about the amplitude and phase with which oscillations at a particular frequency can be observed throughout the system. The term *online* in this respect refers to the fact that the method is suitable for use in an operational context, continuously updating mode and mode shape estimates as new measurements arrive. The aim is to provide operators with increased situational awareness once sustained or low damped oscillations appear by displaying information about frequency and pointing out which areas of the system are involved.

Contribution II-A: This contribution represents an enhancement to a particular type of Power Oscillation Damper (POD) control referred to as the Phasor POD (P-POD) in the literature, which is most often used for modulating FACTS devices for damping oscillatory modes. Fundamental to the operation of this damping controller is an estimator, which estimates a phasor that represents the instantaneous amplitude and phase of oscillations in the measurement. The damping signal is generated from that phasor by performing a suitable phase shift and transforming it to time domain, before it is amplified and used to modulate the actuator. With Contribution II-A, which is published in Paper V, the damping performance of the P-POD is enhanced. This is achieved by introducing a predictor-corrector phasor estimator in the form of a Kalman filter, where the prediction step is based on the control signal applied by the controller. Results indicate that this enhancement facilitates more precise damping of oscillations, where higher damping is achieved for the same control cost.

Contribution II-B: With this contribution, published in Paper VI, the P-POD is developed into an adaptive controller with adaptive phase compensation, capable of adjusting internal parameters to changing operating conditions. This work is an extension of Contribution II-A, based on the main idea of developing a phasor

estimator capable of not only making predictions, but also *improving* its predictions. This is achieved by introducing a Multiple Model Adaptive Estimation (MMAE) scheme, where a bank of Kalman filters are running in parallel. By assessing the estimation accuracy of the different filters, the system model is inferred and used to update the tuning of the controller.

Contribution II-C: This contribution facilitates multiple input measurements to the P-POD, where information about observability mode shapes is also taken into account. The final stage of this work is not published, but an intermediate step is published in Paper III. The aim of this work is to investigate how estimated quantities from the mode estimation method (Contribution I) can be used not only for monitoring/situational awareness, but also for increasing the damping of the system.

Contribution III: This contribution is a power system simulation tool developed throughout the research work related to this thesis, presented in Paper IV. The tool is coded in the programming language Python, which is known for being easy to read and write, aiming to provide a platform for efficient development and testing of WAMPAC applications. The tool was developed specifically to be able to work efficiently with Contributions II-A, II-B, and II-C.

The contributions have been published/submitted for publication in the following papers:

Paper I: H. Haugdal and K. Uhlen, "Mode Shape Estimation using Complex Principal Component Analysis and k-Means Clustering", in 2019 International Conference on Smart Grid Synchronized Measurements and Analytics (SGSMA), May 2019.

Paper II: H. Haugdal and K. Uhlen, "Power Oscillation Monitoring using Statistical Learning Methods", in 2019 IEEE Milan PowerTech, Jun. 2019. (This paper was appointed "candidate for outstanding submission" at the 2019 IEEE Milan PowerTech conference.)

Paper III: H. Haugdal, K. Uhlen, D. Müller, H. Jóhannsson, "Estimation of oscillatory mode activity from PMU measurements", in 2020 IEEE PES Innovative Smart Grid Technologies Europe (ISGT-Europe), Oct. 2020.

Paper IV: H. Haugdal, K. Uhlen and H. Jóhannsson, "An Open Source Power System Simulator in Python for Efficient Prototyp-
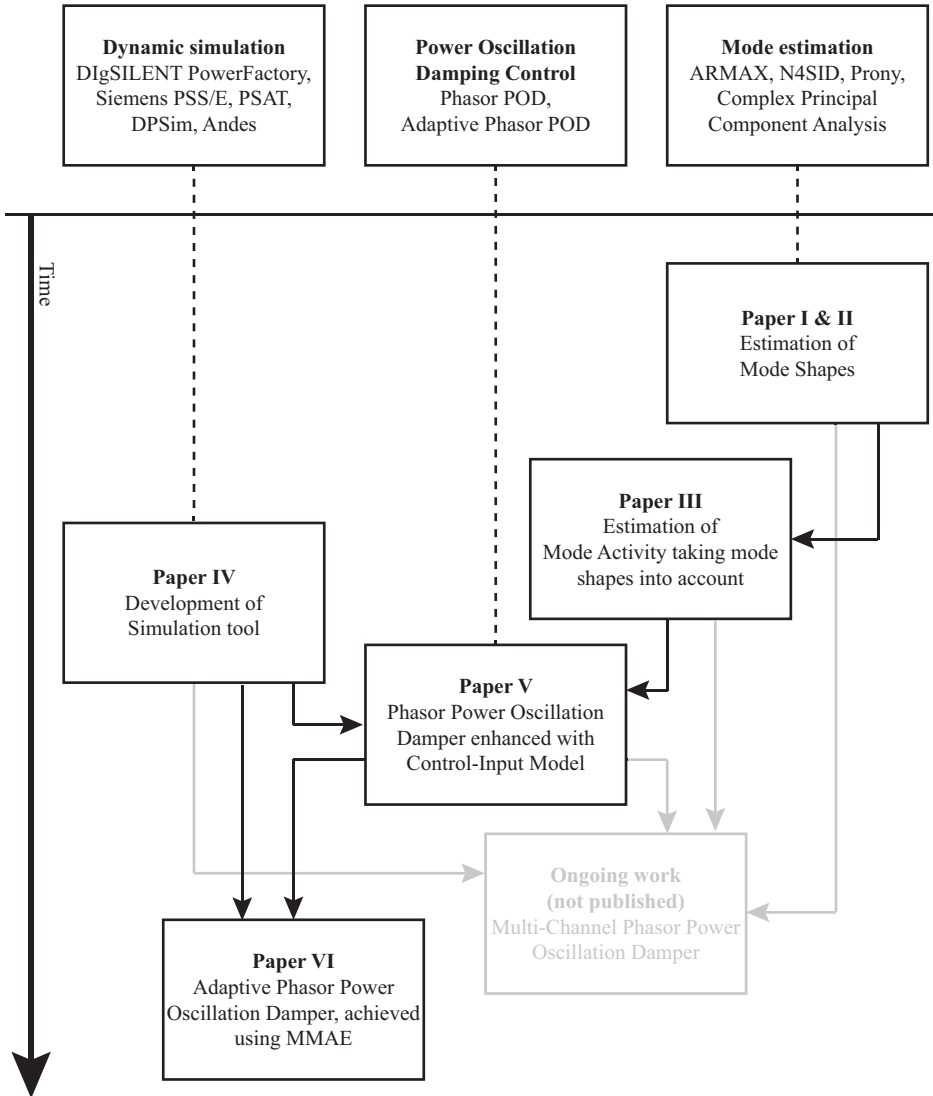
Figure 1.2: An overview of the publications presented in the thesis. The boxes on top indicate relevant topics in the literature, which the presented publications take as starting points.
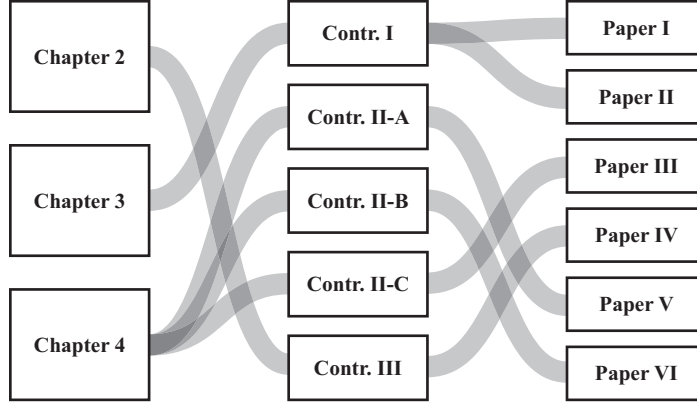
Figure 1.3: The relations between chapters, contributions, and papers.

ing of WAMPAC Applications", in 2021 IEEE Madrid PowerTech, Jun. 2021.

Paper V: H. Haugdal, K. Uhlen and H. Jóhannsson, "Achieving increased Phasor POD performance by introducing a Control-Input Model", submitted to Power Systems Computation Conference (PSCC), 2022.

Paper VI: H. Haugdal, K. Uhlen and H. Jóhannsson, "A Novel Phasor Power Oscillation Damper with Adaptive Phase Compensation, achieved using Multiple Model Adaptive Estimation", submitted to IEEE Transactions on Power Systems.

An overview of the publications is given in Fig. 1.2.

1.3   Outline of the Thesis

The thesis consists of five main chapters, and the six attached papers. In the first (current) chapter, an introduction to the research topic has been given, along with lists of contributions and publications. The second chapter is devoted to modeling and simulation of power systems, and also introduces the simulation tool representing Contribution III. The formulation of the non-linear differential equations that needs solving is given, and in addition the basics of linear system analysis and eigenvalue analysis. The third chapter is devoted to mode estimation, where the mode estimation method, representing Contribution I is presented. The fourth chapter concerns Contributions II-A, II-B and II-C,

which target improved power oscillation damping control. In the fifth chapter, conclusions and recommendations for further work are given. Fig. 1.3 shows how the contributions and papers are related, and in which chapters of the thesis they are presented. Finally, the six papers are attached toward the end of the thesis.

Chapter 2

Simulation Tool for Prototyping WAMPAC Applications

*This chapter concerns the modeling and simulation of transmission systems, and the development of a simulation tool in the programming language Python for efficient prototyping of WAMPAC applications. The simulation tool is presented in **Paper IV**, and represents **Contribution III**.*

Modeling and simulation is an important topic in power systems research; early stages of development of new control and protection schemes can not be tested on real transmission systems (since this could compromise the security of the system), and building accurate models of large systems in the lab is prohibitively expensive and/or practically infeasible. Therefore, new control and protection schemes generally have to be tested in simulations.

Methods for monitoring can also be tested on measured data from real systems. The mode shape estimation method described in Chapter 3 was developed by testing on measured PMU data from the Nordic Power System, but also on data from simulations carried out in the commercial simulation software DIgSILENT PowerFactory [23]. Simulations in this case offer the extra advantage of allowing exact reference values to be calculated, which makes it possible to compare estimated quantities to the actual values.

The research work concerning control, described in Chapter 4, required a Kalman filter interacting with the dynamic simulation. This

was found to be difficult to achieve using, e.g., DIgSILENT PowerFactory or PSS/E, and motivated the development of a new simulation tool in Python. The developed code (which is still in early stages of development) is available on GitHub in a repository called DynPSSimPy [24]. It is currently being used in the power system stability course at NTNU, and has been used by M.Sc. students at NTNU, ETH Zürich [25], and University of Toronto, among others.

This chapter is structured as follows: First, assumptions and simplifications are given. Further, the differential equations that needs solving are introduced, along with dynamic models for the most important components. A section on Modal Analysis follows, before the development of the mentioned simulation tool is described.

2.1 Assumptions

Transmission systems consist of a high number of complex components, like generators, loads, and FACTS, which are interconnected by a grid of lines, transformers, HVDC links, etc. Depending on the type of dynamics studied, simulation of large systems in general requires simplifying individual component models. It is often neither practically feasible nor necessary to model each component in full detail. For instance, modeling Converter-Interfaced Generation in full detail might require modeling of switching dynamics, for which theory on Hybrid Dynamical Systems is advocated [26] for handling interactions between continuous dynamics and discrete events. However, regarding Rotor Angle Stability, which is the focus here, the following is stated in [12]:

> ...all dynamic phenomena considered in the original classification presented in [2004 by the IEEE/Cigre Joint Task Force on Stability Terms and Definitions], are properly modeled using the "phasor (or quasi-sinusoidal) approximation".

The original classification referred to is given in [11], and includes Rotor Angle Stability, Frequency Stability, and Voltage Stability. Since Rotor Angle Stability is the focus in this thesis, the phasor approximation is adopted. With this approximation, all currents and voltages are represented by phasors. Lines, transformers, static loads, and shunts are modeled as static admittances; generators, dynamic loads, converter-interfaced generation, HVDC links. and FACTS devices are interfaced to the grid through time-varying admittances, current injections (phasors), active or reactive power injections or voltage sources (phasors). The problem of simulating the system thus requires integration of the differential equations of all dynamic components while at the same time

14

ensuring that the algebraic equations representing the grid are satisfied. This type of problem is described by a system of Differential Algebraic Equations (DAE), outlined in the next section.

Further, the three phases are assumed to be balanced, which allows a single phase approximation to be used. Thus, only balanced disturbances are considered, i.e. three phase short circuits, simultaneous disconnection of all three phases of a generator or line etc.

The simulations are performed with a constant step size. One disadvantage of this approach is that discontinuous elements like limiters in control systems are not accurately modeled, since the time at which the signal exceeds the threshold does not in general coincide with the simulation time step. Accurate modeling requires special treatment of such discontinuous events, for instance by adjusting the step size when events are detected. However, this modeling inaccuracy is assumed to have negligible effects on the presented results.

To the knowledge of the authors, these assumptions are in line with other research on this topic in the literature.

2.2 Differential Algebraic Equations

The system of Differential Algebraic Equations (DAE) describing the dynamics of the power system can be written in the following form:

$$\dot{\mathbf{x}} = f\left(\mathbf{x}, \mathbf{v}, \mathbf{u}\right) \tag{2.1}$$

$$0 = g\left(\mathbf{x}, \mathbf{v}, \mathbf{u}\right) \tag{2.2}$$

Here, the function f gives the time derivatives of all the states $\mathbf{x}$, the function g contains the algebraic equations describing the grid, and $\mathbf{v}$ is the vector of algebraic variables. $\mathbf{u}$ is a vector containing inputs to the model, for instance, set-points for terminal voltage or turbine power. This system of equations can be solved by a dedicated DAE solver, or by converting the DAE system to a system of Ordinary Differential Equations (ODE). The latter approach is adopted here. This is achieved by introducing a function g', which represents solving g for the algebraic variables:

$$\mathbf{v} = g'\left(\mathbf{x}, \mathbf{u}\right) \tag{2.3}$$

It should be noted that evaluating this function might not be straightforward, and might require iterating to find a solution if the algebraic equations are non-linear. Combining (2.1) and (2.3) gives

$$f\left(\mathbf{x}, g'\left(\mathbf{x}, \mathbf{u}\right), \mathbf{u}\right) = f'\left(\mathbf{x}, \mathbf{u}\right) \tag{2.4}$$

By doing this, the algebraic variables are eliminated, allowing the system of equations to be treated as a system of ODEs. This system can be integrated using any standard integration method (Euler's Method, a Runge-Kutta Method, etc.), and linearized as described in Section 2.3.

2.2.1 Network Equations

The algebraic variables in the DAE system are the bus voltages in the system. Assuming that the dynamic models can be modeled as current injections or time varying admittances, the system of algebraic equations can be written as follows:

$$g(\mathbf{x}, \mathbf{v}, \mathbf{u}) = \mathbf{Y}(\mathbf{x}, \mathbf{u})\mathbf{v} - \mathbf{I}_{inj}(\mathbf{x}, \mathbf{u}) = 0 \tag{2.5}$$

Here, $\mathbf{Y}$ is the admittance matrix used in the dynamic simulation and $\mathbf{I}_{inj}$ is the vector of current injections. This system of algebraic equations is linear, and can be solved very efficiently by an algorithm for sparse systems of linear equations, for instance scipy.sparse.linalg.spsolve [27] in Python.

Pseudocode for evaluating the state derivative function is given in Code Listing 1. On line 7 the states $\mathbf{x}$, the algebraic variables $\mathbf{v}$ and the inputs $\mathbf{u}$ are determined for the current evaluation of the function and can be used directly in the differential equations of the dynamic models, described in the following sections.

---

1 **Function** $f'(\mathbf{x}, \mathbf{u})$
2 $\mathbf{I}_{inj}(\mathbf{x}, \mathbf{u}) \leftarrow$ Get current injections
3 $\mathbf{Y}(\mathbf{x}, \mathbf{u}) \leftarrow$ Get updated admittance matrix

4   Solve for algebraic variables
5 $\mathbf{v} = \mathbf{Y}(\mathbf{x}, \mathbf{u})^{-1}\mathbf{I}_{inj}(\mathbf{x}, \mathbf{u})$

6   Compute state derivatives
7 $\dot{\mathbf{x}} = f(\mathbf{x}, \mathbf{v}, \mathbf{u})$

Code Listing 1: Pseudocode for evaluating the state derivative function.

One limitation of this approach is that the current injections $\mathbf{I}_{inj}$ and the admittance matrix $\mathbf{Y}$ can not be functions of the algebraic variables $\mathbf{v}$. Thus, constant power loads can not be modeled directly using this approach. Including constant power loads would require modifying the linear system of equations into a non-linear system of equations, which could be solved using, e.g., the Newton-Raphson method.

2.2.2 Synchronous Machine

In stability studies, synchronous machines are often modeled using 6th order models. The mechanical dynamics of the rotor, i.e., the swing equation, are represented by two states: Rotor angle and speed. Four states are required to capture electromagnetic dynamics in four rotor windings, specifically: The field winding, the d-axis damper winding, and two q-axis damper windings. The equations describing rotor winding dynamics can be formulated with fluxes as state variables, as in [9], or with voltages as state variables, as in [28]. The latter formulation is adopted here, where the six differential equations describing the synchronous machine are given as follows:

$$
\begin{aligned}
M\Delta\dot{\omega} &= P_m - P_e \\
\dot{\delta} &= \Delta\omega \\
T'_{d0}\dot{E}'_q &= E_f - E'_q - I_d(X_d - X'_d) \\
T'_{q0}\dot{E}'_d &= -E'_d + I_q(X_q - X'_q) \\
T''_{d0}\dot{E}''_q &= E'_q - E''_q - I_d(X'_d - X''_d) \\
T''_{q0}\dot{E}''_d &= E'_d - E''_d + I_q(X'_q - X''_q)
\end{aligned}
\tag{2.6}
$$

The electrical power is calculated from the following relation:

$$
P_e = E''_d I_d + E''_q I_q
\tag{2.7}
$$

Detailed descriptions of the individual variables and parameters are given in [28]. The synchronous machine is interfaced to the grid through the d- and q-axis subtransient voltages E''_d and E''_q:

$$
\begin{bmatrix} E''_d \\ E''_q \end{bmatrix} = \begin{bmatrix} V_d \\ V_q \end{bmatrix} + \begin{bmatrix} R & X''_q \\ X''_d & R \end{bmatrix} \begin{bmatrix} I_d \\ I_q \end{bmatrix}
\tag{2.8}
$$

Using that $X''_d = X''_q = X''$ (i.e., neglecting subtansient saliency), this can be written as

$$
\begin{aligned}
E'' &= E''_d + jE''_q \\
&= (V_d + jV_q) + (R + jX'')(I_d + jI_q) \\
&= V + (R + jX'')I
\end{aligned}
\tag{2.9}
$$

By establishing the Northon Equivalent of the above expression, the synchronous machine can be modeled as a current injection. The current is given by

$$
I_{no} = \frac{E''}{R + jX''}
\tag{2.10}
$$

17

and the shunt impedance by

$$Z_{no} = R + jX''$$ (2.11)

The shunt impedance is included in the dynamic admittance matrix. The current injections I_{no} appear as contributions to the current injection vector $\mathbf{I}_{inj}$ at the indices corresponding to buses where the synchronous machines are connected.

2.2.3 Thyristor Controlled Series Capacitor

The Thyristor Controlled Series Capacitor (TCSC) is a member of the family of devices referred to as FACTS [7]. It consists of a capacitor in parallel with a Thyristor Controlled Reactor (TCR), and is typically installed in series with a transmission line. By controlling the firing angle of the TCR, the series compensation can be adjusted continuously within a certain range. This faciltates provision of ancillary services like improving transient stability and voltage stability, and power oscillation damping.

Modeling and control of a TCSC is treated in detail in [29]. A much simplified TCSC model is adopted here, which is given in [30], where the TCSC is modeled as a controllable admittance in series with a line. A first order model with time constant T_{TCSC} determines the degree of series compensation k_c:

$$\dot{k_c} = \frac{1}{T_{TCSC}} \left(-k_c + k_{c-ref} + k_{c-ss} \right)$$ (2.12)

Here, k_{c-ss} is the steady state compensation. k_{c-ref} is an auxiliary signal which can be modulated, for instance for power oscillation damping purposes (as described in Chapter 4). The reactance of the TCSC is calculated from the degree of compensation and the series reactance of the line:

$$X_{TCSC} = X_L k_c$$ (2.13)

From this, the TCSC admittance is calculated and included in the admittance matrix used in the dynamic simulation.

2.3 Modal Analysis

Electromechanical oscillations can be analyzed using Modal Analysis. This involves determining a linearized version of the power system model, and then performing an eigendecomposition of the linear system matrix. The resulting eigenvalues and eigenvectors provide useful information

about the dynamics of the system at the current operating point, and are often used for design and tuning of control systems.

The modal analysis result is only accurate for the operating point at which the system was linearized. If the system is perturbed by a sufficiently large disturbance, the response will be non-linear, and the modal analysis result does not represent the actual system dynamics accurately. If the system ends up in a new operating point after the disturbance, which would be the case if, for instance, important lines or equipment were disconnected, the modal analysis could be redone by linearizing the system at the new operating point.

The non-linear power system model can be given on the following form:

$$\begin{aligned}
\dot{\mathbf{x}} &= f'\left(\mathbf{x}, \mathbf{u}\right) \\
\mathbf{y} &= h\left(\mathbf{x}, \mathbf{u}\right)
\end{aligned}$$
(2.14)

Here, $\mathbf{y}$ is a vector of measurements. f' is the state derivative function, as defined in 2.4, where the solution of the algebraic variables is included in the function. To linearize the system, the deviations around the linearization point are defined:

$$\begin{aligned}
\mathbf{x} &= \mathbf{x}_0 + \Delta\mathbf{x} \\
\mathbf{y} &= \mathbf{y}_0 + \Delta\mathbf{y} \\
\mathbf{u} &= \mathbf{u}_0 + \Delta\mathbf{u}
\end{aligned}$$
(2.15)

Further, the following Jacobian matrices are evaluated:

$$\mathbf{A} = \left.\frac{\partial f'(\mathbf{x}, \mathbf{u})}{\partial \mathbf{x}}\right|_{\mathbf{x}_0, \mathbf{u}_0} \qquad \mathbf{B} = \left.\frac{\partial f'(\mathbf{x}, \mathbf{u})}{\partial \mathbf{u}}\right|_{\mathbf{x}_0, \mathbf{u}_0}$$

$$\mathbf{C} = \left.\frac{\partial h(\mathbf{x}, \mathbf{u})}{\partial \mathbf{x}}\right|_{\mathbf{x}_0, \mathbf{u}_0} \qquad \mathbf{D} = \left.\frac{\partial h(\mathbf{x}, \mathbf{u})}{\partial \mathbf{u}}\right|_{\mathbf{x}_0, \mathbf{u}_0}$$
(2.16)

The derivatives can be calculated from analytical expressions, or numerically by finite differences. The linearized system can now be written as follows:

$$\begin{aligned}
\Delta\dot{\mathbf{x}} &= \mathbf{A}\Delta\mathbf{x} + \mathbf{B}\Delta\mathbf{u} \\
\Delta\mathbf{y} &= \mathbf{C}\Delta\mathbf{x} + \mathbf{D}\Delta\mathbf{u}
\end{aligned}$$
(2.17)

For sufficiently small disturbances, the linearized model accurately resembles the non-linear model in (2.14).

Performing an eigendecomposition of the system matrix $\mathbf{A}$ yields the decoupled system:

$$\dot{\mathbf{z}} = \mathbf{\Lambda z} + \mathbf{\Psi B}\Delta\mathbf{u} \tag{2.18}$$

Here, the matrix $\mathbf{\Lambda} = \mathbf{\Psi A \Phi}$ contains the eigenvalues of the system on the diagonal, $\mathbf{\Psi}$ contains the left eigenvectors as row vectors, $\mathbf{\Phi}$ contains the right eigenvectors as column vectors, and n is the order of the system:

$$\mathbf{\Lambda} = \text{diag}\left(\lambda_1, ..., \lambda_n\right) \tag{2.19}$$

$$\mathbf{\Psi} = [\boldsymbol{\psi}_1^\mathsf{T}, ..., \boldsymbol{\psi}_n^\mathsf{T}]^\mathsf{T} \tag{2.20}$$

$$\mathbf{\Phi} = [\boldsymbol{\phi}_1, ..., \boldsymbol{\phi}_n] \tag{2.21}$$

The states $\mathbf{x}$ relate to the decoupled states $\mathbf{z}$ as follows:

$$\mathbf{x} = \mathbf{\Phi z} \tag{2.22}$$

Equivalently, since $\mathbf{\Phi} = \mathbf{\Psi}^{-1}$:

$$\mathbf{z} = \mathbf{\Psi x} \tag{2.23}$$

The measurements can also be written as a function of the decoupled states:

$$\mathbf{y} = \mathbf{C\Phi z} \tag{2.24}$$

In [9], the product $\mathbf{C\Phi}$ is referred to as the *mode observability matrix*, determining how modes are observed in each of the measurements. Similarly, the product $\mathbf{\Psi B}$ is referred to as the *mode controllability matrix*, determining how modes are affected by each of the inputs.

It can be shown that the solution to the State Space formulation, given initial conditions $\mathbf{x}(0)$ and input $\mathbf{u}(t)$, can be written as follows:

$$\mathbf{x}(t) = e^{\mathbf{A}t}\mathbf{x}(0) + \int_0^t e^{\mathbf{A}(t-\tau)}\mathbf{B}\mathbf{u}(\tau)d\tau \tag{2.25}$$

From this the states as a function of time can be calculated. A similar expression can be developed for the decoupled system:

$$\mathbf{z}(t) = e^{\mathbf{\Lambda}t}\mathbf{z}(0) + \int_0^t e^{\mathbf{\Lambda}(t-\tau)}\mathbf{\Psi B}\mathbf{u}(\tau)d\tau \tag{2.26}$$

Thus, the degree of excitation of the modes of the system $\mathbf{z}(t)$ by a certain input $\mathbf{u}(t)$ is determined by the mode controllability matrix $\mathbf{\Psi B}$.

When working with controls for damping of power oscillations, it is often convenient to calculate *transfer function residues*. For mode m, the associated matrix of residues is computed as follows:

$$\mathbf{R}_m = \mathbf{C}\boldsymbol{\phi}_m\boldsymbol{\psi}_m\mathbf{B} \tag{2.27}$$

Each column of the matrix corresponds to one control actuator input, and each row corresponds to one measurement output. The magnitude of the residue can be interpreted as the extent to which mode m is *both* affected by perturbing the corresponding input *and* observed in the corresponding measurement. When designing power oscillation damping controls, looking at the matrix of residues for low damped modes gives a good basis for choosing a good combination of measurement and control for mitigating the oscillations.

For a marginal direct feedback between measurement output i and control input j, the angle of the residue gives the direction of the change of the eigenvalue in the complex plane [31], and the magnitude of the residue determines how much the eigenvalue changes. If the measured signal is phase shifted with the following angle [32] before feeding forward to the control input,

$$\beta = 180° - \angle[\mathbf{R_m}]_{ij} \qquad (2.28)$$

it can be shown the eigenvalue moves further into the left half-plane (thereby increasing the damping of the eigenvalue). For a conventional PSS, this phase shift can be approximated by feeding the input signal through a series of lead-lag blocks. For the Phasor POD, treated in detail in Chapter 4, the phase shift is specified directly as a parameter.

2.4 Development of a Simulation Tool in Python

This section concerns the development a simulation tool in the programming language Python, based on the above presented theory. In the following, the motivation for developing the tool is described; a validation study based on a comparison with results from DIgSILENT PowerFactory is presented; prototyping WAMPAC applications is demonstrated using a simple example; and finally, a simple approach to real-time simulation is described.

2.4.1 Motivation

Commercial tools for power system simulation, e.g., DigSILENT PowerFactory [23] or PSS/E [33], are capable of simulating large systems with thousands of buses efficiently. This is a requirement for these tools to be usable by transmission system operators analyzing detailed models of real systems. For power system stability research purposes, smaller test system are often used, e.g., Kundur's Two-Area System [9], the IEEE 39- and 68-Bus Systems [34], [30] and the Nordic 44-Bus System [35].

System of these sizes do not strictly require powerful and expensive simulation tools to be simulated efficiently.

Furthermore, commercial tools are not necessarily well suited for all research purposes. Developing the WAMPAC applications of the future power system calls for advanced techniques for signal processing, handling big data, artificial intelligence, and more. Tight integration of such techniques with commercial power system simulation software is not necessarily straightforward to achieve.

Open source software is typically easier to modify or extend than commercial software. Some open source alternatives for dynamic power system simulations include DPsim [36], developed in C++, which specifically targets real-time- and co-simulation; ANDES [37], written in Python, which uses a hybrid symbolic-numeric framework for modeling systems where numerical code is generated from symbolic expressions; the Open-Instance Power System Library [38] [39], written in the Modellica language, which specifically targets unambiguous model sharing among utilities and researchers. These tools are also capable of simulating large systems with thousands of buses.

The simulation tool developed during the work with this thesis can be viewed as an investigation of the feasibility of performing simulations entirely in Python, making use of only very common standard libraries like NumPy [40] and SciPy [27]. The aim is to be able to work efficiently with small- to medium-sized systems on the scale of the above listed test systems; thus, sophisticated techniques for boosting the performance, which in some cases compromise transparency and extendability, are not required. This comes with several advantages:

- For prototyping WAMPAC applications, having a simulation tool coded entirely in Python is advantageous, which was initially the main motivation for developing the tool. This allows, e.g., a control or protection scheme coded in Python to read results and interact with the simulation on every simulation step, without having to define interfaces between different programs.

- Given basic skills in Python and knowledge on power system simulations, most students and researchers would be able to read and understand the code if everything, including equations, dynamic model definitions, power system model parameters, etc., was written in Python.

- Limiting the dependencies (i.e., required libraries) allows the tool to be run on any platform capable of running standard Python. This makes it easy to install and run the code, and facilitates sharing of code for reproducing research results with fellow researchers.

Although the focus is not performance, experience has shown that for the system sizes considered so far (around 50 buses and generators, with simple generator control models), simulations can be performed sufficiently fast for real-time simulations. This is described in detail toward the end of this chapter.

2.4.2 Core Functionality

The core functionality implemented can be summarized in the following points:

Load flow: A conventional load flow is implemented, based on solving the non-linear equations by the Newton-Rhapson method. The initial conditions for the dynamic simulation are calculated from the load flow.

Dynamic simulation: The phasor (or quasi-sinusoidal) approximation is adopted. The DAE system is converted to an ODE system, which can be integrated by any ODE integration method. The system of algebraic equations is linear.

Modal analysis: The linearization is carried out numerically, according to (2.16). Eigenvalues can be calculated by, e.g., the NumPy function numpy.linalg.eig [40].

Dynamic models: Currently, the 6th order synchronous machine model described in Section 2.2.2 is implemented. Additionally, simple generator control models are implemented, specifically: AVR model SEXS, turbine/governor model TGOV1, and PSS model STAB1. Vectorization is used to enhance the computational efficiency.

2.4.3 Validation

To validate the results produced by the simulation tool, a comparison with results from a model with identical parameters in DIgSILENT PowerFactory is performed. The simulated system is Kundur's Two-Area System, as described in [9]. All four generators are equipped with the simple control models listed in the previous section. The simulated event is a short circuit at the terminals of generator 1.

Fig. 2.1 shows that the results are highly similar, indicating that the results from the developed simulation tool are valid. It is noted that the results are not identical. A potential reason for the discrepancy is that the formulation of the synchronous machine equations in DIgSILENT
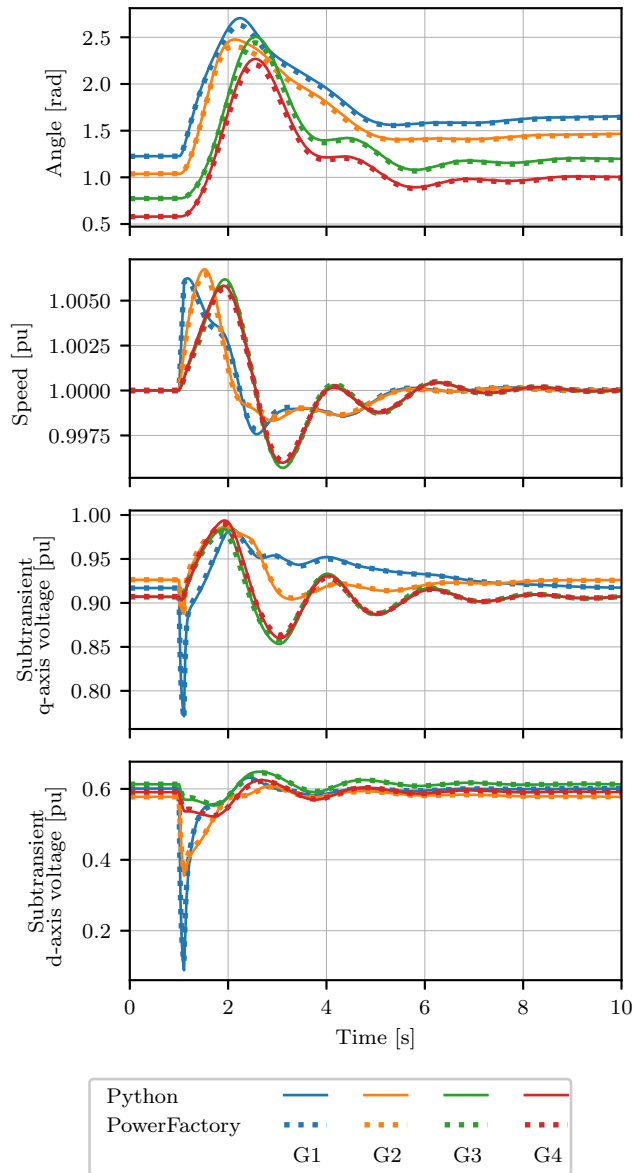
Figure 2.1: Simulations results from the Python simulation tool compared with results from DIgSILENT PowerFactory. © 2021 IEEE.

```
1  while t < t_end do
2  │   Perform integration step
3  │   x = x + Δt · f'(x, u)
4  │   t = t + Δt
   │
5  │   Read variables from simulation
6  │   f_G ← generator frequencies
   │
7  │   Apply protection
8  │   if max(f_G) > 50.3Hz then
9  │   │   Disconnect G3
10 │   end
11 end
```

Code Listing 2: The pseudocode describes testing of a simple protection system in a dynamic simulation.

PowerFactory differs from the model given by (2.8), which is used in the presented tool.

2.4.4 Prototyping WAMPAC Applications

A simple example of a protection system is included to demonstrate how the simulation tool can be used for developing and testing WAMPAC applications. The purpose of the protection system is to limit frequency excursions in Kundur's Two-Area System. If the frequency at one or more of the four generators surpasses 50.3 Hz, generator 3 should be disconnected. Pseudocode for testing this protection system is shown in Code Listing 2. For simplicity, the integration is carried out using Euler's method.

A simulation is performed to test the protection scheme, where a loss of load that is expected to cause over-frequency occurs. Specifically, the largest load is reduced from 1767 MW to 1060 MW. The results from two dynamic simulations, with and without the protection system activated, are shown in Fig. 2.2. Without the protection system the frequency stabilizes around 50.3 Hz. Activating the protection system causes generator 3 to be tripped shortly after the loss of load, which causes the frequency to drop and stabilize around 49.9 Hz.

The purpose of this simple example is to illustrate the advantage of running the simulation entirely in Python. Very little extra effort is required to read variables from the simulation or apply control actions or
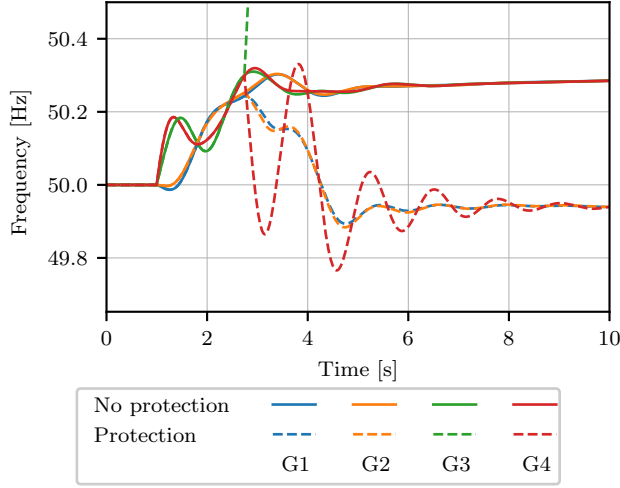
Figure 2.2: The frequency of the four generators in Kundur's Two-Area System during testing of a simple protection scheme. The example demonstrates how simple WAMPAC applications can be developed and tested using the presented simulation tool. As the load in Area 2 decreases, the frequency increases. When the frequency reaches 50.3 Hz, generator 3 is disconnected by the protection system to limit the frequency excursion. © 2021 IEEE.

events to the simulation, since all variables are directly available in the same programming language. This allows the simple protection system to be realized with code that is very similar to the pseudocode in Code Listing 2. Thus, ideas for WAMPAC applications in early stages of development can be tested very easily and efficiently, which represents the main motivation for developing the simulation tool.

2.4.5 Real-Time Simulation

PMU-based online monitoring, control, or protection applications are required to be able to operate in real-time to be applicable in practice. It is therefore interesting to test such applications in real-time simulations. Code for synchronizing the simulation to wall-clock time can be added to the simulation loop in Code Listing 2. For each time step, the difference between the simulation time t_{sim} and elapsed wall-clock time t_{wc} is calculated:

$$t_{err} = t_{sim} - t_{wc} \tag{2.29}$$

Figure 2.3: The synchronization accuracy for a real-time simulation of the IEEE 39-Bus System. The actual time spent by the solver on each time step is shown in blue; the time spent on only calculations is shown in green; and the ideal time is shown in red, which corresponds to the chosen time step (i.e., 5 ms). © 2021 IEEE.
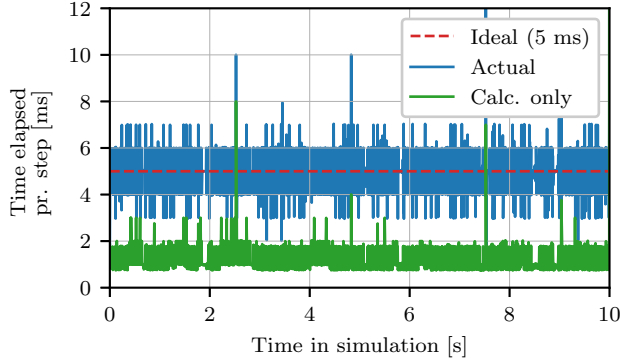
If this difference is positive, then the program is blocked for t_{err} seconds before the next step is simulated. If it is negative, the next step is taken immediately. Of course, the average value of t_{err} over time should be positive; if not, the simulator will not be able to keep track with wall-clock time.

In terms of computation time, the critical step in evaluating the state derivative function is the solution of the algebraic equations. As mentioned previously, in the chosen approach the system of algebraic equations is linear. This is very beneficial for real-time simulation, since the equations are solved without requiring an unknown number of iterations to reach a certain accuracy. Given that the admittance matrix is not singular, there exists a unique solution which is found within a predictable time.

Fig. 2.3 shows in detail the accuracy of the synchronization achieved when testing this simple real-time simulation approach on the IEEE 39-Bus System. The time step is 5 ms, the 10 generators are modeled using the 6th order model given by (2.8), and all generators except generator 1 are equipped with simple AVR, turbine-governor, and PSS control systems.

Furthermore, code for visualizing result variables and receiving user input can be added to the simulation loop. Some example visualizations and user controls are shown in Fig. 2.4. In the "Phasor plot", the magnitudes and angles of the phasors are determined by synchronous machine
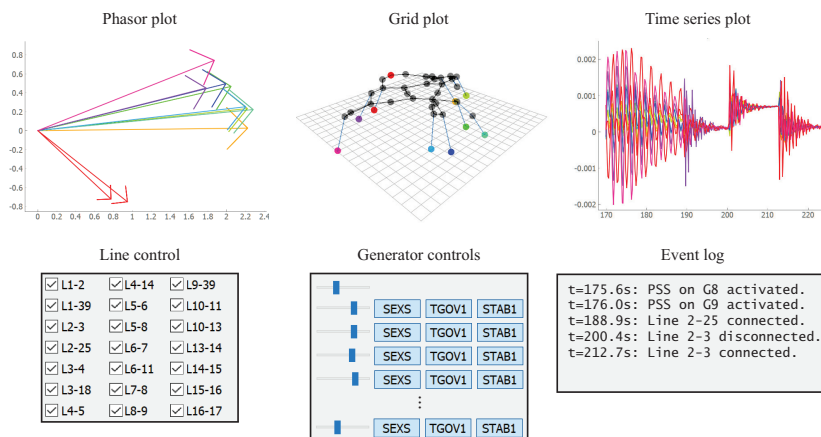
Figure 2.4: Example visualizations and user controls during real-time simulation of the IEEE 39-Bus System. © 2021 IEEE.

excitation voltage magnitudes and rotor angles. The "Grid plot" displays the the network topology, with the z-component determined by bus voltage magnitudes. The "Time series plot" shows synchronous machine speed deviations. The "Line control" panel allows disconnection and connection of lines, the "Generator control" panel allows deactivation and activation of generator controls, and the "Event log" displays a log of recent events. This graphical user interface is developed using the PyQtGraph [41] library in Python, which is a library for developing visualizations and user interfaces for engineering and science applications.

To allow computationally demanding applications to interact with the real-time simulation, it is beneficial to distribute calculations across multiple processes and/or multiple computers. This can be achieved by using the multiprocessing module in Python, which allows the simulation to be run in one dedicated process and other applications to be run in other processes, optionally on other computers. For each simulation step, the simulator process sends the required information (e.g., measurements) to the different applications at a specified frequency, and checks for any received control signals.

Furthermore, an implementation of the C37.118 synchrophasor standard [42] is available in Python [43]. This implementation could be included in the real-time simulation loop, allowing voltage or current phasors from the simulation to be streamed in PMU snapshots according to the C37.118 standard, and received for online analysis and visualization on another computer.

The simple approach to real-time simulation outlined is useful in that it does not require specialized operating systems or hardware. Other tools developed specifically for real-time simulations, like DPsim [36] and ePHASORsim [44], are much more powerful and can simulate much larger systems with much smaller time constants, but can not be deployed on an average computer regardless of operating system and hardware specifications.

For researchers this allows, for instance, demonstrations of WAMPAC applications during presentations. In an educational setting, software for real-time simulation of grids could be distributed among students. Real-time interaction with a running power system simulation could prove to be a useful tool for developing intuition for various concepts, for instance by adjusting system loading, control system parameters, reactive compensation, etc.

In Chapter 4, this real-time simulation approach is used for testing the capability of a specific type of power oscillation damping controller to operate in real-time.

2.5   Summary

In this chapter, the chosen approach for modeling and simulation of power systems has been outlined. Some of the most important dynamic models are described, and the basics of modal analysis are given. Further, development of a simulation tool in the programming language Python has been described, along with a validation study, a demonstration of early stage prototyping of a wide area protection system, and a simple approach to real-time simulation.

Chapter 3

Mode Estimation using Statistical Learning Methods

*In this chapter, a mode estimation method based on statistical learning methods is presented. The method represents **Contribution I**, which is published in **Papers I & II**.*

The deployment of PMUs in most transmission systems have reached a level where electromechanical dynamics can be observed in detail. The focus of the work presented in this chapter is a PMU-based estimation of parameters that describe electromechanical dynamics. In Papers I and II, a method is proposed that estimates mode frequency and observability mode shapes from a set of measurements without requiring prior knowledge of the system. Analysis techniques from the statistical learning and signal processing domains are applied; specifically, a complex variant of Principal Component Analysis (PCA) is used in combination with a clustering algorithm.

Some of the important conclusions that can be drawn based on this work are as follows: The method produces useful and accurate results; both ambient conditions and pronounced oscillations/ringdowns can be analyzed and presented in the same visualization; information about non-linear dynamics can be captured; and finally, the method is suitable for online operation.

In the following, relevant background on mode estimation techniques will be given, before the theory on the proposed method is presented. Further, results from applying the method to simulated data and mea-

sured PMU data are presented. Finally, an online implementation of the method is described.

3.1   Theoretical Foundations, State of the Art

Electromechanical oscillations are observed throughout power systems with different amplitudes and phase shifts, depending on the location of the measurement and the quantity being measured. Local modes are confined to a small area, where a single synchronous machine is oscillating against the system or multiple machines within a small area are oscillating against each other. Inter-area oscillations, on the other hand, can be observed across wide geographical areas.

For a particular operating point of the system, the frequency, damping, and observability of modes can be determined from modal analysis, as described in Section 2.3. The mode observability, defined in (2.24), can be rewritten as follows:

$$\mathbf{y} = \mathbf{C\Phi z} = \sum_i^n \mathbf{C\phi}_i z_i \tag{3.1}$$

Thus, the amplitude and phase with which mode i is observed in different measurements is determined by the product $\mathbf{C\phi}_i$, which is a vector of the same size as $\mathbf{y}$. Here, this vector is referred to as the *observability mode shape* of mode i. Estimating the observability mode shape of mode i is therefore equivalent to estimating the elements of the vector $\mathbf{C\phi}_i$.

There is a rich literature on estimation of electromechanical modes from measurements; a comprehensive overview of the topic is given in [45]. Estimation algorithms are often targeting either ringdowns/standing oscillations or *ambient conditions*. Ambient conditions refers to the system under normal operation (in the absence of large disturbances), where the modes of the system are continuously excited by small disturbances like random load variations. The most frequently estimated quantities include frequency, damping, and observability mode shapes of modes.

Targeting ambient conditions, application of System Identification techniques like N4SID and ARMAX is reported in [46, 47]. These algorithms typically function by fitting a linear model to measured data, where the order of the system is specified by the user beforehand. In [47], a slight deterioration of the performance of some of these techniques is reported when an oscillatory event (i.e., pronounced ringdown or sustained/growing oscillations) is introduced in the analyzed time series.

Other approaches targeting ambient conditions include a Bayesian approach [48], and an approach based on various mode decomposition techniques in combination with power spectral density analysis [49].

Other techniques, like Prony's Method, can be applied to extract frequency and damping of modes from ringdowns or sustained/growing oscillations [50]. In [51], a phasor estimation approach is applied for analyzing ringdowns, where mode shapes are also estimated. Interestingly, this approach is closely related to theory on the Phasor POD, presented in Chapter 4.

The perhaps most relevant references for the work presented in this chapter are represented by [52–55], where variants of CPCA are applied for estimation of modes and mode shapes (where the term Empirical Orthogonal Functions is used instead of Principal Component Analysis). CPCA was first proposed in [56] for analyzing geophysical phenomena, and is a complex variant of the more commonly known PCA, described in [57]. CPCA is based on the same equations as PCA, but also makes use of the Hilbert Transform, and requires some more pre-processing of the input series prior to application.

It is expected that highly accurate estimates of mode shapes can be obtained by applying CPCA to multichannel data with a short (i.e., $5-10\,\text{s}$) time window containing pronounced oscillations. For modes with subtle excitation, it is advantageous to include information from longer time spans. For instance, in [46], modes are estimated using various techniques from time series of lengths 10 and $20\,\text{min}$, where the system is excited by random load variations (i.e., ambient conditions). Extending the time window that is analyzed by CPCA has the disadvantage that the chance of any of the input series containing other disturbances or excitation of other modes increases, which could compromise the accuracy achieved using the short time window. This is particularly due to the fact that the Hilbert Transform is susceptible to noise; as demonstrated in [56], applying the transform to a pulse signal does not provide meaningful results.

With the contribution described in this chapter, a mode estimation method is presented where the aim is combining the advantages of a short time window and a longer time window. With this approach, both pronounced oscillations and ambient conditions are targeted. This is achieved by applying CPCA to short, overlapping segments of longer time series, before a clustering algorithm is used to compute averaged results from the complete time series. The structure of the chosen approach in some ways bears resemblance to Welch's method [58] for spectral density estimation, where the analyzed signal is split up in overlapping segments, and the spectral density of each segment is estimated

using the Fast Fourier Transform, before the final result is computed by averaging the spectral densities.

3.2   Description of the Method

The estimation method consists of two main steps. In Step I, Complex Principal Component Analysis is used to continuously extract mono-frequency oscillatory components from a sliding time window of length 5-10 seconds. The sliding time window is updated as new PMU measurements are received. From each time window, information about the frequency of oscillations and correlation in the input series (in terms of relative amplitude and phase) is extracted and stored as a vector (or a many-dimensional point). Each oscillatory component that is extracted and stored is referred to as an *observation* (i.e., an observation of oscillations). In Step II, a clustering algorithm is applied to the numerous observations from Step I. This allows averaged frequency and averaged observability mode shapes to be computed as the centroids of the clusters.

As mentioned, applying CPCA to extract observability mode shapes has previously been described in the literature [52–55]. The innovation with the presented method (besides minor differences in applying CPCA compared to previous research) is therefore Step II. The aim of introducing this step is to digest the numerous CPCA results from a longer time period (on the scale of minutes to tens of minutes) into more reliable information that can be presented in an informative way to the operators.

3.2.1   Step I: Capturing Oscillations using Complex Principal Component Analysis

The goal of Step I is to extract information about oscillations from a time window, where the length of the window should be sufficiently long that low frequency oscillations can be captured (i.e., for modes with a frequency on the lower end of the electromechanical frequency range, around $0.1\,\text{Hz}$, a time window of $\frac{1}{0.1\,\text{Hz}} = 10\,\text{s}$ is suitable). Frequency or voltage angle measurements from PMUs are assembled in a matrix as follows, where each row corresponds to one measurement and each

column corresponds to one time stamp:

$$\mathbf{X} = \begin{bmatrix} \mathbf{x}_1 \\ \mathbf{x}_2 \\ \vdots \\ \mathbf{x}_M \end{bmatrix} = \begin{bmatrix} x_1(t_1) & x_1(t_2) & \cdots & x_1(t_N) \\ x_2(t_1) & x_2(t_2) & \cdots & x_2(t_N) \\ \vdots & & \ddots & \\ x_M(t_1) & x_M(t_2) & & x_M(t_N) \end{bmatrix} \tag{3.2}$$

Principal Component Analysis is often referred to as a dimensionality reduction method. The fundamental idea is to transform a high number of correlated variables into a lower number of uncorrelated variables, i.e., Principal Components. If there is a high correlation between the input variables, then a lower number of components are sufficient to capture a higher share of the variance.

Complex PCA [56] is closely related to PCA, the main difference being that the input data is complex. In our case, where the input data is represented by the time series $\mathbf{X}$, an imaginary part can be generated by applying the Hilbert Transform. One interpretation of the Hilbert Transform is that it generates a signal that has the same amplitude as the original periodic signal, but is phase shifted by 90°. Successful application of the transform requires that each signal contains oscillations of a single frequency only. To achieve this, some pre-processing of the input time series can be applied. In Papers I & II, an extra PCA step is included prior to applying the Hilbert Transform. This reduces the dimension of the input data, and gives the extra advantage that the Hilbert Transform can be applied to a lower number of time series (thus reducing the computation time). Another alternative, which is more common in the literature, is to use Empirical Mode Decomposition to reduce the input time series into Intrinsic Mode Functions [55]. An overview of pre-processing alternatives is shown in Fig. 3.1.

Here, for simplicity it is assumed that the Hilbert Transform can be applied directly to $\mathbf{X}$ (i.e., no pre-processing necessary, or the necessary pre-processing was already applied). This allows the complex series $\mathbf{Y}$ to be generated as follows:

$$\mathbf{Y} = \mathbf{X} + jH(\mathbf{X}) \tag{3.3}$$

$H(\cdot)$ denotes the series-wise application of the Hilbert Transform. The CPCA equations can now be applied, which involves determining a linear transformation of the complex series $\mathbf{Y}$:

$$\mathbf{Z} = \begin{bmatrix} \mathbf{z}_1 \\ \mathbf{z}_2 \\ \vdots \\ \mathbf{z}_{M_{CPC}} \end{bmatrix} = \mathbf{W}^H \mathbf{Y} = \mathbf{W}^H (\mathbf{X} + jH(\mathbf{X})) \tag{3.4}$$

35

(a) No pre-processing

(b) EMD pre-processing
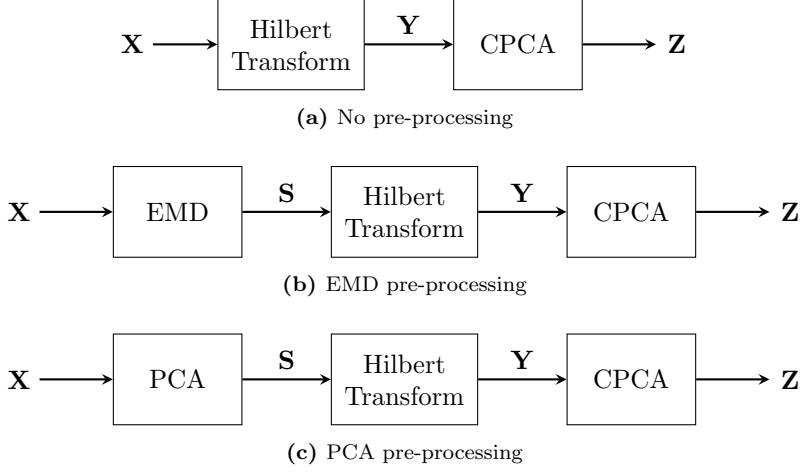

(c) PCA pre-processing

Figure 3.1: Some pre-processing variants. The goal with the pre-processing is to decompose the input series into mono-frequency components before applying the Hilbert Transform.

$(\cdot)^{\mathrm{H}}$ denotes conjugate transpose. To capture as much variance as possible with as few Complex Principal Components (CPCs) as possible, the transformation matrix $\mathbf{W}$ should be chosen such that the series $\mathbf{Z}$ are uncorrelated. To find $\mathbf{W}$, the complex covariance matrix of $\mathbf{Y}$ is first established:

$$\mathbf{\Sigma_Y} = \frac{1}{1-N}\mathbf{Y}\mathbf{Y}^{\mathrm{H}} \Rightarrow (1-N)\,\mathbf{\Sigma_Y} = \mathbf{Y}\mathbf{Y}^{\mathrm{H}} \tag{3.5}$$

Similarly, the covariance matrix $\mathbf{\Sigma_Z}$ of the transformed series $\mathbf{Z}$ can be written as follows:

$$\begin{aligned}
(1-N)\,\mathbf{\Sigma_Z} &= \mathbf{Z}\mathbf{Z}^{\mathrm{H}} \\
&= \mathbf{W}^{\mathrm{H}}\mathbf{Y}\left(\mathbf{W}^{\mathrm{H}}\mathbf{Y}\right)^{\mathrm{H}} \\
&= \mathbf{W}^{\mathrm{H}}\mathbf{Y}\mathbf{Y}^{\mathrm{H}}\mathbf{W} \\
&= \mathbf{W}^{\mathrm{H}}\mathbf{\Sigma_Y}\mathbf{W}
\end{aligned} \tag{3.6}$$

Since the series $\mathbf{Z}$ should be uncorrelated, the covariance matrix $\mathbf{\Sigma_Z}$ should be a diagonal matrix. The transformation matrix $\mathbf{W}$ is therefore chosen such that $\mathbf{\Sigma_Y}$ is diagonalized, which is equivalent to performing an eigendecomposition of $\mathbf{\Sigma_Y}$. The eigenvalues of $\mathbf{\Sigma_Y}$, which appear on the diagonal of $\mathbf{\Sigma_Z}$, are sorted in descending order, such that only the first M_{CPC} components need to be considered to ensure that a given

variance is preserved. The end result is that the input series can be written in terms of the CPCs, as follows:

$$\mathbf{X} = \mathrm{Re}\left(\mathbf{WZ}\right) \tag{3.7}$$

The matrix $\mathbf{W}$ has dimension $M \times M_{CPC}$, where $M_{CPC} < M$ (provided that the input data are correlated). Each of the input series can be considered separately:

$$\mathbf{x}_i = \sum_{j=1}^{M} \mathrm{Re}\left(w_{ij}\mathbf{z}_j\right) \approx \sum_{j=1}^{M_{CPC}} \mathrm{Re}\left(w_{ij}\mathbf{z}_j\right) \tag{3.8}$$

If the CPCA procedure is successful, then the component $\mathbf{z}_j$ will be a complex, periodic signal with oscillations of a single frequency only. The frequency f_j can be estimated from the signal, e.g., by Fast Fourier Transform. The complex element w_{ij} of the matrix $\mathbf{W}$ gives the amplitude and phase with which the jth component is observed in the the ith measurement. This information can be interpreted as an estimate of the observability mode shape of the mode with a frequency close to f_j.

From every run of the CPCA procedure, a number of components $M_{CPC} < M$ are stored for further analysis. CPCs that are stored are referred to as observations. Each observation can be written as a vector or point in many-dimensional space:

$$\mathbf{p} = [f_j, \mathrm{Re}(w_{1j}), \mathrm{Im}(w_{1j}), \mathrm{Re}(w_{2j}), \mathrm{Im}(w_{2j}), ..., \mathrm{Re}(w_{Mj}), \mathrm{Im}(w_{Mj})] \tag{3.9}$$

3.2.2 Step II: Averaging using Clustering

A number of observations N_w from a longer time window (on the scale of minutes to tens of minutes) are assembled in a matrix as follows:

$$\mathbf{P} = \begin{bmatrix} \mathbf{p}_1 \\ \mathbf{p}_2 \\ \vdots \\ \mathbf{p}_{N_w} \end{bmatrix} = \begin{bmatrix} f_1 & \mathrm{Re}(w_{11}) & \cdots & \mathrm{Im}(w_{M1}) \\ f_2 & \mathrm{Re}(w_{12}) & \cdots & \mathrm{Im}(w_{M2}) \\ \vdots & & & \\ f_{N_w} & \mathrm{Re}(w_{1N_w}) & \cdots & \mathrm{Im}(w_{MN_w}) \end{bmatrix} \tag{3.10}$$

By applying a clustering algorithm to this matrix, the euclidean distances between all observations are first calculated, resulting in a distance matrix of dimension $N_w \times N_w$, before observations that are similar are grouped together in clusters. The resulting clusters are assumed to be associated with different modes of the system. Finally, averaged mode frequencies and mode shapes are computed as the centroids of the clusters. The averaged quantities are expected to be more accurate and

reliable than the quantities resulting from applying CPCA to a single time window in Step I.

Choice of Clustering Algorithm

In Paper I, the k-Means [59] clustering algorithm is used. Using this algorithm, every observation is assigned to one of the clusters. The algorithm is therefore highly sensitive to noise, and it is of importance that "bad" observations are filtered out. Bad observations would result if, for instance, the Hilbert transform was applied to a signal containing other disturbances or modes.

As an incremental development of the method described in Paper I, the DBSCAN [60] algorithm is used in Paper II. This algorithm requires two parameters to be specified, which determine the minimum number of observations in a neighborhood for a cluster to form and the size of the neighborhood. Observations in sparsely populated regions of the input space are classified as noise.

The two required parameters of the DBSCAN algorithm are tuned toward a specific density of observations. Thus, clusters with differing densities are not handled well by this algorithm. This is a disadvantage, since clusters corresponding to strongly excited modes with low damping are likely to have different densities than clusters corresponding to subtly excited modes with higher damping. Another interesting candidate for the clustering algorithm, which does not possess this weakness, is the OPTICS (Ordering Points To Identify the Clustering Structure) [61] algorithm. This algorithm is closely related to the DBSCAN algorithm, except that the neighborhood size parameter (which is required by DBSCAN) is not required. Investigating the feasibility of applying the OPTICS algorithm is recommended as a topic of further work.

Quantifying the Similarity of Mode Shapes

Applying the clustering algorithm in Step II is complicated by the fact that mode shape estimates resulting from Step I can be similar, but rotated relative to each other. Applying a clustering algorithm directly to the matrix in (3.10) requires that all the mode shapes have been rotated beforehand. One approach, which is simple, fast, and easy to implement, is to rotate every mode shape estimate from Step I so that the angle of the longest vector is zero. However, in cases where several of the longest vectors in the mode shape have approximately the same length, then due to random variations, the second longest vector will in some estimates appear as the longest. This approach therefore has the
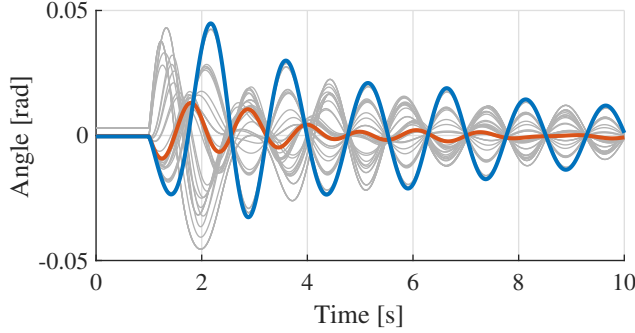
Figure 3.2: Simulated rotor angle time series from the Nordic 44 test network. The time series highlighted in blue and orange has high observabilities of the 0.67 Hz and 0.93 Hz modes, respectively. © 2019 IEEE.

disadvantage that very similar mode shape estimates could be rotated to different angles, resulting in a large distance.

The ideal solution would be a distance metric that does not depend on the rotation of the mode shapes. This problem bears resemblance to the "Orthogonal Procrustes Problem", where the Kabsch algorithm [62] can be applied to find the optimal rotation matrix between two sets of coordinates. Initial development and testing indicates that this a feasible approach. However, this is a topic of ongoing/further work. For obtaining the presented results in the subsequent section, the simpler approach is adopted (i.e., rotating the mode shape so that the angle of the longest vector is zero).

3.3 Application

In this section, application of the mode estimation method is described: first, on simulated data from the Nordic 44 test network; second, on measured PMU data from the transmission system in Norway. The presented results are from Paper II, and in both cases the DBSCAN algorithm is used to perform the clustering.

3.3.1 Simulated Data from the Nordic 44 Test Network

The system, described in detail in [35], is simulated for 20 s in DIgSI-LENT PowerFactory, where a short circuit with a clearing time of 10 ms is applied at $t = 1$ s. A 10 s excerpt of the resulting rotor angle time
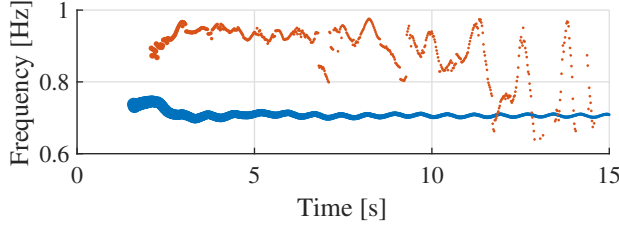
Figure 3.3: The frequency of the individual observations assigned to each of the clusters. The observations clustered together forming the 0.70 Hz estimate are shown in blue, and the observations forming the 0.89 Hz estimate are shown in orange. © 2019 IEEE.

series for each of the 44 online generators is shown in Fig. 3.2.

Applying the method results in two mode estimates with frequencies 0.70 Hz and 0.89 Hz, respectively. In Fig. 3.2, a measurement with a high observability of the 0.70 Hz mode estimate is shown in blue, and similarly for the 0.89 Hz mode estimate in orange. As can be seen, both modes are excited simultaneously. In Fig. 3.3, the observations assigned to each of the two clusters are shown. Each point corresponds to one observation resulting from Step I of the method.

From modal analysis on the linearized model, it is found that the two modes with the lowest damping have frequencies 0.66 Hz and 0.93 Hz, respectively. This matches the estimated frequencies relatively well. Further, a comparison of the mode shapes produced by the estimation method and modal analysis is shown in Figs. 3.4 and 3.5, for the 0.70 Hz estimate and the 0.89 Hz estimate, respectively. The upper plots show magnitudes of phasors in the mode shapes, the lower plots show angles.

Rotor angle time series are usually not measured directly by PMUs. The terminal voltage angle, on the other hand, could be measured and used as an approximation of the rotor angle. Therefore, the resulting magnitudes and angles of mode shape phasors from applying the estimation method to terminal voltage time series are also shown in Figs. 3.4 and 3.5.

The comparison shows that the mode shape of the 0.70 Hz mode, which has lower damping and higher excitation than the other mode, is captured more accurately. The estimate for the 0.89 Hz mode is less accurate, but still can be said to capture the main characteristics of the mode shape. Further, applying the method to rotor angle time series is more accurate than voltage angle time series, which is expected. However, voltage angle time series still provides a reasonable approximation to rotor angle mode shapes.
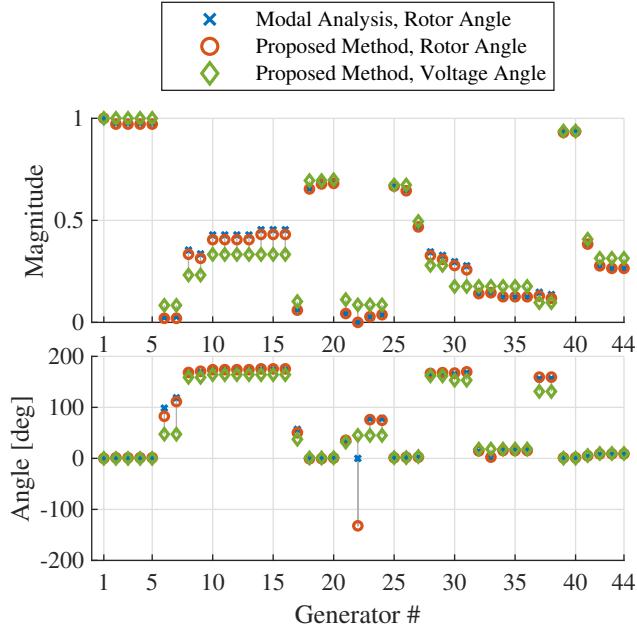
Figure 3.4: The estimated magnitudes and angles of phasors in the mode shape for the 0.70 Hz mode estimate, along with corresponding values calculated from modal analysis. © 2019 IEEE.
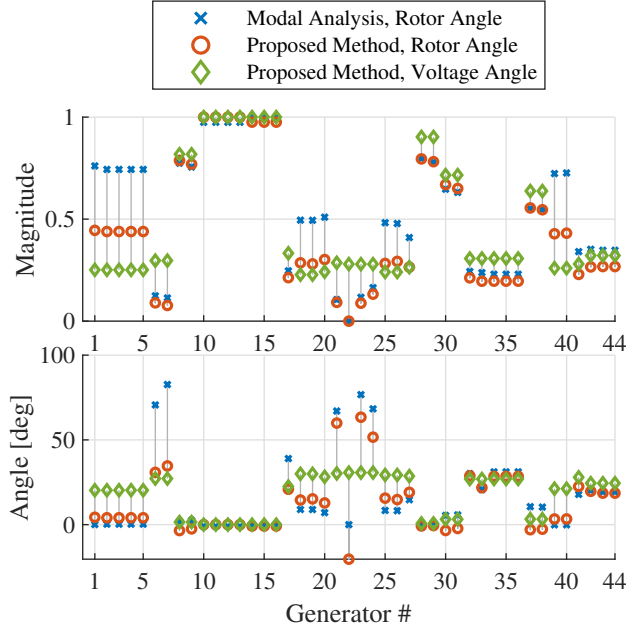
Figure 3.5: A comparison between estimated mode shape phasors and corresponding values calculated from modal analysis For the 0.89 Hz mode estimate. The accuracy is poorer than for the 0.70 Hz estimate, potentially due to the fact that the 0.93 Hz mode has higher damping and lower excitation in the measurements. © 2019 IEEE.
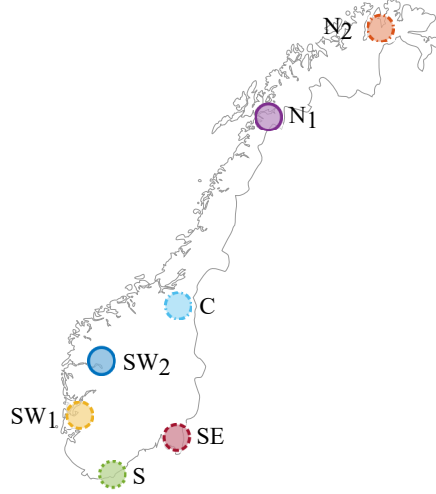
Figure 3.6: The approximate locations of seven PMUs distributed across Norway. © 2019 IEEE.

3.3.2 Measured PMU Data from the Nordic Transmission System

In this section, the result from applying the mode estimation method to measured PMU data from the transmission system in Norway is presented. The approximate locations of seven PMUs distributed throughout Norway are shown in Fig. 3.6, and the measured voltage angle time series are shown in Fig. 3.7. The 10 minute time series contains an oscillatory event occurring at approx. 280 s, lasting for about two minutes. Fig. 3.8 shows an excerpt of the time series, illustrating in detail the phase and amplitude with which the different locations are oscillating.

In Fig. 3.9, the four mode estimates produced by the method are shown. Mode estimate 1 corresponds to the standing 1 Hz oscillations. The estimated mode shape accurately describes the oscillations shown in Fig. 3.8. Mode estimate 2, with a frequency of 0.461 Hz, describes a mode where the north of Norway is oscillating in opposite phase to the south, which is a well known phenomenon in this system. Mode estimate 3 describes oscillations between the two northern locations, and Mode estimate 4 describes oscillations between the two locations S and SW_1.

In Fig. 3.10, the observations assigned to each of the four clusters are shown. The oscillation frequency of each observation is shown on the y-axis, and the coloring indicates to which cluster the observations are assigned. The histogram to the left indicates the number of observations
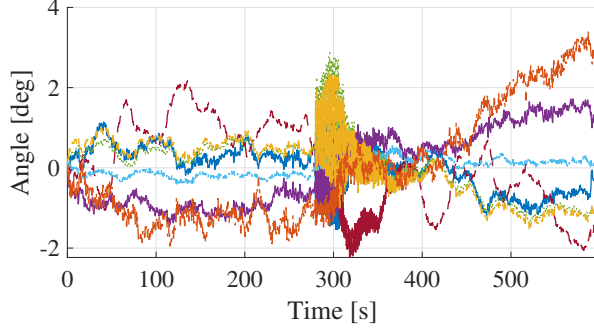
Figure 3.7: The 10 minute voltage angle time series captured by seven PMUs. The colors of the series correspond to the colors of the location markers in Fig. 3.6. Oscillations with a frequency of 1 Hz are captured in the time period between approx. 280 s and 400 s. © 2019 IEEE.
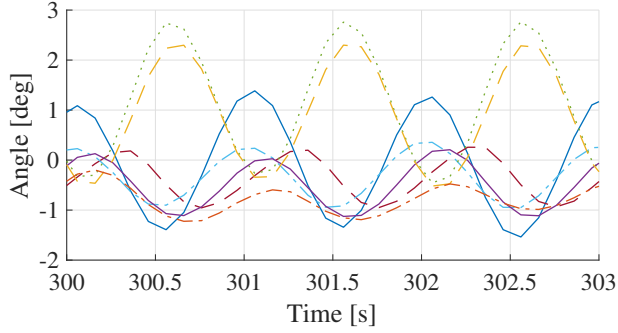
Figure 3.8: An excerpt of the time series in Fig. 3.7, clearly displaying the measured oscillations. The two locations S and SW_1 are oscillating in opposite phase to the location SW_2. The oscillations are also clearly visible with smaller amplitudes in the rest of Norway. © 2019 IEEE.
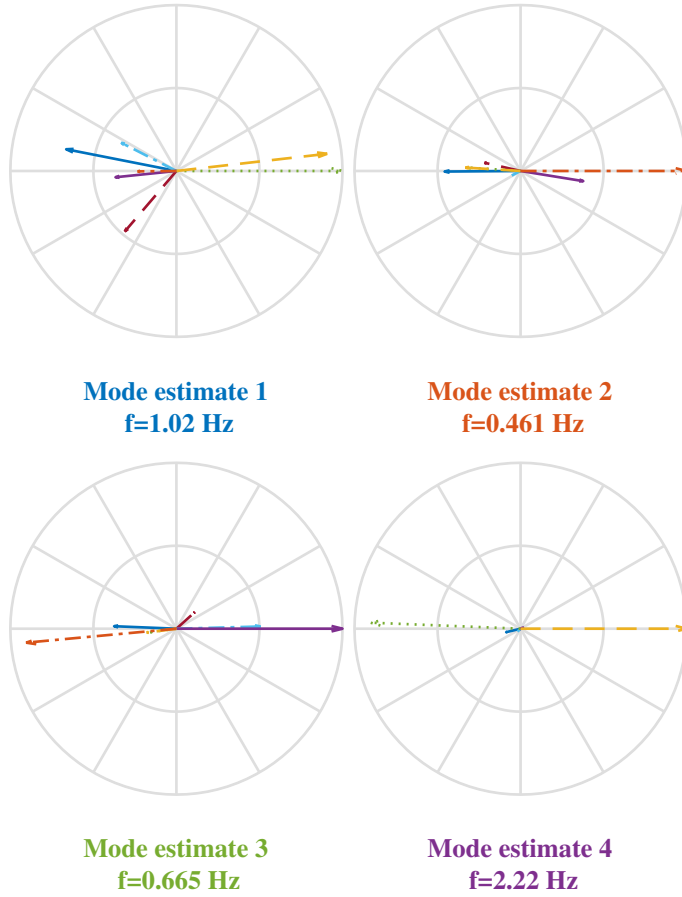
Figure 3.9: The four resulting estimates produced by the mode estimation method. The same coloring is used for the phasors as for the time series in Fig. 3.7 and the locations in Fig. 3.6. The first mode estimate describes the standing oscillations occurring at 280 s, and the three other estimates describe modes excited by random load variations. © 2019 IEEE.
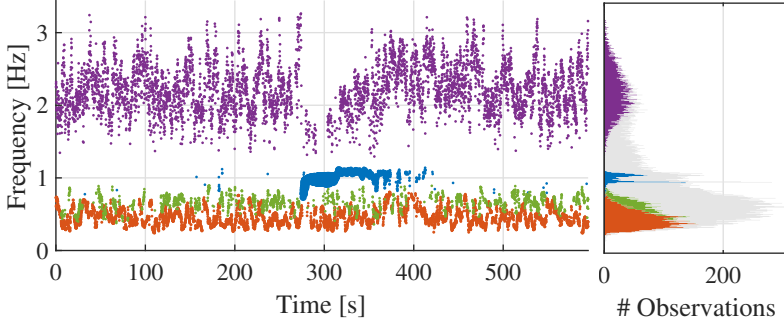
Figure 3.10: The time at which oscillations of a given frequency are observed. The colors indicate to which of the four clusters the observations were assigned. The histogram to the right indicates the number of observations of a given frequency. The gray histogram shows the observations not belonging to any clusters, classified as noise by the DBSCAN clustering algorithm. © 2019 IEEE.

with a given frequency. Fig. 3.11 shows an excerpt of Fig. 3.10, focusing on the problematic 1 Hz mode. It can be seen that the frequency of the oscillations increases at about the same time as the magnitude of the oscillations starts decreasing. This could indicate that remedial action was taken by operators, causing the system to transition from an unstable to a stable operating point.

3.4 Discussion

The results indicate that the proposed mode estimation method produces accurate estimates of frequency and observability mode shapes for low damped modes, where the accuracy increases with the excitation of the modes. Fig. 3.13 exemplifies how the mode estimation method could be visualized in an operator information system. From the visualization, the time at which oscillations occur can be read, and it is easy to see which modes are continuously excited due to random load variations and which modes are critical standing oscillations.

The point where the system starts oscillating (around $t = 280\,\text{s}$) can be understood as the system transitioning from a stable operating point to an unstable operating point. If a sufficiently detailed system model was available, then modal analysis prior to $t = 280\,\text{s}$ would predict a stable system, while after $t = 280\,\text{s}$ a complex conjugate pair eigenvalues with negative damping would be predicted. An important characteristic of the proposed method is that information about both operating points
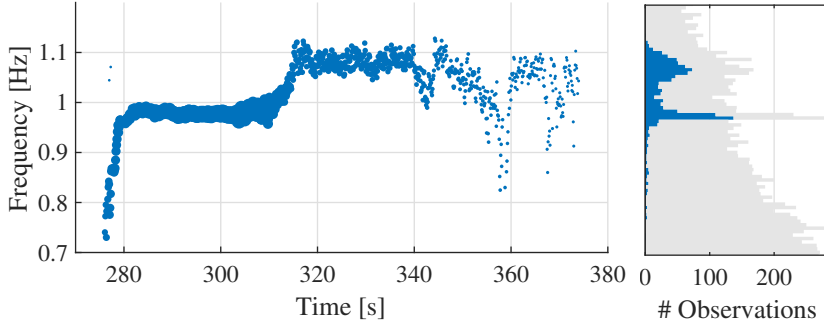
Figure 3.11: An excerpt of Fig. 3.10, focusing on the problematic 1 Hz mode. It is apparent that the oscillation frequency is initially slightly below 1 Hz, and increases to around 1.1 Hz at $t \approx 310\,\mathrm{s}$.

are conveyed in the same visualization. Furthermore, the fact that both standing oscillations and oscillations during ambient conditions are captured and visualized demonstrates a comparative advantage to many other methods, which commonly target either pronounced oscillations or ambient conditions.

Fig. 3.11 shows that the frequency of the problematic mode changes throughout the course of the oscillations. This demonstrates that the proposed method is capable of conveying information about non-linear behavior. This behavior can not be represented by a time-invariant state space model, and would thus be difficult to capture using state space identification methods (for instance, N4SID).

The information obtained by the mode estimation method could be used to determine suitable remedial actions to mitigate oscillations. In [63], it is shown that by making certain assumptions about the system, information about mode controllability can be inferred from observability mode shapes. Based on this information, a FACTS or HVDC device could be chosen where emergency power oscillation damping control could be activated.

3.5 Testing and Implementation

The two-stage structure of the method can be exploited in an online implementation. As indicated in Fig. 3.12, CPCA and the clustering algorithm can be run in two separate, parallel processes (alternatively on separate computers). The CPCA process continuously receives PMU data and runs CPCA analysis at a specified rate, and streams the result
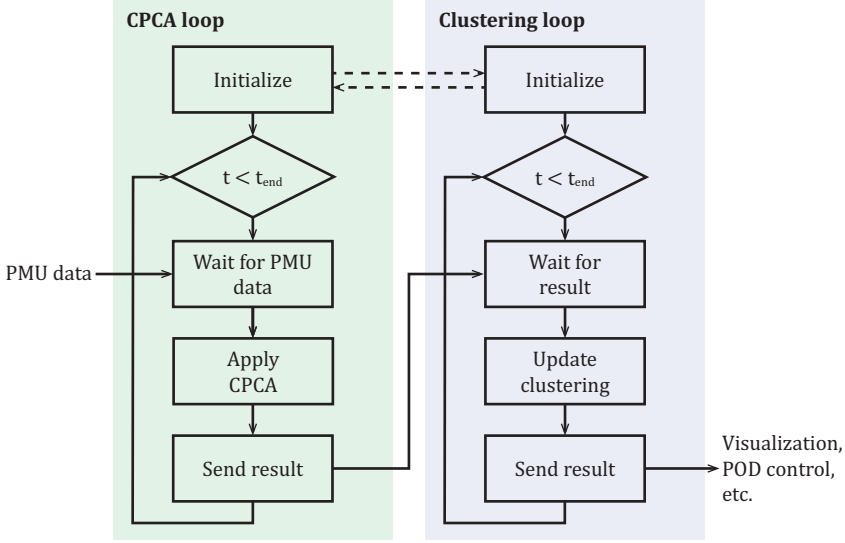
Figure 3.12: An efficient implementation of the mode estimation method can be achieved by running the CPCA step and the clustering step in parallel. In the CPCA process, PMU data is received and analyzed at a specified rate, before the result is streamed to the clustering process. In the clustering process the clustering is updated, and averaged estimates of frequency and observability mode shapes are computed and visualized, or streamed to other applications using this information.

to the clustering process where the final result is computed. Experience indicates that performing the clustering is the most computationally demanding step. To facilitate real-time operation, the CPCA step could be performed at a slower rate than the PMU reporting rate, e.g., once per second, to limit the number of observations.

Fig. 3.13 shows plots captured during simulated online operation of the mode estimation method. The recorded PMU measurements from Section 3.3.2 are played back at a rate of 10 Hz. The CPCA step is run at a rate of 5 Hz, and the clustering step is run approximately two times per second. The length of the clustering time window is 3 minutes in this case (i.e., only observations from Step I from the last 3 minutes are included when running the clustering algorithm). Choosing a longer clustering time window would increase the computation time, which would cause the clustering to be updated slower than two times per second.
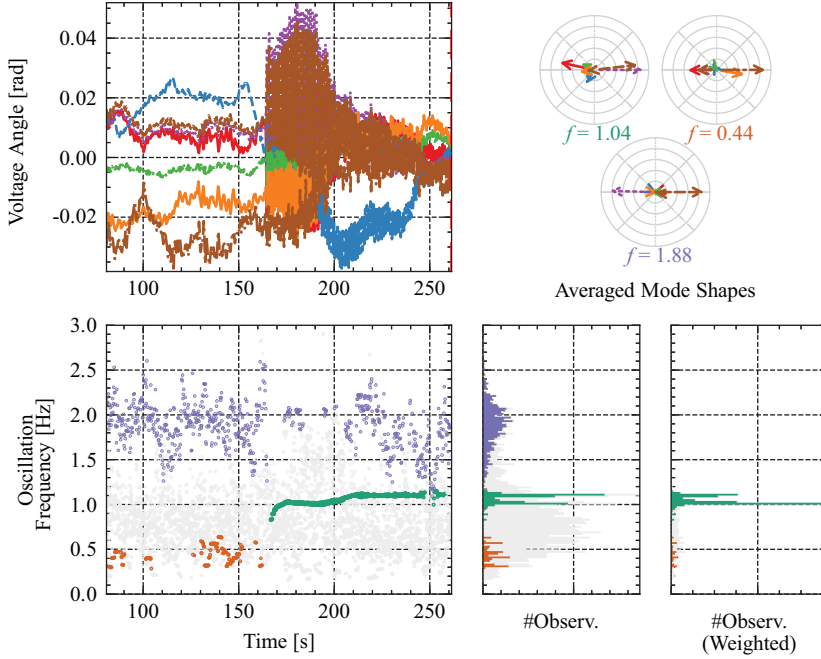
Figure 3.13: An implementation of the mode estimation method during simulated online operation, where recorded PMU measurements from the Nordic power system are played back at a rate of 10 Hz. The CPCA step and the clustering step are running in parallel processes, which is beneficial for the computational efficiency.

3.6 Further Work

An interesting topic of further work is the application of the mode estimation method to longer time spans, e.g., on the scale of hours. Results from this analysis could be used to identify patterns in the variation of frequency and observability of oscillatory modes, or identify problematic operating points associated with low damped oscillations. This information could further be taken into account when designing control systems for power oscillation damping.

Additionally, two interesting potential improvements to the mode estimation method are suggested in Section 3.2: first, using Kabsch algorithm for computing distances between mode shapes; second, using the OPTICS algorithm for performing the clustering, which is expected to make the method more general and easier to tune.

3.7   Summary

An estimation method for estimating frequency and mode shapes of oscillatory modes has been described. Results from applying the method to simulated data shows that accurate estimates are produced, which is confirmed by a comparison with corresponding quantities from modal analysis. Application to PMU data shows that modes can be estimated from both ambient conditions and during standing oscillations. Finally, an online implementation of the method has been described.

Chapter 4

Adaptive Damping Control with Enhanced Phasor POD

This chapter concerns damping control for mitigating electromechanical oscillations. **Contributions II-A, II-B, and II-C** *are presented, which represent enhancements to the well known Phasor Power Oscillation Damper. The contributions are published/submitted for publication in* **Papers III, V, and VI**.

As demonstrated in the previous chapter, PMU-based monitoring applications allow estimation of information about the system at its current operating point. In this chapter, investigations into how this information can be used for damping control purposes are presented. With Contribution II-A, the potential gain in performance when assuming knowledge of a particular transfer function residue is investigated. Contribution II-C represents a similar investigation, where observability mode shapes are assumed to be known. The two contributions are found to cause increased damping performance, given sufficiently accurate estimates of the required parameters. With Contribution II-B, a self-tuning, adaptive controller with automatic phase compensation adjustment is presented, which is found to outperform a comparable adaptive controller in the literature under the tested conditions. This work is a continuation of Contribution II-A. All contributions are developed within the Phasor Power Oscillation Damper (P-POD) framework, which is a well known type of oscillation damping controller in the literature.

In the following, relevant background on power oscillation damping
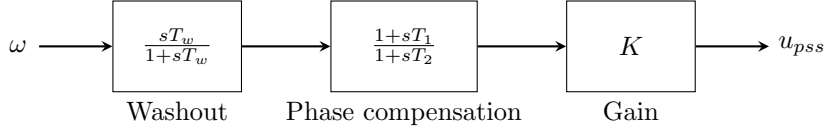
Figure 4.1: A block diagram of a simple PSS.

control is given, before the three contributions are presented. Further, a real-time simulation test setup is described, with the purpose of verifying that the proposed controllers are capable of operating in real-time.

4.1 Theoretical Foundations, State of the Art

The most common way of mitigating low damped electromechanical oscillations is by installing Power System Stabilizers (PSS) in all major generating plants. This is a controller which takes the speed, terminal frequency, and/or active power at the synchronous machine at which it is installed as input, and generates a control signal that modulates the excitation system. A block diagram of a simple, conceptual PSS is shown in Fig. 4.1, representing the basic functionality that must be fulfilled by a PSS.

In this case, the input measurement is the generator speed. The first block is a washout block with the purpose of filtering out the steady state component, since the PSS should apply no control action if there are no oscillations. The second block is a phase compensation block, with the purpose of phase shifting the signal (in order to achieve a suitable control action). Depending on the system, multiple blocks could be cascaded to achieve a suitable phase compensation across a band of frequencies. Finally, the signal is amplified by the gain block, and applied as an auxiliary signal modulating the excitation system.

A similar control structure can also be applied with other measurements and actuators, in which case the controller is often referred to as a Power Oscillation Damper (POD). HVDC systems have been used successfully for many years for mitigating oscillations. Positive experience was reported four decades ago in [64], describing a system where the Pacific HVDC Intertie in the US is modulated. Operating experience from using a TCSC installed on an intertie in the Brazillian North-South interconnection is reported in [65]. In Finland, an SVC was installed in 2009 dedicated to attenuation of inter-area oscillations [66], where the POD control is activated automatically during specific high power trans-

fer conditions. A project in the US, where SVCs were installed primarily for power oscillation damping purposes, is described [67]. Field testing of a POD modulating a Static Var Compensator (SVC) in the transmission system in Norway is described in [68], where the performance of a local POD, with local measurements, is also compared with a Wide Area POD, using PMU measurements from remote locations.

In the above mentioned cases with the TCSC in Brazil and the SVC in Norway, an alternative approach to generating the damping control signal is used, which was introduced in [69], referred to as the Phasor POD (P-POD). A model for the measured signal $S(t)$, consisting of an average component $\bar{S}$ and an oscillatory component, is established as follows:

$$S(t) = \bar{S} + \mathrm{Re}\{\vec{S}e^{j\omega t}\} \tag{4.1}$$

The oscillatory component of frequency ω (in rad/s) is represented by the phasor $\vec{S}$. Separating the measured signal into its average component and oscillatory component can be achieved using Low-Pass Filters (LPF) or an estimation algorithm like Recursive Least Squares (RLS) or a Kalman filter. Once the phasor estimate is available, a control signal is generated by phase shifting the phasor by a suitable amount β and amplifying the signal with gain K as follows:

$$u(t) = \mathrm{Re}\left\{Ke^{j\beta}\left(\vec{S}e^{j\omega t}\right)\right\} \tag{4.2}$$

Proper functioning of the P-POD requires tuning of the phase shift. In [69], a phase shift of 90° is used for a P-POD controlling the reactance setpoint of a TCSC installed on a line, where the measured quantity is the power flow in the same line. However, as shown in [70], this phase shift is not necessarily optimal. In general, if a state space model of the linearized system is available, the phase shift can be determined from transfer function residues. In the state space model, the input matrix $\mathbf{B}$ corresponds to the single input of the device controlled by the P-POD, and the output matrix $\mathbf{C}$ corresponds to the single measured quantity. From the state space formulation, the transfer function residue of the low damped mode can be calculated, as described in Section 2.3. Finally, the phase shift can be determined from (2.28), repeated here for convenience:

$$\beta = 180° - \angle[\mathbf{R}_m]_{ij} \tag{2.28}$$

Here, m is the index of the mode, and the indices i and j point to a specific measurement signal and control actuator, respectively. (If the system has a single input and a single output, then $i = j = 1$).

Comparing the P-POD and the conventional PSS, it is clear that the same basic functionality (separating out the average component, applying a phase shift, and amplifying the signal) is achieved in two different

ways. One clear difference is that the P-POD specifically targets one specific oscillatory mode. Targeting one particular mode with a control structure similar to the PSS would require tuning of time constants of a number of filters. In large power systems, there is often one or a few dominant oscillatory modes where the frequencies are easily obtainable from measurements (e.g., from PMUs). As an example, assume a large power system with a dominant inter-area mode of 0.5 Hz. Following a large disturbance, the frequency of the mode increases to 0.6 Hz. This change in frequency would be very easy to accommodate in the P-POD framework, while in a PSS it would require careful re-tuning of several time constants. Although to the knowledge of the authors, there is no consensus regarding the performance of the P-POD compared to a conventional PSS structure, the P-POD can certainly be said to be more convenient in many situations.

Since the introduction of the P-POD in [69] two decades ago, a number of enhancements have been proposed in the literature. In [70] it is shown that a phase compensation of 90° for the configuration in [69] is not necessarily optimal, and that "an adaptive phase shift scheduling mechanism...needs to be devised." In [71], the P-POD is used in a Wide Area Control framework with PMU signals as input to the controller, where the main focus is latency compensation. An adaptive phase shift mechanism is also proposed, where the phase shift β is controlled directly by a Proportional Integral (PI) regulator driving the amplitude of oscillations toward zero:

$$\beta(t) = -K_p \times |\vec{S}(t)| - K_i \times \int |\vec{S}(t)| dt \qquad (4.3)$$

The interaction between a conventional POD (with a PSS-like structure) and an adaptive P-POD based on this phase compensation scheme is studied in [72]. No adverse interaction is discovered, but it is concluded that more studies are required to substantiate this.

In Paper VI of this thesis, it is demonstrated that the phase compensation scheme given by (4.3) has a weakness: Assuming that β is initially at its ideal value, then once oscillations are observed it will start drifting away from the ideal value due to the monotonically increasing integral of the magnitude of the phasor. This can cause forced oscillations for a short period, before the ideal phase compensation is again reached. The same adaptive phase compensation scheme is used also in [73], where a more comprehensive latency compensation scheme is proposed, and the P-POD applies damping control action through a Doubly Fed Induction Machine.

The contributions presented in the following focus on two main aspects. First, it is interesting to explore how new information derived from

measurements can be used to produce more efficient, precise damping control signals for mitigating oscillations. As mentioned, power oscillation damping is sometimes the main motivation for installing FACTS devices. An improved algorithm for generating the damping control signal could increase the "damping effect per installed MVAr" [74], and thus reduce the cost of the investment. Second, there is a need for a robust scheme for adjusting the phase compensation of the P-POD, facilitating automatic, self-tuning behavior during changing operating conditions. In the following, three contributions addressing these aspects are presented.

4.2 Phasor POD enhanced with a Control-Input Model

*In this section, **Contribution II-A** is presented, which represents enhancing the Phasor Power Oscillation Damper with a Control-Input Model. This contribution is to be published in **Paper V**.*

In previous variants of the P-POD described in the literature, the phasor estimator generates the average component and the phasor that fits best with the measurement. Thus, the only source of information for the estimator is the chosen measured signal. The main objective of Paper V is to investigate the potential benefit of also taking the control signal applied by the P-POD into account in the estimation. Arguably, this signal is definitely available at the estimator and represents a source of information that should not be left unused. Since more information is taken into account in the estimation, it is expected that this will enhance the performance of the controller. In Fig. 4.2, a simple block diagram describing a P-POD is shown, where including the control signal in the phasor estimation corresponds to adding the dashed arrows.

Specifically, the contribution described in this section represents a predictor-corrector phasor estimator in the form of a Kalman filter. The phasor at the next time step is predicted based on the control action that the controller applies at the current time step, and the measurement is used to correct the predicted estimate. The prediction requires a model of how the system responds to the control signal, and this model is established by assuming that the response can be described by a linear power system model. In Paper V it is found that only a single complex number is required to perform the prediction. This complex number is the transfer function residue of the low damped mode, as defined in Section 2.3, where the transfer function is from the applied control signal
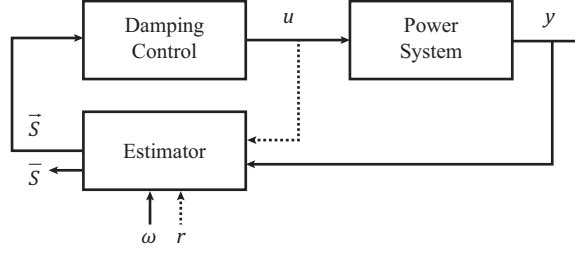
Figure 4.2: The block diagram emphasizes the additional information (dashed arrows) taken into account when enhancing the P-POD with a Control-Input Model, specifically: The applied control signal u, and the transfer function residue r of the mode.

to the output measurement.

In the following, the predictor-corrector estimator will first be presented (based on theory developed in Paper V); second, a comparison with conventional LPF-based and RLS-based P-POD estimators is given; and finally, results that demonstrate the performance gain from the enhancement are presented.

4.2.1 Predictor-Corrector Estimator

A Kalman filter is commonly given on the following form:

$$\mathbf{X}_{k+1} = \mathbf{F}_k\mathbf{X}_k + \mathbf{G}_k u_k + \mathbf{w}_k \tag{4.4}$$

$$Y_k = \mathbf{H}_k\mathbf{X}_k + v_k \tag{4.5}$$

where:

$\mathbf{X}_k$ = Kalman Filter states
$\mathbf{F}_k$ = State Transition Model
$\mathbf{G}_k$ = Control-Input Model
Y_k = Measurement
$\mathbf{H}_k$ = Observation Model
$\mathbf{w}_k$ = Process noise, with covariance matrix $\mathbf{Q}$
v_k = Measurement noise, with variance R

The quantities that are to be estimated by the filter are the signal average $\bar{S}$ and the d- and q-axis components of the phasor (i.e., $\vec{S} = D + jQ$). The Kalman filter states are therefore chosen as follows:

$$\mathbf{X}_k = \begin{bmatrix} \bar{S}_k, & D_k, & Q_{k,} \end{bmatrix}^\mathsf{T} \tag{4.6}$$

Further, the Kalman filter measurement is the same as the measurement of the controller ($S(t)$ in (4.1)):

$$Y_k = S_k \tag{4.7}$$

Mapping the filter states to measurement space is achieved with the Observation Model, which is determined by rewriting (4.1) in terms of the real and imaginary components of the phasor (as described in Paper V). The resulting observation model (which is the same also in RLS-based phasor estimators) is as follows:

$$S_k = \underbrace{\begin{bmatrix} 1 & \cos \omega t & -\sin \omega t \end{bmatrix}}_{\mathbf{H}_k} \begin{bmatrix} \bar{S}_k \\ D_k \\ Q_k \end{bmatrix} \tag{4.8}$$

The prediction model, consisting of the State Transition Model and the Control-Input Model, is developed by introducing linear state space theory. Specifically, based on the solution of the linearized system given in (2.26), the prediction model for the real (D) and imaginary (Q) components of the phasor is established (described in detail in Paper V):

$$D_{k+1} = D_k + (U g(t) + V h(t)) \Delta u_k \tag{4.9}$$

$$Q_{k+1} = Q_k + (-U h(t) + V g(t)) \Delta u_k \tag{4.10}$$

Here, the time dependent functions $g(t)$ and $h(t)$ are sinusoidal functions, given by

$$g(t) = \frac{2}{\omega} \Big[-\sin (\omega t) + \sin (\omega(t + \Delta t)) \Big] \tag{4.11}$$

$$h(t) = \frac{2}{\omega} \Big[\cos (\omega t) - \cos (\omega(t + \Delta t)) \Big] \tag{4.12}$$

The coefficients U and V are the real and imaginary components of the transfer function residue of the mode, where the transfer function is from the applied control signal to the output measurement:

$$r = U + jV \tag{4.13}$$

The prediction model can be rewritten on the following form, which can be used in the Kalman filter:

$$\begin{bmatrix} \bar{S}_{k+1} \\ D_{k+1} \\ Q_{k+1} \end{bmatrix} = \underbrace{\begin{bmatrix} 1 & & \\ & 1 & \\ & & 1 \end{bmatrix}}_{\mathbf{F}_k} \begin{bmatrix} \bar{S}_k \\ D_k \\ Q_k \end{bmatrix} + \underbrace{\begin{bmatrix} 0 \\ U g(t) + V h(t) \\ -U h(t) + V g(t) \end{bmatrix}}_{\mathbf{G}_k} u_k \tag{4.14}$$

The predicted signal average $\bar{S}$ is equal to the current value (since a model for the average is difficult to establish). Observing the above equations, it can be seen that to perform the prediction given control signal Δu, two parameters are required: The frequency of the oscillatory mode ω and the residue r.

This determines the states, the measurement, and the models required to apply the Kalman filter. The next section concerns determining the covariance matrices.

Tuning the Kalman filter by relating to LPF- and RLS-based estimators

The motivation for introducing a Kalman filter-based phasor estimator is that it enables prediction of the amplitude and angle of the phasor based on the applied control signal. In this section, the performance of the proposed estimator is analyzed *without* applying a control signal. Under these circumstances the benefit of the prediction step will not be present, and the performance is expected to be similar to an LPF- or an RLS-based phasor estimator. By comparing the response of the three types of phasor estimators, a starting point for the tuning of the Kalman filter is obtained.

Considering (4.14), it is clear that if the control signal is zero, or the residue parameters U and V are zero, then the predicted states will always be equal to the current states. This results in a Kalman filter with $\mathbf{F}_k = \mathbf{I}_3$ (where $\mathbf{I}_n$ is the $n \times n$-identity matrix) and $\mathbf{G}_k = 0$. A Kalman filter on this form is very closely related to a RLS filter. Where the Kalman filter is tuned using (co)variances $\mathbf{Q}$ and R, the RLS filter is tuned using the forgetting factor λ. If the process noise covariance matrix of the Kalman filter is also set to zero ($\mathbf{Q} = 0$) and the forgetting factor of the RLS filter is equal to one ($\lambda = 1$), then the two filters are equivalent. However, the estimators are much more useful if they can be tuned using the forgetting factor for the RLS-based estimator and the covariance matrices for the Kalman filter-based estimator.

Considering RLS, the forgetting factor can be selected between 0 and 1, most commonly close to 1. A low value increases the "forgetting" and allows the filter to converge more rapidly, while a high value gives a slower, but more predictable response. The relation between LPF- and RLS-based phasor estimators is discussed in detail in [29] and [75]. The bandwidth of the LPF filter is the cutoff frequency. The bandwidth of the RLS filter ω_{bw} relates to the forgetting factor λ as follows:

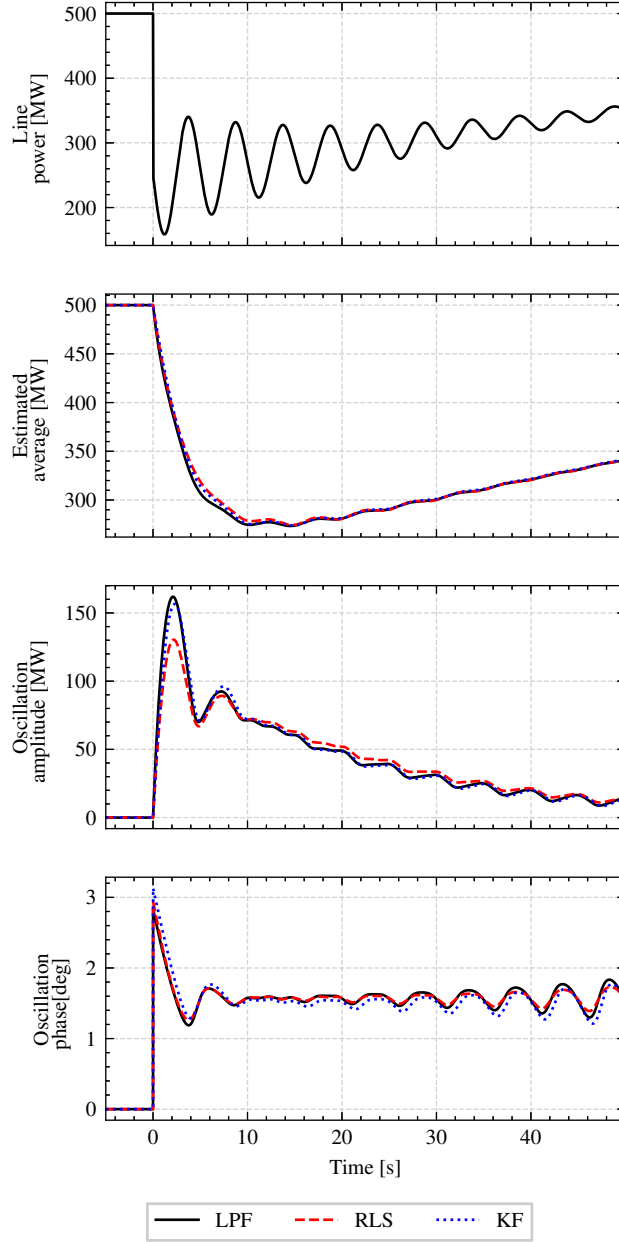$$\omega_{bw} = \frac{1 - \lambda}{\Delta t} \qquad (4.15)$$

Figure 4.3: A comparison of three phasor estimators: An LPF-based, an RLS-based and a Kalman filter-based estimator. This result shows that similar performance is achieved in all three cases. The test signal (in the first subplot) is a reconstruction of a similar test in [69].

Estimator type	LPF	RLS	KF
Tuning parameter	Cutoff frequency	Forgetting factor	Noise covariances
Expression	ω_{bw}	$\lambda = 1 - \omega_{bw}\Delta t$	$\mathbf{Q} = (\omega_{bw}\Delta t)^2 \cdot \mathbf{I}_3$ $R = 1$

Table 4.1: Expressions for tuning of LPF-, RLS-, and Kalman filter-based estimators for similar performance.

In [76], it is shown that the LPF-based and the RLS-based phasor estimators exhibit similar dynamic performance when the condition $\omega_{bw} <<$ ω_{mode} is fulfilled, i.e., the bandwidth is much lower (e.g., one decade) than the frequency of the targeted low damped mode.

The Kalman filter can be tuned using the process noise covariance matrix $\mathbf{Q}$ and the measurement noise variance R. By trial and error, it is found that the Kalman filter-based phasor estimator exhibits highly similar dynamic performance to the LPF- and RLS-based phasor estimators when the following tuning for the covariances is used:

$$\mathbf{Q} = (k_\sigma \cdot \omega_{bw}\Delta t)^2 \cdot \mathbf{I}_3 \tag{4.16}$$

$$R = k_\sigma^2 \tag{4.17}$$

Scaling both matrices by the coefficient k_σ does not affect the dynamic performance. (However, the scaling coefficient does affect performance measures like the likelihood function, which are important for the work on the adaptive P-POD described in Section 4.3.)

The tuning of the three estimator types to a given bandwidth ω_{bw} given time step Δt is summarized in Table 4.1. (For the Kalman filter estimator the parameter k_σ is omitted, i.e., $k_\sigma = 1$, but any other value could be chosen.) In Fig. 4.3, a comparison of the three phasor estimators is shown, where each estimator is tuned for the same bandwidth. No control signal is being applied, i.e., the estimators are simply fitting the average and the phasor to the measurements. The test signal is reconstructed from a similar test in [69]. Observing the curves, it is clear that the dynamic performance is highly similar for the LPF-based, RLS-based, and Kalman filter-based phasor estimators.

4.2.2 Application

In the following, some results from Paper V are presented, where the proposed P-POD enhancement is tested on the Single-Machine Infinite Bus system and the IEEE 39-Bus System. The focus is comparing the
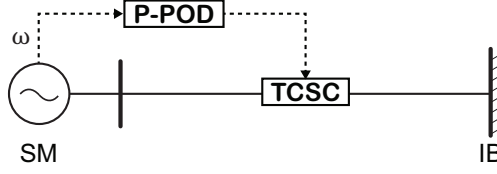
Figure 4.4: The single line diagram shows the Single-Machine Infinite Bus system with a TCSC installed on the line between the synchronous generator and the infinite bus. A P-POD measures the generator speed and modulates the setpoint of the TCSC.

P-POD *without* a Control-Input Model, with a P-POD *with* a Control-Input Model. In the remainder of this section, the former is referred to as P-POD-0, and the latter is referred to as P-POD-CIM. Simulations were carried out using the simulation tool described in Section 2.4. For Kalman filter implementations, the package FilterPy [77] was used.

Single-Machine Infinite Bus System

The parameters of the Single-Machine Infinite Bus System are given in [9, p. 752]. A TCSC is installed on the line between the machine and the infinite bus, and the P-POD measures the generator speed deviation (in %pu) and modulates the reactance setpoint of the TCSC. A single line diagram of the system is shown in Fig. 4.4.

The system has an unstable 1.01 Hz mode with negative damping of -2.09%. A short circuit on the terminals of the synchronous machine is simulated to excite the mode. In Fig. 4.5, the performances of the P-POD-0 and the P-POD-CIM are compared, where it can be seen that both controllers successfully stabilize the oscillations. Comparing the fitted and the measured signals in the two cases, it is apparent that the phasor estimation is more accurate with the P-POD-CIM. The two cases can be compared in terms of performance P and cost C, defined as follows:

$$C = \frac{1}{N}\sqrt{\sum_{k=0}^{N-1} u_k^2}, \quad P = \left(\frac{1}{N}\sqrt{\sum_{k=0}^{N-1} \Delta y_k^2}\right)^{-1} \quad (4.18)$$

The control cost is the RMS value of the control signal, and the performance is the inverse of the RMS value of the measurement signal, which in this case is the speed deviation of the synchronous machine. According to these measures, the damping performance of the P-POD-0 is 7% better, but the control cost is also 22% higher.
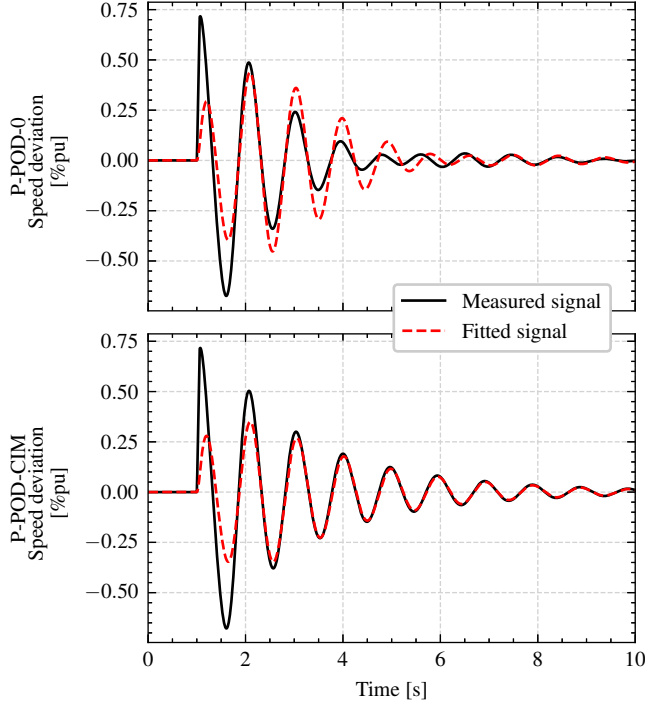
Figure 4.5: Results from the Single-Machine Infinite Bus system, without (P-POD-0, upper plot) and with (P-POD-CIM, lower plot) a Control-Input Model. The measured signals are shown alongside the fitted signals from the estimators. It is evident that a better fit is achieved with the P-POD-CIM.

For a fair comparison, the two controllers are compared for a range of gains, where the control cost and performance are calculated for each case. The result from this procedure is shown in Fig. 4.6, where it demonstrated that the performance of the P-POD-CIM is higher than for the P-POD-0 for the same control cost.

IEEE 39-Bus System

To verify that the above results are valid also for a larger system, the P-POD-CIM is tested on the IEEE 39-Bus System. The single line diagram is given in Fig. 4.7.

To destabilize the system and provoke undamped oscillations, Line 2-25 (i.e., the line between buses 2 and 25) is disconnected and the stabilizers on machines 8 and 9 are deactivated. This results in an oscillatory
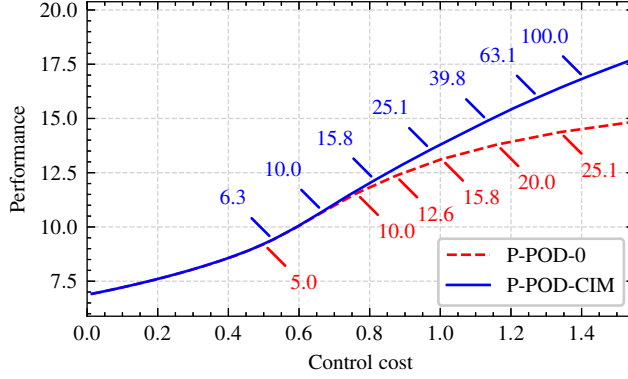
Figure 4.6: The performance and control cost for varying gains for the P-POD, without (P-POD-0) and with (P-POD-CIM) a Control-Input Model. It is evident that the Control-Input Model enhances the performance for the same cost, particularly for higher gains. The gains are indicated along the curves.

mode with frequency 0.44 Hz and zero damping. The controller measures the active power flow in a line and modulates the setpoint of a TCSC. Determining the locations of the measurement and the TCSC is done by performing a preliminary residue analysis: The vector of output measurements $\mathbf{y}$ is chosen such that each element corresponds to the active power flow in one line. Further, a hypothetical TCSC is installed on every line in the system. The control vector $\mathbf{u}$ is chosen such that each element corresponds to the setpoint of one TCSC. Having chosen both $\mathbf{y}$ and $\mathbf{u}$ determines both functions f and h in (2.17), and allows numerical calculation of the matrices $\mathbf{C}$ and $\mathbf{B}$ by finite differences according to (2.16). Finally, the matrix of transfer function residues associated with the low damped mode can be calculated according to (2.27). Assuming the model has N_L lines, the matrix will have dimension $N_L \times N_L$.

The result from this procedure for the IEEE 39-Bus System is shown in Fig. 4.8. The mode observability, shown in the bar plot on top, is given by the product $\mathbf{C}\boldsymbol{\phi}_m$ (where m is the index of the targeted low damped mode), and the mode controllability, shown to the right, by the product $\boldsymbol{\psi}_m \mathbf{B}$. Studying the matrix of residues (where the absolute value is shown in the figure), the largest residues are obtained when modulating a TCSC on Line 26-29. There are multiple good candidates for the measurement; out of these the active power flow in Line 26-27 is chosen due to its proximity to the TCSC.

The simulated event is a short circuit on Bus 2 with a clearing time
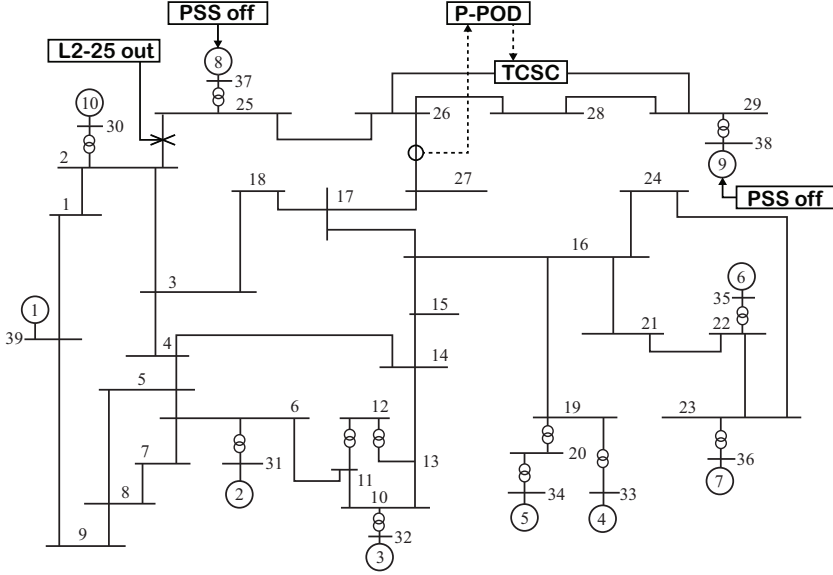
Figure 4.7: A single line diagram showing the IEEE 39-Bus System. For testing the P-POD, stabilizers (PSS) are deactivated on generators 8 & 9 and Line 2-25 is disconnected. A TCSC is installed on Line 26-29. The TCSC is modulated by a P-POD, which measures the active power flow in Line 26-27. Source: Adapted from [34].

of 50 ms. Results from three simulations are shown in Fig. 4.9: Without control, with P-POD-0, and with P-POD-CIM. The uncontrolled case is clearly unstable. By comparing the control signals from the two controlled cases, it is clear that the performance of the P-POD-CIM is preferable. It should be noted that for lower gains the difference in performance for the two controllers is smaller, but this example indicates that taking the control signal into account in the estimation permits a higher gain to be used without introducing unwanted effects (like the erratic control signal in the case of the P-POD-0).

4.2.3 Discussion

The results verify that the proposed predictor-corrector estimator enhances the performance of the P-POD. This should come as no surprise, since more information about the system is required (in terms of the transfer function residue) and an additional signal is taken into account (the control signal). The performance increase is more visible for higher gains, and more subtle for lower gains. Power oscillation damping is

64
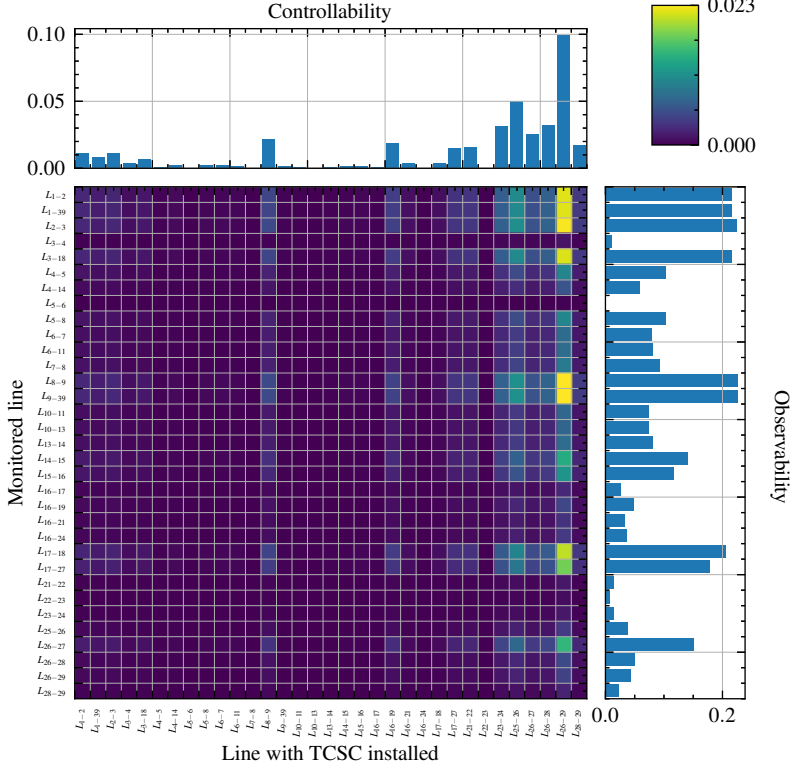
Figure 4.8: The matrix of transfer function residues of the low damped mode in the IEEE 39-Bus System. The upper bar plot shows the mode controllability of different control actuators (setpoints of hypothetical TCSCs, one installed on each line), and the left bar plot shows the mode observability in different output measurements (active power flows in lines). The elements of the residue matrix are the products of corresponding controllability and observability indices, where the absolute value is indicated by the coloring. It is evident that modulating a TCSC on Line 26-29 is a good choice. There are several good candidates for the measurement signal; out of these, Line 26-27 is selected due its proximity to the TCSC.
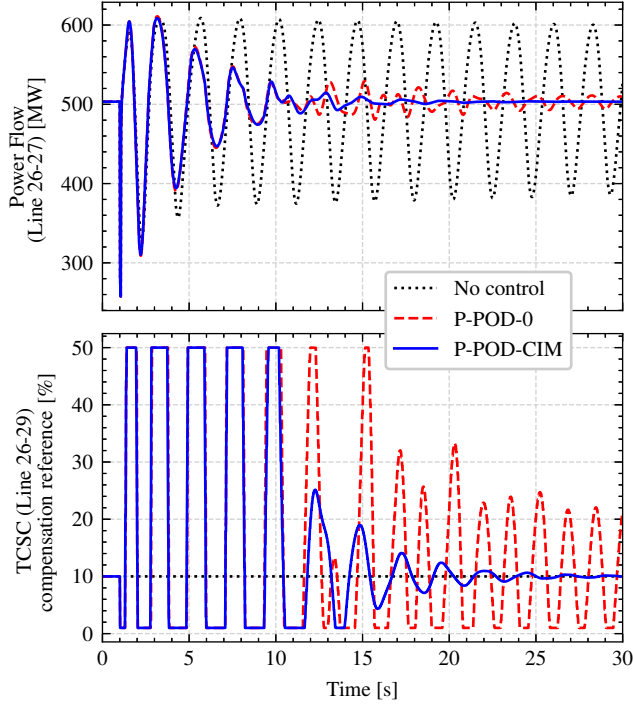
Figure 4.9: Results from simulations in the IEEE 39-Bus System. The uncontrolled case is clearly unstable. Only the P-POD-CIM performs satisfactorily in this case.

sometimes the primary motivation for installing FACTS devices [66,67], and thus the required capacity of the FACTS device would be determined by the required damping performance. Thus, an algorithm providing a more precise and efficient damping control signal could potentially reduce the required MVAr of the device, and thus reduce the cost of the investment.

In the presented results, exact knowledge of the required transfer function residue has been assumed. However, the residue is not necessarily straight-forward to obtain in a real, large-scale power system. In Paper V, the robustness of the controller to residue parameter error is investigated. Results from the Single-Machine Infinite Bus system indicate that under the tested conditions, introducing the Control-Input Model increases the performance of the controller as long as the residue estimate is within $-24°$ and $+60°$ of the exact residue. In a practical situation, the required residue could be obtained from model-based modal

analysis, given that a sufficiently detailed power system model was available. Otherwise, it could be estimated from measured data and control signals using system identification techniques. For large scale systems, the latter option is probably more feasible.

Another option for obtaining the required residue is to develop the phasor estimator one step further, to facilitate estimation of the residue. This is the topic of the next section, where this is achieved by introducing a Multiple Model Adaptive Estimation scheme. In addition to eliminating the requirement of knowledge of the residue, this also allows the phase compensation to be adjusted according to the current residue estimate (according to (2.28)), resulting in an adaptive controller.

4.3 Adaptive Phasor POD

*In this section, **Contribution II-B** is presented, which represents developing the Phasor Power Oscillation Damper into a self-tuning, adaptive controller. This work is to be published in **Paper VI**.*

As mentioned in Section 4.1, the adaptive phase compensation scheme for the P-POD proposed in [71], and used in [73], has a weakness in that an initially ideal phase compensation (β in (4.3)) is prone to start drifting away from the ideal value once oscillations are observed. This motivates the development of a novel phase compensation scheme, which is the topic of Paper VI.

The fundamental idea arises from the introduction of the Control-Input Model, described in the previous section, which facilitates prediction of the mode phasor at the next step based on the control signal applied at the current step. The aim is to allow the estimator to not only make predictions, but also to improve the predictions. This is achieved by introducing a Multiple Model Adaptive Estimation (MMAE) scheme.

4.3.1 Multiple Model Adaptive Estimation

MMAE was first proposed in 1965 [78], but was at the time considered impractical for online implementation due to the high computational burden of running a high number of Kalman filters in parallel. Given recent advances in computer technology, this no longer remains an issue. Multiple Model Adaptive Control, which is closely related to MMAE, has been applied previously for damping of inter-area oscillations in [79]. In the following, MMAE is used to develop an adaptive, self-tuning P-POD with automatic phase compensation adjustment during changing operating conditions.

In the previous section, where a Control-Input Model was introduced, it was found that the amplitude and phase of the mode phasor can be predicted based on the applied control signal. The requirement is that the transfer function residue of the mode is known, where the transfer function is from the applied control signal to the measured output signal. The main idea of Paper VI is to run an ensemble of Kalman filters in parallel, each making predictions based on a specific hypothetical value of the transfer function residue. Based on the performance of the filters (in terms of prediction accuracy), a state estimate can be generated from the probability-weighted state estimates of the individual filters. An estimate of the residue can be generated in a similar way, finally allowing the phase compensation to be adjusted according to the current

residue estimate.

The filters in the MMAE bank are chosen such that they are equal except for the Control-Input Model, which is determined from the residue. Residues are generated by rotation of an initial residue guess:

$$r_i = r_0 \cdot e^{j\theta_i}, \quad \theta_i = \frac{2\pi \cdot i}{N+1}, \quad i = 1, 2, ..., N \tag{4.19}$$

The Control-Input Model parameters for each filter are thus determined as $U_i = \mathrm{Re}\{r_i\}$ and $V_i = \mathrm{Im}\{r_i\}$. The prediction equations for filter i are as follows:

$$\begin{bmatrix} \bar{S}_{i,k+1} \\ D_{i,k+1} \\ Q_{i,k+1} \end{bmatrix} = \begin{bmatrix} 1 & & \\ & 1 & \\ & & 1 \end{bmatrix} \begin{bmatrix} \bar{S}_{i,k} \\ D_{i,k} \\ Q_{i,k} \end{bmatrix} + \underbrace{\begin{bmatrix} 0 \\ U_i g(t) + V_i h(t) \\ -U_i h(t) + V_i g(t) \end{bmatrix}}_{\mathbf{G}_{i,k}} u_k \tag{4.20}$$

To quantify the performance of an individual filter i, the the residual $\varepsilon_{i,k}$ is introduced:

$$\varepsilon_{i,k} = Y_k - \mathbf{H}_k \mathbf{X}_{i,k} \tag{4.21}$$

The residual is the difference between the measurement and the state estimate projected into measurement space. Next, the variance of the residual $E_{i,k}$ is introduced:

$$E_{i,k} = \mathbf{H}_k \mathbf{P}_{i,k} \mathbf{H}_k^\mathsf{T} + R \tag{4.22}$$

This allows calculation of the likelihood function, defined as follows:

$$\mathcal{L}_{i,k} = \frac{1}{\sqrt{2\pi E_{i,k}}} \exp\left[-\frac{\varepsilon_{i,k}^2}{2E_{i,k}} \right] \tag{4.23}$$

An interpretation of the likelihood function is that it tells how likely it is that the filter is performing optimally [80]. In the MMAE scheme, the final state estimate is calculated as the weighted sum of the state estimates of the individual filters. The likelihood function is used to calculate these weights. Assuming N_f filters in the bank, the weights are initialized with the value $W_i = 1/N_f$. At each time step the weights are updated recursively. A three-step weighting scheme described in [81] is adopted, as follows:

1. Recursive update of weights:

$$W_{i,k}' = \frac{\mathcal{L}_{i,k} W_{i,k-1}}{\sum_{j=1}^{N} \mathcal{L}_{j,k} W_{j,k-1}} \tag{4.24}$$

2. Bounding from zero, with minimum value δ:

$$W_{i,k} = \begin{cases} W'_{i,k} & \text{if } W_{i,k} > \delta \\ \delta & \text{if } W_{i,k} \leq \delta \end{cases} \tag{4.25}$$

3. Normalization:

$$W_{i,k} = \frac{W_{i,k}}{\sum_{j=1}^{N} W_{j,k}} \tag{4.26}$$

The first step is the standard way of updating weights in a MMAE scheme. The second step is a modification, which is necessary to avoid poorly performing filters from "dying out." The final state estimate from the MMAE filter bank is computed by weighting the state estimates of the individual filters:

$$\mathbf{X}_k = \sum_{i=1}^{N} W_{i,k} \cdot \mathbf{X}_{i,k} \tag{4.27}$$

Similarly, the residue estimate is calculated as follows:

$$r_k = \sum_{i=1}^{N} W_{i,k} \cdot r_i \tag{4.28}$$

Finally, the phase compensation β is adjusted according to the current residue estimate:

$$\beta_k = 180° - \arg\{r_k\} \tag{4.29}$$

A block diagram describing the MMAE scheme is shown in Fig. 4.10.

Tuning of filters

The Kalman filters in the MMAE filter bank are tuned according to the expressions for the P-POD with a Control-Input Model presented in Section 4.2.1. For a P-POD with a single Kalman filter estimator, multiplying the process noise covariance matrix $\mathbf{Q}$ and the measurement noise variance R by a constant does not affect the performance of the controller. However, in a MMAE scheme, the weights of the filters are determined by the likelihood functions of the filters, and the likelihood functions do depend on the scaling of the (co)variances. The speed of convergence of the filter weights can be controlled by choosing the value of the parameter k_σ in (4.16) and (4.17), where lower values lead to faster convergence and higher values lead to slower convergence. Choosing the parameter involves a trade-off between being able to follow changing operating conditions and avoiding erratic, unpredictable evolution of the
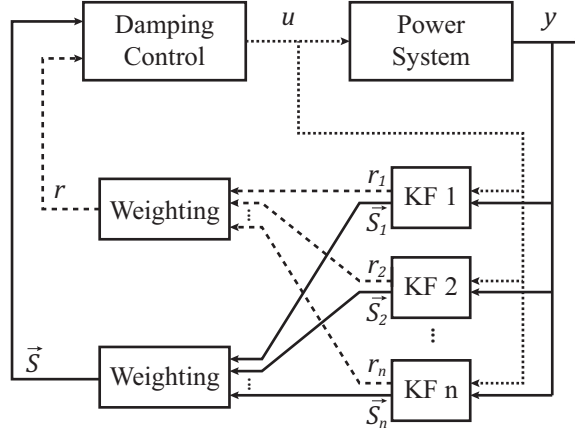
Figure 4.10: The block diagram describes the MMAE scheme, where the Kalman filters (KF1, KF2,...,KFn) are running in parallel. The weighting functions determine the final phasor estimate and the residue estimate. The latter is used to adjust the phase compensation used for generating the control signal.

weights. Experience indicates that choosing the parameter such that the measurement noise variance R is in the same order of magnitude as the amplitude of the targeted oscillations is a good starting point for tuning the covariance scaling parameter.

4.3.2 Application

The adaptive P-POD is tested on three systems: first, on the Single-Machine Infinite Bus system, where the proposed method for adjusting the phase compensation scheme is compared with the mentioned PI control-based scheme described in the literature; second, on Kundur's Two-Area System, where the controller is tested on a large disturbance; and third, on the IEEE 39-Bus System, where the controller is tested in a wide area configuration with communication delay. Similarly as in Section 4.2, the simulations were carried out using the simulation tool described in Section 2.4, and the package FilterPy [77] was used for the Kalman filter implementations.

Single-Machine Infinite Bus

Simulations on the Single-Machine Infinite Bus system are performed to compare the performance of the proposed MMAE-based adaptive P-

POD with the PI control-based scheme used in [71] and [73]. The simulated system is the same as the one described and simulated in Section 4.2.2, where the single-line diagram is given in Fig. 4.4.

A simulation is carried out with three short circuits (at $t = 1\,\mathrm{s}$, $t = 15\,\mathrm{s}$, and $t = 30\,\mathrm{s}$). As a simple test of the two adaptive phase compensation schemes, a polarity reversal of the control signal is applied at $t = 15\,\mathrm{s}$. This shifts the actual residue angle by 180°, requiring the controllers to adjust the phase compensations to avoid amplifying oscillations.

For the MMAE scheme, the covariance scaling coefficient is $k_\sigma = 1$. The magnitude of the required residue is assumed to be known, and is used to generate rotated variants of the residue according to (4.19). No knowledge about the residue angle (and thus the ideal phase compensation) is assumed. The initial setting for the phase compensation is zero for both controllers. For the PI controller, the proportional and integral gains are $K_p = 1$ and $K_i = 1$. The controller gain is $K = 0.2$ in both cases.

The results from simulating the MMAE-based and the PI control-based schemes are shown in Fig. 4.11, where the measurement (active power flow in the line) and the phase compensation is shown for both schemes. Additionally, the MMAE filter weights are shown. Following the first and second disturbances, both controllers find suitable phase compensations and the oscillations are damped. The polarity reversal is also tackled well by both controllers. However, the third disturbance causes the PI control-based phase compensation to drift away from a value close to the ideal value, causing forced oscillations for a short period. The MMAE-based scheme does not exhibit this behavior, and thus outperforms the PI control-based scheme in this case.

Kundur's Two-Area System

The parameters describing the system are given in [9]. All generators are equipped with simple control models; AVR model SEXS, turbine-governor model TGOV1, and PSS model STAB1.

The system consists of two weakly connected areas with two 900 MVA-rated generators in each area, and there is a power transfer of 400 MW between the areas. Modal analysis reveals that the system has three electromechanical modes; two local modes (one for each area) with a frequency of about 1 Hz and one dominant inter-area mode with a frequency around 0.5 Hz. A single line diagram of the system is given in Fig. 4.12.

Choosing the measurement and the location of the TCSC to be modulated by the controller is again done by residue analysis, similar to the
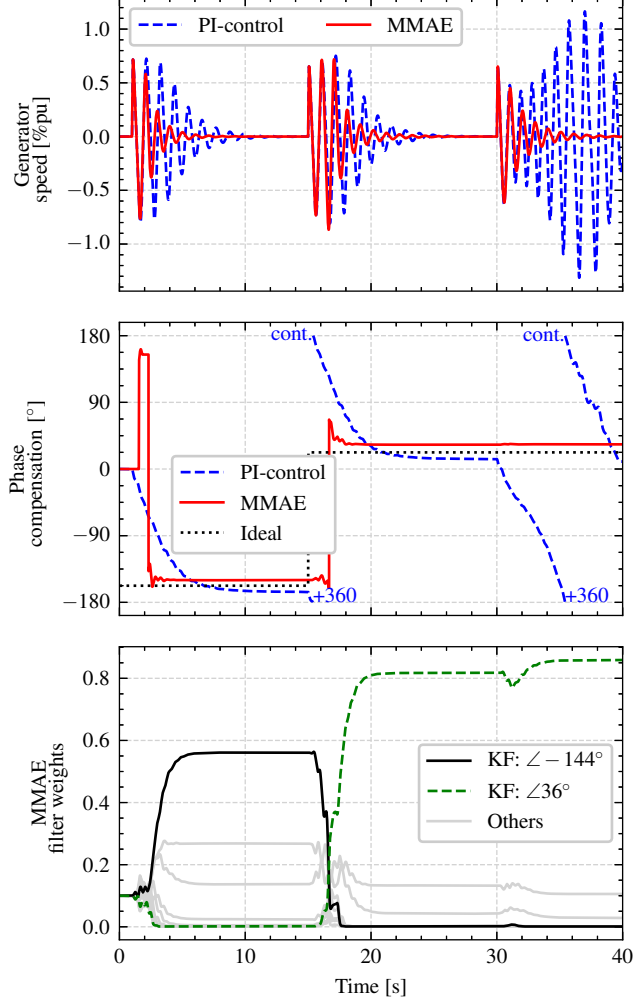
Figure 4.11: The results from two simulations on the Single-Machine Infinite Bus system, where the phase compensation of the P-POD is determined from a PI controller (dashed blue lines) and from the proposed MMAE scheme (red lines). The lower plot shows the evolution of the filter weights for the MMAE scheme, which determine the phase compensation used by the P-POD.
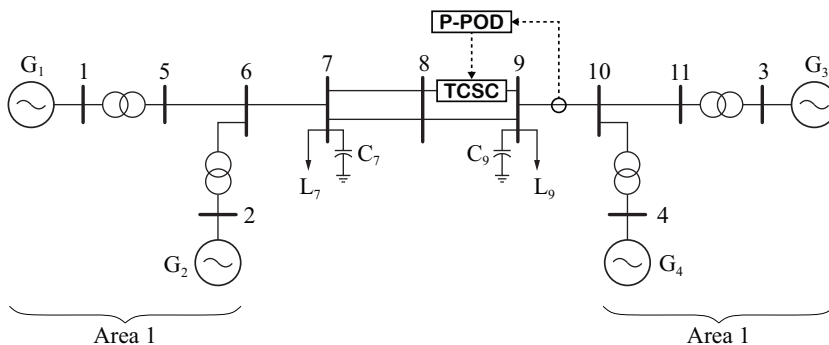
Figure 4.12: The single line diagram shows Kundur's Two-Area System, where a TCSC is installed on one of the inter-ties between the two areas. A P-POD measures the active power flow in Line 9-10 and modulates the setpoint of the TCSC.

procedure for the IEEE 39-Bus System in Section 4.2.2. The residue matrix is displayed in Fig. 4.13, along with mode controllability and observability. It can be seen that measuring the active power flow in Line 9-10 and modulating a TCSC on one of the inter-ties is a good choice. For reference, this is also the chosen combination in a similar investigation in [30].

Three simulations are performed: One with no control, one with a static P-POD with a constant phase compensation determined from the residue angle (according to (2.28)), and one with the proposed adaptive P-POD. For the adaptive P-POD, the covariance scaling coefficient $k_\sigma = 180$ and the gain $K = 0.01$. Similar to in the previous case, the magnitude of the residue is assumed to be known, but not the angle. A short circuit is simulated at $t = 1\,$s, with a clearing time of $50\,$ms. Further, to test the capability of the controller to adjust to changing operating conditions, the largest load in the system is disconnected (i.e., the $1767\,$MW load in Area 2) at $t = 20\,$s.

The measured power flow for the three simulations is shown in Fig. 4.14. After the first disturbance, the uncontrolled system is unstable. Both the static and the adaptive P-POD successfully stabilizes the oscillations. After the loss of load, the uncontrolled system is stable, but the static P-POD causes forced oscillations. Only the adaptive P-POD performs satisfactorily after both disturbances.

In Fig. 4.15 the phase compensation, the control signal for the TCSC, and the filter weights are shown. The ideal value of the phase compensation is computed from modal analysis, before and after the loss of load,
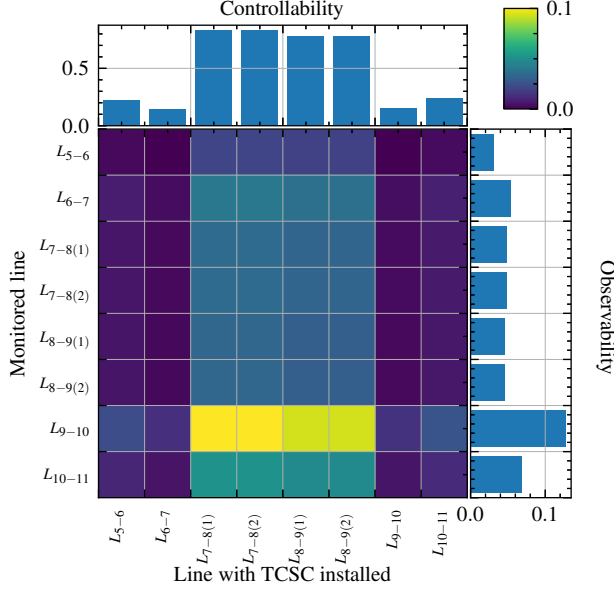
Figure 4.13: The matrix of transfer function residues of the low damped mode in Kundur's Two-Area System, similar to for the IEEE 39-Bus System in Fig. 4.8. It is apparent that measuring active power flow in Line 9-10 and modulating a TCSC on one of the inter-ties is a good choice.

and reveals that a large adjustment is required by the adaptive controller to ensure proper functioning. Observing the filter weights reveals that the 288° filter dominates after the first disturbance, and the 72° filter dominates after the second disturbance. The phase compensation is adjusted accordingly, and is therefore close to 288° and 72° before and after the loss of load, respectively.

IEEE 39-Bus System

In this section, the adaptive P-POD is tested on the IEEE 39-Bus System in a wide area configuration with communication delay. The same system as in Section 4.9 is used, with corresponding single-line diagram shown in Fig. 4.7. The covariance scaling coefficient $k_\sigma = 35$ and the gain $K = 0.03$. Again, the magnitude of the residue is assumed to be known, but not the angle.

A short circuit occurs at $t = 1\,\text{s}$. At the beginning of the simulation, the communication delay is 50 ms. At $t = 15\,\text{s}$, the delay increases to 500 ms. This delay introduces a phase lag which can be calculated from
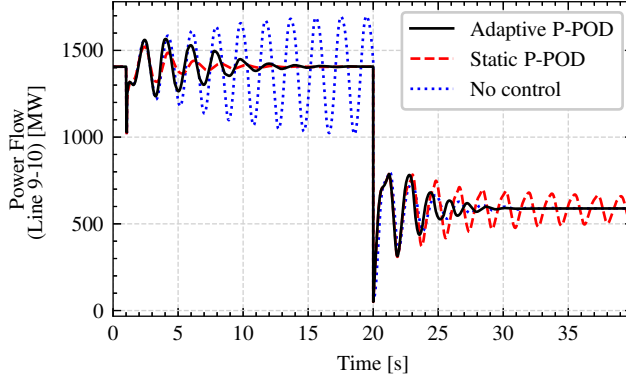
Figure 4.14: The measured active power flows from three simulations on Kundur's Two-Area System; without control, with a static P-POD with constant phase compensation, and with an adaptive P-POD with automatic phase compensation adjustment. Only the adaptive controller successfully stabilizes the system both before and after the loss of load occurring at $t = 20\,\text{s}$.

$\theta_{lag} = \omega t_{lag}$, where ω is the frequency of the targeted mode and t_{lag} is the communication delay. This gives phase lags of 8° and 80° for the two latencies.

The result from this simulation is shown in Fig. 4.16, where the measured active power flow, the phase compensation (ideal and estimated), the control signal modulating the TCSC, and the filter weights are shown. It is demonstrated that the change in communication delay causes growing oscillations from about $t = 15\,\text{s}$ to $t = 35\,\text{s}$. After this, the phase compensation is again adjusted sufficiently to mitigate the oscillations. It should be noted that although the change in latency is handled well by the controller, introducing the sophisticated latency compensation schemes described in [71] and [73] would most likely further enhance the performance.

4.3.3   Discussion

The same adaptive, self-tuning controller is used in three different systems (Single-Machine Infinite Bus System, Kundur's Two-Area System, the IEEE 39-Bus System), differing only in the required parameters specified for each case: The frequency f of the low damped mode, the gain K (in (4.2)), and the covariance matrix scaling coefficient k_σ (in (4.16) & (4.17)). In addition, the initial guess of the magnitude of the residue $|r_0|$ in (4.19) is specified for each case.
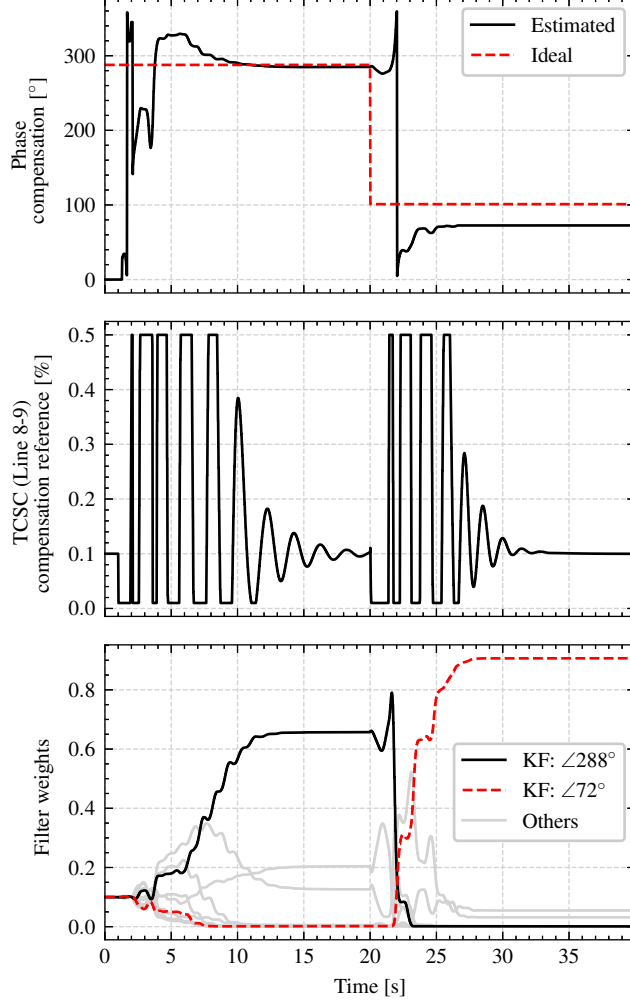
Figure 4.15: The result from applying the MMAE-based adaptive P-POD to Kundur's Two-Area System. The first plot shows the phase compensation used by the controller along with the ideal value (calculated from modal analysis). The second plot shows the control signal modulating the TCSC. The third plot shows the filter weights.
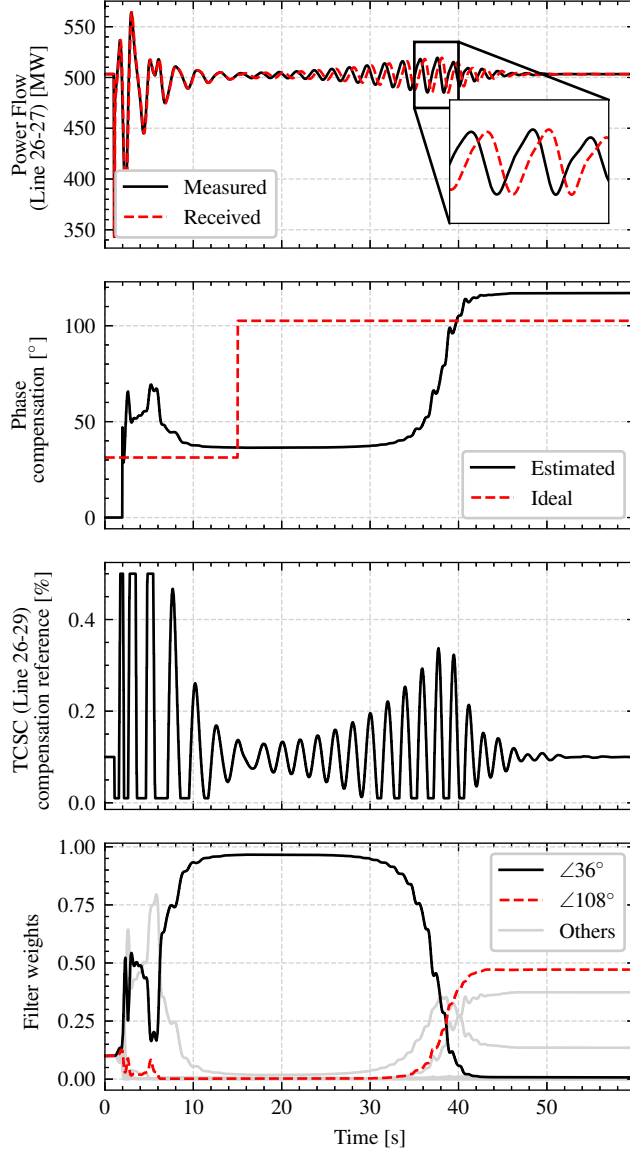
Figure 4.16: The result from testing the adaptive P-POD on the IEEE 39-Bus System. At $t = 15\,\mathrm{s}$ the communication delay increases from $50\,\mathrm{ms}$ to $500\,\mathrm{ms}$, which causes forced oscillations for a short period, before the phase compensation is adjusted sufficiently to mitigate the oscillations.

In the presented results, the Kalman filters in the MMAE bank differ only in that the Control-Input Models are determined from different residue *angles*. Thus, only the residue angle can be inferred from the performance of the filters, and the magnitude is locked to the magnitude of the initial guess $|r_0|$. It is therefore a requirement for successful application of the controller that the value $|r_0|$ is close to the actual value. However, the residue *magnitudes* could also be varied between the filters, which would allow also the magnitude of the residue to be estimated. This would eliminate the mentioned requirement of accurate $|r_0|$, and thus make the controller more general.

In theory, this would allow the adaptive controller to be applied solely based on information obtainable from measurements. Considering a case where standing oscillations of a previously unobserved frequency appear in a system, the proposed adaptive controller could be applied as an emergency power oscillation damper: The approximate frequency f of oscillations could easily and quickly be obtained using Fast Fourier Transform, Prony analysis, or the mode estimation method presented in Chapter 3. The covariance scaling coefficient k_σ could be set equal to (or on the same scale as) the amplitude of oscillations, as suggested in Section 4.3. The gain K could be increased gradually. The best outcome in this case would be that the filter weights converged quickly and provided a reliable residue estimate, and that the oscillations were damped. Another outcome would be that the filter weights did not converge, which could be caused by high activity of other modes or noisy conditions. In this situation, the best option would be to deactivate the controller. Yet another outcome would be that the weights converged to a residue with low magnitude and the oscillations were not damped, which would indicate that the chosen combination of measurement and actuator was not effective for the particular mode. Also in this case the better option would be to deactivate the controller.

In all the presented results, severe events that require drastic shifts in phase compensation are simulated. When tuning the controller for these cases, quick convergence toward the new operating point is prioritized (by choosing a relatively low value of the covariance scaling parameter k_σ). In many practical situations the changes in operating conditions could be more subtle, for instance for a P-POD operating during normal conditions, following slowly drifting operating conditions due to load variations. In this case, it would be reasonable to prioritize slower and more predictable convergence when tuning the controller (i.e., choosing a higher value of the covariance scaling parameter k_σ).

4.4 Phasor POD with Multiple Input Measurements

*In this section, **Contribution II-C** is presented, which represents a Phasor Power Oscillation Damper with multiple input channels. Early stages of this work is published in **Paper III**.*

In Chapter 3, a mode estimation method intended for online operation is presented, capable of estimating mode frequency and observability mode shapes. Other similar algorithms exist in the literature, e.g., [51]. Having such algorithms at hand, it can be reasonably assumed that under certain conditions, accurate estimates of observability mode shapes are available to the operators. The topic of Paper III is to investigate how this information can be used for power oscillation damping purposes.

In Paper III, an estimator is developed which estimates the instantaneous amplitude and phase of the excitation of a low damped mode based on multiple input measurements in combination with knowledge about observability mode shapes. This is achieved by generating a set of sinusoidal functions, one for each measurement, where each function represents oscillations one would expect to observe given excitation of the targeted mode. A least squares-type estimator is used to determine the amplitude and phase which makes all the functions fit best to the measurements. This amplitude and phase can be interpreted as the instantaneous mode activity of the low damped mode, which can further be used to generate the damping control signal.

As a continuation of this work, the main idea in Paper III is incorporated in the Phasor POD framework. This is achieved by introducing multiple measurements in the Kalman filter, and making adjustments to the observation matrix to take information about the observability mode shape into account. This is the topic of the current section.

Developing a POD with multiple measurements is expected to be advantageous for a number of reasons. A controller with a single measurement will be more vulnerable to severe disturbances close to the measurement location. Communication problems could also occur, caused by, for example, loss of GPS signal or network congestion [82]. This could result in missing data or severely delayed measurements. A controller with multiple measurements on the other hand, is expected to be more robust against issues like these.

4.4.1 Extending the Observation model

The fundamental assumption is that the observability mode shape, i.e., the vector $\mathbf{C\phi}_m$ in (3.1), is known, where m is the index of the targeted low damped mode. This vector has one element for each of the n_c measurements, and each element describes the amplitude and phase with which the mode is observed in the corresponding measurement:

$$\mathbf{C\phi}_m = \begin{bmatrix} a_1 \angle \delta_1 \\ a_2 \angle \delta_2 \\ \vdots \\ a_{n_c} \angle \delta_{n_c} \end{bmatrix} \tag{4.30}$$

Thus, the phasor representing the targeted mode is also observed with amplitudes and phase shifts as determined by the mode shape. Equation (4.1) can be modified to take this into account. For measurement i, the observation model can be written as follows:

$$\begin{aligned} S_i(t) =& \bar{S}_i + \text{Re}\{a_i \vec{S} e^{j\omega t + \delta_i}\} \\ =& \bar{S}_i + a_i \left\{ D_i \cos\left(\omega t + \delta_i\right) - Q_i \sin\left(\omega t + \delta_i\right) \right\} \end{aligned} \tag{4.31}$$

The average component in each measurement $\bar{S}_i$ must also be estimated, so the state vector of the Kalman filter is expanded:

$$\mathbf{X}_k = \begin{bmatrix} \bar{S}_{1,k}, & \bar{S}_{2,k}, & \dots & \bar{S}_{n_c,k}, & D, & Q \end{bmatrix}^{\mathsf{T}} \tag{4.32}$$

The Kalman filter measurement is now a vector (not a scalar, as in the previous sections):

$$\mathbf{Y}_k = \begin{bmatrix} S_{1,k}, & S_{2,k}, & \dots & S_{n_c,k} \end{bmatrix}^{\mathsf{T}} \tag{4.33}$$

The observation matrix can be assembled as follows:

$$\begin{bmatrix} S_{1,k} \\ S_{2,k} \\ \vdots \\ S_{n_c,k} \end{bmatrix} = \underbrace{\begin{bmatrix} 1 & & & a_1 \cos(\omega t + \delta_1) & a_1 \sin(\omega t + \delta_1) \\ & 1 & & a_2 \cos(\omega t + \delta_2) & a_2 \sin(\omega t + \delta_2) \\ & & \ddots & \vdots & \vdots \\ & & 1 & a_{n_c} \cos(\omega t + \delta_{n_c}) & a_{n_c} \sin(\omega t + \delta_{n_c}) \end{bmatrix}}_{\mathbf{H}_k} \begin{bmatrix} \bar{S}_{1,k} \\ \bar{S}_{2,k} \\ \vdots \\ \bar{S}_{n_c,k} \\ D_k \\ Q_k \end{bmatrix} \tag{4.34}$$

Further, the observation noise covariance matrix of the Kalman filter $\mathbf{R}$ will have dimension $n_c \times n_c$. Assuming there is no correlation between noise in different measurements, the off-diagonal elements are set to zero.

Assuming the magnitude of the noise to be similar in all measurements, the noise covariance matrix is chosen as follows:

$$\mathbf{R} = k_\sigma^2 \cdot \mathbf{I}_n \tag{4.35}$$

Here, k_σ is defined as in Section 4.2.1.

The extended observation model can be combined with the control-input model introduced in Section 4.2. This only requires taking the extra elements of the state vector into account. The State Transition Model and Control-Input Model are as follows in this case:

$$\begin{bmatrix} \bar{S}_{1,k+1} \\ \vdots \\ \bar{S}_{n_c,k+1} \\ D_{k+1} \\ Q_{k+1} \end{bmatrix} = \underbrace{\begin{bmatrix} 1 & & & & \\ & \ddots & & & \\ & & 1 & & \\ \hline & & & 1 & \\ & & & & 1 \end{bmatrix}}_{\mathbf{F}_k} \begin{bmatrix} \bar{S}_{1,k} \\ \vdots \\ \bar{S}_{n_c,k} \\ D_k \\ Q_k \end{bmatrix} + \underbrace{\begin{bmatrix} 0 \\ \vdots \\ 0 \\ \hline Ug(t) + Vh(t) \\ -Uh(t) + Vg(t) \end{bmatrix}}_{\mathbf{G}_k} u_k \tag{4.36}$$

The process noise covariance matrix can be chosen to be similar as in (4.16), except with higher dimension:

$$\mathbf{Q} = (k_\sigma \cdot \omega_{bw}\Delta t)^2 \cdot \mathbf{I}_{n_c+2} \tag{4.37}$$

Interestingly, in case one or more measurements are missing, the correction step can still be performed. In this case, the corresponding element in the measurement vector and the corresponding row(s) in the observation model $\mathbf{H}_k$ in equation (4.31) is removed for the current time step.

4.4.2 Application

The multi-channel enhancement is tested on Kundur's Two-Area System. The system is as described in Section 4.3.2, with a TCSC installed on one of the interties. The simulated event is a short circuit on Bus 10 with a clearing time of 50 ms.

A conventional P-POD without a Control-Input Model is chosen as the starting point. In the reference case, the single measured signal to the P-POD is the measured active power flow in Line 9-10, as in Section 4.3.2. Further, the effect of including additional measurements in the estimation is investigated. New measurements are included, one at a time, and for each new measurement the corresponding element in the observability mode shape is assumed to be known. The measurements
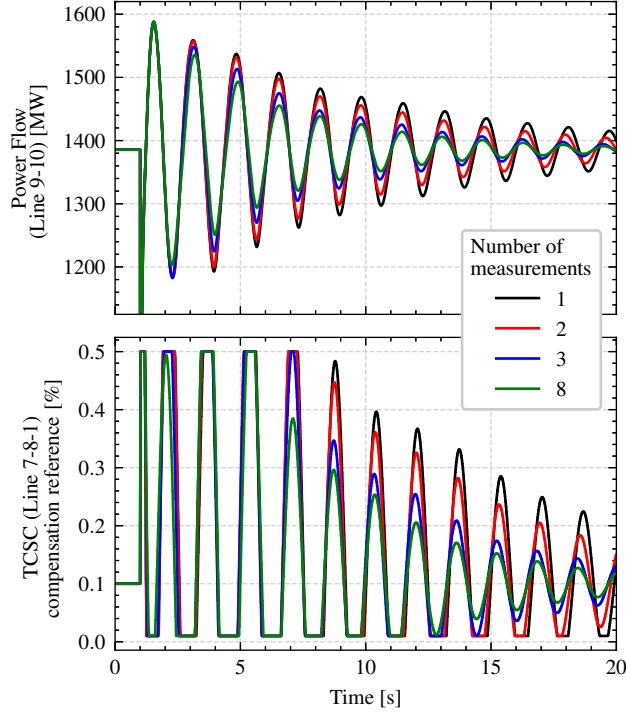
Figure 4.17: The power flow in Line 9-10 and the control signal from four simulations on Kundur's Two-Area System, where the number of measurements to the P-POD is as indicated. The gain is the same in all cases, i.e., $K = 0.005$. Evidently, the damping increases and the control cost decreases as the number of measurements increases.

are chosen among the measurements for which residues are given in Fig. 4.13, specifically: The next measurement to include is the measurement among the remaining ones that has the highest observability of the targeted mode.

The results from four cases are given in Fig. 4.17, where the number of measurements are 1, 2, 3, and 8, respectively. The power flow in Line 9-10 and the control signal are shown for each case. From the curves, it is clear that the damping increases and the control cost decreases as the number of measurements increases. Quantifying performance and control cost according to (4.18) as in Section 4.2.2 yields the result in Fig. 4.18. The same tendency is observed, i.e., increasing performance and decreasing cost with increasing number of measurements.
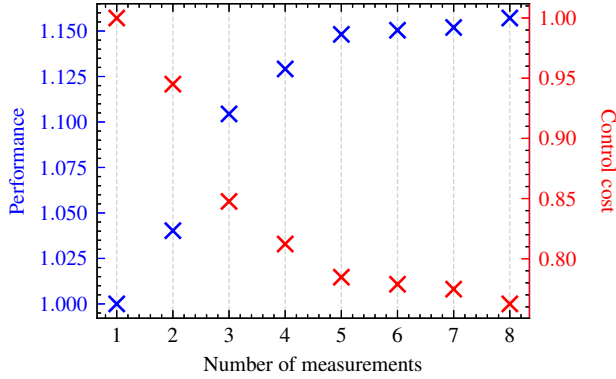
Figure 4.18: The relative performance and control cost of the P-POD with multiple measurements, where the number of measurements varies between 1 and 8. The performance increases and the control cost decreases with the number of measurements. The values are normalized by the performance and cost with a single measurement.

Finally, the controllers with 1, 2, 3, and 8 measurements are tested for varying gains between 2 and 10. This allows the performance at the same control cost to be evaluated. The result from this procedure, shown in Fig. 4.19, indicates that higher performance is achieved for the same control cost when including a higher number of measurements.

4.4.3   Discussion

The results indicate that a higher damping performance is achieved for the same control cost with the proposed enhancement. Similar to in Section 4.2, this should come as no surprise, since more information about the system is required (in the form of observability mode shapes) and more measurement signals are included in the phasor estimation.

Introducing multiple measurements to the P-POD could bring an advantage related to communication issues. In practice, PMU data would be streamed from multiple locations to a PDC. The PDC waits for a fixed amount of time, which can be specified, to receive data from all PMUs. If data is not received within this time, then filler data will be substituted in place of the missing data [19]. For a POD with only a single PMU measurement, it would make sense to have a relatively long maximum waiting time, since delayed data would most likely be better than missing data. Thus, longer time delays would have to be taken into account in the design of the controller, like in [73], where delays
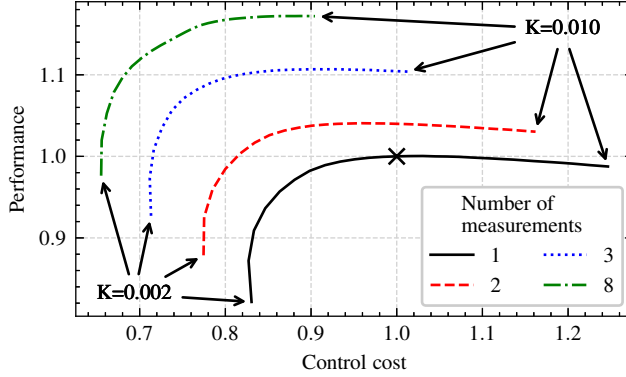
Figure 4.19: The performance and control cost for four different controllers, where the number of measurements varies between 1 and 8. The gain is varied between $K = 0.002$ and $K = 0.010$, which allows comparing the performance of variants of the controller at the same control cost. This result clearly indicates that a higher performance is achieved for the same control cost when the number of measurements increases. The values are normalized by the performance and cost with a single measurement at gain $K = 0.005$ (marked with a black x).

of up to $800\,\text{ms}$ are considered. However, for a POD with multiple input measurements and capability of operating properly in the absence of some measurements, the maximum waiting time could potentially be decreased. Assuming that the probabilities of missing data from different PMUs are independent, then there would be a very low probability that measurements from multiple PMUs are missing at the same time. For instance, if the data loss rate of two PMUs is $10\,\%$, then (assuming no correlation) the simultaneous data loss rate would be $10\,\% \cdot 10\,\% = 1\,\%$. As previously mentioned, the correction step in the Kalman filter algorithm can be performed in the absence of some measurement channels by removing the corresponding rows in the observation model. Thus, the robustness of the controller to communication latency or missing PMU data would be enhanced by introducing a higher number of input measurements.

Obtaining an accurate estimate of the observability mode shape might be difficult in some cases. If the estimate is not sufficiently accurate, it is expected that the performance advantage of introducing additional measurements diminishes. For a case with pronounced, standing oscillations, it is expected that highly accurate observability mode shape estimates can be obtained using an estimation method like the one described in

Chapter 3. If the standing oscillations were to be damped by a P-POD in this case, it would make sense to include the available knowledge in the phasor estimation, thus realizing the mentioned advantages of increased robustness to communication problems and potentially enhanced performance.

Another option would be to include estimation of the observability mode shape in the estimation algorithm. This could be achieved using a MMAE scheme, similar to as described in Section 4.3, where different filters in the filter bank would have differing observation models. Estimating the observability of a high number of locations would probably be intractable using this approach, since it would require very many filters in the filter bank. However, introducing only one or two additional measurements would still most likely bring some of the mentioned advantages, and should be practically feasible.

4.5   Testing and Implementation

Control applications like the P-POD are required to be able to run in real-time to be applicable in practice. Thus, it is important that the capability to operate in real-time is verified for the enhancements presented in the preceding sections. Among these, the MMAE-based adaptive controller is by far the one expected to be the most computationally demanding, since this involves running a high number of Kalman filters in parallel.

Testing the capability of the MMAE-based controller to operate in real-time is achieved through the approach outlined in Section 2.4.5. The multiprocessing module in Python is used, allowing the simulation loop to run in one process and the control loop to run in another process. In the simulation process, the chosen measured signals are obtained from the current state of the simulation and streamed to the control process, and any received control messages are read and used to update the setpoint of the controlled device. In the control process, the measurement is received and used to update the Kalman filters, before the control signal is calculated and streamed back to the simulator process. This setup is outlined in Fig. 4.20.

Curves captured during real-time testing of the MMAE-based P-POD in a simulation of the IEEE 39-Bus System are shown in Fig. 4.21, where estimated quantities (signal average, phasor components, ideal phase compensation) as well as the applied control signal are shown.

The simulated case is the same as described in Section 4.3.2, where the system is destabilized by deactivating two stabilizers and disconnecting an important line. This causes standing oscillations with a frequency
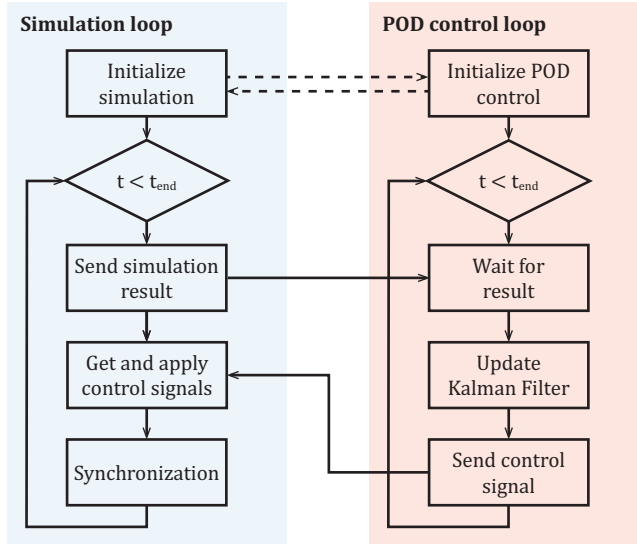
Figure 4.20: A setup for testing the capability of the presented P-PODs to operate in real-time. The simulator runs in one process and the control algorithm runs in another process, which is achieved using the multiprocessing module in Python. Measurements and control signals are streamed between the processes as indicated.
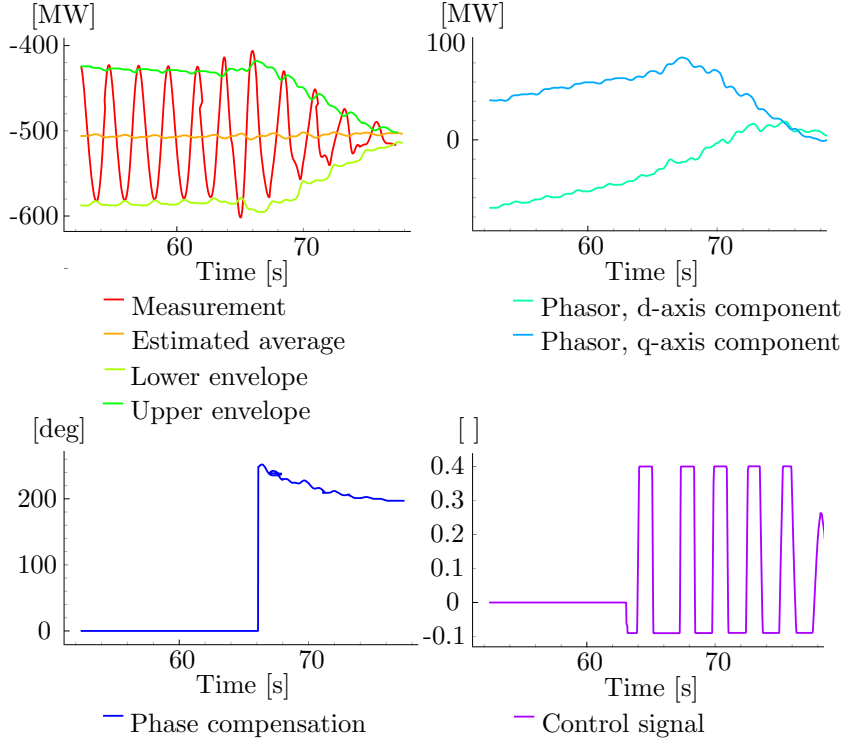
Figure 4.21: Curves captured during real-time simulation of an adaptive MMAE-based P-POD. The upper left plot shows the measured signal versus time (which is the power flow in Line 26-27), the estimated average and the envelope of the oscillations. The upper right plot shows the estimated d- and q-axis components of the phasor. The lower left plot shows the estimated ideal phase compensation. The lower left plot shows the control signal, which modulates the compensation setpoint (k_{c-ref} in (2.12)) for the TCSC installed on Line 26-29.
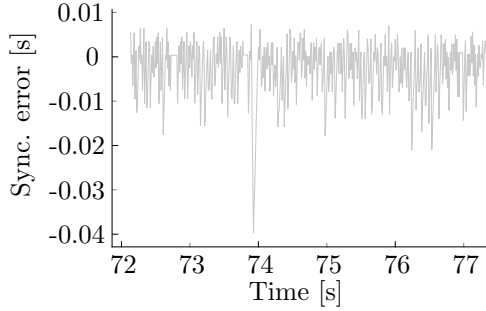
Figure 4.22: The synchronisation error versus time during real-time simulation of IEEE 39-Bus System with an adaptive MMAE-based P-POD, defined as the difference between wall-clock time and simulation time.

of about $0.44\,\mathrm{Hz}$. At approx. $t = 135\,\mathrm{s}$, the gain of the controller is increased manually from 0 to about 0.03 (which is the same gain as used in Section 4.3.2). Shortly after, the phase compensation (which is initially zero) is adjusted automatically so that an effective damping control signal is generated, which results in successful damping of the targeted oscillations.

The synchronisation error during this simulation is shown in Fig. 4.22, where the error is defined as the difference between wall clock time and simulation time. As can be seen, the error is mostly around $10 - 20\,\mathrm{ms}$, and sometimes higher. The synchronisation accuracy is not very high, but the simulator is capable of keeping track with wall-clock time. This test verifies that there are no computational problems with running the MMAE-based adaptive controller on an average laptop computer.

4.6 Further Work

4.6.1 Feasibility of Phasor POD Enhancements

With Contributions II-A and II-C, the potential advantages gained by assuming availability of more system knowledge and more measurement signals are investigated. As expected, the analysis indicates that significant performance enhancements can be achieved provided exact knowledge of the required system parameters. A natural topic of further work is to identify situations where the required parameters can be estimated with sufficient accuracy to realize the indicated advantages and performance enhancements.
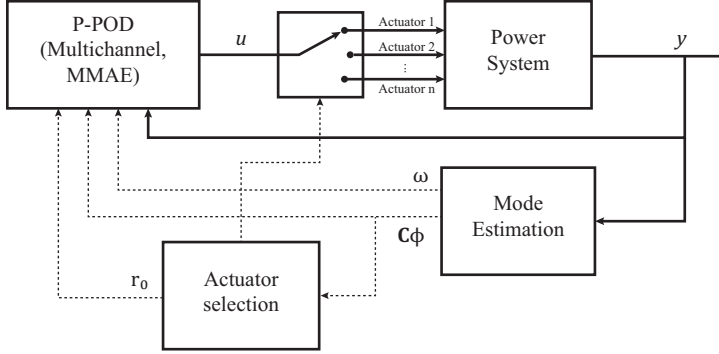
Figure 4.23: A block diagram describing a wide area emergency power oscillation damping scheme. The "Mode Estimation" block continually produces estimates of frequency ω and observability mode shapes $\mathbf{C\phi}$. In case standing oscillations are detected, the "Actuator selection" block selects a controllable device (FACTS, HVDC, CIG, etc.) expected to be efficient at providing damping to the low damped mode based on the observability mode shape. The frequency and mode shape is also sent to the "P-POD" block, along with the initial guess of the residue r_0.

For instance, for a conventional P-POD in operation, a system identification technique could be applied to estimate the required transfer function residue for introducing the Control-Input Model (i.e., Contribution II-A). If the estimates of this residue were consistent over a longer period, then this would indicate that the estimates were accurate, and thus that introducing the Control-Input Model would be feasible. However, if the estimates varied a lot, either due to insufficient estimation accuracy or due to that the "exact" residue actually varied (due to that the operating point of the system was undergoing large variations), then introducing the Control-Input Model would most likely not be feasible.

4.6.2 Wide Area POD for Emergency Situations

The mode estimation method described in Chapter 3 could be used in combination with the presented P-POD enhancements for developing a wide area power oscillation damping scheme for emergency situations. The three steps of the scheme would be as follows: First, problematic oscillations are detected; second, a controllable device is proposed through which remedial damping control can be applied; and third, damping control is activated on the selected device.

The first step could be achieved by running the mode estimation method continuously. Once standing or growing oscillations are ob-

served, the frequency and observability mode shape will be available to the operators potentially seconds later. If the amplitude of the oscillations is sufficiently high, then activating a POD on a controllable device should be proposed to the operators.

In the second step, a device is selected through which the damping control will be applied. For the control signal to be effective, the targeted mode should be controllable from the selected actuator. Assessing mode controllability requires information about left eigenvectors. In [63], relationships between left and right eigenvectors are derived, based on simplified models (i.e., lossless transmission lines, classical generator models etc.). From these relationships, approximate information about mode controllability can be inferred from mode observability. This information could further be used to select the device through which damping control should be applied.

In the third step, the adaptive P-POD described in Section 4.3 could be used to generate the damping control signal for the selected actuator (as described in Section 4.3.3). The initial guess for the required residue could be chosen based on the mentioned relationships between left and right eigenvectors in [63]. Additionally, since the observability mode shape would be available from the mode shape estimation algorithm, the multi-channel observation model described in Section 4.4 could be used for improved robustness against communication delay or data loss.

This emergency power oscillation damping scheme is inspired by a comparable scheme proposed in [83], where feedback loops are generated online once oscillations are detected. The feedback loops are tuned based on the expressions derived in [63]. A notable difference from the above presented idea is that if the approximate controllability estimates are inaccurate (i.e., the system is not accurately described by the simplified models), then the damping control might be ineffective. The MMAE-based adaptive P-POD, on the other hand, would allow the tuning (i.e., the phase compensation) to be improved from the initial guess.

4.7   Summary

Three enhancements to the Phasor Power Oscillation Damper have been presented. First, the performance of the controller is enhanced by introducing a predictor-corrector estimator in the form of a Kalman filter. The amplitude and phase of oscillations (represented by a phasor) are predicted based on the applied control signal, and the measurement is used to correct the prediction. It is found that this results in a more precise and efficient damping control signal.

Second, the controller is enhanced with adaptive phase compensation, which is achieved by running a bank of Kalman filters in a Multiple Model Adaptive Estimation scheme. By assessing the performance of individual filters, the system model is inferred and used to adjust the phase compensation. The proposed scheme is successfully tested on three systems, and requires very little tuning or customization for each case. The controller is found to outperform a similar adaptive phase compensation scheme found in the literature, and is capable of adapting to changing operating conditions caused by a large disturbance and by varying communication latency.

Third, the controller is enhanced with multi-channel input, where information about observability mode shapes is taken into account. Given accurate estimates of observability mode shapes, this is found to enhance the performance of the controller, and is expected to provide an advantage related to communication issues.

Further, the most computationally demanding among the presented variants of the Phasor POD, which is the adaptive version based on Multiple Model Adaptive Estimation, has been successfully demonstrated in a real-time simulation, verifying that there are no significant computational problems with running the proposed Phasor PODs in real-time.

Finally, an idea for an emergency power oscillation damping scheme is proposed as further work. The scheme makes use of all the presented contributions on monitoring and control (i.e. Contributions I, II-A, II-B, & II-C), and thus ties together all the work in this thesis.

Chapter 5

Conclusions and Recommendations for Further Work

5.1 Conclusions

In this thesis, contributions in two main areas of research are presented, aiming to answer the research question posed in Chapter 1. First, within the topic of monitoring of electromechanical oscillations, a mode estimation method based on statistical learning methods is developed. Second, within the topic of damping control of electromechanical oscillations, enhancements to the controller known as the Phasor Power Oscillation Damper in the literature are presented.

Results from testing the mode estimation method show that accurate results are obtained, where the accuracy increases with the mode excitation. The method is suitable for online operation, continually providing operators with updated estimates of oscillatory modes. An informative visualization is presented, which conveys information about where and when oscillations are observed, and an online implementation of the method is described.

The first proposed enhancement to the Phasor Power Oscillation Damper is found to increase its performance, achieved using a predictor-corrector estimator in the form of a Kalman filter. The second enhancement introduces adaptive phase compensation, achieved by introducing a Multiple Model Adaptive Estimation scheme. With the third enhancement, information about observability mode shapes is introduced

and used in combination with multiple measurement signals to enhance the performance and robustness of the controller against communication problems. The adaptive controller is tested in a real-time simulation, verifying the capability of operating online.

A final contribution is represented by a power system simulation tool that was developed throughout the work of this thesis. This tool has been found to be useful for prototyping WAMPAC applications, like the monitoring and control methods representing the main contributions.

With these contributions, the aim of this thesis is to provide transmission system operators with new tools for handling future challenges represented by faster fluctuations in generation, a wider range of expected operating points, and more extreme weather, with the ultimate goal of facilitating stable, secure, and resilient operation of the future power system.

5.2   Further Work

Recommendations for further work given throughout the thesis are reproduced here for convenience:

- Applying the mode estimation method to longer time spans, e.g., on the scale of hours, which would allow searching for patterns in variations of frequency or observability of electromechanical oscillations throughout a day, or aid in identifying problematic operating points associated with low damped oscillations.

- Further development of the mode estimation method, specifically: Introducing the Kabsch algorithm for computing distances between estimated mode shapes, and the OPTICS algorithm for performing the clustering.

- Investigating the practical feasibility of the proposed Phasor POD enhancements (representing Contributions II-A, II-B, & II-C), i.e., identifying situations/cases where required information can be identified with sufficient accuracy to realize the indicated advantages and performance enhancements.

- Development of a wide area POD for emergency situations, making use of the mode estimation method and the Phasor POD enhancements (representing Contributions I, II-A, II-B, & II-C).

Bibliography

[1] United Nations, "The Paris Agreement," 2015.

[2] ——, "The Glasgow Climate Pact," 2021.

[3] IRENA (International Renewable Energy Agency), *World Energy Transitions Outlook: 1.5° C Pathway*, Abu Dhabi, 2021. [Online]. Available: www.irena.org/publications

[4] ENTSO-E, "Completing the map. Power system needs in 2030 and 2040. Ten-year network development plan 2020," 2021. [Online]. Available: https://tyndp.entsoe.eu/

[5] IEA, "World Energy Outlook 2021, IEA," Paris, 2021. [Online]. Available: https://www.iea.org/reports/world-energy-outlook-2021

[6] L. Meegahapola, A. Sguarezi, J. S. Bryant *et al.*, "Power system stability with power-electronic converter interfaced renewable power generation: Present issues and future trends," *Energies*, vol. 13, no. 13, 2020.

[7] N. G. Hingorani and L. Gyugyi, *Understanding FACTS: Concepts and technology of flexible ac transmission systems.* IEEE, 1999.

[8] M. Klein, G. J. Rogers, and P. Kundur, "A fundamental study of inter-area oscillations in power systems," *IEEE Transactions on Power Systems*, vol. 6, no. 3, pp. 914–921, 1991.

[9] P. Kundur, *Power System Stability and Control.* New York: McGraw-Hill, 1994.

[10] D. N. Kosterev, C. W. Taylor, and W. Fellow, "Model Validation for the August 10, 1996 WSCC System Outage," *IEEE Transactions on Power Systems*, vol. 14, no. 3, pp. 967–979, 1999.

[11] P. Kundur, J. Paserba, V. Ajjarapu *et al.*, "Definition and Classification of Power System Stability," *IEEE Transaction on Power Systems*, vol. 19, no. 2, pp. 1387–1401, 2004.

[12] N. Hatziargyriou, J. Milanovic, C. Rahmann *et al.*, "Definition and Classification of Power System Stability - Revisited & Extended," *IEEE Transactions on Power Systems*, vol. 36, no. 4, pp. 3271–3281, 2021.

[13] CIGRE Task Force 38.01.07 on Power System Oscillations, "Analysis and Control of Power System Oscillations," *CIGRE Technical Brochure*, no. 111, 1996.

[14] ENTSO-E SubGroup System Protection and Dynamics, "Analysis of CE Inter-Area Oscillations of 19 and 24 February 2011," Tech. Rep. February, 2011.

[15] ——, "Analysis of CE Inter-Area Oscillations of 1st December 2016," Tech. Rep. December, 2017.

[16] ——, "Oscillation Event 03.12.2017," Tech. Rep. March, 2018.

[17] A. G. Phadke, J. S. Thorp, and M. G. Adamiak, "A new measurement technique for tracking voltage phasors, local system frequency, and rate of change of frequency," *IEEE Transactions on Power Apparatus and Systems*, vol. PAS-102, no. 5, pp. 1025–1038, 1983.

[18] A. Phadke, "Synchronized phasor measurements in power systems," *IEEE Computer Applications in Power*, vol. 6, no. 2, pp. 10–15, 4 1993.

[19] CIGRE Working Group C4.34, "Application of Phasor Measurement Units for Monitoring Power System Dynamic Performance," *CIGRE Technical Brochure*, no. 702, 2017.

[20] D. T. Duong and K. Uhlen, "Online Voltage Stability Monitoring Based on PMU Measurements and System Topology," in *3rd International Conference on Electric Power and Energy Conversion Systems, EPECS*. Istanbul: IEEE, 2013.

[21] H. Jóhannsson, A. H. Nielsen, and J. Østergaard, "Wide-Area Assessment of Aperiodic Small Signal Rotor Angle Stability in Real-Time," *IEEE Transactions on Power Systems*, vol. 28, no. 4, pp. 4545–4557, 2013.

[22] D. Müller, H. Jóhannsson, A. H. Nielsen, and K. Uhlen, "A Method to Determine the Distance to the Critical Oscillatory Stability Limit in Terms of Active Power Injections," in *Proceedings of 2021 IEEE Madrid PowerTech*. IEEE, 2021.

[23] "PowerFactory," *DIgSILENT*. [Online]. Available: digsilent.de/en/powerfactory

[24] H. Haugdal, "DynPSSimPy," *Zenodo*, 2020. [Online]. Available: http://doi.org/10.5281/zenodo.4290126

[25] G. Hotz, "Online Feedback Optimization for Emergency Power System Operation," 12 2021. [Online]. Available: https://www.research-collection.ethz.ch:443/handle/20.500.11850/518176

[26] N. Hatziargyriou, J. V. Milanović, C. Rahmann *et al.*, "Stability definitions and characterization of dynamic behavior in systems with high penetration of power electronic interfaced technologies," IEEE Power & Energy Society, Tech. Rep. April, 2020.

[27] P. Virtanen, R. Gommers, T. E. Oliphant *et al.*, "SciPy 1.0: fundamental algorithms for scientific computing in Python," *Nature Methods*, vol. 17, no. 3, pp. 261–272, 2020.

[28] J. Machowski, J. Bumby, and J. Bialek, *Power system dynamics: Stability and control*, 2nd ed. Wiley, 2008.

[29] L. Ängquist, "Synchronous Voltage Reversal Control of Thyristor Controlled Series Capacitor," Ph.D. dissertation, KTH Royal Institute of Technology, 2002.

[30] B. Pal and B. Chaudhuri, *Robust Control in Power Systems*, ser. Power Electronics and Power Systems. Boston: Springer US, 2005.

[31] G. Rogers, *Power System Oscillations*. Boston: Springer US, 2000.

[32] X. Yang and A. Fellachi, "Stabilization of inter area oscillation modes through excitation systems," *IEEE Transactions on Power Systems*, vol. 9, no. 1, pp. 494–502, 1994.

[33] "PSS/E," *Siemens PTI*. [Online]. Available: siemens.com/pss-e

[34] M. A. Pai, *Energy Function Analysis for Power System Stability*. Boston, MA: Springer US, 1989.

[35] S. H. Jakobsen and E. H. Solvang, "The Nordic 44 test network," 2018. [Online]. Available: https://figshare.com/articles/The_Nordic_44_test_Network/7464386

[36] M. Mirz, S. Vogel, G. Reinke, and A. Monti, "DPsim - A dynamic phasor real-time simulator for power systems," *SoftwareX*, vol. 10, p. 100253, 2019.

[37] H. Cui, F. Li, and K. Tomsovic, "Hybrid Symbolic-Numeric Framework for Power System Modeling and Analysis," *IEEE Transactions on Power Systems*, 2020.

[38] L. Vanfretti, T. Rabuzin, M. Baudette, and M. Murad, "iTesla Power Systems Library (iPSL): A Modelica library for phasor time-domain simulations," *SoftwareX*, vol. 5, pp. 84–88, 2016.

[39] M. Baudette, M. Castro, T. Rabuzin *et al.*, "OpenIPSL: Open-Instance Power System Library Update 1.5 to iTesla Power Systems Library (iPSL): A Modelica library for phasor time-domain simulations," *SoftwareX*, vol. 7, pp. 34–36, 2018.

[40] C. R. Harris, K. J. Millman, S. J. van der Walt *et al.*, "Array programming with NumPy," *Nature*, vol. 585, no. 7825, pp. 357–362, 9 2020.

[41] L. Campagnola, "PyQtGraph - Scientific Graphics and GUI Library for Python." [Online]. Available: http://www.pyqtgraph.org/

[42] "IEEE Standard for Synchrophasor Measurements for Power Systems," *IEEE Std. C37.118-2011*, pp. i –48, 2011.

[43] S. Sandi, B. Krstajic, and T. Popovic, "PyPMU - Open source python package for synchrophasor data transfer," *24th Telecommunications Forum, TELFOR 2016*, pp. 9–12, 2017.

[44] V. Jalili-Marandi, F. J. Ayres, E. Ghahremani *et al.*, "A real-time dynamic simulation tool for transmission and distribution power systems," *IEEE Power and Energy Society General Meeting*, 2013.

[45] IEEE Task Force on Identification of Electromechanical Modes, "Identification of Electromechanical Modes in Power Systems," IEEE, Tech. Rep. PES-TR15, 2012.

[46] L. Dosiek and J. W. Pierre, "Estimating electromechanical modes and mode shapes using the multichannel ARMAX model," *IEEE Transactions on Power Systems*, vol. 28, no. 2, pp. 1950–1959, 2013.

[47] L. Dosiek, N. Zhou, J. W. Pierre *et al.*, "Mode shape estimation algorithms under ambient conditions: A comparative review," *IEEE Transactions on Power Systems*, vol. 28, no. 2, pp. 779–787, 2013.

[48] J. Seppanen, S.-K. Au, J. Turunen, and L. Haarla, "Bayesian Approach in the Modal Analysis of Electromechanical Oscillations," *IEEE Transactions on Power Systems*, vol. 32, no. 1, pp. 316–325, 2017.

[49] L. Kumar and N. Kishor, "Determination of mode shapes in PMU signals using two-stage mode decomposition and spectral analysis," *IET Generation, Transmission & Distribution*, vol. 11, pp. 4422–4429, 2017. [Online]. Available: http://digital-library.theiet.org/content/journals/10.1049/iet-gtd.2017.0316

[50] J. F. Hauer, C. J. Demeure, and L. L. Scharf, "Initial Results in Prony Analysis of Power System Response Signals," *IEEE Transaction on Power Systems*, vol. 5, no. 1, pp. 80–89, 1990.

[51] N. R. Chaudhuri and B. Chaudhuri, "Damping and relative mode-shape estimation in near real-time through phasor approach," *IEEE Transactions on Power Systems*, vol. 26, no. 1, pp. 364–373, 2011.

[52] A. R. Messina and V. Vittal, "Extraction of Dynamic Patterns From Wide-Area Measurements Using Empirical Orthogonal Functions," *IEEE Transactions on Power Systems*, vol. 22, no. 2, pp. 682–692, 2007.

[53] P. Esquivel and A. R. Messina, "Complex Empirical Orthogonal Function analysis of wide-area system dynamics," in *IEEE Power and Energy Society 2008 General Meeting: Conversion and Delivery of Electrical Energy in the 21st Century*, 2008, pp. 1–7.

[54] P. Esquivel, "Wide-area wave motion analysis using complex empirical orthogonal functions," in *CCE International Conference on Electrical Engineering, Computing Science and Automatic Control*, vol. 52, no. 33, 2009, pp. 1–6.

[55] A. R. Messina, P. Esquivel, and F. Lezama, "Wide-area PMU data monitoring using spatio-temporal statistical models," in *Power Systems Conference and Exposition*. IEEE/PES, 3 2011, pp. 1–7.

[56] J. D. Horel, "Complex Principal Component Analysis: Theory and Examples," *Journal of Climate and Applied Meteorology*, vol. 23, no. 12, pp. 1660–1673, 1984.

[57] J. E. Jackson, *A User's Guide to Principal Components*, ser. Wiley Series in Probability and Statistics. Hoboken, NJ, USA: John Wiley & Sons, Inc., 1991.

[58] P. Welch, "The use of fast Fourier transform for the estimation of power spectra: A method based on time averaging over short, modified periodograms," *IEEE Transactions on Audio and Electroacoustics*, vol. 15, no. 2, pp. 70–73, 6 1967. [Online]. Available: http://ieeexplore.ieee.org/document/1161901/

[59] S. Theodoridis and K. Koutroumbas, *Pattern recognition.* Academic Press, 2009.

[60] M. Ester, H.-P. Kriegel, J. Sander, and X. Xu, "A density-based algorithm for discovering clusters in large spatial databases with noise," in *Proc. Second International Conf. on Knowledge Discovery and Data Mining (KDD)*, E. Simoudis, J. Han, and U. M. Fayyad, Eds. AAAI Press, 1996, pp. 226–231.

[61] M. Ankerst, M. M. Breunig, H.-p. Kriegel, and J. Sander, "OPTICS: Ordering Points To Identify the Clustering Structure." ACM Press, 1999, pp. 49–60.

[62] W. Kabsch, "A solution for the best rotation to relate two sets of vectors," *Acta Crystallographica Section A*, vol. 32, no. 5, pp. 922–923, 9 1976.

[63] U. P. Mhaskar and A. M. Kulkarni, "Power oscillation damping using FACTS devices: Modal controllability, observability in local signals, and location of transfer function zeros," *IEEE Transactions on Power Systems*, vol. 21, no. 1, pp. 285–294, 2006.

[64] R. L. Cresap, D. N. Scott, W. A. Mittelstadt, and C. W. Taylor, "Operating Experience with Modulation of The Pacific HVDC Intertie," *IEEE Transactions on Power Apparatus and Systems*, vol. PAS-97, no. 4, pp. 1053–1059, 1978.

[65] C. Gama, L. Ängquist, G. Ingeström, and M. Noroozian, "Commissioning and operative experience of TCSC for damping power oscillation in the Brazilian north-south interconnection," in *Session CIGRE Proceedings.* Cigre, 2000.

[66] M. Lahtinen, T. Rauhala, H. Kuisti *et al.*, "Static Var Compensator enhancing the operational reliability of Finnish transmission network." Cigre, 2010.

[67] E. Larsen, K. Clark, A. Hill *et al.*, "Control design for SVC's on the Mead-Adelanto and Mead-Phoenix transmission project," *IEEE Transactions on Power Delivery*, vol. 11, no. 3, pp. 1498–1506, 7 1996.

[68] K. Uhlen, L. Vanfretti, M. M. de Oliveira *et al.*, "Wide-Area Power Oscillation Damper implementation and testing in the Norwegian transmission network," in *2012 IEEE Power and Energy Society General Meeting.* IEEE, 2012, pp. 1–7.

[69] L. Ängquist and C. Gama, "Damping algorithm based on phasor estimation," in *IEEE Power Engineering Society Winter Meeting*, vol. 3, 2001, pp. 1160–1165.

[70] N. R. Chaudhuri, S. Ray, R. Majumder, and B. Chaudhuri, "A case study on challenges for robust wide-area phasor POD," in *IEEE Power Engineering Society Winter Meeting*, 2009.

[71] ——, "A new approach to continuous latency compensation with adaptive phasor power oscillation damping controller (POD)," *IEEE Transactions on Power Systems*, vol. 25, no. 2, pp. 939–946, 2010.

[72] ——, "Interaction between conventional and adaptive phasor power oscillation damping controllers," *IEEE PES General Meeting, PES 2010*, pp. 1–7, 2010.

[73] S. S. Yu, T. K. Chau, T. Fernando, and H. H. C. Iu, "An Enhanced Adaptive Phasor Power Oscillation Damping Approach with Latency Compensation for Modern Power Systems," *IEEE Transactions on Power Systems*, vol. 33, no. 4, pp. 4285–4296, 2018.

[74] L. Angquist, B. Lundin, and J. Samuelsson, "Power oscillation damping using controlled reactive power compensation - a comparison between series and shunt approaches," *IEEE Transactions on Power Systems*, vol. 8, no. 2, pp. 687–700, 1993.

[75] M. Beza, "Control of Energy Storage Equipped Shunt-connected Converter for Electric Power System Stability Enhancement," Ph.D. dissertation, Chalmers University of Technology, 2012.

[76] M. Beza and M. Bongiorno, "A fast estimation algorithm for low-frequency oscillations in power systems," in *Proceedings of the 14th European Conference on Power Electronics and Applications, EPE 2011.* IEEE, 2011.

[77] R. Labbe, "FilterPy." [Online]. Available: https://github.com/rlabbe/filterpy

[78] D. T. Magill, "Optimal Adaptive Estimation of Sampled Stochastic Processes," *IEEE Transactions on Automatic Control*, vol. 10, no. 4, pp. 434–439, 1965.

[79] B. Chaudhuri, R. Majumder, and B. C. Pal, "Application of multiple-model adaptive control strategy for robust damping of interarea oscillations in power system," *IEEE Transactions on Control Systems Technology*, vol. 12, no. 5, pp. 727–736, 2004.

[80] R. Labbe, "Kalman and Bayesian Filters in Python." [Online]. Available: https://github.com/rlabbe/Kalman-and-Bayesian-Filters-in-Python/

[81] J. F. Martin, A. M. Schneider, and N. T. Smith, "Multiple-Model Adaptive Control of Blood Pressure Using Sodium Nitroprusside," *IEEE Transactions on Biomedical Engineering*, vol. BME-34, no. 8, pp. 603–611, 1987.

[82] J. H. Chow and S. G. Ghiocel, "An Adaptive Wide-Area Power System Damping Controller using Synchrophasor Data," in *Control and Optimization Methods for Electric Smart Grids*, A. Chakrabortty and M. D. Ilić, Eds.   New York, NY: Springer New York, 2012, pp. 327–342.

[83] V. Pradhan, A. M. Kulkarni, and S. A. Khaparde, "A Model-Free Approach for Emergency Damping Control Using Wide Area Measurements," *IEEE Transactions on Power Systems*, vol. 33, no. 5, pp. 4902–4912, 2018.

Publications

Paper I

The paper **"Mode Shape Estimation using Complex Principal Component Analysis and k-Means Clustering"** is published in the proceedings of the **2019 International Conference on Smart Grid Synchronized Measurements and Analytics (SGSMA)**.

Mode Shape Estimation using Complex Principal Component Analysis and k-Means Clustering

Hallvar Haugdal and Kjetil Uhlen, *Member, IEEE*
Department of Electric Power Engineering, NTNU
Trondheim, Norway

Abstract—**We propose an empirical method for identifying low damped modes and corresponding mode shapes using frequency measurements from a Wide Area Monitoring System. The method consists of two main steps: Firstly, Complex Principal Component Analysis is used in combination with the Hilbert Transform and Empirical Mode Decomposition to provide estimates of modes and mode shapes. The estimates are stored as multidimensional points. Secondly, the points are grouped using a clustering algorithm, and new averaged estimates of modes and mode shapes are computed as the centroids of the clusters. Applying the method on data resulting from a non-linear power system simulator yields estimates of dominant modes and corresponding mode shapes that are similar to those resulting from modal analysis of the linearized system model. Encouraged by the results, the method is further tested with real PMU data at transmission grid level. Initial results indicate that the performance of the proposed method is promising.**

Index Terms—**Complex Principal Component Analysis, Hilbert Transform, Empirical Mode Decomposition, mode shapes, observability, k-Means, clustering**

I. INTRODUCTION

Power system operators are facing the increasingly evident challenge of operating the grid securely during complex, uncertain and rapidly changing generation and demand. This challenge can and must be met by providing the operators with better tools for monitoring and control of the grid. In this paper we focus on the monitoring part and how the operators can improve their situational awareness and gain better knowledge about stability properties and dynamic phenomena occurring in the grid.

Worldwide, Phasor Meaurement Units (PMUs) are being installed within transmission grids at increasingly faster rates. It is expected that the information from PMUs will replace the current remote terminal units (RTUs) as source of voltage and current measurements to SCADA/EMS systems. This will change the way operators can monitor the system state. First of all, Wide Area Monitoring Systems opens new possibilities for getting fast and precise information about system dynamics. While WAMS have been in use many places for offline studies and fault analysis, the development of applications for online use has not yet matured. One reason for this may be that it takes time for operators to get used to and take advantage of the new technology. Research is therefore needed in order to develop applications that are readily accepted and understood by the operators. This paper aims to contribute to that development.

The method proposed in this paper takes advantage of the high number of frequency (or potentially voltage angle) measurements available in the transmission grid in order to extract precise information about low damped oscillatory modes and their observability.

Multiple empirical methods for estimating information about modes have been proposed in the litterature. In [1], Prony analysis is used to extract frequencies and damping ratios from measured oscillations. This method, however, does not provide information about mode shapes. In [2], a method for estimating modes and mode shapes using various mode decomposition techniques and Power Spectral Density analysis is proposed. In [3], a Bayesian approach is proposed for monitoring of electromechanical modes.

The proposed method is based on using Principal Component Analysis (PCA) and k-Means clustering for estimating modes and corresponding mode shapes from PMU frequency measurements. The method consists of two main parts: In Part I, the oscillatory behavior measured in a number of measurements is decomposed into a few main oscillatory components using a variant of Complex Principal Component Analysis (CPCA). The decomposition allows the oscillatory behavior to be reduced to a set of parameters, which can be stored in the form of a multidimensional point, referred to as an observation. Finally, in Part II of the method, the observations from Part I are clustered using the k-Means algorithm, to determine which of the observations to include when computing averaged modes and mode shapes.

CPCA is well described in [4], where it is aimed at extracting dynamic patterns in geophysical data sets. Variants of CPCA has been applied to power system analysis in [5]–[7]. The implementation used in this paper is slightly different, but functions in much the same way. An important contribution from this paper is the addition of the additional layer, referred to as Part II of the method, where the information provided by CPCA is processed further into more easily understandable information, i.e. by filtering and clustering observations and computing averaged quantities.

Compared with many other methods for estimation of modes, the proposed method differs in that it does not assume an underlying linear model. Oscillations are observed when they happen, and the output of the method is simply the average of the oscillations happening most frequently/with the highest intensity.

We present and describe the necessary background theory

in section II, and describe the proposed method in section III. Application examples on simulated as well as real PMU data are presented in section IV. Finally, discussion and conclusions are given in sections V and VI.

II. BACKGROUND THEORY

This section provides a short introduction to modal analysis, and presents theory on the most important tools used by the proposed method.

A. Modal Analysis

Modal analysis of power systems provides useful knowledge of the system dynamics, and can be used for multiple purposes, including assessment of small signal stability, and design and tuning of power oscillation dampers [8].

Fundamental to modal analysis of power systems is the linearization of the dynamic equations of the system. The state space form, assumed familiar to the reader, is given as follows [9]:

$$\Delta \dot{\mathbf{x}} = \mathbf{A}\Delta\mathbf{x} + \mathbf{B}\Delta\mathbf{u} \tag{1}$$

Through eigendecomposition of the system matrix $\mathbf{A}$, the dynamic modes of the system are determined from the eigenvalues, and the observability of the modes (mode shapes) are contained within the elements of the right eigenvectors. It can be shown that the response of the system can be written

$$\Delta\mathbf{x}(t) = \sum_{j=1}^{n} \mathbf{\Phi}_j c_j e^{\lambda_j t} \tag{2}$$

where

$\mathbf{\Phi}_j$ = right eigenvector j of system matrix
c_j = magnitude of excitation of the jth mode
λ_j = eigenvalue j of system matrix
n = order of the system

The element Φ_{ij} of $\mathbf{\Phi}_j$ describes the amplitude and phase with which mode j appears in state Δx_i.

When performing modal analysis analytically, difficulties arise when modelling large systems due to insufficient knowledge of the system topology, component characteristics and controller tuning. Therefore, methods are developed for online identification of electromechanical modes that are based on measurements only. However, whether the methods are model based utilizing a state estimator or purely based on measurements, the concept of modes is inherently related to linear theory. Power systems, however, are nonlinear by nature and what appears as critical modes may change rapidly during a disturbance or any changes in operation.

B. Principal Component Analysis

Principal Component Analysis (PCA, sometimes referred to as Empirical Orthogonal Functions) is a powerful dimensionality reduction technique, which allows the variance in a set of time series to be decomposed into a few orthogonal Principal Components (PCs) that explain the main share of the variance.

A brief introduction of the method is given below, based on the thorough description of the method given in [10].

Assuming we have M measurement series, each containing N samples, assembled in a $M \times N$ matrix as follows:

$$\mathbf{X} = \begin{bmatrix} \mathbf{x}_1 \\ \mathbf{x}_2 \\ \vdots \\ \mathbf{x}_M \end{bmatrix} = \begin{bmatrix} x_1(t_1) & x_1(t_2) & \cdots & x_1(t_N) \\ x_2(t_1) & x_2(t_2) & \cdots & x_2(t_N) \\ \vdots & & \ddots & \\ x_M(t_1) & x_M(t_2) & & x_M(t_N) \end{bmatrix} \tag{3}$$

Here, the notation $x_i(t_k)$ denotes the value of series i at time t_k. We assume that each of the series has zero mean (if this is not the case, the mean is subtracted prior to the analysis).

We want to transform the correlated series $\mathbf{x}_1, \mathbf{x}_2 \ldots \mathbf{x}_M$ into the uncorrelated series $\mathbf{s}_1, \mathbf{s}_2 \ldots \mathbf{s}_M$ using the the linear transformation

$$\mathbf{S} = \begin{bmatrix} \mathbf{s}_1 \\ \mathbf{s}_2 \\ \vdots \\ \mathbf{s}_M \end{bmatrix} = \mathbf{U}^T\mathbf{X} \tag{4}$$

To find the matrix $\mathbf{U}$, we start by establishing the correlation matrix of $\mathbf{X}$:

$$\mathbf{C} = \frac{1}{1-N}\mathbf{X}\mathbf{X}^T \Rightarrow (1-N)\,\mathbf{C} = \mathbf{X}\mathbf{X}^T \tag{5}$$

Similarly, the covariance matrix of $\mathbf{S}$ is given by

$$\begin{aligned} (1-N)\,\mathbf{\Lambda} &= \mathbf{S}\mathbf{S}^T \\ &= \mathbf{U}^T\mathbf{X}\left(\mathbf{U}^T\mathbf{X}\right)^T \\ &= \mathbf{U}^T\mathbf{X}\mathbf{X}^T\mathbf{U} \\ &= \mathbf{U}^T\mathbf{C}\mathbf{U} \end{aligned} \tag{6}$$

Since we want the series $\mathbf{S}$ to be uncorrelated, we want the matrix $\mathbf{\Lambda}$ to have non-zero elements only along the diagonal. Thus, we want to choose the matrix $\mathbf{U}$ such that $\mathbf{C}$ is diagonalized. The diagonalization is carried out by performing an eigendecomposition of $\mathbf{C}$, where the eigenvalues and eigenvectors are given by

$$\mathbf{C}\mathbf{u}_j = \lambda_j \mathbf{u}_j, j = 1 \ldots M \tag{7}$$

The relative magnitudes of the eigenvalues describe how much variance the corresponding PC explains. The eigenvalues are sorted based on magnitude in descending order and collected in the eigenvalue matrix $\mathbf{\Lambda}$, and the eigenvectors are collected as column vectors in the transformation matrix $\mathbf{U}$ in the same order. Finally, this gives us the M uncorrelated series $\mathbf{S}$, which can be referred to as the Scores of the PCs. If the input series $\mathbf{X}$ are highly correlated, then we can represent a high share of the variance using only a low number $M_{PC} << M$ of the first PCs.

We can also invert the transformation in (4). Since it can be shown that $\mathbf{U}$ is an orthonormal matrix [10], the inverse of the matrix $\mathbf{U}$ is simply the transpose of the matrix:

$$\mathbf{X} = (\mathbf{U}^T)^{-1}\mathbf{S} = \mathbf{US}$$
$$\Rightarrow \mathbf{x}_i = \sum_{j=1}^{M} u_{ij}\mathbf{s}_j \approx \sum_{j=1}^{M_{PC}} u_{ij}\mathbf{s}_j \tag{8}$$

From the above relation we can state that PC j appears in measurement i with a magnitude given by the coefficient u_{ij}.

C. Complex Principal Component Analysis

One limitation with conventional PCA is that a travelling wave, occuring in multiple measurements with different phase, can not be captured by only one PC. However, an extended version of PCA, often referred to as Complex Principal Component Analysis (CPCA), is better suited for this purpose. The method, described in detail in [4], uses the same equations as conventional PCA presented above, but some additional steps are required prior to the analysis.

CPCA is, in short, the same equations as presented above applied to complex time series, where the real part of the series is the input series, and the complex part is generated by applying the Hilbert Transform. To get sensible results when using the Hilbert Transform, it is important to make sure that the signal to be transformed contains only one frequency, and that any non-oscillatory trends are subtracted. This can be achieved using Empirical Mode Decomposition (EMD), or by applying PCA in two layers, discussed further in section II-D.

The Hilbert Transform is also strongly influenced by end effects [4]. When taking the transform of a measured series, this often results in very high values at the beginning and end of the series. To avoid that this influences consecutive steps in the algorithm, roughly $10\,\%$ of the series should be tapered in each end [4] after taking the Hilbert Transform.

After applying the necessary pre-processing to ensure a well-posed Hilbert Transform, the complex series can be written on the form

$$\mathbf{y}_i = \mathbf{x}_i + jH(\mathbf{x}_i) \tag{9}$$

where $H(\cdot)$ denotes the Hilbert Transform, and $\mathbf{x}_i$ is the real input series (with zero mean).

The complex series are collected in a matrix,

$$\mathbf{Y} = \begin{bmatrix} \mathbf{y}_1 \\ \mathbf{y}_2 \\ \vdots \\ \mathbf{y}_M \end{bmatrix} \tag{10}$$

The complex covariance matrix is given by

$$(1 - N)\tilde{\mathbf{C}} = \mathbf{Y}\mathbf{Y}^H \tag{11}$$

where the superscript $(\cdot)^H$ denotes conjugate transpose (not to be confused with the Hilbert Transform). Diagonalizing results

in real eigenvalues [4] and complex eigenvectors. Analogously to (8), we have

$$\mathbf{Y} = (\mathbf{V}^H)^{-1}\mathbf{Z} = \mathbf{VZ}$$
$$\Rightarrow \mathbf{y}_i = \sum_{j=1}^{M} v_{ij}\mathbf{z}_j \approx \sum_{j=1}^{M_{CPC}} v_{ij}\mathbf{z}_j \tag{12}$$

where $\mathbf{V}$ is the matrix of complex eigenvectors $\mathbf{v}_i$, with elements v_{ij}, and $\mathbf{Z}$ contains the Scores of the CPCs $\mathbf{z}_j$ as column vectors. The complex components of the eigenvectors describe the amplitude and phase of the contribution of each of the CPCs to each of the measurements. Here, the correlation matrix is Hermitian [4], the matrix $\mathbf{V}$ is unitary, and thus its inverse is the conjugate transpose.

D. Two-layer combination of PCA and CPCA

Applying the Hilbert Transform requires the input signal to have only one frequency, and that any non-oscillatory trends are subtracted. This can be achieved by using EMD to decompose the input signal into Intrinsic Mode Functions (IMFs) and a Residual [7]. The Hilbert Transform can then be applied to the IMFs, before CPCA is applied on the resulting complex series.

An alternative to using EMD for decomposition into IMFs, is to apply a to a two-layer structure of PCA: In the first layer conventional PCA is applied on the input series, resulting in a number of PCs. In the second layer, the PCs from the first layer are detrended by subtracting the residual from EMD, the Hilbert Transform is applied, before finally CPCA is applied. Thus, EMD is used only for computing the non-oscillatory residual, not for decomposition into IMFs. Detrending by EMD is described in [11].

In equations we can write, for the first layer (where PCA is applied),

$$\mathbf{S} = \mathbf{U}^T\mathbf{X} \tag{13}$$

The scores from the first layer are detrended (i.e. the residual computed using EMD is subtracted),

$$\mathbf{S}' = \mathbf{S} - \mathbf{R} \tag{14}$$

the Hilbert Transform is applied,

$$\mathbf{Y} = \mathbf{S}' + jH(\mathbf{S}') \tag{15}$$

(Here, $H(\mathbf{S}')$ denotes series-wise application of the Hilbert Transform, similarly as in (9). Also, although not shown with equations here, in a practical implementation roughly $10\,\%$ should be tapered in each end at this stage, to limit end effects.)

This gives the complex series which constitutes the input of the second layer (where CPCA is applied),

$$\mathbf{Z} = \mathbf{V}^H\mathbf{Y} = \mathbf{V}^H(\mathbf{S}' + jH(\mathbf{S}')) \tag{16}$$

Combining the above equations, we can write

$$\begin{aligned}
\mathbf{X} &= \mathbf{US} \\
&= \mathbf{U}\left(\mathbf{S}' + \mathbf{R}\right) \\
&= \mathbf{U}\left(\mathrm{Re}\left(\mathbf{Y}\right) + \mathbf{R}\right) \\
&= \mathbf{U}\left(\mathrm{Re}\left(\mathbf{VZ}\right) + \mathbf{R}\right)
\end{aligned} \tag{17}$$

Neglecting the residual and defining the matrix $\mathbf{W} = \mathbf{UV}$, we get

$$\mathbf{X} = \mathrm{Re}\left(\mathbf{UVZ}\right) = \mathrm{Re}\left(\mathbf{WZ}\right) \tag{18}$$

Finally, we can write

$$\mathbf{x}_i = \sum_{j=1}^{M} w_{ij}\mathbf{z}_j \approx \sum_{j=1}^{M_{CPC}} w_{ij}\mathbf{z}_j \tag{19}$$

This gives the contribution of the CPC $\mathbf{z}_j$, to the measurement $\mathbf{x}_i$ as the coefficient w_{ij}, i.e. element (i, j) of the matrix $\mathbf{W}$.

Note that if no components are discarded in either of the layers, then the matrices $\mathbf{U}$, $\mathbf{V}$ and $\mathbf{W}$ will be $M \times M$-matrices. If components are discarded, such that only M_{PC} components are kept from the first layer and M_{CPC} from the second layer, $\mathbf{U}$, $\mathbf{V}$ and $\mathbf{W}$ will be of dimension $M \times M_{PC}$, $M_{PC} \times M_{CPC}$ and $M \times M_{CPC}$, respectively.

Comparing modal analysis with CPCA as described, we see that the coefficients w_{ij} in (19) become very similar to the observability phasors ϕ_{ij} in (2). Thus, if the decomposition successfully produces CPCs with frequency and damping similar to that of the modes of the system, then the coefficients w_{ij} can be considered estimates of observability mode shapes.

E. k-Means Clustering

Clustering, in general, refers to the task of dividing a set of observations into groups, such that observations belonging to the same group are relatively similar, while the observations belonging to different groups are relatively different [12]. In the proposed method, clustering is used to determine which mode estimates, or observations, are similar enough to be included when computing averages of different modes and mode shapes. The k-Means clustering algorithm is widely used due to its computational simplicity. However, the method is prone to noise [13], and requires the number of clusters to be determined before the clustering.

To determine the number of clusters, a simple approach is to carry out the clustering multiple times with a range of different numbers of clusters, and then determining the most optimal solution by assessing some measure of the "goodness" of each clustering. The *Silhouette index* can be adopted for this purpose. For a thorough description of the k-Means algorithm and formal definitions of the silhouette index, the interested reader is referred to [13].

F. Exponential fitting by Linear Regression

Linear regression can be used for estimating the decay rate of an exponentially decaying series. We would like to describe the data Y_i measured at X_i using the exponential function $Y_i = \alpha e^{\beta X_i} + \varepsilon$, where ε is the error in the estimate. The parameters α and β are estimated by taking the logarithm of the values Y_i in the series, and then using Simple Linear Regression to find the linear relationsship between X_i and $\ln(Y_i)$. Expressions for α and β are given in [14].

Once we know the parameters, we can compute the average squared error by $R = \frac{1}{N}\sum_{i=1}^{N}\left(\alpha e^{\beta X_i} - Y_i\right)^2$.

III. PROPOSED METHOD

The two main parts of the proposed method are described in detail below; in short, the purpose of the first part of the method is to provide numerous estimates of modes using dimensionality reduction techniques, while in the second part averaged estimates of modes and mode shapes are computed using clustering. We assume M frequency measurement streams from which we want to extract information about modes and mode shapes.

Part I - Mode estimation

The first part of the method acts on a sliding time window containing N samples (for each of the M series). The length of the sliding window should be sufficiently long to capture low frequency oscillations, i.e. in the range $5 - 10\,\mathrm{s}$.

For each time window, we would like to decompose the oscillatory behaviour into a number of components, and find the amplitude and phase with which this behaviour happens in each measurement. Each time window is analyzed according to the following sequence:

1) The two-layer combination of PCA and CPCA, descibed in section II-D, is applied to the $M \times N$ matrix of input series:
   a) Each of the time series are normalized such as to have zero mean.
   b) PCA is applied,
   c) The scores are detrended,
   d) The Hilbert Transform is applied, and 10% of the ends of the resulting complex series are tapered
   e) CPCA is applied.

2) The frequency and decay rate of the resulting CPCs are estimated. The frequency is computed using the built-in MATLAB-function `meanfreq()`. The decay rate is computed using exponential regression on the absolute value of the CPCs ($\mathrm{Abs}(\mathbf{z}_i) = \sqrt{\mathrm{Re}(\mathbf{z}_i)^2 + \mathrm{Im}(\mathbf{z}_i)^2}$), described in II-F.

3) To limit the amount of uninteresting observations and noise in the clustering, only the estimates with a frequency between $0.1\,\mathrm{Hz}$ and $2\,\mathrm{Hz}$ (in the range of electromechanical oscillations) and a regression error below $4 \cdot 10^{-3}$, computed as described in section II-F, are used in the further analysis. The CPCs passing this criterion, along with the corresponding coefficients describing the amplitude and phase of their presence in the measurements, are expected to be relatively good estimates of modes and mode shapes.

4) Each of the accepted CPCs are rotated such that the largest coefficient, corresponding to the longest observability phasor in the mode shape, is at $0°$.

5) Finally, each mode estimate and the corresponding mode shape is stored as a $2M + 2$-dimensional point on the form

$$\mathbf{p} = [f, \sigma, \mathrm{Re}(G_1), \mathrm{Im}(G_1), \mathrm{Re}(G_2), \mathrm{Im}(G_2)... \\ ...\mathrm{Re}(G_M), \mathrm{Im}(G_M)] \quad (20)$$

where

f	= frequency
σ	= decay rate
$\mathrm{Re}(\cdot)$	= real part
$\mathrm{Im}(\cdot)$	= imaginary part
G_i	= observability phasor for measurement i

Once we have the mode estimates, it does not matter from which CPCs they were derived. Assuming that CPC j fulfilled the criterions in step 3, then the observability phasor of measurement i would be given by the coefficient w_{ij} in (19), i.e., we have $G_i = w_{ij}$. In the following, the stored points on the form (20) are referred to as "observations", to avoid confusion with the final, averaged mode estimates resulting from Part II, which are referred to as "mode estimates".

Step 3 in the sequence above is included to filter out bad observations, due to the k-Means algorithm being susceptible to noise. If a CPC resulting from the two-layer PCA-decomposition successfully captures a mode, then the absolute value of the CPC should decay (or grow) exponentially. Applying regression as described in section II-F gives an estimate of the decay rate of the mode, along with the average error in the estimate. A large error implies that the CPC does not decay or grow exponentially, and therefore is probably not a good estimate of one of the modes of the system. The threshold value of $4 \cdot 10^{-3}$ is found empirically, resulting in reasonable balance between acceptance and rejection of observations.

Part II - Computing mode averages

The PCA-decomposition in Part I is able to produce snap-shots of modes and mode shapes, but with some uncertainty. To digest the numerous observations and provide more reliable estimates, we would like to compute averaged modes- and mode shapes.

To determine which of the observations to include when averaging each mode, we apply a clustering algorithm: Observations that are similar are be grouped together, and the different groups/clusters are assumed to be associated with different modes. The averaged mode shapes are then computed as the centroids of the clusters.

Assuming we have Q point estimates resulting from Part I, these can be organized in a $Q \times (2M + 2)$-matrix:

$$\mathbf{P} = \begin{bmatrix} \mathbf{p}_1 \\ \mathbf{p}_2 \\ \vdots \\ \mathbf{p}_Q \end{bmatrix} = \begin{bmatrix} f & \sigma & \mathrm{Re}(G_1) & \ldots & \mathrm{Im}(G_M) \\ f & \sigma & \mathrm{Re}(G_1) & \ldots & \mathrm{Im}(G_M) \\ \vdots & & & & \\ f & \sigma & \mathrm{Re}(G_1) & \ldots & \mathrm{Im}(G_M) \end{bmatrix} \quad (21)$$
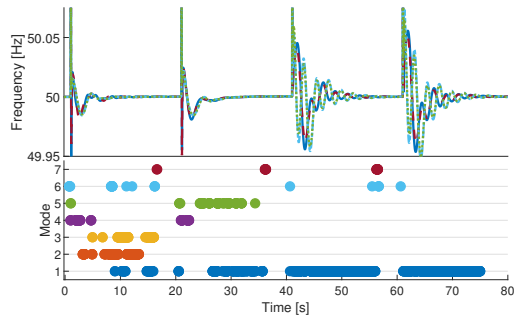
Fig. 1. Short circuits with clearing time $20\,\mathrm{ms}$ at four different locations are simulated in the Kundur Two Area System using DigSILENT PowerFactory, resulting in the time series shown in the upper plot. The lower plot shows where in time the observations contributing to the different mode estimates are detected. The same colors are used in Figs. 2 to 4 to indicate the cluster division.

Clustering of the points is carried out using the k-Means algorithm as described in II-E: The data is clustered multiple times with different numbers of clusters (for instance 1 to 10 clusters), and the final clustering is chosen to be the one with the highest silhouette index.

Finally, the averaged modes are derived from the centroids of the clusters.

IV. APPLICATION

The method is tested on simulated data from The Kundur Two Area System, performed in DigSILENT PowerFactory, and on PMU data recorded during an oscillatory event in the Nordic Power System. In the case with simulated data, the analysed time series has very high modal content and no ambient noise, and should be regarded as a demonstrational example. The case with PMU data contains ambient noise, and demonstrates the applicability of the method to measurements from a real system.

A. Simulated data from the Kundur Two Area System

This system is widely used for studying local and interarea modes. The system parameters are described in [9], but the model is modified according to the following: Generators 1 & 2 emulate hydro power plants, with governor model HYGOV, inertia constants $H = 10\,\mathrm{s}$ and synchronous reactances $X_d = 1.2$ & $X_q = 0.9$. Generators 3 & 4 emulate thermal power plants, with governor model TGOV1. All generators are equipped with the excitation system model SEXS. Finally, the load flow is modified, in order to achieve lower damping of the interarea mode, such that Generators 1, 2, 3 and 4 produce $600\,\mathrm{MW}$, $500\,\mathrm{MW}$, $801\,\mathrm{MW}$ and $900\,\mathrm{MW}$, respectively. Other parameters are as described in [9].

Short circuits with a clearing time of $20\,\mathrm{ms}$ are applied subsequently near each of the four generators, with $20\,\mathrm{s}$ between each short circuit. The resulting frequencies (measured at the generator buses), are shown in Fig. 1.
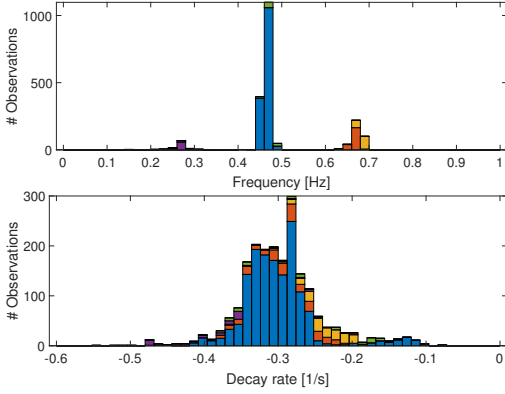
Fig. 2. The two histograms indicate the number of observations on the y-axis, and the frequency (upper plot) and decay rate (lower plot) on the x-axis, where the colors indicate the share of each column belonging to each cluster. The same colors as in Fig. 1 to indicate the cluster division.

Figs. 2 and 3 show histograms resulting from Part I of the method, indicating the number of observations with a given frequency, damping and observability phasor for each generator. Considering the histogram for frequency in Fig. 2, we see that higher densities of observations form around frequencies $0.3, 0.5$ and $0.7\,\text{Hz}$.

Part II of the method performs the clustering of the densely populated areas, and results in 7 clusters. The lower plot in Fig. 1 shows the time instants where observations assigned to the different clusters are obtained.

The coloring of the columns of the histograms indicate the share of the observations being assigned to different clusters, for instance, most of the $\approx 0.5\,\text{Hz}$-observations are assigned to the cluster shown in blue, and most of the $\approx 0.7\,\text{Hz}$-observations are assigned to the cluster shown in red, and so on. The same colors are used in the lower part of Fig. 1 and Figs. 2 to 4 to indicate the clustering division. Considering the observations around $0.5\,\text{Hz}$ in Fig. 2, shown in blue, we can study Fig. 3 to find that in these observations, the observability phasors for generators 1 & 2 (shown in the two upper plots) in average appear to have a real part around -0.4, and an imaginary part of about zero. For generators 3 & 4, the corresponding real and imaginary parts appear to be situated around 0.7 and zero. This indicates that this is an interarea mode, where generators 1 & 2 are swinging against generators 3 & 4. Considering the lower plot in Fig. 2, the decay rate of the same mode appears to be less accurately estimated due to the high variance compared to the other histograms, but the average appears to be around $0.3\,1/\text{s}$.

Once the clustering is performed, we know which observations to include when averaging each mode. The averaged modes from three of the clusters are shown in the upper part Fig. 4. For comparison, the corresponding modes computed using modal analysis in `DigSILENT PowerFactory` are shown below, indicating that the method is capable of provid-
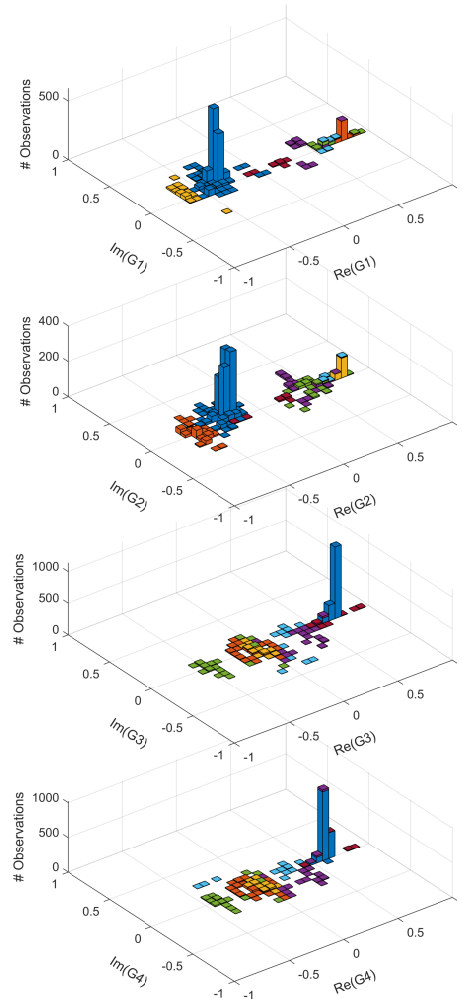
Fig. 3. The plots above show 2D histograms indicating the number of occurences (z-axis) of real and imaginary parts (x and y-axis) of the observability phasors of the four generators (first plot = Generator 1, second plot = Generator 2, and so on.). The colors indicate the share of each column belonging to each cluster. The same colors as in Figs. 1 and 2 are used to indicate the cluster division.

ing accurate estimates of system modes. The most significant deviation is the decay rate of the third mode shown, where the proposed method produces an estimate of $-0.37\,1/\text{s}$, while modal analysis gives the value $-0.939\,1/\text{s}$. Note that this mode is nevertheless very well damped, and that it is a mode associated with turbine governors. The method is thus not limited to identification of electromechanical modes.

As mentioned, the method results in 7 clusters, representing 7 averaged modes, whereof three are shown in 4. By comparing with results from modal analysis, it is found that two of

Mode estimate 1
f=0.466 Hz, σ=-0.301 1/s

Mode estimate 3
f=0.68 Hz, σ=-0.241 1/s

Mode estimate 4
f=0.269 Hz, σ=-0.368 1/s

Mode 19,
f=0.446 Hz, σ=-0.295 1/s

Mode 16,
f=0.664 Hz, σ=-0.211 1/s

Mode 26,
f=0.26 Hz, σ=-0.939 1/s
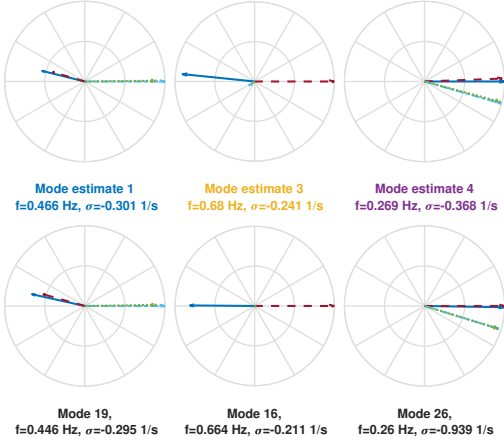
Fig. 4. The three upper mode shapes result from applying the method to simulated time series from the Kundur Two Area System, while the lower three mode shapes are computed using modal analysis on a linearized model of the same system. In the colored captions of the upper three mode shapes, the same colors as in Figs. 1 to 3 are used to indicate the cluster division. For the phasors in all the mode shapes, the colors and line types correspond to those of the time series in Fig. 1.
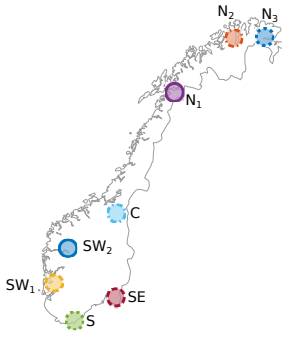
Fig. 5. This map shows the approximate locations of the eight PMUs recording the oscillations shown in Figs. 6 and 7. The appearance of the markers correspond to the colors and line types of the time series in Figs. 6, 7 and the phasors in Fig. 8.

Fig. 6. The PMU measurements in the upper plot show oscillations following an event, recorded at 8 different locations. The lower plot shows where in time the observations contributing to the different mode estimates are detected, similarly as for the case with the Kundur Two Area System in Fig. 1.

Fig. 7. A zoomed view of the original time series are shown. From the period of almost sustained oscillations we see that the method is able to correctly identify the locations with highest oscillations and the phase shift between the various locations. The sampling frequency is 10 Hz in this case, which is lower than what can be achieved with most PMUs.

B. PMU measurements from oscillatory event

The recorded PMU data is shown in the upper part of Fig. 6. Applying the method yields the three mode shapes shown in Fig. 8. Studying Fig. 7, which shows a zoomed view at the beginning of the oscillatory period, we see that the oscillations are most prominent in the two signals shown in green and yellow, corresponding to locations S and SW_1 in Fig. 5. These locations are oscillating roughly in phase. Considering locations SW_2 and SE, the amplitudes of the oscillations are a bit lower, and the respective phase shifts are about 135° to the left, and 90° to the right. Mode Estimate 1 fits well with this description, indicating that the method is able to produce

the averaged mode estimates, number 6 and 7, do not resemble any of the modes from modal analysis.

Further, it is found that mode estimate 2 and 3 are very similar, except that the mode shape is rotated 180°, which is probably due to the mode shapes from Part I being rotated such that the longest observability phasor lies at 0°. Due to some inaccuracy in the CPCA decomposition, the next longest observability phasor will in some estimates appear the longest, thus flipping the whole mode shape around. The same is the case for estimates 1 and 5, the averaged mode shapes are very similar, but appear at different angular positions.

Mode estimate 1
f=0.987 Hz, σ=0.023 1/s

Mode estimate 2
f=1.014 Hz, σ=-0.087 1/s

Mode estimate 3
f=1.109 Hz, σ=-0.001 1/s

Fig. 8. In the colored captions, the same colors as in Fig. 6 are used to indicate the cluster division, while for the phasors, the colors and line types correspond to those of the markers indicating PMU positions in Fig. 5, and those of the time series in Figs. 6 and 7.

a reasonable estimate of the mode and corresponding mode shape.

From the lower plot in Fig. 6, it can be seen that the observations from which Mode estimate 1 is computed, are captured shortly after the oscillations started, Mode estimate 2 was captured shortly after that, and and finally Mode estimate 3 was captured at the end of the period with oscillations. The three mode shapes are similar, but in particular the angle of the phasor corresponding to location SE in Fig. 5 (shown with dashed, red lines) changes during the course of the oscillations. Also, the frequencies of Estimates 2 and 3 are a bit higher than the first. This could indicate that some remedial action was taken to mitigate the oscillations.

V. Discussion

The above results are promising; first and foremost, the method is able to produce relatively accurate estimates of modes of the power system.

The results from the case with PMU data reveals a potential benefit of the described empirical approach, namely that the method could facilitate tracking of how modes change during a period. In the presented case, the oscillatory mode and the corresponding mode shape appears to change slightly during the course of the oscillations. This is information that would be difficult to obtain using modal analysis, which could potentially contribute to increased situational awareness.

When applying the method to the Kundur Two Area system, two of the resulting mode estimates are copies of other estimates, appearing at different angular positions. This is caused by the way the observations are stored, i.e. with the longest observability phasor at $0°$. This could be avoided in a post processing step, checking if any of the mode estimates are replicates of each other, or by storing the observations in a format that is independent of the angle of the mode shape.

Further testing needs to be done to improve the method, and facilitate development into a form that is useful for grid operators. Imaginably, the dynamics decomposition in Part I would run continuously, analyzing numerous PMU data streams on the go, while the clustering in Part II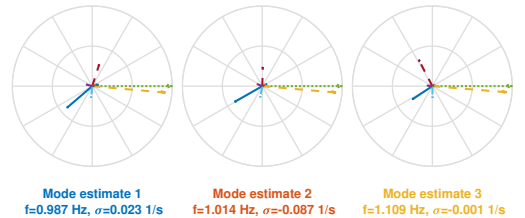 could be performed on a longer-term moving window, for instance of lengths on the scale of minutes or hours. This would provide operators with continuously updated information on the power system modes, which could in turn be taken into account when designing future wide area control applications.

For the implementation, there is a large potential for improvement. Other input quantities than the frequency could be tested as input to the method, for instance the voltage angle. Further, in Part I of the method, the criterion for determining whether observations should be included in the clustering part could take many forms. If a clustering algorithm less susceptible to noise was used, the criterion could be less strict, or even be omitted. Other variants of the dynamics decomposition could also be tested, for instance as described in [7], where EMD is used to decompose the input signals into IMFs rather than the two-layer combination of PCA and CPCA implemented here.

An important next step in the further development of the method will be to compare it with other methods serving the same purpose, for instance those described in [2] and [3], which could give an indication of the relative performance of the method in terms of accuracy and speed. Other important aspects that must be explored include testing on larger grids (with more measurements) and sensitivity to noise.

VI. Conclusion

Testing on simulated data and recorded PMU data indicates that the presented method could be a useful tool for digesting numerous PMU measurements into useful knowledge of the system, in the form of information about the oscillatory modes and their mode shapes. The main conclusion is that the method is feasible, and shows promising result on measured and simulated data. Further work is required to improve the different constituents of the method, including the dynamics decomposition using CPCA, the filtering/handling of noise/bad observations and the clustering part. Additionally, the method must be compared with other similar methods, and further testing on measured data will be necessary to verify the robustness and efficiency of the method for online use.

References

[1] Dinh Thuc Duong and Kjetil Uhlen. An Empirical Method for Online Detection of Power Oscillations in Power Systems. In *2018 IEEE Innovative Smart Grid Technologies - Asia (ISGT Asia)*, pages 758–763. IEEE, 5 2018.

[2] Lalit Kumar and Nand Kishor. Determination of mode shapes in PMU signals using two-stage mode decomposition and spectral analysis. *IET Generation, Transmission & Distribution*, 11:4422–4429, 2017.

[3] Janne Seppanen, Siu Kui Au, Jukka Turunen, and Liisa Haarla. Bayesian Approach in the Modal Analysis of Electromechanical Oscillations. *IEEE Transactions on Power Systems*, 32(1):316–325, 2017.

[4] J.D. Horel. Complex Principal Component Analysis: Theory and Examples, 1984.

[5] Arturo Roman Messina and Vijay Vittal. Extraction of Dynamic Patterns From Wide-Area Measurements Using Empirical Orthogonal Functions. *IEEE Transactions on Power Systems*, 22(2):682–692, 2007.

[6] P. Esquivel. Wide-area wave motion analysis using complex empirical orthogonal functions. *2009 6th International Conference on Electrical Engineering, Computing Science and Automatic Control (CCE)*, 52(33), 2009.

[7] A. R. Messina, P. Esquivel, and F. Lezama. Wide-area PMU data monitoring using spatio-temporal statistical models. In *2011 IEEE/PES Power Systems Conference and Exposition*, pages 1–7. IEEE, 3 2011.

[8] E. Johansson, K. Uhlen, A. B. Leirbukt, P. Korba, J. O. Gjerde, and L. K. Vormedal. Coordinating power oscillation damping control using wide area measurements. *Power Systems Conference and Exposition, 2009. PSCE '09. IEEE/PES*, pages 1–8, 2009.

[9] Prabha Kundur. *Power System Stability and Control*. McGraw-Hill, New York, 1994.

[10] J. Edward Jackson. *A User's Guide to Principal Components*. Wiley Series in Probability and Statistics. John Wiley & Sons, Inc., Hoboken, NJ, USA, 3 1991.

[11] Patrick Flandrin, Paulo Goncalves, and Gabriel Rilling. Detrending and denoising with empirical mode decompositions. *European Signal Processing Conference*, 06-10-Sept(3):1581–1584, 2015.

[12] Gareth James, Daniela Witten, Trevor Hastie, and Robert Tibshirani. *An Introduction to Statistical Learning*, volume 103 of *Springer Texts in Statistics*. Springer New York, New York, NY, 2013.

[13] Sergios Theodoridis and Konstantinos Koutroumbas. *Pattern recognition*. Academic Press, 2009.

[14] P. Glaister. Exponential curve fitting with least squares. *International Journal of Mathematical Education in Science and Technology*, 38(3):422–427, 2007.

Paper II

The paper **"Power Oscillation Monitoring using Statistical Learning Methods"** is published in the proceedings of the **2019 IEEE Milan PowerTech** conference.

Power Oscillation Monitoring using Statistical Learning Methods

Hallvar Haugdal and Kjetil Uhlen
Department of Electric Power Engineering
Norwegian University of Science and Technology
Trondheim, Norway

Abstract—**This paper describes development and testing of a method for estimation of electromechanic modes and corresponding mode shapes from frequency or voltage angle measurements in Wide Area Monitoring Systems. The method uses Complex Principal Component Analysis to perform a decomposition of the dynamics captured in the measurements, reducing any detected oscillations into sets of parameters. The numerous sets of parameters generated after a time period can be interpreted as points or observations in high-dimensional space, on which a clustering algorithm can be applied to pinpoint areas where high densities of points are accumulated. Results show that highly accurate estimates of oscillatory modes in the power system and their mode shapes can be derived by averaging the point observations belonging to each cluster.**

Important development described in this paper includes the use of voltage angle as input and testing on a medium size power system simulation model with synchronized measurements from 44 nodes. Furthermore, introduction of the DBSCAN clustering algorithm shows very promising results when applying the method to recorded phasor measurements from the Nordic power system.

Index Terms—**Clustering, Mode Shapes, Phasor Measurement Units, Power Oscillations, Complex Principal Component Analysis**

I. Introduction

New methods for estimation of modes and mode shapes are frequently reported in the literature, motivated by blackouts in the past that could possibly have been avoided given sufficient information about oscillatory modes. Most methods are either aimed at providing estimates during ambient conditions, or from more pronounced oscillations during transient responses or ringdowns. In [1], a monitoring scheme based on two algorithms is proposed: Ambient conditions are analyzed using a wavelet-based method, while Prony's method, triggered by a pre-defined rule, is used to analyze ringdowns. This method, however, is not able to capture information about mode shapes. The method described in [2] also captures mode shapes from ringdowns, but is not applicable during ambient conditions. In [3], a Multichannel AutoRegressive Moving Average eXogenous (ARMAX) model is used to extract information on modes and mode shapes from ambient conditions. A slight deterioration of most ambient methods is reported when an oscillatory event is introduced in the analyzed time series [4]. In [5], a Bayesian approach to mode estimation from ambient conditions is proposed, where specific frequency bands are targeted to reduce the complexity of the problem.

The method described in this paper was developed for analyzing short time series of pronounced ringdown events. However, results indicate that mode estimates can also be produced from longer time spans of ambient conditions. In this respect, this method can be considered more general than most of the above mentioned methods.

The method consists of two main parts: In Part I, a sliding time window containing the samples from the last 5 to 10 seconds is analyzed using Complex Principal Component Analysis (CPCA). The oscillatory dynamics in the time window are decomposed into monofrequency components and a set of coefficients that describe the amplitude and phase of each frequency in the measurements. This information is stored as a set of point observations. In Part II of the method, the DBSCAN clustering algorithm is applied to all the observations from a given period (on the scale of minutes). The observations in densely populated areas of the input space are associated with dynamics that occur frequently, and are grouped together. Finally, averaged modes and mode shapes can be computed as the average of all the observations belonging to each cluster.

CPCA is described in [6], intended for analysis of geophysical phenomena. Similar work on analysis of electromechanical modes is reported in [7]–[10], where the term Empirical Orthogonal Functions (EOF) is used instead of Principal Component Analysis (PCA). An important contribution from the proposed method described in this paper is the second part, where the observations are clustered. The purpose of this part is to present the information from the CPCA dynamics decomposition in a more meaningful and understandable way to the operators.

The basic structure of the method (CPCA dynamics decomposition combined with clustering for averaging) has been described previously in [11], where it is applied to analysis of large disturbances/ringdowns. Continuing this work, we propose further development of the method by introducing the DBSCAN clustering algorithm, in addition to further testing on a medium size grid and on ambient conditions.

Section II gives a description of the method, based on the more thorough description in [11], however with some modifications. Section III describes results from applying the method to simulated and recorded PMU data, followed by discussions and conclusions in Sections IV and V.

II. EMPIRICAL METHOD FOR ESTIMATION OF MODES AND MODE SHAPES

The proposed method consists of two main parts: In Part I, a sliding time window is analyzed using CPCA. The dynamics in the input series are decomposed into monofrequency components, allowing the dynamics occurring to be quantified in terms of frequency and correlation. The dynamics are reduced to a set of parameters, which are stored and used in the further analysis. One set of parameters, describing an oscillation with a specific frequency and amplitude- and phase correlation between all input measurements, is referred to as an *observation*.

As the time window slides through time, numerous observations are generated. In Part II of the method, the point observations are clustered, such that similar observations are grouped together. Finally, the averaged modes and mode shapes are computed as the centroids of the clusters.

Part I: Dynamics Decomposition using Complex Principal Component Analysis

The sliding time window can be considered as an $M \times N$-matrix, where M is the number of measurement series and N is the number of samples per series:

$$\mathbf{X} = \begin{bmatrix} \mathbf{x}_1 \\ \mathbf{x}_2 \\ \vdots \\ \mathbf{x}_M \end{bmatrix} = \begin{bmatrix} x_1(t_1) & x_1(t_2) & \cdots & x_1(t_N) \\ x_2(t_1) & x_2(t_2) & \cdots & x_2(t_N) \\ \vdots & & \ddots & \\ x_M(t_1) & x_M(t_2) & & x_M(t_N) \end{bmatrix} \quad (1)$$

Applying PCA, as described in [12], we effectively transform the correlated series above into a set of uncorrelated series, or Principal Components (PCs),

$$\mathbf{S} = \begin{bmatrix} \mathbf{s}_1 \\ \mathbf{s}_2 \\ \vdots \\ \mathbf{s}_{M_{PC}} \end{bmatrix} = \mathbf{U}^T \mathbf{X} \quad (2)$$

The matrix $\mathbf{U}$ is constituted by the eigenvectors of the covariance matrix of $\mathbf{X}$. The PCs are sorted such that the first PC captures the most variance in the input series, the second component captures second most variance, and so on. The number of components M_{PC} is chosen such that the significant variance in the input series is captured (i.e. $\approx 99\%$ etc.). Given that the input series are highly correlated, we can analyze the dynamics following a disturbance by considering only a few PCs, rather than the full set of input series.

If phase shifted oscillations occur in two different measurements, we can not capture the oscillations using only one component. This makes the case for employing a complex variant of PCA. Complex Principal Component Analysis (CPCA), as described in [6], is very similar to PCA, but prior to applying the linear transform in (2), the Hilbert transform is applied to the input series to generate a complex time series. Applying PCA (as described above) to the complex series yields a complex covariance matrix and a complex transformation matrix.

Ensuring a well posed Hilbert Transform requires that the input series contains only one frequency, and that any non-oscillatory trends are subtracted prior to applying the transform. This can be achieved by adopting a two-layer structure of PCA: In the first layer, PCA is applied to the input measurement series. Given some correlation, this significantly reduces the number of components that needs to be analyzed by CPCA.

In the second layer, CPCA is applied: First, the non-oscillatory trend of each signal is computed as the residual from Empirical Mode Decomposition, as described in [13]. Further, the Hilbert transform is computed before the second layer of PCA equations is applied.

Proceeding with the PCs computed as shown above, we subtract the residuals $\mathbf{R}$ computed using EMD:

$$\mathbf{S}' = \mathbf{S} - \mathbf{R} \quad (3)$$

Applying the Hilbert Transform yields the complex series:

$$\mathbf{Y} = \mathbf{S}' + jH(\mathbf{S}') \quad (4)$$

Here, $H(\mathbf{S}')$ denotes series-wise application of the Hilbert transform. Also, in the practical implementation roughly 10% should be tapered in each end of the series at this stage, to limit end-effects [6].

The complex series $\mathbf{Y}$ is the input to the second layer, where CPCA is applied:

$$\mathbf{Z} = \mathbf{V}^H \mathbf{Y} = \mathbf{V}^H(\mathbf{S}' + jH(\mathbf{S}')) \quad (5)$$

The superscript $(\cdot)^H$ denotes the conjugate transpose. $\mathbf{V}$ is the CPCA transformation matrix, analogously to the PCA transformation matrix $\mathbf{U}$ in (2).

It can be shown that $\mathbf{U}$ is orthonormal [12] and $\mathbf{V}$ is unitary [6], such that their inverses are simply the transpose and the conjugate transpose, respectively. Inverting the above transformation matrices, we can write the input measurement series in terms of PCs and CPCs:

$$\begin{aligned} \mathbf{X} &= \mathbf{US} \\ &= \mathbf{U}(\mathbf{S}' + \mathbf{R}) \\ &= \mathbf{U}(\mathrm{Re}(\mathbf{Y}) + \mathbf{R}) \\ &= \mathbf{U}(\mathrm{Re}(\mathbf{VZ}) + \mathbf{R}) \end{aligned} \quad (6)$$

Neglecting the residual and defining the matrix $\mathbf{W} = \mathbf{UV}$, we get

$$\mathbf{X} = \mathrm{Re}(\mathbf{UVZ}) = \mathrm{Re}(\mathbf{WZ}) \quad (7)$$

Finally, we can write

$$\mathbf{x}_i = \sum_{j=1}^{M} \mathrm{Re}(w_{ij}\mathbf{z}_j) \approx \sum_{j=1}^{M_{CPC}} \mathrm{Re}(w_{ij}\mathbf{z}_j) \quad (8)$$

This gives the contribution of the Complex Principal Component (CPC) $\mathbf{z}_j$, to the measurement $\mathbf{x}_i$ as the coefficient w_{ij}, i.e. element (i, j) of the matrix $\mathbf{W}$.

Insignificant components are discarded during the decomposition, such that only M_{PC} components are kept from the first

layer and M_{CPC} from the second layer. Thus, the matrices $\mathbf{U}$, $\mathbf{V}$ and $\mathbf{W}$ will be of dimension $M \times M_{PC}$, $M_{PC} \times M_{CPC}$ and $M \times M_{CPC}$, respectively.

At the end of the dynamics decomposition of each time window, a point on the following form is stored for each of the CPCs:

$$\mathbf{p} = [f_j, \text{Re}(w_{1j}), \text{Im}(w_{1j}), \text{Re}(w_{2j}), \text{Im}(w_{2j})... \qquad (9)$$
$$...\text{Re}(w_{Mj}), \text{Im}(w_{Mj})])$$

All the point observations from a given period are analyzed further in Part II of the method, discussed next.

Part II: Mode averaging using DBSCAN Clustering

In the second part of the method, we cluster the observations generated by the dynamics decomposition in Part I. This allows us to filter out bad observations/noise, and to compute averages of the frequency and mode shape of different modes.

The clustering is carried out using the DBSCAN clustering algorithm, described in [14]. The algorithm clusters observations in densely populated areas together, and classifies observations in areas with low densities as noise. This algorithm requires the user to input two parameters, which determines the density of points requred to form clusters, described thoroughly in [14]. In the results reproduced below, the parameter values Eps $= 0.2$ and MinPts $= 75$ are found by trial and error to give good results.

Clustering the observations allows us to compute the average of all the observations in each cluster, resulting in the final, averaged modes and corresponding mode shapes.

III. RESULTS

The method is tested on a 44-generator model of the Nordic Power System [15], and on recorded PMU data from an oscillatory event in the real Nordic Power System.

A. The Nordic 44 test network

A short circuit with a clearing time of $10\,\text{ms}$ is simulated in `DIgSILENT PowerFactory`. A $10\,\text{s}$ excerpt from the resulting rotor angle time series (of total length $20\,\text{s}$) is shown in Fig. 1. Applying the method to these time series results in two averaged modes and corresponding mode shapes; the first with a frequency of $0.70\,\text{Hz}$, the second $0.89\,\text{Hz}$. Examining Fig. 1, the $0.70\,\text{Hz}$-mode is the one most clearly visible. One of the time series with a high observability of this mode is highlighted in blue. The $0.89\,\text{Hz}$-mode is slightly less excited, but is also clearly visible in the time series highlighted in red. The observations contributing to each of the modes are indicated in Fig. 2.

Further, the averaged mode estimates are compared with results from modal analysis on the linearized model, conducted in `DIgSILENT PowerFactory`: It is found that both estimates computed using the proposed method resemble modes from linear analysis quite accurately. The two most poorly damped modes computed using modal analysis have frequencies of $0.66\,\text{Hz}$ and $0.93\,\text{Hz}$ respectively, which matches the above results well. Here, one has to keep in mind that since
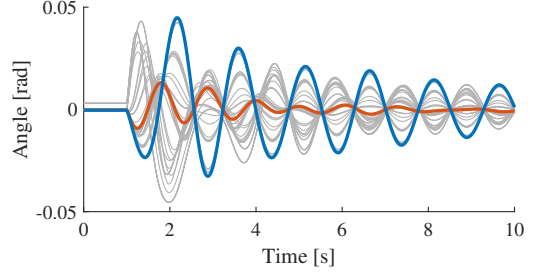
Fig. 1: Rotor angle time series generated by simulating a short circuit near one of the generators in the Nordic 44 test network. The mean of each time series is subtracted to clearly indicate the characteristics of the oscillations. The time series highlighted in blue and red has high content of the $0.67\,\text{Hz}$ and $0.93\,\text{Hz}$ modes, respectively.
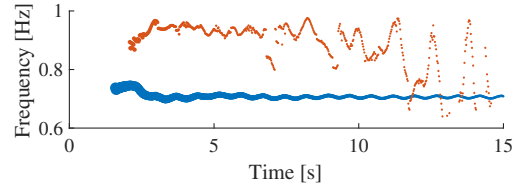
Fig. 2: The observations shown in blue are grouped together in one cluster, similarly for the observations shown in red. Averaging the observations in the clusters yields mode estimates of $0.70\,\text{Hz}$ and $0.89\,\text{Hz}$, which are close to the modes produced by modal analysis of the linearized model. The variance in the observations shown in red is larger than for the blue observations, caused by higher excitation and lower damping of the mode indicated in blue.

the system is not linear, one should not expect the oscillations following a large disturbance to match perfectly the results from small signal (modal) analysis.

A comparison of the mode shapes is shown in Figs. 3 and 4, for the $0.67\,\text{Hz}$-mode and the $0.93\,\text{Hz}$-mode respectively. For the $0.67\,\text{Hz}$-mode, the mode shape computed using modal analysis is very similar to the mode shape produced by the proposed method when using the rotor angle as input. The $0.93\,\text{Hz}$-mode is slightly less accurately reproduced by the proposed method, probably due to this mode being less excited and having higher damping.

The rotor angles of generators are not directly available from the data provided by PMUs. Instead, the voltage angle at the bus nearest to each generator could be used as an approximation to the rotor angle. The mode shapes computed using voltage angles as input are also shown in the two figures, revealing that this is slightly less accurate, but still well capable of capturing the main characteristics of the rotor angle dynamics.
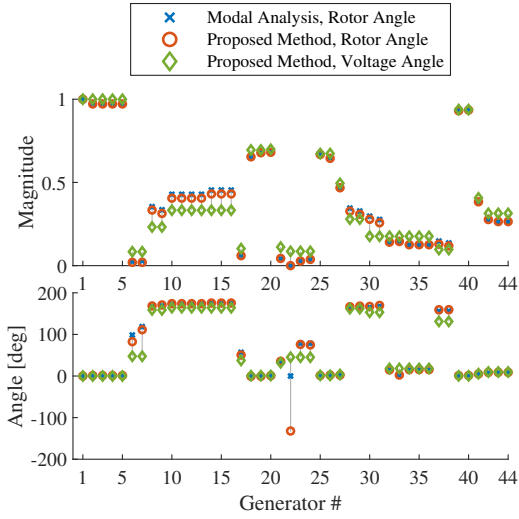
Fig. 3: Estimation accuracy of the 0.67 Hz-mode for each of the 44 measurements. The results produced by the method applied to rotor angle measurements is very accurate, while using the voltage angle as input gives slightly less accurate results.
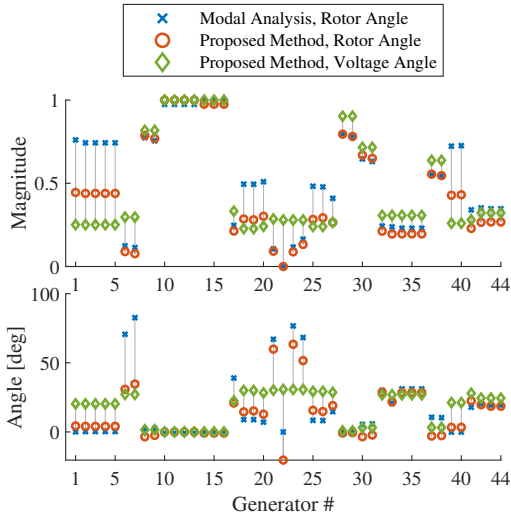
Fig. 4: Estimation accuracy of the 0.93 Hz-mode for each of the 44 measurements. The accuracy of this estimate is poorer than the accuracy for the more excited, less damped 0.67 Hz mode.
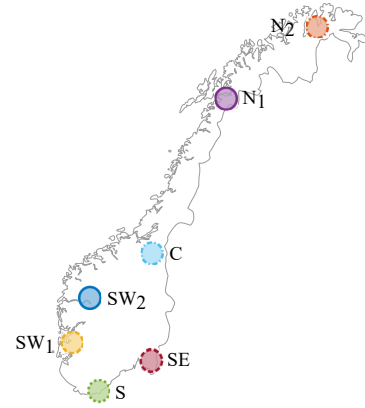
Fig. 5: The approximate locations of the seven PMUs recording the oscillatory event in the Nordic Power System.
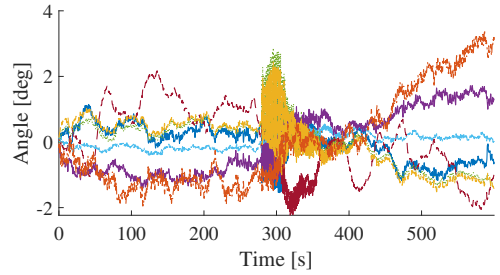
Fig. 6: Voltage angle time series measured by PMUs at the seven locations indicated in Fig. 5, using the same colors and styles for the locations.
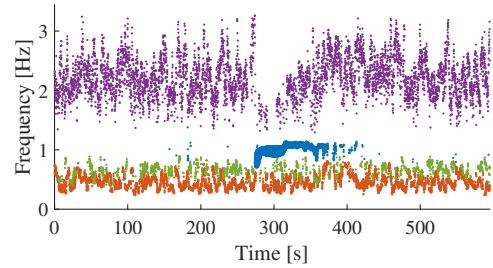
Fig. 7: The time instants and frequencies of the observations contributing to each of the four clusters are indicated by the coloring of the markers. The same colors are used in Figs. 8 and 9 to indicate the clustering division. Further, the size of each marker indicates the severity of the oscillations.

Mode estimate 1
f=1.02 Hz

Mode estimate 2
f=0.461 Hz

Mode estimate 3
f=0.665 Hz

Mode estimate 4
f=2.22 Hz
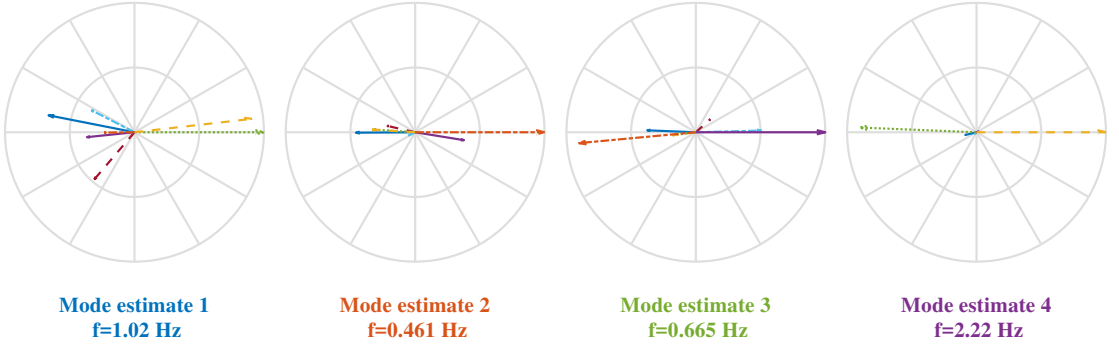
Fig. 8: The four resulting averaged mode shapes resulting from applying the method to the time series measured by PMUs during an oscillatory event in the Nordic Power System.
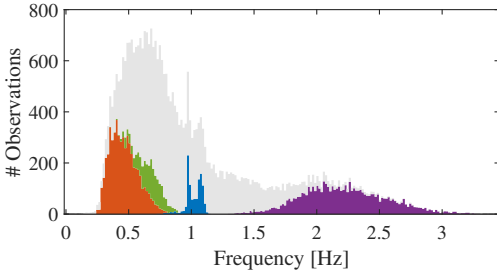
Fig. 9: The histogram indicates the number of observations with a given frequency. The coloring indicates the number of observations assigned to the different clusters.
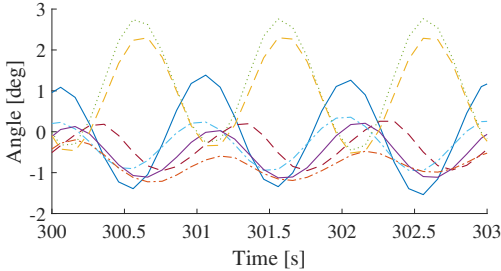
Fig. 10: An excerpt of the time series in Fig. 6 is shown, clearly indicating the amplitude and phase of the oscillations in each of the measurements. The same colors and styles are used to indicate the locations as in Fig. 5.

B. PMU-data from the Nordic Power System

Fig. 5 indicates approximate locations of seven PMUs in the Nordic Power System, where time series of voltage angles are recorded during a disturbance event that created system oscillations; as indicated in Fig. 6. Applying the proposed method to these time series results in four averaged modes and mode shapes. The observations contributing to each cluster are indicated in Fig. 7, and the final averaged mode shapes are shown in Fig. 8. The histogram in Fig. 9 indicates the number of observations with a given frequency assigned to the different clusters.

The first mode estimate of about $1\,\mathrm{Hz}$, indicated in blue in Figs. 7, 8 and 9, describes the severe oscillations starting around $280\,\mathrm{s}$ and lasting until about $400\,\mathrm{s}$. Observing the excerpt of the recorded time series in Fig. 10, it is clear that this mode shape accurately describes the oscillations. The second mode estimate of about $0.45\,\mathrm{Hz}$, shown in red, corresponds to a well-known inter-area mode in the Nordic power system; here observed as oscillations between the north and south of Norway. The third estimate of about $0.67\,\mathrm{Hz}$, appears to describe oscillations between the two northern locations N_1 and N_2, but also involving locations further south. The fourth estimate of about $2.2\,\mathrm{Hz}$ (in average) could possibly describe a local mode involving generators in the south of Norway oscillation against each other. However, the sample rate in this recording is $10\,\mathrm{Hz}$, which is too low to capture oscillations at $2\,\mathrm{Hz}$ with a high degree of certainty. Moreover, the magnitude of these oscillations is very low. It is therefore difficult to say whether the fourth mode estimate is just noise, or if it really describes an electromechanical mode.

IV. DISCUSSION

The results from testing the method on the simulated data indicates that the proposed method is able to produce relatively accurate estimates of modes and mode shapes. The two most poorly damped modes of the Nordic 44 test network are detected quite accurately from a $20\,\mathrm{s}$-measurement series following a short circuit, where both modes are excited at the same time.

Testing the method on recorded data from PMUs reveals that the proposed method is able to produce time averaged estimates of modes and mode shapes from ambient data, but also accurate descriptions of pronounced oscillations and ringdowns.

In a practical implementation, the CPCA-dynamics decomposition in Part I of the method would run continuously, producing mode observations for each new set of synchronized samples received from the PMUs. The clustering algorithm could be run a bit less frequent, but including all the observations from a given period back in time in the clustering.

Fig. 7 indicates the results that would constitute the detailed information to be included in an operator information system. The figure gives information about the certainty and accuracy of each of the four estimates, and gives a clear indication of the severity of the oscillations. Before the 1 Hz oscillations started, the operators would be presented with only the three estimates produced from ambient data (estimates 2, 3 and 4). As the oscillations started the operators would be presented with the 1 Hz mode estimate potentially seconds or tens of seconds after the oscillations started. In this case, the mode shape indicated the approximate location of the generator causing the instability (which was in the proximity of locations S and SW_1 in Fig. 5), and would have given the operators valuable and useful information for determining the proper remedial action. This example illustrates how critical information could be obtained very quickly, and as such contribute to increase operators' situational awareness.

To be able to provide an early warning of initiated oscillations, it would be of interest to perform the clustering as fast and often as possible, while at the same time having a clustering window of at least some minutes to be able to capture information of well-damped modes with low excitation from ambient data. The 35 000 observations from the 600 s-period in the PMU-example above takes approximately 50 s to cluster on a laptop with a Intel Core i7 2.80 GHz processor and 16.0 GB of RAM. However, this was carried out using a very naive implementation of the DBSCAN algorithm. The computation time could potentially be reduced significantly using a more sophisticated implementation; in [16] and [17], it is shown that the computation time for the clustering can be reduced by factors in the range 10 to 100 by taking advantage of parallel computing and graphics computing units (GPUs). If this was achievable in our case, the operators could be given an alert about the 1 Hz oscillations discussed above only seconds after they started, with an accurate mode shape supplementing the alert.

Regarding the computational complexity of the dynamics decomposition in Part I of the method, this is presumably less of a challenge. In the case with 44 simulated measurements from the Nordic 44 test network, the average and maximum computation time for the decomposition of one time window was about 20 ms and 70 ms, respectively, on the same computer as described above. Since the decomposition of one time window is independent on the previous and the next, this could be paralleled to allow the method to run online.

V. CONCLUSION

The results from applying the proposed method to both simulated data and recorded PMU data from the Nordic Power System are promising. The results from the case with simulated data indicate that relatively accurate estimates of simultaneously excited modes and corresponding mode shapes can be produced from ringdowns. Further, the case with recorded PMU data indicates that the method is able to estimate modes from ambient conditions at the same time as severe ongoing oscillations are captured; this is a comparative advantage to many other methods. Further work needs to be done to quantify the accuracy of the method, as well as improving the computational efficiency to a level required by online monitoring applications.

REFERENCES

[1] D. T. Duong and K. Uhlen, "An Empirical Method for Online Detection of Power Oscillations in Power Systems," in *Proc. IEEE Innovative Smart Grid Technologies (ISGT)*, 2018, pp. 758–763.

[2] N. R. Chaudhuri and B. Chaudhuri, "Damping and relative mode-shape estimation in near real-time through phasor approach," *IEEE Transactions on Power Systems*, vol. 26, no. 1, pp. 364–373, 2011.

[3] L. Dosiek and J. W. Pierre, "Estimating electromechanical modes and mode shapes using the multichannel ARMAX model," *IEEE Transactions on Power Systems*, vol. 28, no. 2, pp. 1950–1959, 2013.

[4] L. Dosiek, N. Zhou, J. W. Pierre, Z. Huang, and D. J. Trudnowski, "Mode shape estimation algorithms under ambient conditions: A comparative review," *IEEE Transactions on Power Systems*, vol. 28, no. 2, pp. 779–787, 2013.

[5] J. Seppanen, S. K. Au, J. Turunen, and L. Haarla, "Bayesian Approach in the Modal Analysis of Electromechanical Oscillations," *IEEE Transactions on Power Systems*, vol. 32, no. 1, pp. 316–325, 2017.

[6] J. D. Horel, "Complex Principal Component Analysis: Theory and Examples," *Journal of Climate and Applied Meteorology*, vol. 23, no. 12, pp. 1660–1673, 1984.

[7] A. R. Messina and V. Vittal, "Extraction of Dynamic Patterns From Wide-Area Measurements Using Empirical Orthogonal Functions," *IEEE Transactions on Power Systems*, vol. 22, no. 2, pp. 682–692, 2007.

[8] P. Esquivel and A. R. Messina, "Complex Empirical Orthogonal Function analysis of wide-area system dynamics," in *IEEE Power and Energy Society 2008 General Meeting: Conversion and Delivery of Electrical Energy in the 21st Century*, 2008, pp. 1–7.

[9] P. Esquivel, "Wide-area wave motion analysis using complex empirical orthogonal functions," in *CCE International Conference on Electrical Engineering, Computing Science and Automatic Control*, vol. 52, no. 33, 2009, pp. 1–6.

[10] A. R. Messina, P. Esquivel, and F. Lezama, "Wide-area PMU data monitoring using spatio-temporal statistical models," in *2011 IEEE/PES Power Systems Conference and Exposition*. IEEE, 3 2011, pp. 1–7.

[11] H. Haugdal and K. Uhlen, "Mode Shape Estimation using Complex Principal Component Analysis and k-Means Clustering," *arXiv:1812.02966*, 2018.

[12] J. E. Jackson, *A User's Guide to Principal Components*, ser. Wiley Series in Probability and Statistics. Hoboken, NJ, USA: John Wiley & Sons, Inc., 1991.

[13] P. Flandrin, P. Goncalves, and G. Rilling, "Detrending and denoising with empirical mode decompositions," in *Proc. European Signal Processing Conf.*, no. 3, 2015, pp. 1581–1584.

[14] M. Ester, H.-P. Kriegel, J. Sander, and X. Xu, "A density-based algorithm for discovering clusters in large spatial databases with noise," in *Proc. Second International Conf. on Knowledge Discovery and Data Mining (KDD)*, E. Simoudis, J. Han, and U. M. Fayyad, Eds. AAAI Press, 1996, pp. 226–231.

[15] S. H. Jakobsen and E. H. Solvang, "The Nordic 44 test network," 2018. [Online]. Available: https://figshare.com/articles/The_Nordic_44_test_Network/7464386

[16] C. Böhm, R. Noll, C. Plant, and B. Wackersreuther, "Density-based clustering using graphics processors," in *Proc. 18th ACM conference on Information and knowledge management (CIKM)*, 2009, p. 661.

[17] G. Andrade, G. Ramos, D. Madeira, R. Sachetto, R. Ferreira, and L. Rocha, "G-DBSCAN: A GPU accelerated algorithm for density-based clustering," *Procedia Computer Science*, vol. 18, pp. 369–378, 2013.

Paper III

The paper **"Estimation of oscillatory mode activity from PMU measurements"** is published in the proceedings of the **2020 IEEE PES Innovative Smart Grid Technologies Europe (ISGT-Europe)** conference.

Estimation of Oscillatory Mode Activity from PMU Measurements

Hallvar Haugdal, Kjetil Uhlen
Department of Electric Power Engineering
Norwegian University of Science and Technology
Trondheim, Norway
{hallvar.haugdal, kjetil.uhlen}@ntnu.no

Daniel Müller, Hjörtur Jóhannsson
Department of Electrical Engineering
Technical University of Denmark
Kgs. Lyngby, Denmark
{danmul, hjjo}@elektro.dtu.dk

Abstract—We propose a method for estimating the activity of oscillatory modes in power systems. The frequencies and mode shapes of the modes of interest are assumed to be known beforehand, either from linear modal analysis or from empirical mode estimation methods, and are used in combination with measurements from Phasor Measurement Units to estimate the instantaneous mode excitation in terms of amplitude and phase. The estimation is carried out using non-linear least squares to fit a set of curves to the measured data. Combining mode shapes with measured data allows the activity to be estimated from only a low number of consecutive measurement snapshots, resulting in a problem of low computational complexity that can be solved fast enough for the method to run online.

The purpose of estimating the mode activity is, firstly, to contribute to increased situational awareness and facilitate methods that build further upon this information, and secondly, to be able to synthesize signals that can serve as input to controllers for power oscillation damping. It is expected that using this excitation measure will result in a more robust controller that is less prone to disturbances and noise.

Index Terms—Empirical modal analysis, non-linear least squares, power oscillations, wide area monitoring and control

I. INTRODUCTION

Inter-area oscillations often appear in power systems consisting of areas of generation that are connected by weak interties. Increasing the intertie transfer generally reduces the damping of the oscillations [1], potentially leaving the full thermal capacity of the lines unexploited. Low-damped or negatively damped oscillations might also appear when the system is operated in a critical state, e.g. following severe faults or disturbances [2]. This motivates the development of monitoring applications that increase our knowledge about oscillatory modes of the power system. More accurate information allows the system to be operated closer to the stability limits, and enables us to take proper action in case of critical, growing oscillations.

Further measures can be implemented to ensure secure operation of the grid; A Power Oscillation Damper (POD) can be introduced, whose basic functioning is to measure the activity of oscillatory modes, and to apply control action attempting to damp the oscillations. The control action could for instance be applied through generator excitation systems, SVCs or HVDC links.

To measure the activity of the oscillatory mode, serving as the input to the controller, the voltage angle can be measured using a Phasor Measurement Unit (PMU) at a location where the oscillatory mode to be damped has a high observability. The observability of a mode at a specific location can be obtained by performing an offline model based modal analysis. The right eigenvectors resulting from the modal analysis determine the relative amplitude and phase of the oscillatory mode within a measurement, often referred to as the observability mode shape. Choosing the location with the highest amplitude therefore ensures a good observability of the mode.

In [3], a Wide Area POD is described, which uses the angle difference between two widely separated locations as input to the POD, which controls the voltage setpoint of a Static VAr Compensator. In [4] a Phasor POD is described, which controls a Thyristor Controlled Series Capacitor in order to mitigate oscillations. The frequency of the particular mode to be damped is assumed to be known on beforehand in this case, and a phasor which represents the amplitude and phase of the mode is estimated and used to modulate the reactance reference of the device.

The method presented in this paper can be viewed as the first development steps towards an extended version of the Phasor POD described above. Given recent development of empirical modal analysis [5]–[9], from which estimates of mode shapes can be obtained in near real-time, we assume that not only the frequency of the mode to be damped is known, but also that the corresponding observability mode shape is prior knowledge. We further use this in combination with a high number of input measurements to estimate the mode phasors.

The scope of this paper is solely demonstrating the proposed phasor estimation method. The obvious next step, which will constitute the continuation of this work, is to use this information to synthesize control signals to be injected with a suitable phase at suitable locations to damp oscillations. Ultimately, this is expected to result in a power oscillation damper that applies control action only when all the generators involved in the observability mode shape oscillate with the particular frequency of the mode, and also with the relative phase and amplitude as determined by the mode shape.

Estimating the mode activity is carried out by generating a set of functions that represent curves one would expect to

observe given the frequency and observability mode shape of the mode. Further, non-linear least squares is used to find the amplitude and phase of the mode that best fits with the measurements.

The work presented is a continuation of previous research on power oscillation monitoring. In [8], [9], it is shown that the frequency and observability mode shape of oscillatory modes can be estimated within seconds after standing oscillations appear in measurements. This motivates the development of monitoring and control applications that make use of this information.

The current stage of development of the method is described in the succeeding sections, specifically: In Section II relevant modal analysis theory is presented, Section III presents the proposed method, Section IV presents the results obtained when testing the method on simulated data and on PMU measurements, and finally Section V and VI contains discussion and conclusions.

II. MODAL ANALYSIS

Analysing electromechanical oscillations in power systems is often approached using modal analysis on a linearized system model. The linearized state space equations, describing the dynamics of the system perturbed by small disturbances at a given operating point, can be written as [10]:

$$\Delta \dot{\mathbf{x}}(t) = \mathbf{A}\Delta \mathbf{x}(t) + \mathbf{B}\Delta \mathbf{u}(t) \tag{1}$$

$$\Delta \mathbf{y}(t) = \mathbf{C}\Delta \mathbf{x}(t) + \mathbf{D}\Delta \mathbf{u}(t) \tag{2}$$

Performing an eigendecomposition of the system matrix $\mathbf{A}$, we get a set of eigenvalues and left- and right eigenvectors. The eigenvalues characterize the modes of the system, of which the ones with a non-zero imaginary part are related to oscillatory modes. Further, the left and right eigenvectors describe controllability- and observability mode shapes for each of the modes. The time evolution of the system states can be written as a function of the modes of the system:

$$\Delta \mathbf{x}(t) = \sum_{j=1}^{n_s} \mathbf{\Phi}_j z_j(t) \tag{3}$$

Here, $\mathbf{\Phi}_j$ is the observability mode shape (right eigenvectors) of mode j, z_j is the time variation of mode j and n_s is the order of the system. For oscillatory modes, the right eigenvectors determine the amplitude and phase with which mode j is observed in the states. We can also define the mode shape describing how the modes are observed in each of the measurements:

$$\Delta \mathbf{y}(t) = \mathbf{C}\Delta \mathbf{x}(t) = \sum_{j=1}^{n_s} \mathbf{C}\mathbf{\Phi}_j z_j(t) \tag{4}$$

Assuming that the system is excited by an arbitrary input $\Delta \mathbf{u}$, the time variation of mode j can be written as [11]

$$z_j(t) = \int_0^t e^{\lambda_j(t-\tau)} \mathbf{\Psi}_j \mathbf{B}\Delta \mathbf{u}(\tau)d\tau \tag{5}$$

where λ_j and $\mathbf{\Psi}_j$ are the eigenvalue and left eigenvector corresponding to mode j. The product of left eigenvector and input matrix $\mathbf{B}$ describes how the mode j is excited by the disturbance $\Delta \mathbf{u}$ and therefore indicates the controllability of mode j by the inputs related to the disturbance.

Since the eigenvalues corresponding to oscillatory modes are complex, the series $z_j(t)$ is also complex for these modes. One can therefore describe the mode activity in terms of amplitude $|z_j(t)|$ and phase $\arg z_j(t)$. The proposed method described in the following section allows to extract this information by estimating the amplitude and phase of a given mode from PMU measurements.

III. AMPLITUDE AND PHASE ESTIMATION USING NON-LINEAR LEAST SQUARES

Applying to intuition, one could consider the following simple example: We assume a power system consisting of a number of generators divided into two main areas, where the dominant mode is the inter area mode related to oscillations between the areas. We assume that the frequency and observability mode shape of the dominant mode is available. Following a disturbance, one would from studying only a few consecutive PMU snapshots be able to say that the inter area mode was excited if the generators in the first area accelerated while those in the other area decelerated. An even clearer indicator would be that the magnitude of the acceleration of each individual generator was according to the corresponding magnitudes in the observability mode shape of the mode.

This idea forms the basis of the proposed method where we use the mode shape and a set of measurements to formulate a fitting problem that is solved using non-linear least squares minimization [12].

We start by collecting the last n voltage angle snapshots from m PMU locations in the matrix $\mathbf{Y}$ as follows:

$$\mathbf{Y} = \begin{bmatrix} \mathbf{y}_1 \\ \mathbf{y}_2 \\ \vdots \\ \mathbf{y}_m \end{bmatrix} = \begin{bmatrix} y_{11} & y_{12} & \cdots & y_{1n} \\ y_{21} & y_{22} & \cdots & y_{2n} \\ \vdots & & \ddots & \\ y_{m1} & y_{m2} & & y_{mn} \end{bmatrix} \tag{6}$$

The indexing is such that the element y_{ik} corresponds to the measurement obtained at location i at time t_k. We assume that each measurement closely resembles the state corresponding to the rotor angle of one generator. (This assumes deployment of PMUs in major substations. If necessary, the rotor angle could also be estimated based on measured voltage and current.)

We further assume that the frequency $\hat{f}_j$ of the mode is known. For the observability mode shape, we need to know the elements which correspond to the states we are measuring, i.e. the states corresponding to rotor angles. The elements of the mode shape, which are complex for oscillatory modes, can be written in terms of amplitude and angle:

$$\mathbf{C}\mathbf{\Phi}_j = \begin{bmatrix} a_{1j}\angle\delta_{1j} \\ a_{2j}\angle\delta_{2j} \\ \vdots \\ a_{mj}\angle\delta_{mj} \end{bmatrix} \tag{7}$$

In the following, we focus on only one mode and skip the mode index j. From the frequency and mode shape of the mode, we construct the following set of functions, which represent signals one would expect to observe given activity of the mode:

$$\mathbf{g}(A,\theta,t) = \begin{bmatrix} g_1(A,\theta,t) \\ g_2(A,\theta,t) \\ \vdots \\ g_m(A,\theta,t) \end{bmatrix} \qquad (8)$$

The individual functions are defined as follows:

$$g_i(A,\theta,t) = A a_i \cos\left(\omega t + \delta_i + \theta\right) \qquad (9)$$

Here, $\omega = 2\pi f$ is the angular frequency of the mode of interest.

Further, we evaluate the functions at the same time instants as the measurements in $\mathbf{Y}$ are obtained:

$$\mathbf{S}(A,\theta) = \begin{bmatrix} \mathbf{g}(A,\theta,t_1) & \mathbf{g}(A,\theta,t_2) \dots \mathbf{g}(A,\theta,t_n) \end{bmatrix} \qquad (10)$$

The matrix $\mathbf{S}$ now has the same dimension as $\mathbf{Y}$, where each element is a function that can be fitted to the corresponding measured data in $\mathbf{Y}$. The residuals are given by

$$\mathbf{R}(A,\theta) = \mathbf{Y} - \mathbf{S}(A,\theta) \qquad (11)$$

Finally, we perform a non-linear least squares minimization to find the amplitude A and angle θ that minimizes the error, given by

$$e = \sum_{i=1}^{m} \sum_{k=1}^{n} r_{ik}(A,\theta)^2 \qquad (12)$$

where $r_{ik}(A,\theta)$ denotes the elements of $\mathbf{R}(A,\theta)$.

The minimization is performed for each new PMU snapshot received at t_k, resulting in one estimate of amplitude and phase of $z(t_k)$ per time stamp.

IV. RESULTS

The above described method is tested on simulated data from the Kundur Two-Area System and on measured PMU-data from the nordic power grid.

A. Simulated data from the Kundur Two-Area System

The Kundur Two-Area system, described in [1] is often used as a benchmark system for small signal stability related methods. The system consists of four generators distributed among two areas which are connected by a relatively weak intertie. The system has three electromechanical oscillatory modes; one negatively damped interarea mode whith a frequency of $0.61\,\text{Hz}$, and two local modes with a frequency around $1\,\text{Hz}$ and a damping of about $9\,\%$.

In order to demonstrate the performance of the proposed method, a time series based on the linearized system model is generated where the modes are excited by two separate disturbances: The first disturbance occurs at $t = 1\,\text{s}$, where a step change of $0.01\,p.u.$ is applied to the voltage reference
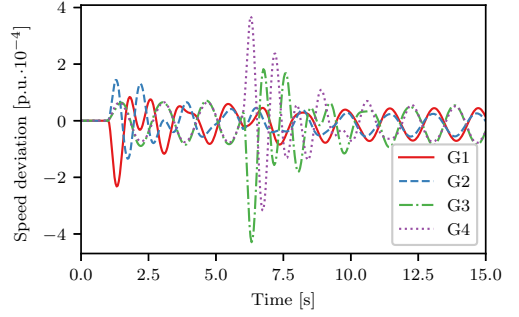
Fig. 1. The speed response obtained from the linear simulation of a model of the Kundur Two-Area System is shown.
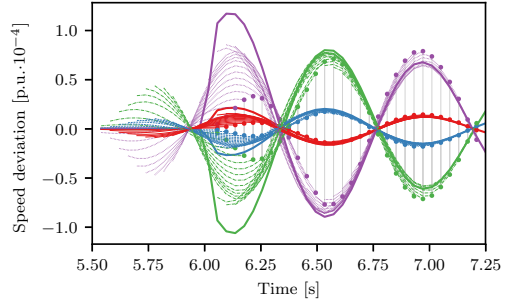
Fig. 2. The oscillations caused by the second local mode, involving G_3 & G_4, are shown (where the same colors as those in Fig. 1 are used for each generator). The four thick lines shows the oscillations for each generator computed using the linear model. The thin lines show the fitted curves for each time instant, and the markers correspond to the instantaneous estimate at that time.

of generator 1. Additionally the voltage reference of generator 3 is increased by $0.02\,p.u.$ at $t = 6\,\text{s}$.

The simulated time series is shown in Fig. 1, where the sampling frequency is $25\,\text{Hz}$. The method is applied, using 15 consecutive PMU snapshots in the curve fitting problem, resulting in matrices $\mathbf{Y}$ and $\mathbf{S}$ both having dimensions 4×15. An impression of the curve fitting is presented in Fig. 2 where the estimate of local mode 2 during the second disturbance is compared with the response of the linear system. The estimates of amplitude and phase are shown in Fig. 3, along with the mode shapes corresponding to each of the modes.

The estimation converges to the value obtained from the linearized system showing that it is possible to accurately estimate the phase and magnitude of the mode activity. As might be expected, the amplitude and phase are estimated more accurately with an increasing level of excitation. From both the linear system and the estimate it is apparent that the two disturbances affect both the amplitude and phase of all the modes.
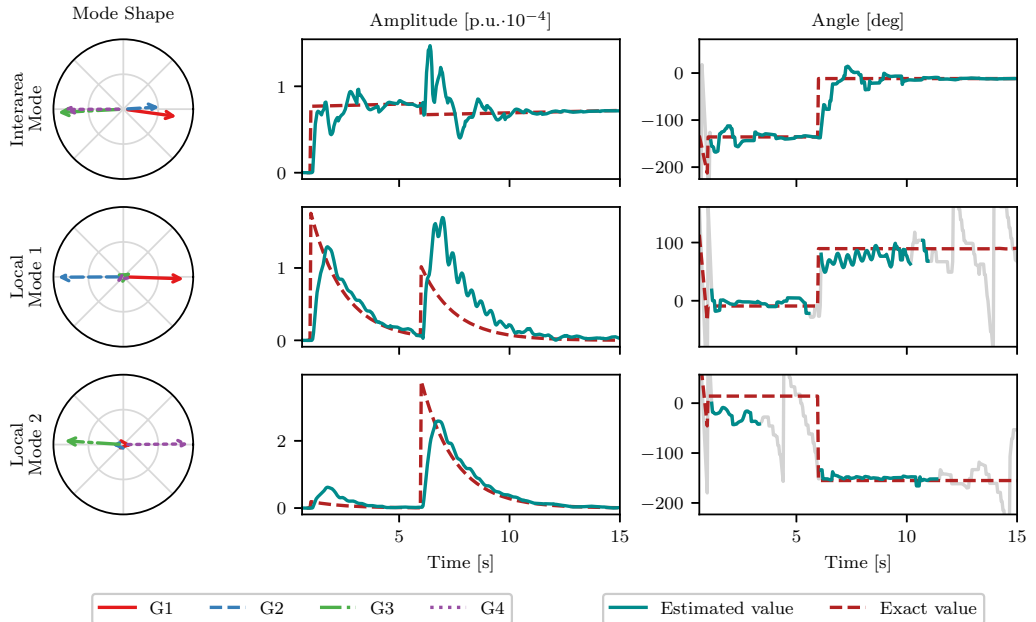
Fig. 3. The result from applying the method to simulated time series from the Kundur Two-Area System is shown. Each row corresponds to one mode, where the mode shapes (which are prior knowledge) are shown to the left. The estimated amplitude $|z_j|$ and phase $\arg z_j$ are shown in cyan for each mode in the two plots to the right, while the values from the linear model are shown in dashed red lines. The estimated phase is colored in grey in regions where the estimated amplitude of the mode is approximately zero.

B. Measured PMU-data from the Nordic Power Grid

The measured PMU-data is shown in the first plot of Fig. 4, captured with a sampling frequency of $10\,\text{Hz}$. The voltage angle is measured at seven locations distributed across Norway. The mode being analyzed describes the severe oscillations starting around $t = 280\,\text{s}$, lasting until around $t = 400\,\text{s}$. The frequency and mode shape of the oscillations are estimated beforehand using the empirical method described in [9]. The frequency of the oscillation is $1.04\,\text{Hz}$ in average, and the observability mode shape is shown in Fig. 5.

Applying the proposed method using five consecutive snapshots in the fitting problem (i.e. the matrices $\mathbf{Y}$ and $\mathbf{S}$ both have dimensions 7×5) yields the result shown in the two lower plots of Fig. 4. The second plot shows the estimated amplitude of the oscillations, while the last plot shows the estimated angle (where the regions where the amplitude is approximately zero is colored in grey).

V. DISCUSSION

The results indicate that the method provides reasonable estimates of amplitude and phase of oscillatory modes. The accuracy generally increases with the level of excitation.

From the result when testing the method on measured PMU data, two main conclusions can be drawn: Firstly, the estimated amplitude and phase appear to fit well with what one would expect by observing the measured time series. Both the amplitude and angle estimates are relatively smooth during the

course of the oscillations. This indicates that a reliable control signal can be synthesized based on these quantities. Given knowledge of the controllability mode shape, synthesized signals could be injected with a suitable phase at suitable locations to contribute to the damping of the oscillations.

Secondly, the estimated angle and amplitude contributes to situational awareness. Observing the third plot, we see that the oscillations are increasing in amplitude until about $t = 310\,\text{s}$, where they start decreasing. There is also a distinct turn in the trajectory of the angle at about the same time. The continually decreasing angle before $t = 310\,\text{s}$ indicates that the frequency of oscillations is slightly lower than the mean frequency used as input to the method, while the opposite is true for the period after $t = 310\,\text{s}$. Observing that the trajectories of both the amplitude and angle make distinct turns at the same time could indicate that some remedial action was applied that changed the operating point. The same observation is also made in [8].

One potential application building further upon the information provided by this method could be to estimate information about controllability mode shapes. From (5), we see that the activity of a mode $z_j(t)$ can be determined from convolutions of the mode impulse response and input signals. Assuming that we also measure the inputs, the result from the proposed method could be used to estimate the elements of the matrix $\mathbf{\Psi}_j \mathbf{B}$. In practice, this could be used to indicate at what locations and with which phase control signals could be injected to mitigate the oscillations, or point out locations
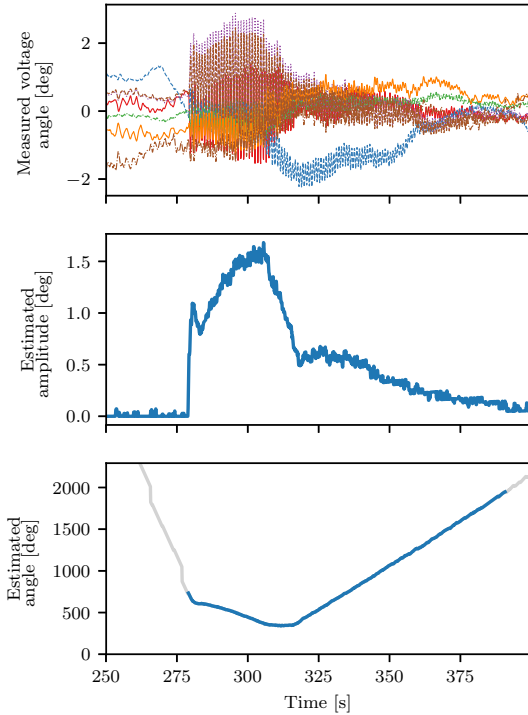
Fig. 4. The first plot shows the measured voltage angle time series. The oscillations last from about $t = 280\,\text{s}$ to $t = 380\,\text{s}$. The second and third plots show the estimated amplitude and phase, respectively. The phase is colored in grey in time regions where the amplitude is approximately zero.
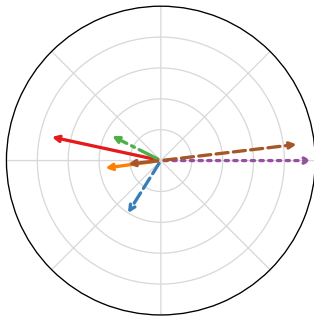
Fig. 5. The observability mode shape describing the phase and amplitude of the oscillations captured in the PMU measurements analysed in Fig. 4 is shown.

where disturbances should be minimized.

The computation time for each instantaneous estimate in the results above is in the range of milliseconds to tens of milliseconds. The current implementation uses a general non-linear least squares minimization. It is expected that significant improvement can be achieved regarding the speed by customizing the minimization algorithm, such that there should be no issue with running the method online.

It should be mentioned that accurate frequency and observability mode shapes might be difficult to obtain in real life. Assessing the performance of the method subject to inaccurate frequency and mode shape estimates will constitute an important part of the continuation of this research.

VI. CONCLUSION

The results from applying the method to simulated and measured PMU data are promising. This indicates that the fundamental idea, i.e. combining measurements with prior knowledge of oscillatory modes in the form of frequency and mode shapes, is feasible. At the current stage of development, the activity estimates appear suitable for generating control signals for damping of power oscillations, and also arguably contributes to situational awareness. Further development will reveal the potential benefit of using the output of the proposed method as input in power oscillation dampers, and the potential for estimating controllability from the mode activity.

REFERENCES

[1] M. Klein, G. J. Rogers, and P. Kundur, "A fundamental study of inter-area oscillations in power systems," *IEEE Transactions on Power Systems*, vol. 6, no. 3, pp. 914–921, 1991.

[2] D. N. Kosterev, C. W. Taylor, and W. Fellow, "Model Validation for the August 10, 1996 WSCC System Outage," *IEEE Transactions on Power Systems*, vol. 14, no. 3, pp. 967–979, 1999.

[3] E. Johansson, K. Uhlen, A. B. Leirbukt, P. Korba, J. O. Gjerde, and L. K. Vormedal, "Coordinating power oscillation damping control using wide area measurements," in *Power Systems Conference and Exposition*. IEEE/PES, 2009, pp. 1–8.

[4] L. Ängquist and C. Gama, "Damping algorithm based on phasor estimation," in *Power Engineering Society Winter Meeting*, vol. 3. IEEE, 2001, pp. 1160–1165.

[5] N. R. Chaudhuri and B. Chaudhuri, "Damping and relative mode-shape estimation in near real-time through phasor approach," *IEEE Transactions on Power Systems*, vol. 26, no. 1, pp. 364–373, 2011.

[6] L. Dosiek and J. W. Pierre, "Estimating electromechanical modes and mode shapes using the multichannel ARMAX model," *IEEE Transactions on Power Systems*, vol. 28, no. 2, pp. 1950–1959, 2013.

[7] A. R. Messina, P. Esquivel, and F. Lezama, "Wide-area PMU data monitoring using spatio-temporal statistical models," in *Power Systems Conference and Exposition*. IEEE/PES, 3 2011, pp. 1–7.

[8] H. Haugdal and K. Uhlen, "Mode Shape Estimation using Complex Principal Component Analysis and k-Means Clustering," in *2019 International Conference on Smart Grid Synchronized Measurements and Analytics (SGSMA)*. IEEE, 5 2019, pp. 1–8.

[9] ——, "Power Oscillation Monitoring using Statistical Learning Methods," in *2019 IEEE Milan PowerTech*. IEEE, 2019, pp. 1–6.

[10] P. Kundur, *Power System Stability and Control*. New York: McGraw-Hill, 1994.

[11] G. Rogers, *Power System Oscillations*. Boston, MA: Springer US, 2000.

[12] J. Nocedal and S. J. Wright, *Numerical Optimization*, ser. Springer Series in Operations Research and Financial Engineering. Springer New York, 2006.

Paper IV

The paper **"An Open Source Power System Simulator in Python for Efficient Prototyping of WAMPAC Applications"** is published in the proceedings of the **2021 IEEE Madrid PowerTech** conference.

Paper IV

An Open Source Power System Simulator in Python for Efficient Prototyping of WAMPAC Applications

Hallvar Haugdal, Kjetil Uhlen
Department of Electric Power Engineering
Norwegian University of Science and Technology
Trondheim, Norway
{hallvar.haugdal, kjetil.uhlen}@ntnu.no

Hjörtur Jóhannsson
Department of Electrical Engineering
Technical University of Denmark
Kgs. Lyngby, Denmark
hjjo@elektro.dtu.dk

Abstract—An open source software package for performing dynamic RMS simulation of small to medium-sized power systems is presented, written entirely in the Python programming language. The main objective is to facilitate fast prototyping of new wide area monitoring, control and protection applications for the future power system by enabling seamless integration with other tools available for Python in the open source community, e.g. for signal processing, artificial intelligence, communication protocols etc. The focus is thus transparency and expandability rather than computational efficiency and performance.

The main purpose of this paper, besides presenting the code and some results, is to share interesting experiences with the power system community, and thus stimulate wider use and further development. Two interesting conclusions at the current stage of development are as follows:

First, the simulation code is fast enough to emulate real-time simulation for small and medium-size grids with a time step of 5 ms, and allows for interactive feedback from the user during the simulation. Second, the simulation code can be uploaded to an online Python interpreter, edited, run and shared with anyone with a compatible internet browser. Based on this, we believe that the presented simulation code could be a valuable tool, both for researchers in early stages of prototyping real-time applications, and in the educational setting, for students developing intuition for concepts and phenomena through real-time interaction with a running power system model.

Index Terms—Dynamic RMS simulation, wide area monitoring, protection and control, real-time simulation, Python

I. INTRODUCTION

Python ranks high among the worlds most popular programming languages. Although slow compared to several other alternatives (e.g. C++), it has the advantage of being easy to learn, read and write. Development of new applications is therefore generally considered to be easier and faster in Python. Furthermore, a rich library of open source packages is available, making it straightforward to make use of artificial intelligence, communication protocols, powerful visualizations and more.

In this paper, we present an open source package for performing dynamic RMS-simulations, written entirely in Python. With this, we seek to contribute with a highly transparent, easily modifiable and expandable power system simulator that allows tight integration with powerful tools that already exist

in the open source community. We believe that open solutions are essential for developing the Wide Area Monitoring, Control and Protection (WAMPAC) applications of the future power system.

The initial motivation for development of such a package arose during research towards a controller for damping of power oscillations. The particular study required a non-linear dynamic power system simulator with detailed generator models, capable of incorporating signal processing techniques like Kalman Filters in the simulation loop, as well as the ability to perform eigenvalue analysis on linearizations of the model. This was found to be surprisingly difficult.

Using Python as a scripting language is standard functionality in many commercial tools, for instance DIgSILENT PowerFactory [1], and is well described in the documentation of the software. Including Python in the dynamic simulation loop is much more difficult, and is not standard functionality. Interfacing Python with dynamic simulations in PowerFactory can be achieved with the repository described in [2]. This functions by making PowerFactory call a dll extension a number of times during each simulation step. The dll file, compiled from C code, calls Python. This potentially expands the functionality of PowerFactory a great deal, but might to some appear complicated to use, for instance requiring some knowledge on compilation C code.

PSS/E is very well interfaced with Python through the psspy module [3]. However, small signal stability analysis requires separate modules to be installed. These modules are not that well interfaced with Python, and potentially complicates the workflow. Also, the full, linearized system matrix, which might be required in some applications, is not directly available.

Among open source alternatives for dynamic power system simulations, we have DPsim [4], which is a simulator written in highly efficient C++ code, specifically developed for real-time- and co-simulation. ANDES [5] is a Python software for symbolic modelling and numerical analysis of power systems. The Open-Instance Power System Library (OpenIPSL) [6], [7], written in the Modellica language, specifically targets unambiguous model sharing among utilities and researchers.

The above mentioned tools are powerful enough to simulate systems with thousands of buses. This is necessary for these tools to be able to perform simulations on detailed models of

real transmission grids. However, for research or educational purposes, smaller aggregated systems with tens to hundreds of buses are often used. Frequently used test systems include the Kundur Two-Area System, the IEEE 9, 14, 39 and 68-bus systems and the Nordic 32 and 44-test systems. Systems of this size can be simulated entirely in Python, without strictly requiring sophisticated performance-boosting techniques that in some cases compromise transparency and expandability.

Having developed the simulation code, the encouraging experience obtained this far regarding performance and ease of use motivates us to present the code in this paper.

The entire code is developed in Python, where the core functionality relies only on standard packages like NumPy [8] and SciPy [9]. This comes with the advantage that the software is cross platform-compatible and easily deployable, and does not require compilation. Further, the software can easily be uploaded to an online Python interpreter and shared, edited and run in the cloud, which could represent a major benefit for reproducibilty of research.

The code is available in a repository called DynPSSimPy [10] (Dynamic Power System Simulator in Python) on GitHub, released under the GPLv3 license. By following links provided on the GitHub-page, simple examples can be launched online (using Binder [11]) to demonstrate some of the basic functionality of the software.

Finally, it should be mentioned that the package is in its very early stages of development at this point, with a limited number of dynamic models and somewhat limited functionality in some areas.

The rest of this paper is structured as follows: Section II goes into detail on the core functionality; in Section III simulation results are validated against commercial simulation software; in Section IV, a simple use case where we test a simple Wide Area Protection Scheme is demonstrated; in Section V we elaborate on the real-time simulation functionality; finally, Sections VI and VII contain discussion and conclusions.

II. CORE FUNCTIONALITY

In dynamic analysis of large scale power systems, the AC electrical variables (voltages and currents) are usually represented as phasors when the focus is on electromechanical dynamics and primary control. The relevant models applied are referred to as RMS-models. The fundamental problem that needs to be solved by the RMS-model simulator is the integration of the differential equations of all the dynamic models in the system, while at the same time making sure that the algebraic equations representing the network are satisfied.

A. Dynamic RMS-simulation

The Differential Algebraic Equations (DAE) describing the dynamics of the system can be written on the form

$$\dot{\mathbf{x}} = f(\mathbf{x}, \mathbf{y})$$
$$0 = g(\mathbf{x}, \mathbf{y}) \tag{1}$$

The function f describes the differential equations for all states, while g describes the algebraic equations representing the network equations. $\mathbf{x}$ is the vector of state variables, while $\mathbf{y}$ is the vector of algebraic variables.

With the dynamic models implemented this far, the algebraic variables are constituted solely by the bus voltages of the simulated system. The set of algebraic equations is linear, and can be written on the form

$$\mathbf{Y}\mathbf{V} = \mathbf{I}_{inj}(\mathbf{x}) \tag{2}$$

where $\mathbf{Y}$ is the admittance matrix, $\mathbf{I}_{inj}(\mathbf{x})$ is the vector of current injections and $\mathbf{V} = \mathbf{y}$ the vector of bus voltages.

Solving the algebraic equations is very efficient with the system sizes considered this far (up to 45 buses), allowing us to convert the DAE system into a system of Ordinary Differential Equations (ODE) without significant deterioration of performance. First, we rewrite the algebraic equations as

$$\mathbf{y} = \mathbf{V} = \mathbf{Y}^{-1}\mathbf{I}_{inj}(\mathbf{x}) = h(\mathbf{x}) \tag{3}$$

(In practice, of course, the admittance matrix is not inverted for each time step, but rather it is solved by an efficient algorithm for sparse systems of linear equations, for instance using the function scipy.sparse.linalg.spsolve.) Further, we eliminate the algebraic variables:

$$\dot{\mathbf{x}} = f(\mathbf{x}, h(\mathbf{x})) = f(\mathbf{x}) \tag{4}$$

This system of ODEs can now be integrated with any suitable integration method, for instance the Runge-Kutta implementation found in scipy.integrate.RK45 [9].

For real-time simulation, it makes sense to use integration methods with fewer evaluations of the ODE function per step taken by the solver. This allows the step size to be decreased, which in turn results in more accurate representation of continuously changing inputs. The Euler- or Modified Euler methods, requiring one or more evaluations, are thus better alternatives than the fourth order Runge-Kutta method, which requires four evaluations per time step.

B. Initialization of dynamic simulation

To make sure that the system stays on the initial operating point after the simulation started (assuming no disturbances are applied), the system must be initialized such that all time-derivatives are equal to zero. Essentially, this means determining the state vector $\mathbf{x}_0$ that gives

$$0 = f(\mathbf{x}_0) \tag{5}$$

Initialization of the simulation can be summarized as follows:
1) Perform a Newton-Rhapson power flow calculation to determine the bus voltages and active and reactive power injections at each bus.
2) From the power flow result, determine the terminal voltage and the active and reactive power produced by each generator.
3) Perform Kron-reduction of the dynamic admittance matrix. All other buses than the generator buses can be

eliminated. However, other buses that should not be eliminated can also be specified. For instance, line outages require less computation effort if the buses of the line in question are present in the reduced system, which might be interesting when performing real-time simulations.

4) The number of states is determined, and the ordering of the state vector is determined. According to the dynamic model definitions in the model library and the number of instances of each model, the appropriate number of states is added. (For instance, for 10 generators with 6 states each, 60 states are added in the state vector.)

5) The state vector that makes all the differential equations equal to zero is found. This is done by solving the algebraic equations resulting from setting the differential equations equal to zero.

C. Modal Analysis

Modal analysis is performed by numerical linearization of the system of ODEs. We find the linearized system matrix as the Jacobian of the ODE function, as follows:

$$\mathbf{A} = \frac{\partial f(\mathbf{x})}{\partial \mathbf{x}} \qquad (6)$$

Finally, we perform an eigendecomposition of the system matrix to get the eigenvalues and eigenvectors of the system at this operating point (for instance using the function numpy.linalg.eig).

D. Dynamic models

At present, one generator model, one AVR, one GOV and one PSS model are implemented. Generator controls can be applied on arbitrary units with varying parameters. Furthermore, the software is written such that implementation of additional models is possible.

The formulation of the differential equations representing the synchronous machine is based on the formulation in [12]:

$$
\begin{aligned}
M\Delta\dot{\omega} &= P_m - P_e \\
\dot{\delta} &= \Delta\omega \\
T'_{d0}\dot{E'_q} &= E_f - E'_q - I_d(X_d - X'_d) \\
T'_{q0}\dot{E'_d} &= -E'_d + I_q(X_q - X'_q) \\
T''_{d0}\dot{E''_q} &= E'_q - E''_q - I_d(X'_d - X''_d) \\
T''_{q0}\dot{E''_d} &= E'_d - E''_d + I_q(X'_q - X''_q)
\end{aligned}
\qquad (7)
$$

Subtransient saliency is neglected, i.e. we require $X''_d = X''_q$. Interfacing each generator with the grid is achieved using the following equations:

$$
\begin{bmatrix} E''_d \\ E''_q \end{bmatrix} = \begin{bmatrix} V_d \\ V_q \end{bmatrix} + \begin{bmatrix} R & X''_q \\ X''_d & R \end{bmatrix} \begin{bmatrix} I_d \\ I_q \end{bmatrix}
\qquad (8)
$$

Subscripts d and q denote quantities in the generator reference frame. Using that $X''_d = X''_q = X''$, this can be simplified to

$$
\begin{aligned}
E'' &= E''_d + jE''_q \\
&= (V_d + jV_q) + (R + jX'')(I_d + jI_q) \\
&= V + (R + jX'')I
\end{aligned}
\qquad (9)
$$

Further, we establish the Northon Equivalent of the synchronous machine, where the current source is given by

$$I_{no} = \frac{E''}{R + jX''} \qquad (10)$$

and the shunt impedance by

$$Z_{no} = R + jX'' \qquad (11)$$

The impedances Z_{no} of each of the synchronous machines are included in the admittance matrix used during dynamic simulation, $\mathbf{Y}$ in (2), appearing as contributions on the diagonal entries. The currents I_{no} appear as contributions to the current injection vector $\mathbf{I}_{inj}(\mathbf{x})$. (Note that since E'' is referred to the generator reference frame, the current injections must be transformed to the system reference frame.)

Finally, the electrical power is given by

$$P_e = E''_d I_d + E''_q I_q \qquad (12)$$

For generator controls, the standard models SEXS for AVR, TGOV1 for turbine/governor and STAB1 for PSS are implemented, modelled after the corresponding models in DIgSILENT PowerFactory [1].

E. Implementation

Each dynamic model is defined as a class in Python. Within each class, the function for calculating the state derivatives of the dynamic model is defined. Functions for initialization and computing current injections are also implemented for models where this is required. Evaluating the complete state derivative vector in (4) is achieved by looping through the state derivative functions of all the individual dynamic models included in the power system model. For the implemented models described above, the state derivative functions make use of vectorization, which significantly improves the computational efficiency. A further increase in computational efficiency can be achieved by leveraging Just-In-Time compilation of the derivative functions of each model, available in Python using Numba [13]. This introduces some overhead, but speeds up the state derivative functions significantly once the compilation is done.

III. VALIDATION

The simulator is validated by comparing results from the Kundur Two-Area System, obtained using the presented Python package, with results obtained when simulating a model with identical parameters in DigSILENT PowerFactory. The "Standard/Detailed model 2.2" synchronous machine model is chosen for all synchronous machines in PowerFactory. This is also a sixth order model, but the differential equations are formulated using fluxes instead of voltages. Saturation is neglected, and all the loads are constant impedance loads.

Figure 1 shows results from simulating a short circuit on Generator 1 in the Kundur Two-Area System, where the results from the Python simulation are shown alongside reference results from PowerFactory. The angle, speed and subtransient d- and q-axis voltages are shown. The results are very similar in this case, substantiating the validity of the model.
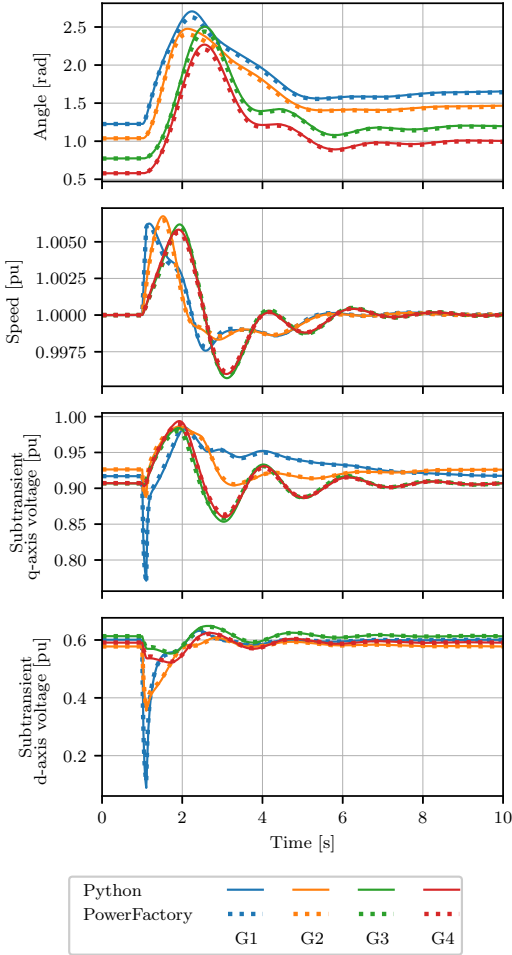
Fig. 1. The results from simulating the Kundur Two-Area System in Python are shown alongside corresponding results from a model with identical parameters simulated in PowerFactory. The transient d- and q-axis voltages are not shown, since these are not directly available from the PowerFactory simulation (since in PowerFactory the dynamic generator equations are formulated in terms of fluxes instead of voltages). The results are not identical, but very similar.

IV. SIMPLE WIDE AREA PROTECTION EXAMPLE

In this section, we present a simple use case which demonstrates how the simulator could be used for prototyping a Wide Area Protection Scheme in the Kundur Two-Area System. The protection scheme functions by measuring the electrical frequency at each of the generators. If the frequency at one or more of the generators surpasses 50.3 Hz, then Generator 3 is tripped to limit the frequency excursion. Pseudocode for this use case is shown in Fig. 2.

To test the protection scheme, a time domain simulation is

```
1  while t < t_end do
2      Perform integration step
3      x = x + Δt · f(x)
4      t = t + Δt

5      Read variables from simulation
6      f_G ← generator frequencies

7      Apply protection
8      if max(f_G) > 50.3Hz then
9          Disconnect G3
10     end
11 end
```

Fig. 2. This code example shows how a simple protection scheme can be implemented in the Kundur Two-Area System. After each simulation step (lines 2-4), the electrical frequency at each generator is read from the simulation (lines 5-6). If any of the generator frequencies are above 50.3 Hz, then Generator 3 is disconnected (lines 7-10).

performed where at $t = 1$s the largest load is decreased by 40%. The results from this simulation are shown in Fig. 3, confirming that the protection scheme functions as intended. For simplicity, we have used Euler's method in its simplest form to carry out the integration. Of course, a Runge-Kutta method could just as well be used.

This is a very simple use case, but the importance lies in the fact that lines 5-6 in Fig. 2 (for reading data/results from the simulation) and lines 7-10 (for influencing the simulation) could be replaced by virtually any other Python code. This software-in-loop setup allows very tight integration of e.g. artificial intelligence or signal processing libraries into the dynamic simulation, and facilitates efficient prototyping of new WAMPAC applications.

V. REAL-TIME SIMULATION

For smaller grids, the simulator is fast enough to perform real-time simulation with a time step of around 5 ms. To perform real-time simulation, a timer is started at the beginning of the simulation, which is used to synchronize the simulation time with the wall clock time. After each step taken by the solver, the simulator is set on hold until the next time step is due. Although Python is by no means a language tailored for real-time simulation, experience shows that the impression of continuous real-time interaction with the simulated model can be achieved.

Fig. 4 shows the amount of time spent on each time step by the solver during real-time simulation of the IEEE 39-bus system with a time step of 5 ms. All generators are modelled using the sixth order model, and all generators except the largest synchronous machine (which represents the rest of USA and Canada) are equipped with the AVR, PSS and turbine-governor models presented in section II-D. The model has a total of 123 states in this case, and is simulated using the Modified Euler method, with constant step size and one correction iteration. Numba was used for Just-In-Time compilation of the state derivative functions to increase
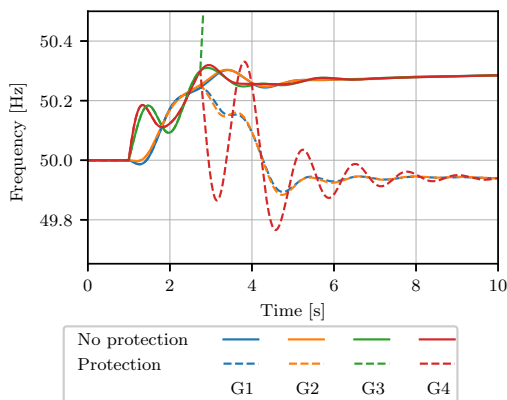
Fig. 3. The results from testing a simple protection scheme in the Kundur Two-Area System are shown. At $t = 1s$, the load in Area 2 decreases from 1767 MW to 1060 MW, causing the frequency to increase. Without the protection scheme activated, the frequency stabilizes around 50.3 Hz (shown in full lines). Activating the protection scheme causes the frequency to stabilize slightly above 49.9 Hz, which is much closer to nominal frequency (shown in dashed lines).
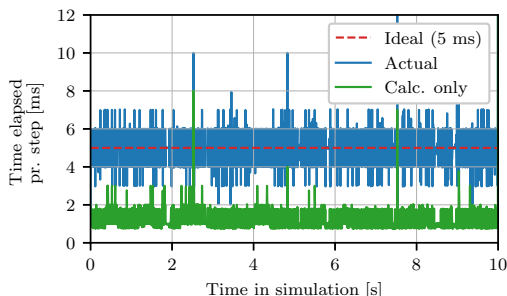
Fig. 4. The figure indicates how the synchronization between exact time and simulation time is performed during real-time simulation of the IEEE 39-bus system, with a total of 123 states. The simulation step in this case is 5 ms (red, dashed line). The actual loop time varies somewhat around the ideal loop time (blue line). It can also be seen that the time spent only on the calculation of each step (green line) is on average around 1 to 2 ms, i.e. well below 5 ms.

computational efficiency. The simulation was performed on a laptop with an Intel i7 CPU with two 2.8 GHz-cores and 16 GB RAM.

It can be seen that the calculation time (shown in green) on average is around 1 to 2 ms, which is fast enough for a time step of 5 ms (shown in red). The calculation time surpasses 5 ms in some occasions. Also, the actual time spent on each time step (shown in blue) varies approximately ±2 ms around the ideal time step (with some more extreme outliers). Over time, the simulation time is relatively well synchronized with the real world time. It should be noted that the calculation time achieved here is orders of magnitude longer than what can be achieved with, for instance, DPsim [4], which is specifically

made to handle real-time simulation.

Most parameters of the power system model can be controlled directly during real-time simulation, and changes can be made to the admittance matrix. This makes it straight-forward to, for instance, apply short circuits, line outages etc. at will during the simulation, or change voltage references or active power set-points of generators.

For visualization and interaction with the real-time simulation, a simple Graphical User Interface (GUI) is implemented using the PyQtGraph [14] library. This library allows custom GUIs to be implemented easily, with customized live plots and controls. The implemented components of the GUI are shown in Fig. 5 during real-time simulation of the IEEE 39-bus system.

VI. DISCUSSION

Based on the presented results, we elaborate on the following ideas:

A. Desktop Real-Time Simulator

It is found that real-time simulations of small to medium sized systems can be performed on an average laptop computer, without requiring specialized operative systems or hardware. For researchers, this potentially simplifies testing real-time capability and performing live demonstrations of WAMPAC applications significantly. In the educational setting, interactive real-time simulation and visualization allows students to get hands on experience with a running simulation model, which is valuable for developing intuitive understanding of different stability problems, control systems etc.

B. Reproducibilty of research

For researchers, it is often more time consuming than necessary to reproduce results from other simulation studies. Even small power system models have hundreds of parameters that need to be correct for researchers to be able to accurately reproduce results. Furthermore, the specific implementation of dynamic models might differ across simulation tools. If the entire code for reproducing results for a particular study could be made available for the community, complete with the power system model, dynamic models and the simulation code, this could significantly reduce the time spent on establishing the reference case.

The presented simulation code being developed entirely in Python (relying only on standard packages for the core functionality) comes with the advantage that it is straightforward to upload the code to an online Python interpreter. This makes it easy to share, edit and run simulations in the cloud. This could make reproducing results even easier, as the simulation required to produce the published result could be performed in the internet browser.

VII. CONCLUSION

Dynamic RMS simulations of small to medium sized grids can be performed efficiently in Python using the presented simulation software. This enables tight integration of power
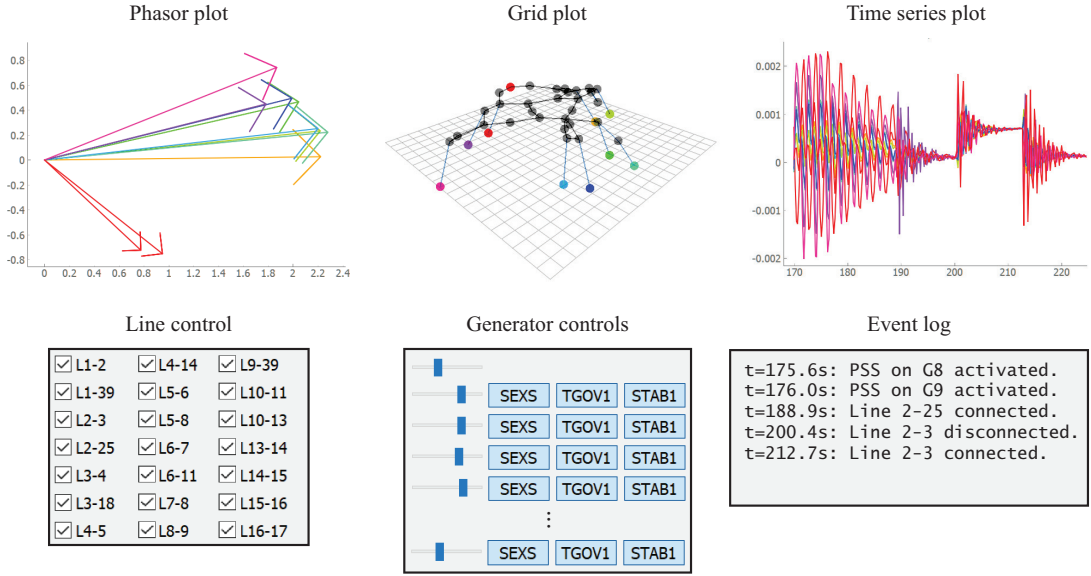
Fig. 5. The different components of the implemented GUI during real-time simulation of the IEEE 39-bus system are shown. The plots are continuously updated as the simulation develops over time. The phasor plot displays the rotor angle and excitation voltage magnitude ($E_f \angle \delta$) for each generator. The grid plot displays the grid layout, where the z-component in the diagram is set to be proportional to the voltage magnitude, and the colored nodes correspond to generator nodes. The time series plot shows curves for generator speed in this case. The shown control panels allow the user to interact with the simulation by disconnecting/connecting lines or activation/deactivation of AVR, governor or PSS on any of the generators. If the AVR is deactivated, the excitation of the generator can be controlled manually by a slider. Finally, the event log displays the events applied by the user.

system simulations with other open source packages available for Python, which is the main objective. Although transparency and expandability is prioritized over computational efficiency and performance, it is found that real-time simulation with a reasonably short time step is possible. The possibility of uploading the entire code required for reproducing results from a publication is also emphasized.

Finally, adding that the package is free, easily deployable and cross-platform compatible, we believe that it could be a valuable tool, both for researchers prototyping WAMPAC applications, and in the educational setting.

REFERENCES

[1] "PowerFactory," *DIgSILENT*. [Online]. Available: digsilent.de/en/powerfactory

[2] C. D. Lopez, M. Cvetkovic, and P. Palensky, "Enhancing PowerFactory Dynamic Models with Python for Rapid Prototyping," in *2019 IEEE 28th International Symposium on Industrial Electronics (ISIE)*, vol. 2019-June. IEEE, 6 2019, pp. 93–99. [Online]. Available: https://ieeexplore.ieee.org/document/8781432

[3] "PSS/E," *Siemens PTI*. [Online]. Available: siemens.com/pss-e

[4] M. Mirz, S. Vogel, G. Reinke, and A. Monti, "DPsim A dynamic phasor real-time simulator for power systems," *SoftwareX*, vol. 10, p. 100253, 2019. [Online]. Available: https://doi.org/10.1016/j.softx.2019.100253

[5] H. Cui, F. Li, and K. Tomsovic, "Hybrid Symbolic-Numeric Framework for Power System Modeling and Analysis," *IEEE Transactions on Power Systems*, 2020. [Online]. Available: https://ieeexplore.ieee.org/document/9169830/

[6] L. Vanfretti, T. Rabuzin, M. Baudette, and M. Murad, "iTesla Power Systems Library (iPSL): A Modelica library for phasor time-domain simulations," *SoftwareX*, vol. 5, pp. 84–88, 2016. [Online]. Available: http://dx.doi.org/10.1016/j.softx.2016.05.001

[7] M. Baudette, M. Castro, T. Rabuzin *et al.*, "OpenIPSL: Open-Instance Power System Library Update 1.5 to iTesla Power Systems Library (iPSL): A Modelica library for phasor time-domain simulations," *SoftwareX*, vol. 7, pp. 34–36, 2018. [Online]. Available: https://doi.org/10.1016/j.softx.2018.01.002

[8] C. R. Harris, K. J. Millman, S. J. van der Walt *et al.*, "Array programming with NumPy," *Nature*, vol. 585, no. 7825, pp. 357–362, 9 2020. [Online]. Available: http://www.nature.com/articles/s41586-020-2649-2

[9] P. Virtanen, R. Gommers, T. E. Oliphant *et al.*, "SciPy 1.0: fundamental algorithms for scientific computing in Python," *Nature Methods*, vol. 17, no. 3, pp. 261–272, 2020.

[10] H. Haugdal, "DynPSSimPy," *Zenodo*, 2020. [Online]. Available: http://doi.org/10.5281/zenodo.4290126

[11] M. Bussonnier, J. Forde, J. Freeman *et al.*, "Binder 2.0 - Reproducible, interactive, sharable environments for science at scale," 2018, pp. 113–120.

[12] J. Machowski, J. Bumby, and J. Bialek, *Power system dynamics: Stability and control*, 2nd ed. Wiley, 2008.

[13] S. K. Lam, A. Pitrou, and S. Seibert, "Numba: A LLVM-based Python JIT Compiler," in *Proceedings of the Second Workshop on the LLVM Compiler Infrastructure in HPC - LLVM '15*. New York, New York, USA: ACM Press, 2015, pp. 1–6. [Online]. Available: http://dl.acm.org/citation.cfm?doid=2833157.2833162

[14] L. Campagnola, "PyQtGraph - Scientific Graphics and GUI Library for Python." [Online]. Available: http://www.pyqtgraph.org/

Paper V

The paper **"Achieving increased Phasor POD performance by introducing a Control-Input Model"** was submitted to the **XXII Power Systems Computation Conference (PSCC) 2021**.

Paper V

Achieving increased Phasor POD performance by introducing a Control-Input Model

Hallvar Haugdal, Kjetil Uhlen
Department of Electric Power Engineering
Norwegian University of Science and Technology
Trondheim, Norway
{hallvar.haugdal, kjetil.uhlen}@ntnu.no

Hjörtur Jóhannsson
Department of Electrical Engineering
Technical University of Denmark
Kgs. Lyngby, Denmark
hjjo@elektro.dtu.dk

Abstract—In this paper, an enhancement to the well known Phasor Power Oscillation Damper is proposed, aiming to increase its performance. Fundamental to the functioning of this controller is the estimation of a phasor representing oscillatory behaviour at a particular frequency in a measured signal. The phasor is transformed to time domain and applied as a setpoint signal to a controllable device. The contribution in this paper specifically targets the estimation algorithm of the controller: It is found that increased estimation accuracy and thereby enhanced damping performance can be achieved by introducing a prediction-correction scheme for the estimator, in the form of a Kalman Filter. The prediction of the phasor at the next step is performed based on the control signal that is applied at the current step. This enables more precise damping of the targeted mode.

The presented results, which are obtained from simulations on a Single-Machine Infinite Bus system and the IEEE 39-Bus system, indicate that the proposed enhancement improves the performance of this type of controller.

Index Terms—Power Oscillation Damping, FACTS, Phasor Estimation, Kalman Filtering

I. INTRODUCTION

Electromechanical oscillations, although extensively investigated in the literature, is still a recurring problem in power grids around the globe [1]–[4] . Trends like increasing penetration of renewable energy sources, increased electricity demand and increasing import/export of energy between countries cause larger and less predictable fluctuations in both generation and demand. This makes it more difficult to tune and design stabilizing controllers for power oscillation damping.

Installing Power System Stabilizers on most large synchronous machines is a very cost-effective way of mitigating low damped power oscillations [5]. However, in some cases it has been beneficial to utilize separate controllable devices for efficient power oscillation damping purposes, such as Flexible AC Transmission Systems (FACTS).

FACTS devices can be installed to perform specific functions, like load flow control, enhancing the usable transfer capacity, or mitigation of power oscillations [6]. Installing new FACTS devices for the purpose of power oscillation damping is a costly investment. The value of the investment depends on the performance of the algorithms responsible for generating the damping control signal, so it is of utmost importance that the algorithms are effective as possible. This motivates the research work presented in this paper, where an enhancement to the well known Phasor Power Oscillation Damper (P-POD) is proposed.

The P-POD was introduced in [7], where it is used for mitigating inter-area oscillations by modulating a Thyristor Controlled Series Capacitor (TCSC). The P-POD functions by estimating a phasor representing the oscillations in a measured signal. The estimated phasor is phase shifted and used to generate a damping control signal, which modulates some controllable device. In [7], Low Pass Filters (LPF) are used for the estimation. Numerous variants and enhancements of the P-POD have been proposed since its introduction: In [8], a scheme for latency compensation and adaptive phase compensation is proposed, and Recursive Least Squares (RLS) is used for the estimation. Latency compensation is also the focus in [9], where the P-POD is used to control a Doubly Fed Induction Machine. In [10], a RLS estimator with variable forgetting factor is introduced, aiming to increase the phasor estimation accuracy during transient conditions.

In all the mentioned research works, the only source of information for the phasor estimator is the chosen output measurement, typically power or frequency. One additional signal that is definitely always available, which we argue should be taken into account in the estimation, is the control signal applied by the controller. We show that this can be achieved by introducing a prediction-correction scheme in the form of a Kalman Filter: In the prediction step, the amplitude and phase of the oscillations at the next time step is predicted based on the control signal applied by the controller. In the correction step, the measured signal is used to correct the predicted estimate. The expectancy is that this will facilitate damping of oscillations in a more controlled manner.

The proposed estimation scheme is developed by combining a state space representation of the linearized power system model with equations describing the P-POD estimator found in the literature. Not surprisingly, it is found that the prediction step can be performed if we assume that the transfer function residue of the targeted low damped mode is known (i.e. a single complex number), where the transfer function is from the applied control signal to the output measurement. Obtaining the required residue is not straight-forward in a large scale system, but an approximate estimate could be obtained from model based modal analysis or from a measurement-

based technique.

The motivation for the presented research is twofold: First, for systems where a sufficiently accurate residue estimate can be obtained, the performance of the P-POD is expected to increase. Second, the proposed scheme opens up for further work towards a self-correcting estimator which continually adjusts the residue estimate in order to improve predictions, allowing the P-POD to be developed into a self-tuning/adaptive controller (this possibility being explored in ongoing work).

The derivation of the enhanced P-POD is presented in Section III. In Section IV, results are presented, where the focus is on comparing the P-POD with and without the proposed enhancement. Further, the robustness of the enhanced controller against residue parameter error is investigated. Finally, discussion and conclusions are given in Sections V and VI, respectively.

II. BACKGROUND

Fundamental to the operating principle of the conventional P-POD is the separation of the measured signal $S(t)$ into an average component $\bar{S}$ and an oscillatory component, where the oscillatory component is represented by the phasor $\vec{S}$ [7]:

$$S(t) = \bar{S} + \mathrm{Re}\{\vec{S}e^{j\omega t}\} \tag{1}$$

Here, ω is the assumed frequency of the targeted low damped mode. The separation is achieved using LPFs [7], or by an estimation algorithm like RLS [8], [9], [10], or a Kalman filter [11]. Further, the control signal is generated by applying a suitable phase shift β and a gain K to the estimated phasor:

$$u(t) = \mathrm{Re}\left\{Ke^{j\beta}\left(\vec{S}e^{j\omega t}\right)\right\} \tag{2}$$

Finally, the control signal is applied by modulating the control setpoint (reference) of a controllable unit. In [7], the measured signal is the power flow in a line, and the control signal modulates the reactance reference of a TCSC installed on the line. In this case, the compensation angle β is set to 90°.

In general, assuming that a sufficiently accurate model of the system is available, the ideal phase compensation for any given measurement and control can be calculated from modal analysis. Considering a single input-single output system, the state space representation can be written as follows [12]:

$$\Delta\dot{\mathbf{x}} = \mathbf{A}\Delta\mathbf{x} + \mathbf{b}\Delta u \tag{3}$$

$$\Delta y = \mathbf{c}\Delta\mathbf{x} \tag{4}$$

Applying the modal transformation, we get the decoupled system,

$$\dot{\mathbf{z}} = \mathbf{\Lambda}\mathbf{z} + \mathbf{\Psi}\mathbf{b}\Delta u \tag{5}$$

where $\mathbf{\Lambda}$ is a diagonal matrix containing the eigenvalues of the system, i.e. $\mathbf{\Lambda} = \mathrm{diag}(\lambda_1, \lambda_2 \ldots \lambda_n)$. Electromechanical oscillations are associated with complex eigenvalues $\lambda_i = \alpha_i \pm j\omega_i$, from which the damping and frequency of oscillations can be determined. A given eigenvalue λ_i has associated right and left eigenvectors $\boldsymbol{\phi}_i$ and $\boldsymbol{\psi}_i$, respectively. From the eigenvectors,
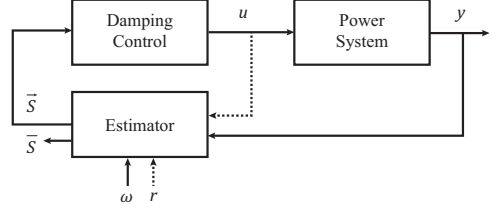
Fig. 1. The figure shows a simplified block diagram of the P-POD. From the measured signal y, the "Estimator" block produces the estimate of the phasor $\vec{S}$. The "Damping Control" block rotates the phasor according to the desired phase compensation, and generates a time-domain control signal u. The dashed arrow indicates the additional information taken into account in the phasor estimation when introducing the proposed enhancement.

the transfer function residue associated with the mode can be calculated (as defined in e.g. [12], [13]):

$$r_i = \mathbf{c}\boldsymbol{\phi}_i\boldsymbol{\psi}_i\mathbf{b} \tag{6}$$

Finally, the ideal phase compensation for the P-POD can be determined from the angle of the residue [14]:

$$\beta = 180° - \arg\{r\} \tag{7}$$

It can be shown that a marginal feedback between the output and input with this phase shift moves the eigenvalue further into the left half-plane, thus increasing the damping.

III. ENHANCING THE ESTIMATION ALGORITHM OF THE PHASOR POD

In previous research on variants of the P-POD, the only information taken into account in the estimation of the phasor is the measured signal (based on (1)). The fundamental idea of the proposed enhancement is to also take the control signal applied by the P-POD into account in the phasor estimation. Specifically, the amplitude and angle of the phasor at the next time step is predicted based on the applied control signal at the current step. A prediction-correction estimator in the form of a Kalman Filter (KF) is suitable for this purpose. Fig. 1 shows a conceptual block diagram of the P-POD, where the proposed enhancement corresponds to adding the dashed arrow (i.e. feeding the control signal u into the estimator block).

A. Phasor Estimation: Prediction-Correction

A standard Kalman Filter [15] can be given as follows,

$$\mathbf{X}_{k+1} = \mathbf{F}_k\mathbf{X}_k + \mathbf{G}_k\mathbf{u}_k + \mathbf{w}_k \tag{8}$$

$$\mathbf{Y}_k = \mathbf{H}_k\mathbf{X}_k + \mathbf{v}_k \tag{9}$$

where $\mathbf{X}_k$ is the Kalman Filter states, $\mathbf{F}_k$ is the State Transition Matrix, $\mathbf{G}_k$ is the Control-Input Model, $\mathbf{Y}_k$ is the measurement, $\mathbf{H}_k$ is the Observation Model, $\mathbf{w}_k$ is the process noise with covariance matrix $\mathbf{Q}$, and $\mathbf{v}_k$ the measurement noise with covariance matrix $\mathbf{R}$.

The Observation Model $\mathbf{H}_k$ relates the measurement to the states of the filter. The measurement is given by (1), which can be written as follows:

$$
\begin{aligned}
S_k &= \bar{S}_k + \mathrm{Re}\{\vec{S}_k e^{j\omega t}\} \\
&= \bar{S}_k + D_k \cos \omega t - Q_k \sin \omega t \\
&= \underbrace{\begin{bmatrix} 1 & \cos \omega t & -\sin \omega t \end{bmatrix}}_{\mathbf{H}_k} \begin{bmatrix} \bar{S}_k \\ D_k \\ Q_k \end{bmatrix}
\end{aligned}
\tag{10}
$$

This determines the observation model $\mathbf{H}_k$ for the Kalman filter, as indicated, where the states are given by $\mathbf{X}_k = \begin{bmatrix} \bar{S}_k, & D_k, & Q_k \end{bmatrix}^{\mathsf{T}}$, and the measurement by $\mathbf{Y}_k = S_k$.

To determine the State Transition Matrix $\mathbf{F}_k$ and the Control-Input Matrix $\mathbf{G}_k$, we start by investigating how the phasor relates to the State Space representation of the linearized power system model given by (3), (4) and (5). Assuming that mode m is the dominant oscillatory mode, the phasor we are attempting to estimate can be written as

$$
\vec{S} e^{j\omega_m t} = C z_m
\tag{11}
$$

where C is a complex number determining the amplitude and phase of the oscillation in the measurement, relative to the modal response z_m. To determine C we relate the measured signal S in (1) to the linearized system in (4):

$$
\begin{aligned}
S(t) = y(t) &= y_0 + \Delta y \\
\bar{S} + \mathrm{Re}\{\vec{S} e^{j\omega t}\} &= y_0 + \mathbf{c} \Delta \mathbf{x} \\
&= y_0 + \mathbf{c} \cdot \boldsymbol{\Phi} \mathbf{z} \\
&= y_0 + \mathbf{c} \cdot \sum_{j \in \mathbb{A}} \boldsymbol{\phi}_j z_j
\end{aligned}
\tag{12}
$$

Here, we have used that $y(t) = y_0 + \Delta y$, and $\Delta \mathbf{x} = \boldsymbol{\Phi} \mathbf{z}$, where $\boldsymbol{\Phi}$ is the matrix of right eigenvectors. $\boldsymbol{\phi}_j$ is the right eigenvector (of dimension $n \times 1$, where n is the order of the system) corresponding to mode j. $\mathbb{A}$ is the set of indices of all modes (i.e. $\mathbb{A} = \{1 \dots n\}$). Introducing the sets $\mathbb{M} = \{m, \bar{m}\}$ (where $\bar{m}$ is the index of the complex conjugate of mode m) and $\mathbb{A}' = \mathbb{A} - \mathbb{M}$ allows us to separate out the terms associated with the targeted oscillations from the sum:

$$
\bar{S} + \mathrm{Re}\{\vec{S} e^{j\omega t}\} = y_0 + \mathbf{c} \cdot \left[\left(\sum_{j \in \mathbb{A}'} \boldsymbol{\phi}_j z_j \right) + \boldsymbol{\phi}_m z_m + \boldsymbol{\phi}_{\bar{m}} z_{\bar{m}} \right]
\tag{13}
$$

We would like to capture oscillations associated with mode m with the phasor, so we assemble terms as follows:

$$
\mathrm{Re}\{\vec{S} e^{j\omega t}\} = 2\mathbf{c} \cdot \mathrm{Re}\{\boldsymbol{\phi}_m z_m\}
\tag{14}
$$

$$
\bar{S} = y_0 + \mathbf{c} \cdot \sum_{j \in \mathbb{A}'} \boldsymbol{\phi}_j z_j
\tag{15}
$$

As shown in the second equation, the remaining terms not associated with the targeted oscillations are collected in the average $\bar{S}$. Combining (11) and (14), we see that

$$
\vec{S} e^{j\omega t} = 2\mathbf{c} \boldsymbol{\phi}_m z_m
\tag{16}
$$

We now have an expression relating the phasor $\vec{S}$ to the modal response z_m, which can be combined with the solution of the decoupled state space system. The decoupled, discretized system can be written as follows:

$$
\mathbf{z}_{k+1} = e^{\boldsymbol{\Lambda} \Delta t} \mathbf{z}_k + \boldsymbol{\Lambda}^{-1} \left(e^{\boldsymbol{\Lambda} \Delta t} - \mathbf{I} \right) (\boldsymbol{\Psi} \mathbf{b}) \Delta u_k
\tag{17}
$$

Here, the subscript k denotes the time step, and $\boldsymbol{\Psi}$ is the matrix of left eigenvectors. In the decoupled system, we can consider mode m independently:

$$
z_{m,k+1} = e^{\lambda_m \Delta t} z_{m,k} + \frac{\boldsymbol{\psi}_m \mathbf{b}}{\lambda_m} \left(e^{\lambda_m \Delta t} - 1 \right) \Delta u_k
\tag{18}
$$

Here, $\boldsymbol{\psi}_m$ is the the left eigenvector (of dimension $1 \times n$) corresponding to the low damped mode. Since the damping is low it can be assumed that the real part of the eigenvalue is zero, i.e. $\lambda_m = j\omega_m$. In the following, since we are focusing on a single mode only, we skip the index m (i.e $z = z_m$, $\boldsymbol{\phi} = \boldsymbol{\phi}_m$, $\boldsymbol{\psi} = \boldsymbol{\psi}_m$, $\omega = \omega_m$). We introduce discrete notation also in (16):

$$
\vec{S}(t) e^{j\omega t} = 2\mathbf{c} \boldsymbol{\phi} z(t) \Leftrightarrow \vec{S}_k e^{j\omega t} = 2\mathbf{c} \boldsymbol{\phi} z_k
\tag{19}
$$

Here, and in the following, $t = t_k$. Combining (18) and (19) gives:

$$
\vec{S}_{k+1} e^{j\omega(t+\Delta t)} = e^{j\omega \Delta t} \vec{S}_k e^{j\omega t} + \frac{2\mathbf{c} \boldsymbol{\phi} \boldsymbol{\psi} \mathbf{b}}{\lambda} \left(e^{\omega \Delta t} - 1 \right) \Delta u_k
\tag{20}
$$

This expression can be written on the form

$$
\vec{S}_{k+1} = \vec{S}_k + r \left(g(t) - jh(t) \right) \Delta u_k
\tag{21}
$$

where we have introduced the residue $r = \mathbf{c} \boldsymbol{\phi} \boldsymbol{\psi} \mathbf{b}$ and defined the functions

$$
g(t) = \frac{2}{\omega} \Big[-\sin(\omega t) + \sin(\omega(t + \Delta t)) \Big]
\tag{22}
$$

$$
h(t) = \frac{2}{\omega} \Big[\cos(\omega t) - \cos(\omega(t + \Delta t)) \Big]
\tag{23}
$$

Further, we define the real and imaginary components of the residue:

$$
r = U + jV
\tag{24}
$$

Finally, we arrive at the prediction equations for the real and imaginary components of the phasor:

$$
D_{k+1} = D_k + (Ug(t) + Vh(t)) \Delta u_k
\tag{25}
$$

$$
Q_{k+1} = Q_k + (-Uh(t) + Vg(t)) \Delta u_k
\tag{26}
$$

The two equations (25) and (26) are used to predict the states of the filter at the next time step. For the average $\bar{S}_k$ we have no model (which does not require us to know the complete system model), so the best prediction is that the average remains unchanged, i.e. $\bar{S}_{k+1} = \bar{S}_k$. The prediction model on the form given by (8) becomes as follows:

$$
\begin{bmatrix} \bar{S}_{k+1} \\ D_{k+1} \\ Q_{k+1} \end{bmatrix} = \underbrace{\begin{bmatrix} 1 & & \\ & 1 & \\ & & 1 \end{bmatrix}}_{\mathbf{F}_k} \begin{bmatrix} \bar{S}_k \\ D_k \\ Q_k \end{bmatrix} + \underbrace{\begin{bmatrix} 0 \\ Ug(t) + Vh(t) \\ -Uh(t) + Vg(t) \end{bmatrix}}_{\mathbf{G}_k} u_k
\tag{27}
$$

This determines the State Transition Model $\mathbf{F}_k$ and the Control-Input Model $\mathbf{G}_k$. $\mathbf{G}_k$ is a function of time, and needs to be recalculated for each time step.

To summarize: The Kalman filter as the P-POD estimator is given by the Observation Model in (10) and the State Transition- and Control-Input Model in (27). The required parameters for the filter are the frequency of the targeted mode ω (in rad/s) and the residue $r = U + jV$. The frequency of the mode is easy to obtain, while the residue can be obtained either from modal analysis or from a measurement-based technique.

B. Kalman Filter-based estimator vs Low Pass Filter- or Recursive Least Squares-based estimator

In [7], where the P-POD was first presented, the phasor estimation is carried out using LPFs. For estimating a 0.2 Hz phasor, a cut-off frequency of 0.06 Hz is used for the filters, and in general a cut-off frequency of 0.2 to 0.5 times the targeted frequency is advised. A higher cut-off permits faster fluctuations in the estimated average and phasor components, while a lower cut-off gives a slower response.

The principal difference between the proposed phasor estimator given by (27) and previous LPF- or RLS-based variants is the control-input model $\mathbf{G_k}$. If no control action is applied, or if the residue estimate is zero, the Kalman Filter-based estimator is expected to behave similarly as the LPF- or RLS-based estimator. However, this requires that the Kalman Filter covariances are tuned properly. A starting point for the tuning of the Kalman filter can be obtained by comparing the response of the Kalman filter-based estimator with the LPF-based estimator. To achieve similar performance, the comparison is carried out without applying damping control (thus eliminating the effect of the Control-Input Model $\mathbf{G}_k$). By trial and error it is found that very similar performance is achieved with the two estimators when using the following covariance matrices:

$$\mathbf{R} = 1, \quad \mathbf{Q} = (2\pi f \cdot \Delta t \cdot k_c)^2 \cdot \mathbf{I}_3 \qquad (28)$$

Here, Δt is the time step, f is the mode frequency and k_c is the ratio of the LPF cut-off frequency to the mode frequency (typically in the range 0.2 to 0.5, as mentioned). This similarity is present also when varying the targeted mode frequency f, the time step Δt or the cut-off frequency to mode frequency ratio k_c. Multiplying both covariance matrices $\mathbf{R}$ and $\mathbf{Q}$ by the same factor does not affect the performanc.

This is a good starting point for tuning of the Kalman filter. Similarly as with the LPF-based P-POD estimator, as discussed above, the Kalman filter-based estimator can be tuned by specifying the time step, the frequency of the targeted mode and selecting a value for k_c in the range 0.2 to 0.5. Again, higher values allow faster fluctuations, while lower values result in a slower response.

For the initial conditions for the Estimate Covariance Matrix, commonly denoted by $\mathbf{P}_0$, higher values causes quicker convergence, but could lead to erratic control actions imme-

diately after starting the estimator. Here, we have initialized this matrix as follows:

$$\mathbf{P}_0 = 10^4 \cdot 2\pi f \cdot \Delta t \cdot k_c \cdot \mathbf{I}_3 \qquad (29)$$

Experience indicates that this choice does not affect results to a great deal, except at the first few hundreds of milliseconds of the simulation.

IV. RESULTS

In this section, the focus is comparing the performance of the P-POD *with* and *without* the proposed enhancement. To emphasize the performance advantage of introducing the proposed enhancement, the P-POD in its simplest form is considered. Frequency correction or other enhancements found in the literature, like adaptive forgetting factor, adaptive phase compensation, latency compensation etc. are not considered. It should be mentioned, however, that most, if not all of these enhancements are compatible with the proposed enhancement.

In the following, the conventional LPF- or RLS-based P-POD, without a Control-Input Model, is considered as the reference case, and is referred to as P-POD-0. The enhanced P-POD, with the proposed Control-Input Model (CIM), is referred to as P-POD-CIM.

As mentioned in [7], the main motivation for installing FACTS devices is the mitigation of severe oscillations following major disturbances. Therefore, controllers are tested on standing oscillations or low damped ringdowns, rather than e.g. using random load variations for exciting the system.

All simulations are carried out in Python using a simulation package described in [16], which was developed specifically for research work towards enhancing the P-POD. Generators are represented by 6th order generator model given in [5], and all currents and voltages are represented by phasors. The TCSC is modelled as described in [17]. Integration of differential equations is performed with a constant time step size of 5 ms using the Modified Euler method with one correction iteration. The Kalman Filters are updated every 20 ms.

A. Single-Machine Infinite Bus

The synchronous machine parameters are based on the case described in [12, p. 752], but leakage reactance, armature resistance and saturation are neglected. The machine is equipped with a simple excitation system (AVR model SEXS). The P-POD measures the generator speed deviation, and modulates the reactance reference of a TCSC installed on the line connecting the synchronous machine and the infinite bus. Following the example established in [18], the TCSC has a steady state compensation of 10%, and minimum and maximum compensation limits of 1% and 50%, respectively. The simulated event is a short circuit with a clearing time of 50 ms applied on the terminals of the synchronous machine.

Through modal analysis on the linearized model, it is found that this system has an unstable electromechanical eigenvalue with a frequency of 1.01 Hz and damping of -2.09%. The residue corresponding to the measurement,
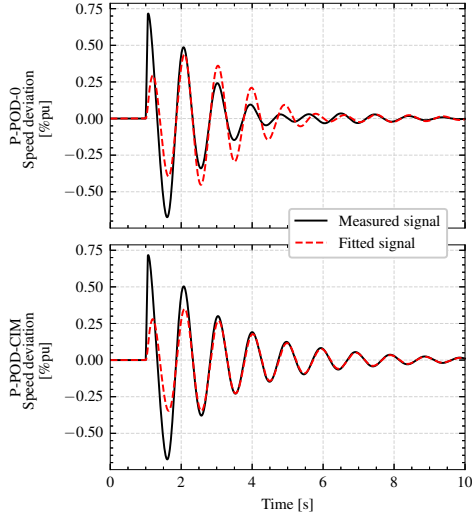
Fig. 2. The figure shows the results from testing the P-POD-0 (upper plot) and the P-POD-CIM (lower plot) on the Single-Machine Infinite Bus-system. The measured signal is shown along the estimated oscillations, revealing that the accuracy is higher with the P-POD-CIM.

control actuator and mode is $r = 0.036\angle158°$, from which the phase compensation is determined (according to (7)), i.e. $\beta = 180° - 158° = 22°$. The residue also determines the coefficients U and V in (27).

1) Comparison - Equal gain: Fig. 2 shows the results from two simulations performed on the above described system, where the P-POD-0 (upper) and the P-POD-CIM (lower) are used to generate the damping signal. The gain used in both cases is 15. The fitted signals are shown along the measured signals, and comparing the two plots shows that a more accurate fit is achieved with the P-POD-CIM. The two cases can be compared in terms of control cost C and performance P, which can be defined as follows:

$$C = \sqrt{\sum_{k=0}^{N-1} u_k^2}, \quad P = \left(\sqrt{\sum_{k=0}^{N-1} \Delta x_k^2} \right)^{-1} \quad (30)$$

where N is the number of time steps, u_k is the control action, Δx_k is the generator speed deviation and k is the time step. Both the cost ($\approx 22\%$) and the performance ($\approx 7\%$) are higher with the P-POD-0 than with the P-POD-CIM. However, for a fair comparison, the gain should be adjusted such that the control cost is the same in the two cases.

2) Comparison - Varying gain: To compare the P-POD-0 and the P-POD-CIM on equal terms, the same two simulations are performed for a range of gains between 0 and 100. The cost and performance are calculated using (30), and plotted in Fig. 3. This result clearly shows that for the same control cost, the P-POD-CIM performs better than the P-POD-0.
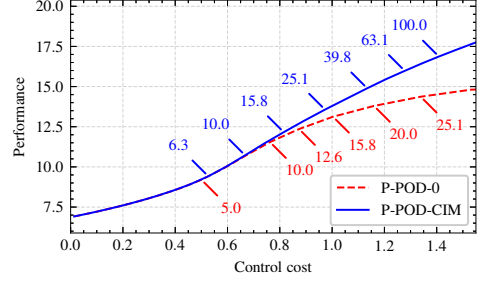
Fig. 3. The performance and control cost for varying gains are shown for the P-POD-0 and the P-POD-CIM. The gain is indicated along the curves. The result indicates that the P-POD-CIM has a higher performance than the P-POD-0 for the same control cost.
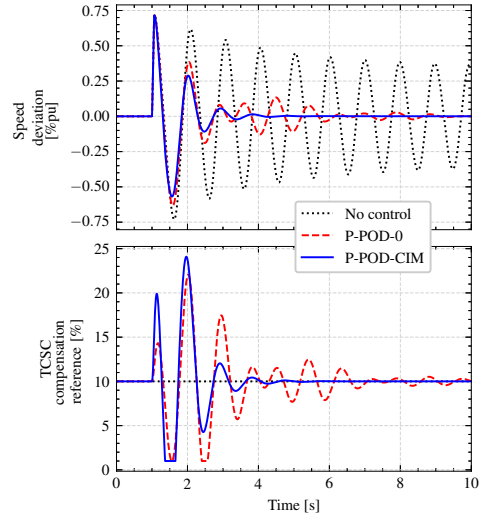
Fig. 4. A comparison of three cases on the Single-Machine Infinite Bus system shown: No control, P-POD-0 and P-POD-CIM. The gains are adjusted so the control cost is about the same in the two cases with control (28 and 100 respectively). In both cases with control the oscillations are stabilized, but the case with P-POD-CIM is clearly preferable.

3) Comparison - Equal cost: From Fig. 3, it is observed that the control cost is approximately the same when the P-POD-0 is applied with a gain slightly above 25, and the P-POD-CIM is applied with a gain of 100. Fig. 4 shows a comparison of the two controls under these circumstances (the actual gain used for the P-POD-0 is 28, resulting in a 1% higher control cost for the P-POD-0 than for the P-POD-CIM). For reference, the unregulated system is also shown, which exhibits standing oscillations. The performance is 15% better for the P-POD-CIM in this case. Also, looking at the curves, it is clear that the P-POD-CIM is preferable to the P-POD-0.

B. Effect of Residue Parameter Error

The above results indicates that the P-POD-CIM provides a more effective damping control signal than the P-POD-0,
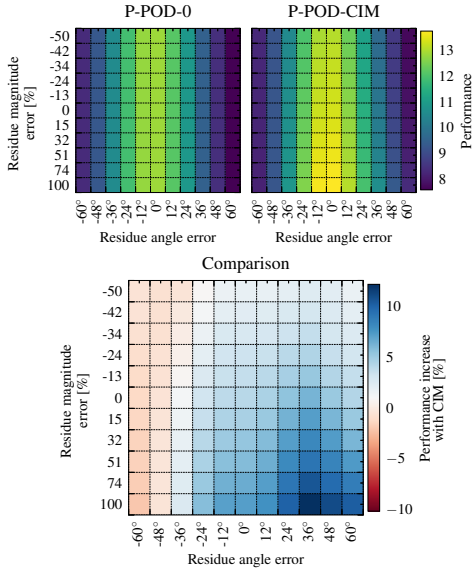
Fig. 5. The figure shows a performance comparison of the P-POD-0 and the P-POD-CIM, operating with non-optimal phase compensation and inaccurate Control-Input Model. The performance of the P-POD-0 is shown to the upper left, and the P-POD-CIM to the upper right. The control cost required to achieve the given performance is equal in all cases. The percentage-wise performance advantage is shown in the lower plot.

provided accurate knowledge of the required residue. However, an accurate residue value might not be straightforward to obtain in practice. Furthermore, the residue will likely change with changing operating conditions. An important next step in the analysis is therefore to investigate how an inaccurate residue affects the performance of the P-POD-CIM.

Assuming that some inaccurate residue estimate is provided, either from model based modal analysis or from a measurement-based method, the goal is to assess whether the P-POD-0 or the P-POD-CIM will perform better. Again, to make a comparison on equal terms, the performance of the controllers should be compared at the same cost. However, instead of looking at the full curve, as in Fig. 3, one specific control cost is chosen where the performance is evaluated.

The same system and scenario is analysed for various test residues. The test residues are generated by scaling and/or rotating the exact residue. Scaling values are chosen between 0.5 and 2, and rotation angles between $-60°$ and $+60°$. This results in a 2D-grid of test residues.

For each test residue, a number of simulations with varying gains are simulated, both with the P-POD-0 and the P-POD-CIM (similarly as in Fig. 3). For the P-POD-0, the phase compensation β is determined from the residue, and for the P-POD-CIM, the residue determines both the phase compensation β and the parameters U and V. Further, the performance achieved at a specific control cost is found by interpolation (for example, considering Fig. 2, which corresponds to zero residue
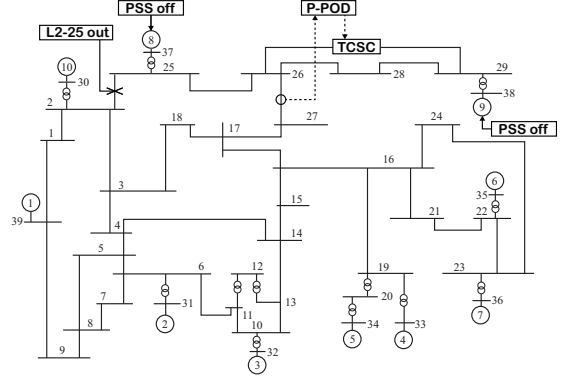
Fig. 6. The IEEE 39 bus system is shown. The P-POD measures the power flow in the line between buses 26 and 27, and modualtes the reactance reference for the TCSC installed on the line between buses 26 and 29.

error, the performance achieved at control cost 1.0 is about 13.7 for P-POD-CIM, and about 13.1 for P-POD-0). Finally, the percentage improvement of the P-POD-CIM relative to the P-POD-0 can be found by $(P_{CIM} - P_0)/P_{CIM} \cdot 100\%$.

The result from the above procedure is presented in Fig. 5. The plot to the upper left shows the performance achieved with the P-POD-0. Since the phase compensation for the P-POD-0 is chosen based on the residue angle, the performance varies with residue angle error. As expected, the performance is maximised when β is chosen according to (7). The residue magnitude does not affect the performance of the P-POD-0.

For the P-POD-CIM, shown in the upper right plot, the performance varies both with angle error and magnitude error. Interestingly, the performance increases when the magnitude of the test residue is larger than the exact residue.

The lower plot indicates that the performance achieved with the P-POD-CIM is higher than that achieved with the P-POD-0 for test residues within a deviation of $-24°$ and $+60°$ from the exact residue.

C. Application to the IEEE 39-Bus System

A final comparison of the P-POD with and without Control-Input Model is made based on simulations on the IEEE 39 Bus System [19], which is a significantly larger and more complex system than the Single-Machine Infinite Bus system. This system consists of 39 buses and 10 generators. All generators except the large machine (generator 1) representing the rest of USA and Canada are equipped with AVR, turbine-governor and PSS controls. A TCSC is installed on the line between buses 26 and 29, which is modulated by the P-POD. The input measurement for the P-POD is the active power flow in the line between buses 26 and 27, and the gain is 20. An unstable operating condition is provoked by disconnecting the line between buses 2 and 25 and deactivating the stabilizers on generators 8 and 9. By modal analysis it is found that the system is unstable with a 0.44 Hz mode with zero damping.

The simulated event is a short-circuit on bus 2, with a clearing time of 50 ms. The result in Fig. 7 shows that
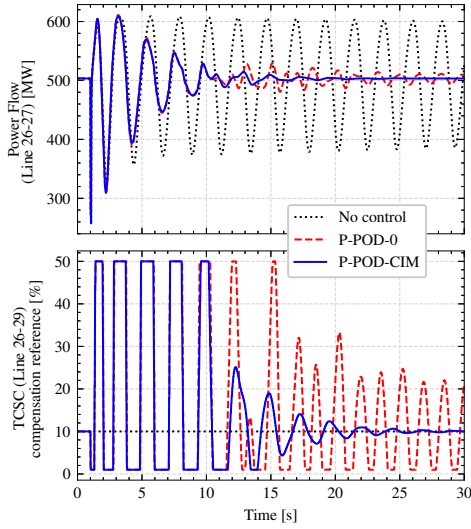
Fig. 7. The performance of the P-POD-0 is compared with the P-POD-CIM on the IEEE 39 bus system. The performance of the P-POD-CIM is superior in this case.

only the P-POD-CIM performs satisfactorily. The P-POD-0 applies unwanted control action after the targeted oscillations have died out. It should be mentioned that for lower gains both controllers perform similarly, but this result indicates that a higher gain is permitted with the P-POD-CIM without producing unwanted effects.

V. Discussion

Three important conclusions can be drawn based on the presented results: First, the results indicate that the proposed enhancement to the P-POD increases the damping performance of the controller. This is as expected, given that more information is taken into account in the phasor estimation, and that more knowledge of the system is required (in the form of the transfer function residue). Second, with the proposed enhancement, higher gains are permitted before the controller produces unwanted effects. Third, the enhanced estimator is robust against residue parameter error. This is important, since acquiring an accurate estimate of the required transfer function residue might not be straightforward.

An interesting possibility that opens up with the introduction of the proposed prediction-correction estimator scheme, is to develop the P-POD into an adaptive P-POD: Multiple Kalman filter-based P-POD estimators could be running in parallel, each making predictions based on a specific, assigned residue. Estimators with a high prediction accuracy would indicate that the corresponding residue was close to the actual residue, and vice versa for estimators with a low prediction accuracy. The phase compensation could then be adjusted according to the most accurate estimators, resulting in an adaptive/self-tuning P-POD responding to changing operating conditions. This is the topic of further research.

Finally, it should be mentioned that there are no expected challenges with running the enhanced P-POD in real-time. This is also verified by testing the controller in a real-time simulation environment.

VI. Conclusion

An enhancement to the Phasor Power Oscillation Damper has been presented. The results indicate that the performance of this type of controllers can be improved with the proposed solution, based on analysis both for a Single-Machine Infinite Bus system and for the IEEE 39-Bus System. It is also found that the controller is robust against residue parameter error. Finally, the presented theory lays the foundation for developing the P-POD into an adaptive controller for mitigating power oscillations under changing operating conditions.

References

[1] D. N. Kosterev, C. W. Taylor, and W. Fellow, "Model Validation for the August 10, 1996 WSCC System Outage," *IEEE Transactions on Power Systems*, vol. 14, no. 3, pp. 967–979, 1999.

[2] ENTSO-E SubGroup System Protection and Dynamics, "Analysis of CE Inter-Area Oscillations of 19 and 24 February 2011," Tech. Rep. February, 2011.

[3] ——, "Analysis of CE Inter-Area Oscillations of 1st December 2016," Tech. Rep. December, 2017.

[4] ——, "Oscillation Event 03.12.2017," Tech. Rep. March, 2018.

[5] J. Machowski, J. Bumby, and J. Bialek, *Power system dynamics: Stability and control*, 2nd ed. Wiley, 2008.

[6] N. G. Hingorani and L. Gyugyi, *Understanding FACTS: Concepts and technology of flexible ac transmission systems*. IEEE, 1999. [Online]. Available: http://ieeexplore.ieee.org/xpl/bkabstractplus.jsp?bkn=5264253

[7] L. Ängquist and C. Gama, "Damping algorithm based on phasor estimation," in *IEEE Power Engineering Society Winter Meeting*, vol. 3, 2001, pp. 1160–1165.

[8] N. R. Chaudhuri, S. Ray, R. Majumder, and B. Chaudhuri, "A new approach to continuous latency compensation with adaptive phasor power oscillation damping controller (POD)," *IEEE Transactions on Power Systems*, vol. 25, no. 2, pp. 939–946, 2010.

[9] S. S. Yu, T. K. Chau, T. Fernando, and H. H. C. Iu, "An Enhanced Adaptive Phasor Power Oscillation Damping Approach with Latency Compensation for Modern Power Systems," *IEEE Transactions on Power Systems*, vol. 33, no. 4, pp. 4285–4296, 2018.

[10] M. Beza and M. Bongiorno, "A Modified RLS Algorithm for Online Estimation of Low-Frequency Oscillations in Power Systems," *IEEE Transactions on Power Systems*, vol. 31, no. 3, pp. 1703–1714, 2016.

[11] N. R. Chaudhuri and B. Chaudhuri, "Damping and relative mode-shape estimation in near real-time through phasor approach," *IEEE Transactions on Power Systems*, vol. 26, no. 1, pp. 364–373, 2011.

[12] P. Kundur, *Power System Stability and Control*. New York: McGraw-Hill, 1994.

[13] G. Rogers, *Power System Oscillations*. Boston: Springer US, 2000.

[14] X. Yang and A. Fellachi, "Stabilization of inter area oscillation modes through excitation systems," *IEEE Transactions on Power Systems*, vol. 9, no. 1, pp. 494–502, 1994.

[15] R. G. Brown, *Introduction to random signals and applied Kalman filtering*, 4th ed. Hoboken, N.J: Wiley, 2012.

[16] H. Haugdal, "DynPSSimPy," *Zenodo*, 2020. [Online]. Available: http://doi.org/10.5281/zenodo.4290126

[17] B. Pal and B. Chaudhuri, *Robust Control in Power Systems*, ser. Power Electronics and Power Systems. Boston: Springer US, 2005. [Online]. Available: http://link.springer.com/10.1007/b136490

[18] B. Chaudhuri, R. Majumder, and B. C. Pal, "Application of multiple-model adaptive control strategy for robust damping of interarea oscillations in power system," *IEEE Transactions on Control Systems Technology*, vol. 12, no. 5, pp. 727–736, 2004.

[19] M. A. Pai, *Energy Function Analysis for Power System Stability*. Boston, MA: Springer US, 1989. [Online]. Available: http://link.springer.com/10.1007/978-1-4613-1635-0

Paper VI

The paper **"A Novel Phasor Power Oscillation Damper with Adaptive Phase Compensation, achieved using Multiple Model Adaptive Estimation"** was submitted for publication in the journal **IEEE Transactions on Power Systems** in November 2021.

Paper VI

A Novel Phasor Power Oscillation Damper with Adaptive Phase Compensation, achieved using Multiple Model Adaptive Estimation

Hallvar Haugdal, *Student Member, IEEE,* Kjetil Uhlen, *Member, IEEE,* and Hjörtur Jóhannsson, *Member, IEEE,*

Abstract—In this paper, an adaptive version of the well known Phasor Power Oscillation Damper is presented. The proposed controller is adaptive in the sense that the phase compensation between the measured input and the applied control action is adjusted online during changing operating conditions. This is achieved through Multiple Model Adaptive Estimation, where a bank of Kalman filter estimators are run in parallel. A system model is inferred by assessing the performance of the individual filters, and used to update the tuning of the controller online.

The proposed adaptive phase compensation scheme is compared with a similar scheme found in the literature, and is found to exhibit superior performance under the tested conditions. Simulation results from the Single-Machine Infinite Bus system, Kundur's Two-Area System and the IEEE 39-Bus System demonstrate that the proposed controller is able to adjust the phase compensation in response to severe non-linear events, and to eliminate phase lag due to communication latency.

Index Terms—Phasor estimation, Kalman filtering, thyristor controlled series capacitor (TCSC), power oscillation damper (POD), multiple model adaptive estimation (MMAE), adaptive control.

I. INTRODUCTION

PROBLEMATIC electromechanical oscillations appear regularly in power systems around the world. Global trends like increasing penetration of renewable energy sources, increasing electricity demand and increasing import and export of energy between countries cause larger and less predictable fluctuations in both generation and demand. This makes it more difficult to tune and design control systems responsible for stabilizing oscillations, since stability must be ensured for a wider range of expected operating conditions. Adding that the frequency of extreme weather events is increasing due to climate change, the system must also be expected to end up in unscheduled operating points more often. Under such circumstances, for instance unusually high or low loading in combination with loss of crucial equipment or disconnection of important lines, conventional stabilizing control systems like Power System Stabilizers (PSS) might not be effective. Such circumstances resulted in unstable oscillations in the often mentioned 1996 WSCC System Outage [1], and also in more recent events in Europe, e.g. [2], [3].

H. Haugdal and K. Uhlen are with the Department of Electrical Power Engineering, Norwegian University of Science and Technology, Trondheim, Norway (e-mail: hallvar.haugdal@ntnu.no, kjetil.uhlen@ntnu.no).

H. Jóhannsson is with the Department of Electrical Engineering, Technical University of Denmark, Kgs. Lyngby 2800, Denmark (e-mail: hjjo@elektro.dtu.dk).

As a means of providing damping in situations where conventional PSS are not effective, the Phasor Power Oscillation Damper (P-POD) was introduced in [4]. Characteristic to the operation of the P-POD is that a phasor is estimated from the measured signal, representing the instantaneous phase and amplitude of power oscillations of a given frequency, and the control signal is generated by applying an appropriate phase shift to the estimated phasor. In [4], the phasor is estimated from the measured power flow on an inter-tie, and the control signal modulates the reactance setpoint of a Thyristor Controlled Series Capacitor (TCSC) installed on the line. A phase shift of 90° is used between the measured oscillations and the applied control signal.

In [5], the authors elaborate on the limitations and challenges of the original P-POD. Specifically, it is shown that a phase compensation of 90° is not necessarily optimal for the configuration in [4], and that the ideal compensation also varies with the operating conditions. It is further concluded that "an adaptive phase shift scheduling mechanism...needs to be devised".

An Adaptive P-POD (referred to as APPOD) is proposed in [6]. The main focus here is a solution to alleviate latency issues when using the P-POD in a Wide Area framework, but an adaptive phase compensation scheme is also proposed. Specifically, the phase compensation is controlled by a Proportional Integral (PI) controller driving the magnitude of oscillations towards zero. One apparent disadvantage of this scheme is that if the P-POD is not able to eliminate oscillations completely, then the integrator will continue increasing monotonically. This will cause the phase compensation to also increase, even if it was initially at the optimal value. The same adaptive phase compensation scheme is adopted in the Enhanced APPOD (EAPPOD) proposed in [7], where the damping control action is applied through a Doubly Fed Induction Machine (DFIG) in a wind power plant.

During the last decades, many innovative approaches to adaptive power oscillation damping have been proposed in the literature. In [8], a Multiple Model Adaptive Control scheme is described, which is based on tuning a bank of controllers to a bank of corresponding models describing expected operating conditions of the system. In [9], linear state feedback control is used, where the feedback gain matrix is tuned online based on an estimated dynamic system matrix. In [10], a model-free approach to power oscillation damping is described, where analytical expressions derived for a simplified model are used to tune the controller parameters when standing oscillations

occur. For the P-POD in particular, previously described adaptive functionality includes, among other, frequency correction loop [4] and increased phasor estimation accuracy during transient conditions using a recursive least squares algorithm with variable forgetting factor [11]. To the knowledge of the authors, no other *adaptive phase compensation* schemes for the P-POD are described in the literature (other than the PI-controlled phase compensation mentioned above). Thus, this is what we seek to contribute with in this paper.

In most variants of the P-POD described in the literature, the phasor estimation is carried out using Low Pass Filters or Recursive Least Squares, where the only source of information for the estimator is the chosen output measurement. In recent research, the potential benefit of including the control signal applied by the P-POD in the estimation is explored, since this information is obviously always available. In [12], this is achieved by introducing a predictor-corrector estimator in the form of a Kalman Filter; specifically, the amplitude and phase of oscillations at the next time step are predicted based on the control signal that the P-POD applies at the current step, and the measurement is used to correct the estimate. The prediction step requires a simple system model which is determined by the transfer function residue of the targeted low damped mode, where the transfer function is from the applied control signal to the output measurement.

In this paper, we make use of the predictor-corrector estimator introduced in [12] to develop the P-POD into an adaptive controller. This is achieved by introducing a Multiple Model Adaptive Estimation scheme: A number of Kalman filters are running in parallel, each making predictions based on a specific, assigned transfer function residue. By assessing the accuracy of the individual estimators, the actual value of the residue can be inferred. The phase compensation is adjusted according to the residue estimate, resulting in a P-POD with adaptive phase compensation.

The proposed adaptive P-POD is first tested on the Single-Machine Infinite Bus system, where we demonstrate the concept and investigate the expected gain in robustness and performance compared to the PI controlled phase compensation scheme used in [6] and [7]. Further, the controller is tested on Kundur's Two-Area System, demonstrating the performance during a severe non-linear event. Finally, results from the IEEE 39-Bus System shows that the controller is capable of eliminating phase lag introduced by communication latency.

The relevant background is described in Section II, the proposed MMAE scheme is developed in Section III, results are given in Section IV, before discussion and conclusions in Sections V and VI, respectively.

II. BACKGROUND

At the core of the original P-POD [4] is an estimator that decomposes the measured signal into an average component $\bar{S}$ and an oscillatory component, where the latter is represented by a phasor $\vec{S}$:

$$S(t) = \bar{S} + \mathrm{Re}\{\vec{S}e^{j\omega t}\} \quad (1)$$

Here, ω is the assumed frequency (in rad/s) of the targeted oscillatory mode. From the phasor estimate, the control signal

is generated by applying a suitable phase shift β and amplification K, and transforming to time domain:

$$u(t) = \mathrm{Re}\left\{Ke^{j\beta}\left(\vec{S}e^{j\omega t}\right)\right\} \quad (2)$$

Assuming a sufficiently accurate power system model is available, a suitable phase shift can be determined from modal analysis. The linearized system on state space form is given as follows [13]:

$$\Delta\dot{\mathbf{x}} = \mathbf{A}\Delta\mathbf{x} + \mathbf{b}\Delta u \quad (3)$$

$$\Delta y = \mathbf{c}\Delta\mathbf{x} \quad (4)$$

Performing an eigendecomposition gives the decoupled system:

$$\dot{\mathbf{z}} = \mathbf{\Lambda}\mathbf{z} + \mathbf{\Psi}\mathbf{b}\Delta u \quad (5)$$

where $\mathbf{\Lambda}$ contains the system eigenvalues on the diagonal, i.e. $\mathbf{\Lambda} = \mathrm{diag}(\lambda_1, \lambda_2 \ldots \lambda_n)$. Assuming $\lambda_m = \alpha_m + j\omega_m$ is the eigenvalue corresponding to the low damped mode, and $\boldsymbol{\psi}_m$ and $\boldsymbol{\phi}_m$ are the corresponding left and right eigenvectors, the transfer function residue of the mode is given by

$$r = \mathbf{c}\boldsymbol{\phi}_m\boldsymbol{\psi}_m\mathbf{b} \quad (6)$$

where the transfer function is, again, from the applied control signal to the output measurement. From this residue, the ideal phase compensation can be determined [14]:

$$\beta = 180° - \arg\{r\} \quad (7)$$

This phase compensation can be used directly in (2).

A. Predictor-Corrector Phasor Estimation Scheme

Using a predictor-corrector estimator in the form of a Kalman filter in a P-POD is described in [12]. The phasor at the next step is predicted based on the control signal applied at the current step, and the predicted value is corrected with the measurement. In this section, the resulting expressions from the derivations in [12] are reproduced.

Using a Kalman Filter for a single-input single-output system requires a model on the following form [15]:

$$\mathbf{X}_{k+1} = \mathbf{F}_k\mathbf{X}_k + \mathbf{G}_k u_k + \mathbf{w}_k \quad (8)$$

$$Y_k = \mathbf{H}_k\mathbf{X}_k + v_k \quad (9)$$

Here, $\mathbf{X}_k$ is the Kalman filter states, $\mathbf{F}_k$ is the State Transition Matrix, $\mathbf{G}_k$ is the Control-Input Model, Y_k is the Measurement, $\mathbf{H}_k$ is the Observation Model, $\mathbf{w}_k$ is the Process noise (with covariance matrix $\mathbf{Q}$), v_k is the Measurement noise (with variance R), and k is the time step index.

The states of the filter are chosen as $\mathbf{X}_k = \begin{bmatrix} \bar{S}_k & D_k & Q_k \end{bmatrix}^\mathsf{T}$, where $\bar{S}$ is the signal average and D_k and Q_k are the real and imaginary components of the phasor (i.e. $\vec{S} = D_k + jQ_k$). The Kalman Filter measurement is the same as the P-POD measurement, i.e. $Y_k = S_k$. As given in [12], the measurement relates to the states as follows:

$$S_k = \underbrace{\begin{bmatrix} 1 & \cos\omega t & -\sin\omega t \end{bmatrix}}_{\mathbf{H}_k} \begin{bmatrix} \bar{S}_k \\ D_k \\ Q_k \end{bmatrix} \quad (10)$$

This equation is equivalent to (1), and determines the observation model $\mathbf{H}_k$ of the Kalman filter.

Developing the prediction step (also described in [12]) is achieved by introducing the solution to the State Space formulation. The resulting State Transition Matrix $\mathbf{F}_k$ and the Control-Input Model $\mathbf{G}_k$ are as follows:

$$\begin{bmatrix} \bar{S}_{k+1} \\ D_{k+1} \\ Q_{k+1} \end{bmatrix} = \underbrace{\begin{bmatrix} 1 & & \\ & 1 & \\ & & 1 \end{bmatrix}}_{\mathbf{F}_k} \begin{bmatrix} \bar{S}_k \\ D_k \\ Q_k \end{bmatrix} + \underbrace{\begin{bmatrix} 0 \\ Ug(t) + Vh(t) \\ -Uh(t) + Vg(t) \end{bmatrix}}_{\mathbf{G}_k} u_k \quad (11)$$

The coefficients U and V are determined from the transfer function residue of the low damped mode (with index m), where the transfer function is from the applied control signal to the output measurement:

$$r = \mathbf{c}\boldsymbol{\phi}_m\boldsymbol{\psi}_m\mathbf{b} = U + jV \quad (12)$$

Further, the two time-dependent functions $g(t)$ and $h(t)$ are given by

$$g(t) = \frac{2}{\omega}\Big[-\sin(\omega t) + \sin(\omega(t + \Delta t))\Big] \quad (13)$$

$$h(t) = \frac{2}{\omega}\Big[\cos(\omega t) - \cos(\omega(t + \Delta t))\Big] \quad (14)$$

Regarding tuning of the Kalman filter in terms of covariance matrices, the following expressions are proposed in [12]:

$$R = 1, \quad \mathbf{Q} = (2\pi f \cdot \Delta t \cdot k_c)^2 \cdot \mathbf{I}_3 \quad (15)$$

Here, Δt is the time between successive filter updates, f is the frequency of the targeted mode. k_c is a chosen factor, typically in the range 0.2 to 0.5, where low values gives slower convergence of the filter states and a less responsive controller, and high values gives faster convergence but potentially a more erratic control signal.

The Kalman filter estimator on this form assumes knowledge of the frequency of the mode and the specific transfer function residue, and allows prediction of the amplitude and angle of the phasor based on the applied control signal. The next section describes use of this estimator in a MMAE scheme.

III. MULTIPLE MODEL ADAPTIVE ESTIMATION: ADAPTIVE PHASOR POD

In this section, a MMAE scheme is introduced, where a number of Kalman filters are run in parallel. Each individual filter is on the form given in the previous section, but the filters differ in that they have different Control-Input Models ($\mathbf{G}_k$). The final state estimate from the filter bank is produced by weighing the state estimates of the individual filters according to a weighting function. A block diagram describing the scheme is shown in Fig. 1.

The prediction step, as given by (11), depends on the parameters associated with the residue, i.e. U and V. The filters in the filter bank are chosen such that the Control-Input Model of each filter corresponds to one specific, assigned

Fig. 1. A block diagram of the MMAE scheme is shown. Multiple Kalman filters (KF1, KF2,...,KFn) are running in parallel. The filters estimate the phasor based on different models. The models are determined by different assigned transfer function residues. The final phasor estimate used for generating the damping control signal is generated by weighting the individual filter state estimates. Similarly, the residue estimate, from which the phase compensation of the P-POD is determined, is generated by weighting the residue values assigned to the filters. The weighting is determined by the performance of the filters.

residue. Assuming an approximate initial guess of the actual residue r_0, other variants of this residue are generated by rotation or scaling, and then one residue is assigned to each filter. In this paper, for the sake of simplicity only rotation is considered. Assuming N filters, the residues are distributed evenly around a circle with a radius determined by $|r_0|$ as follows:

$$r_i = r_0 \cdot e^{j\theta_i}, \quad \theta_i = \frac{2\pi \cdot i}{N+1}, \quad i = 1, 2, ..., N \quad (16)$$

From this, the parameters of the Control-Input Model for each filter are determined by $U_i = \operatorname{Re}\{r_i\}$ and $V_i = \operatorname{Im}\{r_i\}$. For filter i, the following model determines the prediction step:

$$\begin{bmatrix} \bar{S}_{i,k+1} \\ D_{i,k+1} \\ Q_{i,k+1} \end{bmatrix} = \begin{bmatrix} 1 & & \\ & 1 & \\ & & 1 \end{bmatrix} \begin{bmatrix} \bar{S}_{i,k} \\ D_{i,k} \\ Q_{i,k} \end{bmatrix} + \underbrace{\begin{bmatrix} 0 \\ U_ig(t) + V_ih(t) \\ -U_ih(t) + V_ig(t) \end{bmatrix}}_{\mathbf{G}_{i,k}} u_k \quad (17)$$

Due to the different residue values assigned to each filter, the performance of the filters will vary. Filters whose assigned residues are close to the actual residue will perform better, and vice versa for filters whose assigned residues are far from the actual residue. To quantify the performance of a single filter i, the residual $\varepsilon_{i,k}$ and the variance of the residual $E_{i,k}$ are introduced:

$$\varepsilon_{i,k} = Y_k - \mathbf{H}_k\mathbf{X}_{i,k} \quad (18)$$

$$E_{i,k} = \mathbf{H}_k\mathbf{P}_{i,k}\mathbf{H}_k^\mathsf{T} + R \quad (19)$$

Here, $\mathbf{P}_{i,k}$ is the Estimate Covariance Matrix. The measurement Y_k, the measurement noise variance R and the observation model $\mathbf{H}_k$ are the same for all filters in the bank. This allows the likelihood function to be calculated, which tells how likely it is that a filter is performing optimally:

$$\mathcal{L}_{i,k} = \frac{1}{\sqrt{2\pi E_{i,k}}} \exp\left[-\frac{\varepsilon_{i,k}^2}{2E_{i,k}}\right] \quad (20)$$

The weighting is determined by the likelihood functions of the filters. Initially, each filter is assigned a weight $W_{i,0} = 1/N$. Further, the filter weights are updated at each step according to the following three-step weighting scheme, inspired by the procedure in [16]:

1) Recursive update of weights:

$$W'_{i,k} = \frac{\mathcal{L}_{i,k} W_{i,k-1}}{\sum_{j=1}^{N} \mathcal{L}_{j,k} W_{j,k-1}} \qquad (21)$$

2) Bounding from zero, with minimum value δ:

$$W_{i,k} = \begin{cases} W'_{i,k} & \text{if } W_{i,k} > \delta \\ \delta & \text{if } W_{i,k} \leq \delta \end{cases} \qquad (22)$$

3) Normalization:

$$W_{i,k} = \frac{W_{i,k}}{\sum_{j=1}^{N} W_{j,k}} \qquad (23)$$

Step 1 is the standard MMAE way of updating the weights. In Step 2, the weights are bounded from zero, which is necessary to prevent poorly performing estimators from "dying out". Step 3 normalizes the weights so the sum equals one. Finally, the MMAE state estimate is computed as the weighted sum of the state estimates of the individual filters:

$$\mathbf{X}_k = \sum_{i=1}^{N} W_{i,k} \cdot \mathbf{X}_{i,k} \qquad (24)$$

In a similar fashion, the transfer function residue estimate is calculated:

$$r_k = \sum_{i=1}^{N} W_{i,k} \cdot r_{i,k} \qquad (25)$$

The phase compensation β used by the P-POD is determined from the estimated residue:

$$\beta_k = 180° - \arg\{r_k\} \qquad (26)$$

It should be noted that if the residue estimate is close to zero (which is the case immediately after initializing the MMAE filter bank), the angle of the residue estimate is not clearly defined. Therefore, to avoid unpredictable behavior, the phase compensation β is not updated before the magnitude of the residue estimate is above a certain threshold. In all the presented results this threshold is set to 0.2.

Tuning of the Kalman Filters

In [12], it is found that multiplying both covariance matrices R and $\mathbf{Q}$ by the same constant does not affect the power oscillation damping performance of the P-POD. However, when running multiple filters in a MMAE scheme, the weights are determined by the likelihood functions of the filters, and the likelihood functions (as defined in (20)) are not independent of the scaling of the covariance matrices. A scaling coefficient k_σ is therefore introduced in (15), which scales the covariances of all filters as follows:

$$R = k_\sigma^2, \quad \mathbf{Q} = (2\pi f \cdot \Delta t \cdot k_c k_\sigma)^2 \cdot \mathbf{I}_3 \qquad (27)$$

The scaling coefficient should be chosen such that the filter weights converge fast enough (lower values of k_σ) to follow
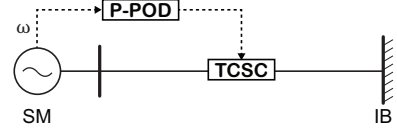

Fig. 2. The single line diagram shows the Single-Machine (SM) Infinite Bus (IB) system with a TCSC installed on the line. The P-POD measures the speed of the generator, and controls the TCSC.

changing operating conditions, but slow enough (higher values of k_σ) to avoid erratic, unpredictable evolution of the weights. Experience indicates that choosing the scaling coefficient such that the measurement noise variance R is in the same order of magnitude as the amplitude of the targeted oscillations is a good choice. In all the presented results, this is used as a starting point for choosing the covariance scaling coefficient.

IV. RESULTS

In this section, the MMAE-enhanced P-POD is tested on three different systems: The Single-Machine Infinite Bus system, Kundur's Two-Area System and the IEEE 39-Bus System. All simulations are carried out entirely in Python using the simulator described in [17] (available online [18]) which was developed specifically for the purpose of testing the proposed enhancement to the P-POD. In the simulations, all generators are represented by the 6th order synchronous machine model described in [19] (leakage reactance, armature resistance and saturation are neglected). Simulations are carried out with a time step of 5 ms, and the Kalman filters and control signals are updated every 20 ms. Common to all three systems is that the device modulated by the P-POD is a TCSC installed on one of the lines. The TCSC is modelled as described in [8], with a steady state compensation of 10% and minimum and maximum compensation limits of 1% and 50%, respectively. Further, the parameter $k_c = 0.2$ (as suggested in [12]), the minimum bound for the weights $\delta = 0.001$, and the number of filters $N = 10$.

A. Single-Machine Infinite Bus: Comparison with state of the art

In this section, the proposed adaptive P-POD is demonstrated and compared with an adaptive phase compensation scheme for the P-POD found in the literature: In [6] and [7], the P-POD is made adaptive by controlling the compensation angle using a Proportional Integral (PI) controller, aiming to drive the magnitude of the oscillations towards zero,

$$\beta(t) = -K_p \times |\vec{S}(t)| - K_i \times \int |\vec{S}(t)| dt \qquad (28)$$

where K_p and K_i are the proportional and integral gains. However, this scheme assumes that the P-POD is actually able to eliminate the oscillations completely. Considering the situation where the phase compensation β is initially at its optimal value, it is clear that β will immediately start drifting off this optimal value once oscillations are observed again, due to the integral of the magnitude of the phasor $|\vec{S}(t)|$.
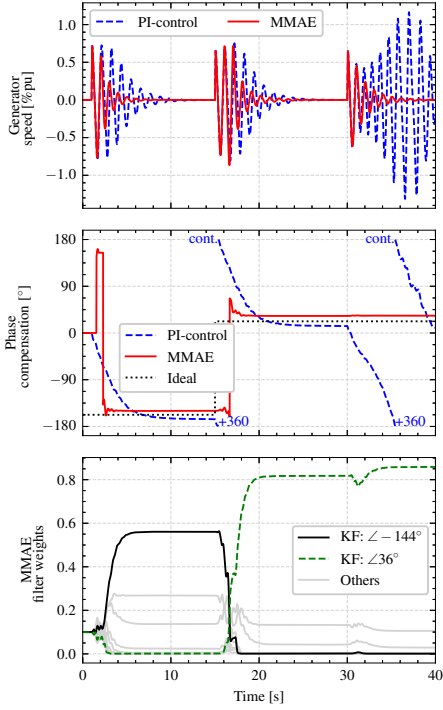
Fig. 4. The single-line diagram shows Kundur's Two-Area System. The locations where the TCSC is installed and where the measurement for the P-POD is obtained are indicated. (Source: Adapted from [13].)

Fig. 5. The results from three simulations from Kundur's Two-Area System are shown, as indicated. At $t = 20$ s, the largest load is disconnected. Prior to the loss of load, the uncontrolled system is unstable, and the two controlled cases are stable. After the loss of load, the static P-POD is unstable; only the adaptive P-POD is stable following both disturbances. This emphasizes the need for an adaptive controller.

Fig. 3. Two adaptive phase compensation schemes for the P-POD are compared on the Single-Machine Infinite Bus system. During the second disturbance ($t = 15$ s), a polarity reversal of the control signal is applied, requiring the controllers to change the phase compensation by $180°$ to avoid forced oscillations. During the third disturbance (at $t = 30$ s), the PI control-based scheme exhibits a weakness in that the phase compensation drifts away from a suitable value, causing forced oscillations for a short period. Thus, the MMAE scheme outperforms the PI control scheme in this case.

This PI control-based phase compensation scheme is compared with the proposed MMAE-based scheme. The covariance scaling coefficient $k_\sigma = 1$ for the filters in the MMAE filter bank. For the PI controller, the proportional and integral gains are $K_i = 1$ and $K_p = 1$. The control signal is amplified with gain $K = 0.2$ in both cases. The simulated system is a Single-Machine Infinite Bus system, with parameters given in [13, p. 752]. The output measurement is the rotor speed of the synchronous machine (in %pu), and the control signal modulates the reactance setpoint of a TCSC installed on the line. The system is shown in Fig. 2.

The simulated case contains three consecutive short circuits (at $t = 1$ s, $t = 15$ s and $t = 30$ s) at the terminals of the synchronous machine. Moreover, to test the capability of the two methods to properly adjust the phase compensation, an extra challenge is introduced: From the time of the second short circuit and onwards, a polarity reversal of the output from the controllers is simulated by multiplying the control signal by negative one. This means that an additional $180°$ is added to the actual residue angle. Thus, if the phase compensation is not adjusted at this point, the controllers will amplify rather
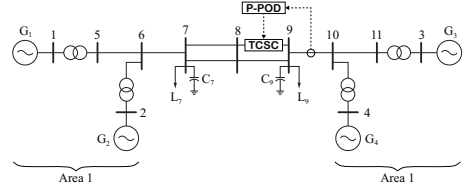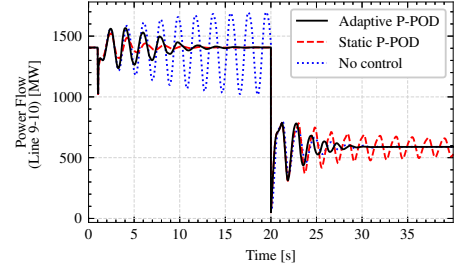
than mitigate the oscillations.

The results from the two simulations are shown in Fig. 3. It is observed that after the first short circuit, the ideal phase compensation is approximately reached for both controllers. Similarly, after the second short circuit, the phase compensation is adjusted to cope with the polarity reversal in both cases. However, after the third short circuit it is clear that the PI-controlled phase compensation drifts away from the ideal value, as postulated, causing growing oscillations for a short period until the phase compensation again starts converging towards the ideal value. For the proposed MMAE-based scheme, the estimated phase compensation stays close to the ideal value. Thus, the MMAE-based scheme outperforms the PI control-based scheme in this case.

The lower subplot in Fig. 3 shows how the weights evolve during the simulation. Following the first disturbance, the weight of the filter corresponding to a phase compensation of $-144°$ dominates, causing a phase compensation close to this value. Following the polarity reversal, the $36°$ filter dominates.

B. Kundur's Two-Area System: Loss of load

In this section, the proposed controller is tested on the often used two-area system, described in [20], which consists of two areas with two generators in each area. The two areas are interconnected by long transmission lines. All the generators are equipped with AVR and governor controls, but the stabilizers are deactivated. Modal analysis reveals that the system has an unstable inter-area mode under these conditions, with a frequency of 0.54 Hz and damping of -3%.
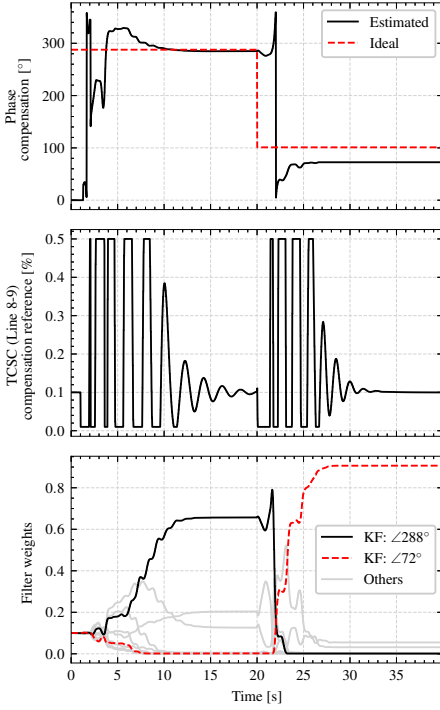
Fig. 6. From the simulation on Kundur's Two-Area System with the proposed MMAE P-POD, the phase compensation, the control signal and the evolution of the filter weights are shown. The phase compensation is shown along with the ideal value (computed from modal analysis). The control signal varies between the TCSC compensation limits of 1% and 50%. The filter weights shows that the filter corresponding to a phase compensation of 288° dominates before the loss of load, and after the loss of load the 72°-filter is the dominant.

Similarly as in the previous case, we would like to measure the power flow in a line and modulate the reactance reference of a TCSC in order to provide damping to the unstable inter-area mode. A preliminary residue analysis reveals that measuring the power flow in the line between buses 9 and 10 and modulating a TCSC on one of the inter-ties is a good choice. For reference, this is also the combination used for a similar problem in [21]. A single line diagram is given in Fig. 4. The gain $K = 0.01$ is used for the P-POD, and the covariance scaling coefficient for the MMAE scheme is $k_\sigma = 180$. The simulated event is a short circuit with a clearing time of 50 ms, which occurs at $t = 1$ s. Further, to test the capability of the adaptive controller to adjust to changing operating conditions, a loss of the largest load in the system (1767 MW on bus 9) occurs at $t = 20$ s.

Fig. 5 shows the active power measured in the line for three different cases, first: No control action being applied, second: A static (non-adaptive) P-POD with a constant phase compensation, third: The proposed adaptive P-POD with a MMAE estimator, where the phase compensation is adjusted automatically. The results show that the system is initially unstable without supplementary damping control of the TCSC.
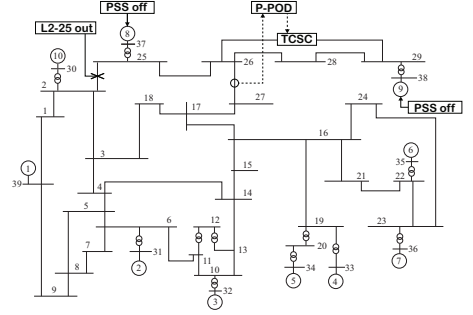

Fig. 7. The single line diagram shows the IEEE 39-Bus System, consisting of 39 buses and 10 generators. The system is stressed by deactivating two stabilizers and disconnecting a line, as indicated. (Source: Adapted from [22].)

Either of the two controls successfully stabilizes the system after the first short circuit. After the loss of load, the case with no control is stable, but the static P-POD produces forced oscillations. The adaptive P-POD stabilizes the situation both before and after the loss of load.

Fig. 6 shows in detail how the adaptive P-POD functions in this case: The first plot shows the phase compensation used by the controller, along with the ideal phase compensation (which is computed from modal analysis). The second plot shows the setpoint of the TCSC, which is modulated by the controller. The third plot shows the weights of the filters, where the dominant filters before and after the loss of load are highlighted; the 288°-filter causes a phase compensation close to this value before the loss of load, and similarly for the 72°-filter after the loss of load.

C. IEEE 39-Bus System: Varying communication latency

Finally, the proposed adaptive P-POD is tested on the IEEE 39-Bus system [22]. In this case, the aim is to test the robustness of the controller against data transmission latency. This is an important practical problem that must be addressed when working with wide area control, as the time delay between sending a PMU measurement and receiving it at the control center is not necessarily negligible.

Again, the measurement and the actuator is chosen based on preliminary residue analysis: The P-POD controls a TCSC installed on the line between buses 26 and 29, and the measurement is the active power flow in the line between buses 26 and 27. A single line diagram of the system is shown in Fig. 7. To stress the system and provoke an unstable operating condition, the stabilizers (PSS) at generators 8 and 9 are deactivated, and the line between buses 2 and 25 is disconnected. This makes the area constituted by buses 25, 26, 28, 29 and 38 weakly connected to the rest of the system, and results in an unstable 0.44 Hz mode with zero damping. The relevant residue in this case is $26.4\angle156°$, which gives an ideal phase compensation of $\beta = 180° - 156.6° = 23.4°$ (without latency compensation). The gain of the controller is set to $K = 0.03$, and the covariance scaling coefficient is $k_\sigma = 35$.
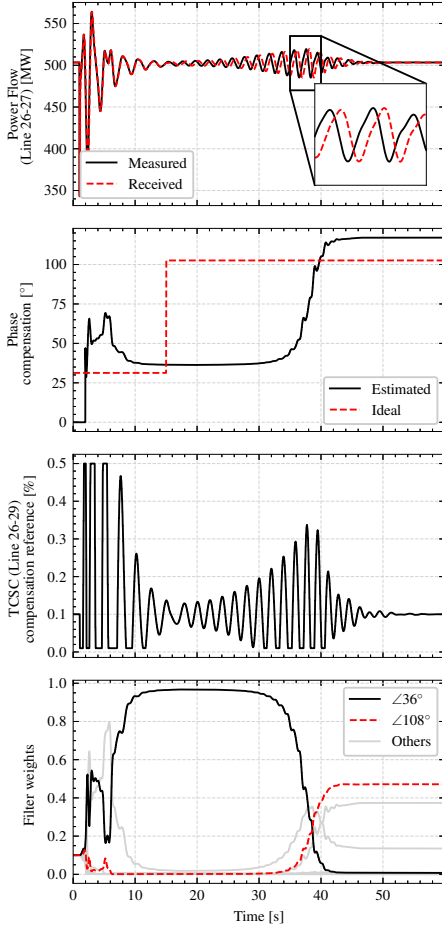
Fig. 8. Results from testing the proposed P-POD on the IEEE 39-Bus System are shown. As shown in the first plot, the received measurement at the location of the P-POD is delayed by 50 ms before $t = 15$ s, and 500 ms after $t = 15$ s. The second plot shows the phase compensation resulting from MMAE along with the ideal, latency-adjusted compensation. The third plot shows the applied control signal, and the final plot shows the evolution of the filter weights.

The simulated event is a short circuit occuring at $t = 1$ s. At the beginning of the simulation, there is a constant latency of 50 ms. At $t = 15$ s, the latency increases to 500 ms and stays constant throughout the simulation. The phase lag caused by the latency can be computed from $\omega \cdot t_{lag}$, which gives approx. $8°$ and $80°$ for the two latencies, respectively. Thus, the ideal phase compensation at the beginning of the simulation is is $23.4° + 8° = 31.4°$, and after the latency increase it is $23.4° + 80° = 103°$.

The results in Fig. 8 shows that the P-POD finds a suitable phase compensation close to the ideal value after the short circuit. The latency increase causes growing oscillations for a short period, before the phase compensation is adjusted in order to cope with the phase lag caused by time delay.

V. DISCUSSION

The proposed controller is tested on three different systems, and is capable of eliminating low damped oscillations in all cases despite drastic changes in operating conditions. For each case the controller requires tuning of the gain K (in (2)) and the covariance matrix scaling coefficient k_σ (in (27)). Also, the frequency of the low damped mode and the magnitude of the required residue are specified as parameters of the controller. Apart from this, no tuning or customization of the controller is required for each specific case.

Furthermore, the magnitude of the residue could be estimated by adding more filters to the bank. In the presented results the residues assigned to the filters differ only in rotation angle (as given by 16). More filters could be added and assigned residues with varying magnitudes, which would allow also the residue magnitude to be estimated. This would eliminate the requirement of knowledge of the residue magnitude, thus making the proposed controller more general.

In the first result, the proposed adaptive phase compensation scheme based on MMAE outperforms the PI-controlled adaptive phase compensation scheme used in [6] and [7]. The latter scheme is found to possess a weakness (i.e. drifting away from an optimal phase compensation) that the proposed scheme does not possess.

In the second result, the proposed P-POD is demonstrated on a large, non-linear disturbance. The capability to adapt to changing operating conditions is a valuable trait in the future power system, where it is expected that the system will have a wider range of operating points, and the operating point will vary more rapidly. Furthermore, extreme weather is expected to become more frequent in he future, which could cause severe events like loss of large loads (as in the simulated case) to become more frequent.

In the third result, the controller is tested on a significantly larger and more complex system. Robustness against latency opens up for using the P-POD in a wide-area framework, allowing remote measurements from PMUs to be used as the measurement signal for the P-POD. It should be noted, however, that sophisticated methods for alleviating the issue of latency specifically for the P-POD are developed in [6] and [7]. Combining these methods with the proposed MMAE scheme would most probably improve the result in Fig. 8.

Oscillations are successfully damped in all cases, which is the main objective. However, the ideal phase compensation is only approximately reached in some cases (e.g. in Fig. 6, the phase compensation is about 20 to $25°$off the ideal value at the end of the simulation, and in Fig. 8 it is about 15 to $20°$off). This can be understood by considering the fact that all filters in the MMAE filter bank are equal if the control signal is zero (as can be seen by studying (17)). Thus, if the ideal phase compensation is not reached before the oscillations are damped out, then the filter weights will stop evolving, and the final phase compensation will not be equal to the ideal value.

In 1965, when the MMAE scheme was invented, it was considered impractical for online implementation [15] due to the computational burden of running a high number of Kalman filters in parallel. However, given advances in computer technology since then, this no longer remains an issue.

For the presented MMAE-based adaptive P-POD, this has been confirmed by testing all the presented systems in simulations which are synchronized to wall-clock time. By using the multiprocessing-module in Python, the simulation is run in one process, and the MMAE-based controller in another process. Testing indicates that there is no issue with operating a MMAE filter bank of 10 filters online, running on an average laptop. If a higher number of filters is required, the computational burden could easily be reduced by parallelization of the filter updates.

For the sake of simplicity the presented theory and results consider systems with only a single low damped mode. However, in large transmission systems, multiple low damped modes might be excited at the same time. Modifications to the P-POD estimation algorithm to accommodate multiple low damped modes are described in e.g. [23]. A topic of further research is to introduce similar modifications to the phasor estimation algorithm proposed in this paper.

VI. CONCLUSION

In this paper, a novel adaptive Phasor Power Oscillation Damper has been developed and tested. Adaptive phase compensation is achieved by introducing a Multiple Model Adaptive Estimator, which results in a controller that requires very little tuning or customization before application to a new system. The proposed scheme outperforms a comparable scheme found in the literature under the tested conditions. It is also found that the controller performs satisfactorily during changing operating conditions caused by a large disturbance, and is capable of eliminating phase lag caused by latency.

REFERENCES

[1] D. N. Kosterev, C. W. Taylor, and W. Fellow, "Model Validation for the August 10, 1996 WSCC System Outage," *IEEE Transactions on Power Systems*, vol. 14, no. 3, pp. 967–979, 1999.

[2] ENTSO-E SubGroup System Protection and Dynamics, "Analysis of CE Inter-Area Oscillations of 1st December 2016," Tech. Rep. December, 2017.

[3] ——, "Oscillation Event 03.12.2017," Tech. Rep. March, 2018.

[4] L. Ängquist and C. Gama, "Damping algorithm based on phasor estimation," in *IEEE Power Engineering Society Winter Meeting*, vol. 3, 2001, pp. 1160–1165.

[5] N. R. Chaudhuri, S. Ray, R. Majumder, and B. Chaudhuri, "A case study on challenges for robust wide-area phasor POD," in *IEEE Power Engineering Society Winter Meeting*, 2009.

[6] ——, "A new approach to continuous latency compensation with adaptive phasor power oscillation damping controller (POD)," *IEEE Transactions on Power Systems*, vol. 25, no. 2, pp. 939–946, 2010.

[7] S. S. Yu, T. K. Chau, T. Fernando, and H. H. C. Iu, "An Enhanced Adaptive Phasor Power Oscillation Damping Approach with Latency Compensation for Modern Power Systems," *IEEE Transactions on Power Systems*, vol. 33, no. 4, pp. 4285–4296, 2018.

[8] B. Chaudhuri, R. Majumder, and B. C. Pal, "Application of multiple-model adaptive control strategy for robust damping of interarea oscillations in power system," *IEEE Transactions on Control Systems Technology*, vol. 12, no. 5, pp. 727–736, 2004.

[9] I. Zenelis, X. Wang, and I. Kamwa, "Online PMU-Based Wide-Area Damping Control for Multiple Inter-Area Modes," *IEEE Transactions on Smart Grid*, vol. 11, no. 6, pp. 5451–5461, 2020.

[10] V. Pradhan, A. M. Kulkarni, and S. A. Khaparde, "A Model-Free Approach for Emergency Damping Control Using Wide Area Measurements," *IEEE Transactions on Power Systems*, vol. 33, no. 5, pp. 4902–4912, 2018.

[11] M. Beza and M. Bongiorno, "A Modified RLS Algorithm for Online Estimation of Low-Frequency Oscillations in Power Systems," *IEEE Transactions on Power Systems*, vol. 31, no. 3, pp. 1703–1714, 2016.

[12] H. Haugdal, K. Uhlen, and H. Jóhannsson, "Achieving increased Phasor POD performance by introducing a Control-Input Model," *arXiv:2111.00968*, 2021.

[13] P. Kundur, *Power System Stability and Control*. New York: McGraw-Hill, 1994.

[14] X. Yang and A. Fellachi, "Stabilization of inter area oscillation modes through excitation systems," *IEEE Transactions on Power Systems*, vol. 9, no. 1, pp. 494–502, 1994.

[15] R. G. Brown and P. Y. C. Hwang, *Introduction to random signals and applied Kalman filtering*, 4th ed. Hoboken, NJ: Wiley, 2012.

[16] J. F. Martin, A. M. Schneider, and N. T. Smith, "Multiple-Model Adaptive Control of Blood Pressure Using Sodium Nitroprusside," *IEEE Transactions on Biomedical Engineering*, vol. BME-34, no. 8, pp. 603–611, 1987.

[17] H. Haugdal, K. Uhlen, and H. Johannsson, "An Open Source Power System Simulator in Python for Efficient Prototyping of WAMPAC Applications," in *2021 IEEE Madrid PowerTech*. IEEE, 2021, pp. 1–6. [Online]. Available: https://ieeexplore.ieee.org/document/9494770/

[18] H. Haugdal, "DynPSSimPy," *Zenodo*, 2020. [Online]. Available: http://doi.org/10.5281/zenodo.4290126

[19] J. Machowski, J. Bumby, and J. Bialek, *Power system dynamics: Stability and control*, 2nd ed. Wiley, 2008.

[20] M. Klein, G. J. Rogers, and P. Kundur, "A fundamental study of inter-area oscillations in power systems," *IEEE Transactions on Power Systems*, vol. 6, no. 3, pp. 914–921, 1991.

[21] B. Pal and B. Chaudhuri, *Robust Control in Power Systems*, ser. Power Electronics and Power Systems. Boston: Springer US, 2005.

[22] M. A. Pai, *Energy Function Analysis for Power System Stability*. Boston, MA: Springer US, 1989.

[23] N. R. Chaudhuri and B. Chaudhuri, "Damping and relative mode-shape estimation in near real-time through phasor approach," *IEEE Transactions on Power Systems*, vol. 26, no. 1, pp. 364–373, 2011.

Hallvar Haugdal received the M.Sc. degree in electrical power engineering from the Norwegian University of Science and Technology (NTNU) in 2016. He is currently pursuing his Ph.D. on Wide Area Monitoring and Control. Current research interests include power system dynamics and simulation, electromechanical oscillations and electric machines.

Kjetil Obstfelder Uhlen received the master's and Ph.D. degrees in control engineering in 1986 and 1994 respectively. He is a Professor of power systems with the Norwegian University of Science and Technology (NTNU), Trondheim, and a Special Adviser at STATNETT (the Norwegian TSO). His main areas of work include research and education within control and operation of power systems, grid integration of renewable energy, and power system dynamics.

Hjörtur Jóhannsson (M'11) received the M.Sc. and Ph.D. degrees in electrical engineering from the Technical University of Denmark, Kongens Lyngby, Denmark, in 2007 and 2011, respectively, where he is currently a Senior Scientific Consultant with the Center of Electric Power and Energy, Department of Electrical Engineering. His research interests include the development of methods for secure and stable operation of power systems with a high share of RES-based production, with special focus on real-time approaches.